

The sedimentary record of submarine channel morphodynamics

Jan de Leeuw

UTRECHT STUDIES IN EARTH SCIENCES

mededelingen van de
Faculteit Geowetenschappen
Universiteit Utrecht
No. 134

Examination committee:

Dr. ing. M. Bolla Pittaluga
Department of Civil, Chemical and Environmental Engineering, University of Genoa
Genoa, Italy

Prof. dr. M.G. Kleinans
Department of Physical Geography, Utrecht University
Utrecht, The Netherlands

Prof. dr. W. Krijgsman
Department of Earth Sciences, Utrecht University
Utrecht, The Netherlands

Prof. dr. A.W. Martinius
Faculty of Civil Engineering and Geosciences, Delft University of Technology
Delft, The Netherlands

Prof. dr. J.J.G. Reijmer
College of Petroleum Engineering and Geosciences, King Fahd University of Petroleum and
Minerals
Dhahran, Saudi Arabia



The research was carried at the Sedimentology Research Group, Department of Earth Sciences,
Faculty of Geosciences, Utrecht University.

This study was financially supported by the Netherlands Organisation for Scientific Research
(grant number: NWO-ALW 864.13.006), ExxonMobil, Shell and Statoil.

ISBN 978-90-6266-476-4

Copyright © Jan de Leeuw, Faculty of Geosciences, Utrecht University, 2017

All rights reserved. No part of this publication may be reproduced in any form, by print or photo
print, microfilm or any other means, without written permission by the author.

The sedimentary record of submarine channel morphodynamics

Het sedimentaire archief van de morfodynamica van onderzeese geulen
(met een samenvatting in het Nederlands)

Proefschrift

ter verkrijging van de graad van doctor aan de Universiteit Utrecht op gezag van de rector
magnificus, prof.dr. G.J. van der Zwaan, ingevolge het besluit van het college voor promoties in
het openbaar te verdedigen op woensdag 6 september 2017 des middags te 2.30 uur

door

Jan de Leeuw
geboren op 28 juni 1988
te Amsterdam

Promotor: Prof. dr. P.L. de Boer

Copromotoren: Dr. J.T. Eggenhuisen
Dr. M.J.B. Cartigny

Contents

| | |
|---|-----------|
| Chapter 1 Introduction..... | 9 |
| 1.1 Deep-water sedimentation..... | 9 |
| 1.2 Historical perspective..... | 10 |
| 1.3 Components of deep-water sediment routing systems..... | 13 |
| 1.4 Large mud-rich vs small sand-rich fans..... | 13 |
| 1.5 Submarine fan activity..... | 14 |
| 1.6 Leveed channels..... | 15 |
| 1.6.1 Morphology and deposits of leveed channels..... | 15 |
| 1.6.2 Flow in leveed channels..... | 16 |
| 1.7 Measuring turbidity currents on the sea floor..... | 17 |
| 1.8 Physical and Numerical modelling..... | 17 |
| 1.9 Aim and objectives of this study..... | 19 |
| 1.10 Overview of this thesis..... | 22 |
| | |
| Chapter 2 Morphodynamics of submarine channel inception revealed by new experimental approach..... | 23 |
| 2.1 Introduction..... | 24 |
| 2.2 Methods..... | 25 |
| 2.2.1 Description of the set-up..... | 25 |
| 2.2.2 Sediment suspensions..... | 25 |
| 2.2.3 Data collection..... | 25 |
| 2.2.4 Calculations of flow conditions..... | 25 |
| 2.3 Results..... | 26 |
| 2.3.1 Scaling approach..... | 26 |
| 2.3.2 Comparison with natural currents and previous experiments..... | 28 |
| 2.3.3 Morphological evolution..... | 28 |
| 2.3.4 Evolution of the flow field..... | 30 |
| 2.4 Discussion..... | 32 |
| 2.5 Supplementary materials..... | 33 |
| | |
| Chapter 3 Linking submarine channel-levee facies and architecture to flow structure of turbidity currents; insights from flume tank experiments..... | 37 |
| 3.1 Introduction..... | 38 |
| 3.2 Methods..... | 40 |
| 3.2.1 3D channel formation experiments..... | 40 |
| 3.2.2 2D flow sampling experiments..... | 42 |
| 3.2.3 Integration of the results from the 2D and 3D experiments..... | 43 |

| | | |
|-------|--|----|
| 3.3 | Results | 44 |
| 3.3.1 | 3D experiments..... | 44 |
| 3.3.2 | 2D experiments..... | 50 |
| 3.4 | Discussion..... | 52 |
| 3.4.1 | Flow structure in the channel | 52 |
| 3.4.2 | Relating vertical sorting in turbidity currents to fining-upward levees | 53 |
| 3.4.3 | Is deposition on the levees driven by competence or near-bed capacity? | 55 |
| 3.4.4 | Predicting the morphological evolution of the channel from the density structure of the flow | 57 |
| 3.5 | Conclusions | 59 |

Chapter 4 | Sediment volume and grain-size partitioning between submarine channel-levee systems and lobes: An experimental study..... 61

| | | |
|-------|--|----|
| 4.1 | Introduction..... | 62 |
| 4.2 | Methods..... | 64 |
| 4.2.1 | Set-up, procedure and measurements..... | 64 |
| 4.2.2 | Mass-balance analysis | 65 |
| 4.3 | Results | 69 |
| 4.3.1 | Deposit volume distribution | 69 |
| 4.3.2 | Grain size of deposits..... | 72 |
| 4.3.3 | Velocity structure of channelised turbidity currents | 74 |
| 4.3.4 | Reconstruction of turbidity current runout | 74 |
| 4.4 | Discussion..... | 78 |
| 4.4.1 | Channel geometry and sediment partitioning..... | 78 |
| 4.4.2 | Sediment partitioning in natural systems compared with experiments | 81 |
| 4.4.3 | Deep-water systems in a mass-balance framework | 85 |
| 4.5 | Conclusions | 85 |

Chapter 5 | Turbulent diffusion modelling of grain-size segregation in polydisperse turbidity currents; an experimental validation and possibilities for application 87

| | | |
|-------|--|-----|
| 5.1 | Introduction..... | 88 |
| 5.2 | Methods..... | 89 |
| 5.2.1 | Grain-size stratification model | 89 |
| 5.2.2 | Experiment procedure..... | 92 |
| 5.2.3 | Inputs from experiments for the analytical model..... | 92 |
| 5.3 | Results | 95 |
| 5.3.1 | Flume experiments | 95 |
| 5.3.2 | Comparison of model results and experiments | 96 |
| 5.4 | Discussion..... | 98 |
| 5.4.1 | Origin of similarities and differences between model and experiments | 98 |
| 5.4.2 | Controls on grain-size gradient in turbidity currents..... | 99 |
| 5.4.3 | Vertical change in grain size distribution in experiments compared to natural systems..... | 100 |
| 5.4.4 | Reconstructing turbidity current flow properties from the rock record..... | 101 |
| 5.5 | Conclusions | 103 |

| | |
|---|------------|
| Chapter 6 Reconstructing turbidity current flow properties from submarine channel deposits using stratification modelling; application to the Gabriela Channel fill, Tres Pasos Formation, Chile | 105 |
| 6.1 Introduction..... | 106 |
| 6.2 Description of the Gabriela Channel outcrop..... | 107 |
| 6.2.1 Geological setting | 107 |
| 6.2.2 Facies descriptions | 110 |
| 6.2.3 Architecture of Gabriela Channel outcrop..... | 113 |
| 6.3 Grain-size distribution of channel axis and margin samples..... | 113 |
| 6.3.1 Methodology: sample collection and thin section grain-size analysis | 113 |
| 6.3.2 Results: grain-size distribution of channel axis and margin deposits | 115 |
| 6.4 Modelling of grain-size stratification..... | 117 |
| 6.4.1 Model approach | 117 |
| 6.4.2 Interpreted channel morphology and flow thickness | 117 |
| 6.4.3 Grain-size stratification from deposits..... | 118 |
| 6.4.4 Matching deposit data with the model to reconstruct flow properties..... | 119 |
| 6.5 Discussion..... | 122 |
| 6.5.1 Synchronicity of channel-axis and margin deposits | 122 |
| 6.5.2 Turbidity-current flow properties..... | 122 |
| 6.5.3 Reconstruction of sediment transfer in the submarine channel | 125 |
| 6.5.4 Interpretation of the shear velocity to settling velocity ratio | 127 |
| 6.6 Conclusions | 127 |
| Chapter 7 Synthesis | 129 |
| 7.1 Morphodynamics of submarine channels in flume experiments | 129 |
| 7.2 Grain-size stratification of channelised turbidity currents | 130 |
| 7.3 Submarine fans in a mass-balance perspective | 131 |
| References | 133 |
| Samenvatting | 142 |
| Acknowledgements..... | 146 |
| Curriculum Vitae..... | 148 |
| List of publications | 149 |

“And so castles made of sand, fall in the sea, eventually”

Jimi Hendrix

Chapter 1

Introduction

1.1 Deep-water sedimentation

Rivers transport erosion products from the continent to the shore where part of the sediment is often stored in deltas. A significant fraction of the sediment is only temporarily stored near the shoreline and eventually transported further into the ocean. Much of the sediment transport on the ocean floor occurs by turbidity currents: sediment-laden gravity flows that move down the continental slope towards and across the sea floor. Figure 1.1 shows a small turbidity current in the Eurotank Laboratory in Utrecht. Turbidity currents derive their driving force from the suspended sediment which gives them a higher density than the surrounding sea water. Some turbidity currents maintain their motion at very low slope angles ($<0.1^\circ$; Talling et al., 2007; Kneller et al., 2016) and have a runout distance of 1000s of kilometres.

Sustained turbidity current activity leads to the formation of submarine fans which form some of the largest sediment bodies on Earth. Submarine fans on the modern sea floor can, in many cases, be linked to rivers acting as sediment sources. The largest submarine fan, both in terms of length and volume, is found in the Bay of Bengal (Fig. 1.2; Covault et al., 2011). Sediment volume of the Bengal Submarine Fan is estimated at $12.5 \times 10^6 \text{ km}^3$; its length is $\sim 3000 \text{ km}$, and the water depth at its distal end is 5000 m (Curry et al., 2002). The exceptional size of the Bengal Fan relates to the drainage from the Himalayan mountain front which supplied a vast volume of sediment to the submarine fan over the past 55 Myr.

Submarine fans appear to have a smooth surface on small-scale maps (Fig. 1.2). However, on close inspection extensive channel networks are seen on all major submarine fans. These channels are the conduits through which turbidity currents cover large distances across the ocean floor. Numerous meandering channels have been identified, for example, on the Amazon Fan (Fig. 1.3; Pirmez et al., 2000). These channels were sequentially active and the channel fills and levees constitute a large part of the stratigraphy of the fan (Fig. 1.3C). Depth of channels in large

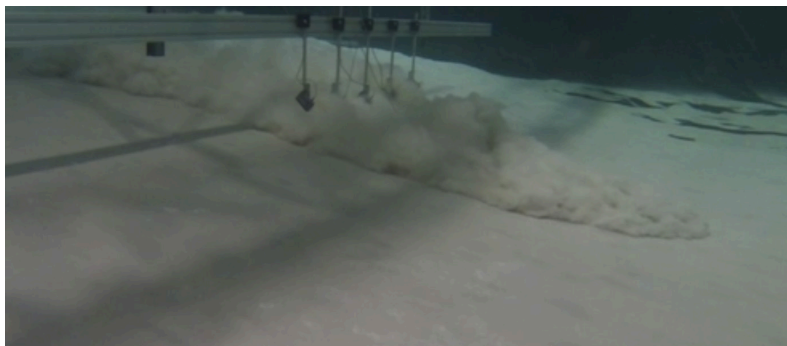


Figure 1.1: *Small-scale turbidity current in the Eurotank Flume Laboratory. Thickness of the current is $\sim 0.1 \text{ m}$ and the maximum velocity is $\sim 1 \text{ m/s}$.*

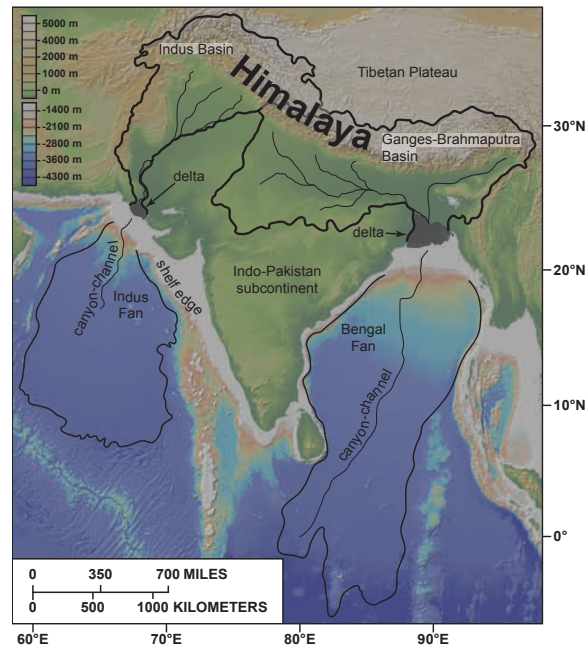


Figure 1.2: *Sediment routing systems from the Himalaya to the deep-sea fans in the Bay of Bengal and the Arabian Sea. The Indus River supplies sediment to the Indus Fan. The Ganges and the Brahmaputra Rivers supply sediment to the Bengal Fan. (Covault et al., 2011)*

submarine fans is of the order of 100 m and the width ~1 km. The planform morphology of these submarine channels is quite similar to that of meandering rivers on the continent but this external similarity is somewhat deceiving, as flows in the two types of channels are vastly different. For example, the density contrast between turbidity currents and the ambient medium (sea water) is much smaller than in rivers (water and air). Also, in contrast to water flowing in rivers, turbidity currents experience significant friction at their upper boundary with the ambient sea water.

Turbidite deposition in submarine fans has been an active research topic in the last decades. One important motive was the hydrocarbon potential of turbidity-current deposits. Thick-bedded turbidite sandstones often have a good reservoir quality while the organic material contained in the deposits can serve as a hydrocarbon source. Many of the frontier exploration targets for oil and gas have recently been in deep-water deposits (cf. Pettingill & Weimer, 2002). Additionally, sedimentation in submarine fans is recognized as a major sink for organic carbon. Sedimentation on submarine fans therefore plays a role in long-term climate regulation (Galy et al., 2007). Turbidity currents can damage sea-floor infrastructure such as pipelines and communication cables. Predicting the likely routes of turbidity currents is therefore important when planning such infrastructure.

1.2 Historical perspective

Prior to the 1920s, it was only possible to measure the depth or to take a sediment sample from the ocean floor by dropping a weighted line. The invention of the echo sounder made depth measurements much more efficient and made it possible to produce detailed bathymetric maps of

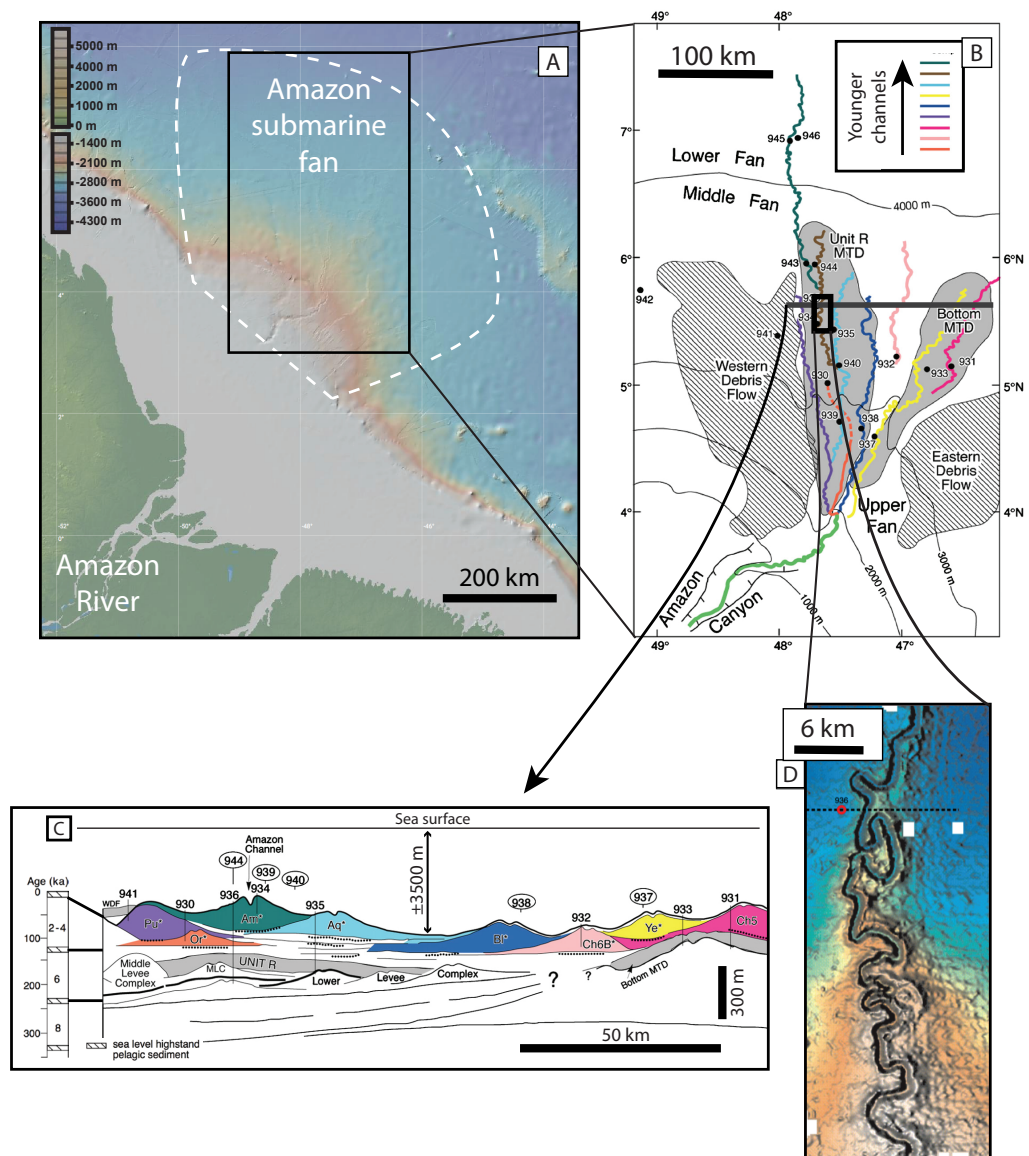


Figure 1.3: Overview of the Amazon submarine Fan. (A) Location of the Amazon Fan along the continental shelf edge. (B) Map of the submarine fan with channel-levee complexes that were sequentially active. (C) E-W oriented cross-section of the middle fan. Numbers indicate the locations of ODP drill sites. Note the overlap of adjacent channel-levee complexes. (D) Map view of a section of the Amazon Channel that is highly sinuous. Modified after Pirmez *et al.* (2000) and Maslin *et al.* (2006).

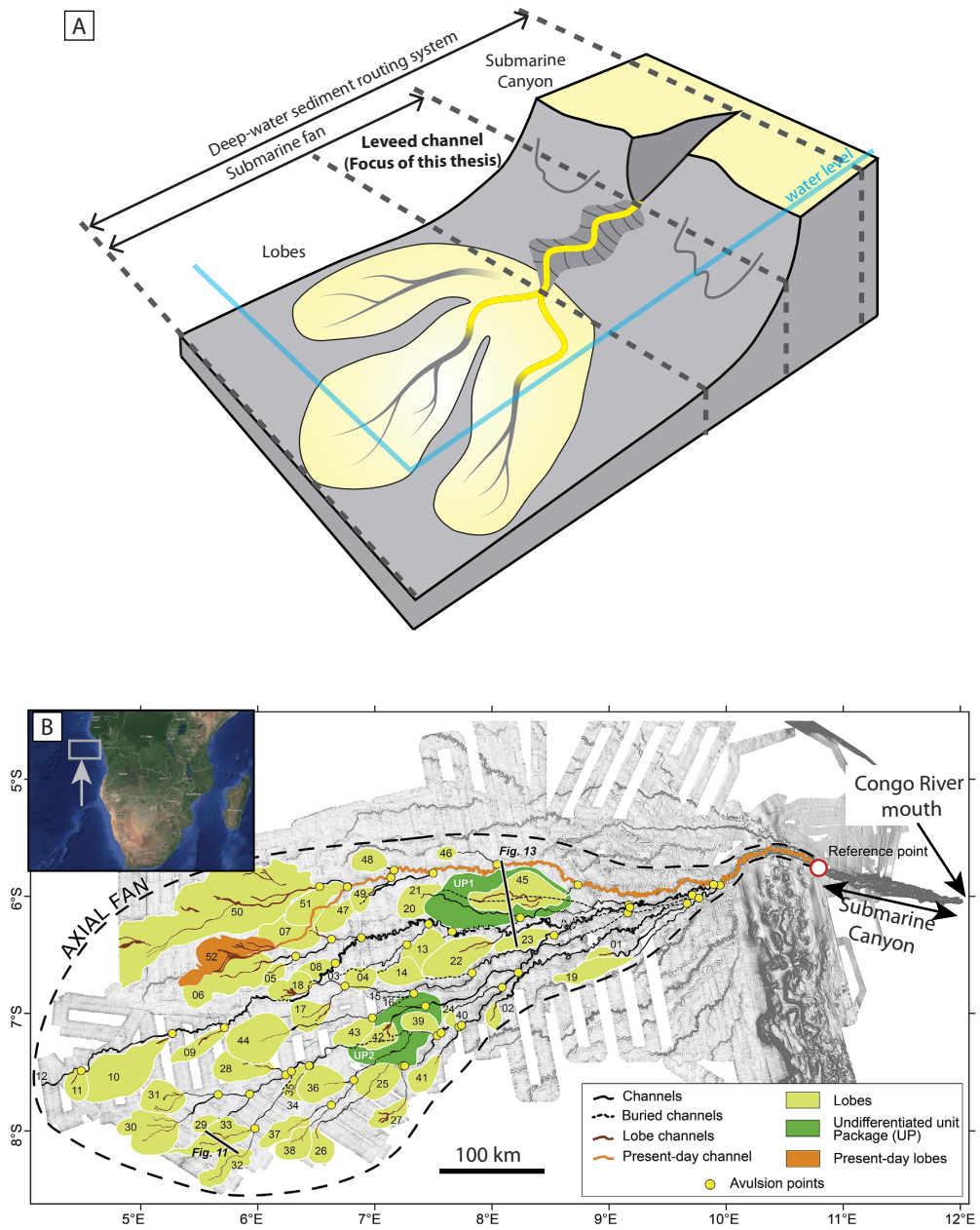


Figure 1.4: Main components of a deep-water sediment routing system. (A) Sketch of a submarine canyon and fan. The fan consists of leveed channels with lobes at the downstream end. (B) Congo Canyon and Fan. The focus of the present study is on the leveed channels. Note that leveed channels represent the longest segment of the sediment routing system in the Congo Fan as well as in many other fans. (modified after Picot et al., 2016 and Haughton, 2013).

the ocean floor. These maps revealed submarine canyons, which were incised into the continental margins, were present at many locations around the world (Daly, 1936). Most submarine canyons were found at the mouth of major rivers. This led to a debate about the origin of these canyons. One possibility was that they had formed during periods of sea-level lowstand, when the shoreline was further out and rivers incised the continental margin. However, sea level during the last ice ages was then estimated about 100 m lower than today, while most of the canyons are much deeper. For example, the Monterey Canyon offshore California is similar in scale to the Grand Canyon. Daly (1936) therefore hypothesized that bottom currents driven by the excess density of suspended sediment had eroded these canyons. These currents would later become known as turbidity currents (Kuenen & Migliorini, 1950). However, it was acknowledged that direct observations would be needed to substantiate this idea.

Direct evidence for turbidity current activity came from the breaking of communication cables. In 1929 an earthquake with magnitude 7.2 occurred off the coast of Newfoundland (Heezen & Ewing, 1952). Transatlantic communication cables on the sea floor started breaking in the hours after the earthquake. Cables that were closest to the earthquake epicentre broke first while cables farther away broke later. Heezen and Ewing (1952) considered different options such as progressive fault activity, but concluded that turbidity currents provided the only satisfactory explanation for these observations. The distance and difference in timing between the cable breaks provided an estimate of the current velocity of up to 70 km/h. Cables broke more than 700 km from the epicentre of the earthquake indicating a very long runout distance of this turbidity current. It was later found that the volume of sediment mobilised on the submarine slope during the 1929 event was $\sim 150 \text{ km}^3$ (Piper et al., 1999).

1.3 Components of deep-water sediment routing systems

Several main components are typically recognised in deep-water sediment routing systems (Fig. 1.4A). Submarine canyons are valleys that incise into the shelf. These canyons grade down-slope into channels with levees, the latter formed by overbank deposition. Lobes form at the downstream end of submarine channels due to loss of confinement of the turbidity current and lateral spreading of the flow. The regions where depositional turbidity currents form the leveed channels and lobes are together named the submarine fan (Normark, 1970). The submarine channels often cover the larger part of the runout distance of turbidity currents. In the Congo Fan for example (Fig 1.4B), the length of the canyon is $\sim 150 \text{ km}$, the length of the most recent leveed channel $\sim 700 \text{ km}$ and the length of the lobe at the end of the channel $\sim 80 \text{ km}$. Volumetrically, channel-related deposits are also the most important component of the Congo Fan. These deposits make up 70% of the total fan volume (Picot et al., 2016). Lobes at the downstream end of these channels make up the remaining 30% of the stratigraphy. Thus, submarine channels do not only facilitate sediment transfer towards the deeper ocean, their levees and channel fill deposits also form a major portion of the stratigraphy.

1.4 Large mud-rich vs small sand-rich fans

Submarine fans occur in different types of basins (Fig. 1.5). The two main basin types that can be distinguished are oceanic basins that are underlain by oceanic crust, and bound by continental margins, and smaller epicontinental basins such as foreland basins. Submarine fans in oceanic basins are generally mud-rich, characterised by extensive meandering leveed channels, and up to 1000s of kilometres long (Figs 1.2, 1.3B, 1.4B). Data obtained from these large mud-rich submarine fans is usually obtained by bathymetric surveys, sometimes in combination with seismic

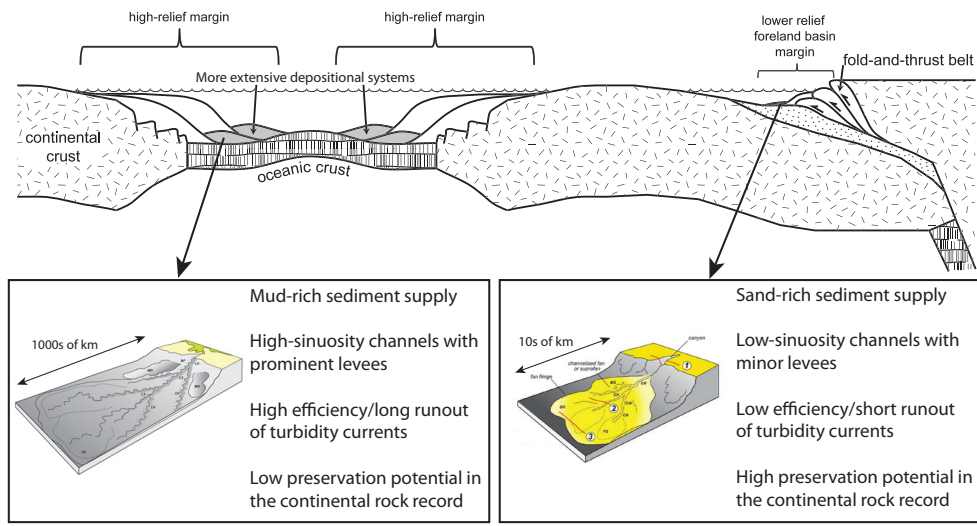


Figure 1.5: Basin configuration and the associated characteristics of submarine fans. Submarine fans on continental margins and in foreland basins have different characteristics. Modified after Covault et al., 2012 and Haughton (2013).

profiling (Fig. 1.6). These types of data provide excellent constraints on the large-scale geometries but lithological control is often absent or limited to a small number of deep-sea cores. Because these submarine fans are located on ocean crust which is prone to subduction they have little chance to be preserved in the continental rock record (Peakall et al., 2000, Kane et al., 2017) (Fig. 1.5).

Submarine fans on foreland basin margins are much smaller in size, partially due to the smaller water depth in such basins. Systems in foreland basins tend to be more sand-rich because the distance between the source area (the adjacent mountain front) and the submarine fan is relatively small (Pickering & Hiscott, 2015). Submarine channels in these systems generally have a lower sinuosity and levees are less prominent. Foreland basin fills have a higher chance to be preserved in the continental rock record and turbidite deposits in this type of basin can therefore be studied in subaerial outcrops at many locations. Outcrops provide the opportunity to make detailed observations on deposit characteristics such as sedimentary structures and grain size. However, the large-scale geometries of the basin infill are often less well constrained because outcrops are limited in size and outcrop data are largely two-dimensional. A few exhumed basins provide the combination of control on the large-scale stratigraphic architecture and detailed lithological control from outcrops. An excellent example is the Magallanes Basin in Chile (Romans et al., 2011).

1.5 Submarine fan activity

The activity of submarine fans is commonly modulated by glacial-interglacial sea-level cycles. For example, the Amazon Fan received turbidity currents every 1-2 years (Pirmez & Imran, 2003) before the Holocene. It ceased to be active when sea level rose after the last glaciation and the submarine canyon got disconnected from the Amazon River (Fig. 1.3A). Other submarine

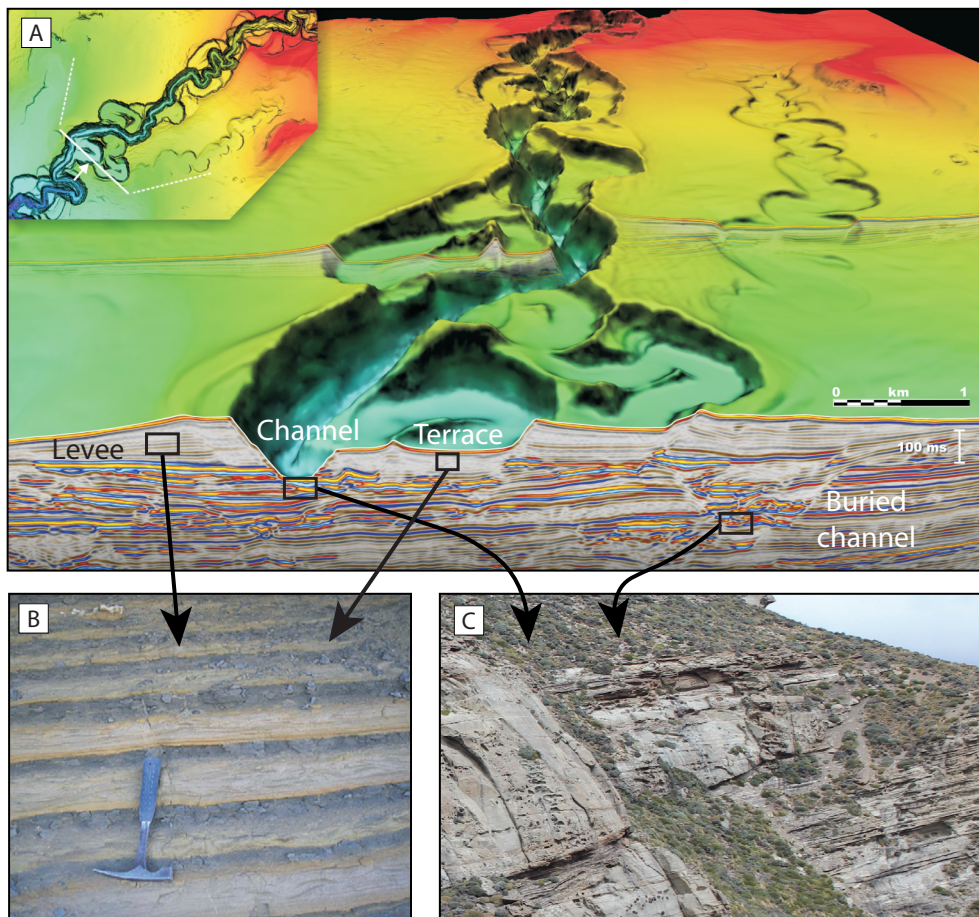


Figure 1.6: (A) Visualisation of a leveed submarine channel from the Niger Delta slope with a bathymetric map and a 3D seismic dataset. Levees on the channel margins form wedges thinning away from the channel. Weak internal reflections indicate fine-grained lithologies. Channel fills are associated with bright seismic reflections indicating coarse-grained lithologies. (B) Outcrop example of levee facies consisting of thin-bedded fine sandstone alternating with mud (Kane et al., 2011). (C) Outcrop example of axial channel-fill facies consisting of thick-bedded structureless sandstone.

fans, such as the Congo Fan (Fig. 1.4B), are presently still active because their canyon remained connected to a river mouth.

Another forcing of fan activity is climate change, which may occur in conjunction with sea-level changes or over longer periods. Climate acts as a control on the release of sediment from the drainage basin that supplies sediment to submarine fans. For example, rainfall and temperature control the amount and type of erosion (mechanical or chemical) and thereby the volume and composition of the sediment delivered.

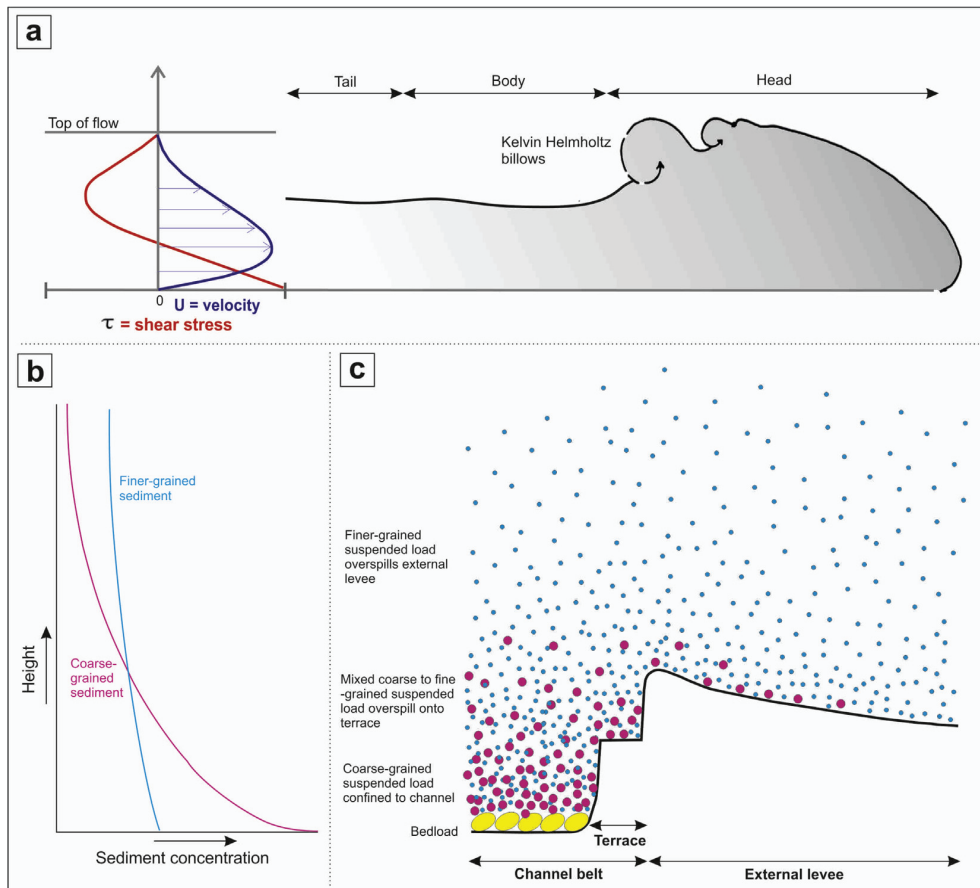


Figure 1.7: (A) Velocity and shear-stress profile of a turbidity current reflecting the combined effect of shear at the base and top of the flow. (B) Concentration profiles for sediment of different grain sizes suspended in the same flow. (C) Schematic representation of a leveed channel containing a stratified turbidity current. Grain-size distribution of the deposits is a function of height above the channel thalweg as a result of grain-size stratification in the flow. Figure from Hansen et al. (2015).

1.6 Leveed channels

1.6.1 Morphology and deposits of leveed channels

Information on leveed submarine channels comes both from the stratigraphic record and from the modern sea floor. In some cases, the two perspectives can be integrated when a combination of sea-floor morphology and architecture of the underlying deposits is available (Fig. 1.6A). The stratigraphic record of leveed channels consists of three main components: levees, terraces and channel fills. Levees are wedge-shaped sediment bodies that thin away from the genetically related channel (Kane & Hodgson, 2011). Their internal stratigraphy consists of thin normally graded beds with a maximum grain size of fine sand or silt at the base of the bed (Fig. 1.6B). The facies of terraces inside the channel is comparable. Channel fills are generally thick-bedded or amalgamated sandstone bodies with an erosional concave-down basis (Fig. 1.6C). The relation

between the original morphology of submarine channels and the geometry of channel fills will be discussed in the subsequent chapters.

1.6.2 Flow in leveed channels

Most submarine channels are characterised by a combination of erosional and constructional confinement (Clark & Pickering, 1996). The erosional confinement is the result of focussed erosion in the channel thalweg while the constructional confinement is the result of the deposition of levees. The timing of these erosional and depositional processes during the inception of a submarine channel is a subject of debate (Fildani et al., 2013). Once a channel has been established it evolves by continued incision in the channel thalweg combined with levee construction. The increasing confinement limits lateral spreading and increases flow thickness. This increases shear stress on the bed and thus promotes further erosion. This internal feedback combines with external forcings, such as changes in sediment supply, to control the morphological evolution of the channel (Hodgson et al., 2016). The prominent nature and continuity of levees along submarine channels indicate that overspill is a continuous process and that flow thickness systematically exceeds the height of the levees (Mohrig & Buttes, 2007). Levee deposits are much more fine-grained than the related channel fills because sediment of different grain sizes is not distributed equally in the flow (Fig 1.7). In a turbidity current with multiple suspended sediment grain sizes, the fine sediment fraction is more homogeneously mixed by turbulence while the coarse sediment fraction is more concentrated at the basis of the flow due to its greater settling velocity. Enhanced overspill, driven by inertia, occurs at the outer bends of submarine channels leading to higher and coarser outer bend levees around the bend apex (Peakall et al., 2000).

1.7 Measuring turbidity currents on the sea floor

Direct measurements of turbidity current flow and turbidite sedimentation are notoriously difficult: turbidity currents occur at great water depth, their occurrence is intermittent, and they have the tendency to destroy or bury any equipment installed on the ocean floor. Nevertheless, there have been successful measurements of turbidity currents in submarine canyons and leveed channels (Khripounoff et al., 2003; Xu et al., 2004; Talling et al., 2015; Hughes Clarke, 2016). The Congo Fan, for example, is presently active and turbidity currents have been measured with monitoring equipment in the submarine canyon (Cooper et al., 2013) as well as around the leveed channel that is currently active at a water depth of ~4000 m, ~600 km offshore (Khripounoff et al., 2003). One limitation is that only velocity measurements were possible in most sea-floor studies, while profiles of suspended sediment concentration or grain size have not yet been measured. Another limitation is the lack of measurements that show how turbidity currents modify channels over longer periods of time.

1.8 Physical and Numerical modelling

Flume experiments have traditionally played an important role in turbidity-current studies because they provide the opportunity to study flow processes in relation to the depositional product. This process-product perspective is hard to obtain in natural systems because of the aforementioned difficulties. Two main groups of experiments can be distinguished (Paola et al., 2009): (1) experiments that focus on the construction of entire fans; and (2) experiments that focus on the interaction of turbidity currents with pre-formed channels. In submarine fan experiments focusing on the construction of entire fans (e.g. Yu et al., 2006; Cantelli et al., 2011), a mud-laden suspension is supplied from a point-source at a low discharge. The weakly turbulent or laminar

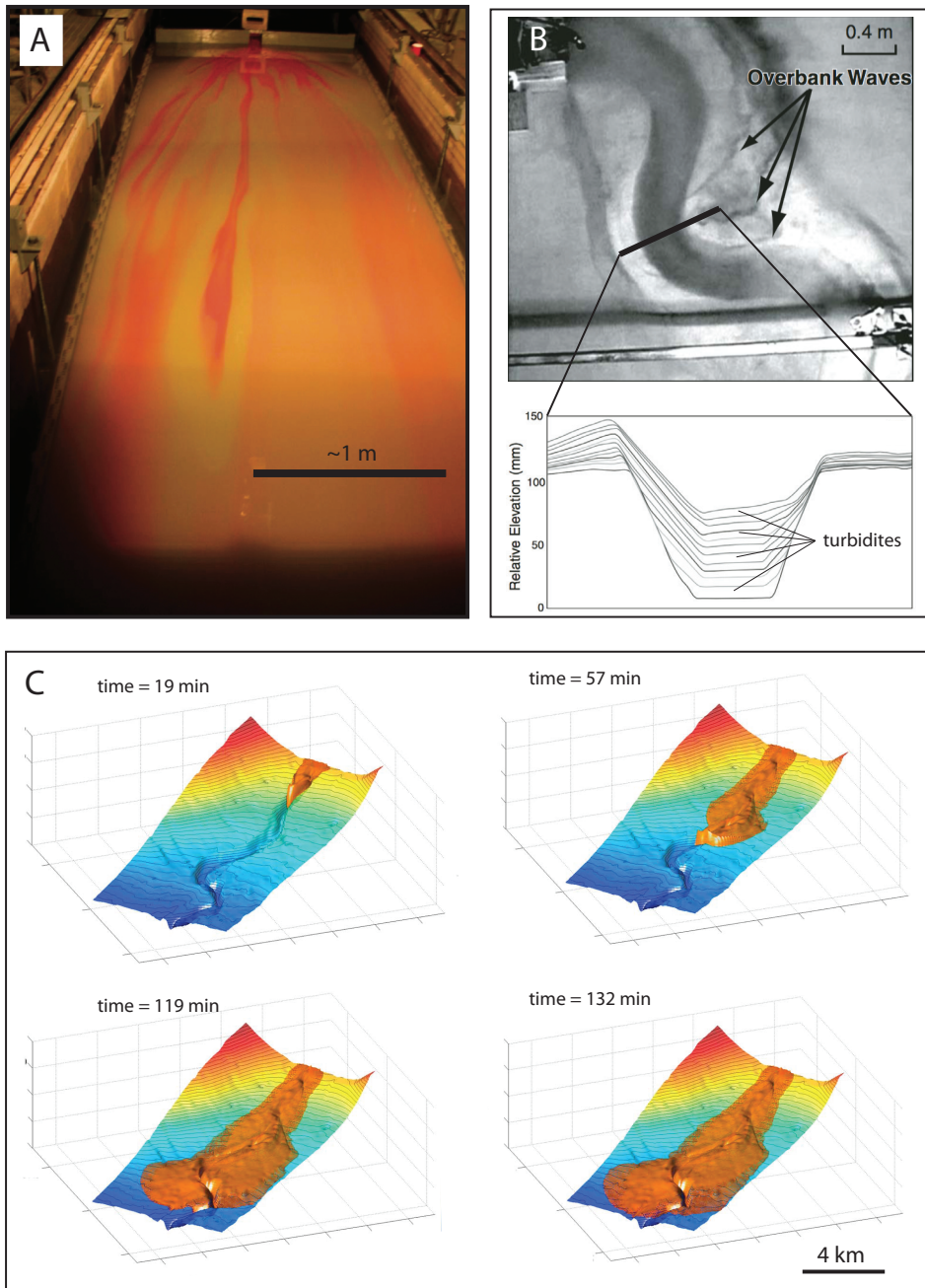


Figure 1.8: *Physical and numerical experiments to study flow processes in submarine channels. (A) Submarine fan experiments by Cantelli et al. (2011). Pink colourant was added to highlight the flow paths. (B) Pre-formed channel experiment by Straub & Mohrig (2008). (C) Numerical simulation of a turbidity current in a submarine channel on the Niger Delta Slope. The orange volume indicates the extend of the current with a 0.2% volumetric sediment concentration (Abd El-Gawad et al., 2012a).*

flow generates low-relief channels that switch across the fan surface (Fig. 1.8A). These experiments are considered to be analogues for the most distal regions of submarine fans where low-relief, subtly branching channels are often observed on lobe surfaces (Cantelli et al., 2011). The other group of experiments use pre-formed channels that are either straight or meandering (Keevil et al., 2006; Mohrig & Buttles, 2007; Kane et al., 2008; Straub & Mohrig, 2008; Ezz et al., 2013). These experiments focus on deposition patterns in and around the channels and the interactions between turbidity currents and channel morphology. These experiments provide insights into topics such as intrachannel deposition relative to channel bends, and patterns of overbank flow. One limitation, however, is that deposition in the channel thalweg exceeds deposition on the levees in each case (Fig. 1.8B). The experiments are therefore most representative for the channel abandonment phase during which the channel is filled by depositional turbidity currents (Peakall & Sumner, 2015). The high deposition rates in the thalweg compared to the levees occur because the turbidity currents cannot maintain all the sediment in suspension that is supplied at the inlet. Thus, in order to simulate the earlier phases of channel evolution, during which channel relief and sinuosity increase, it is essential to generate laboratory currents that can sustain sediment suspension.

Appropriate scaling of sediment transport is essential in all types of geomorphic experiments to produce meaningful results. One common issue is the lower sediment mobility in small-scale experiment. Sediment mobility is commonly quantified with the non-dimensional Shields parameter (e.g. Kleinhans et al., 2014), which represents the ratio between shear stress exerted at the base of the flow and gravity acting on particles in the flow. Particle suspension occurs only above a specific value of the Shields mobility parameter. Furthermore, the suspension capacity increases as the Shields parameter increases (Hiscott, 1994; Eggenhuisen et al., 2017). Appropriate scaling of the suspension process based on the Shields parameter has not yet been applied in experiments that simulate channelised turbidity currents. Maintaining sediment suspension is specifically important for turbidity currents because they are purely driven by the density supplied by suspended sediment.

Abd El-Gawad et al. (2012a,b) present a numerical model that simulates the interaction of turbidity currents with submarine channels (Fig. 1.8C). Numerical models have the advantage that they are not affected by scaling effects and that the flow properties during the simulations can be constrained in detail. However, three-dimensional numerical models of turbidity currents are still in an early stage. For example, in the simulations of Abd El-Gawad et al. (2012a,b) turbidity currents rapidly decelerated due to excessive channel overflow and ambient water entrainment. Thus, the long run-out distance that characterises natural turbidity currents in submarine channels was not yet mimicked in the simulations. An important research aim in deep-water sedimentology is the development of efficient numerical models that can capture the evolution of submarine channels and the resulting stratigraphy. It is important to obtain experimental data on the interaction between turbidity currents and the shaping of a sediment bed to validate these numerical models.

1.9 Aim and objectives of this study

As shown by outcrop studies and modern sea-floor studies, submarine channels are ubiquitous on the modern sea floor as well as in the sedimentary record and the turbidity currents in these channels play an important role in the dispersal of sediment across the Earth's surface. However, process-based interpretations that relate the unique flow processes of turbidity currents to the morphological evolution and the stratigraphic expression of submarine channels have remained speculative. Studies on the sedimentary record and the sea floor provide a perspective that is largely

static. Measurements of turbidity currents, on the other hand, are relatively sparse and do not show how currents modify the bed by many sequential flows over longer timespans. Experiments did not fully capture the morphodynamics of submarine channels either because of scaling issues. Numerous open questions therefore remain. For example, the role of flow stratification in the morphological evolution of submarine channels and facies of their fill and levees remains unclear. Some degree of stratification, which leads to vertical variation in sediment concentration and grain size, is likely to be present in all turbidity currents. Additionally, it remains difficult to use ancient channel deposits to estimate past flow conditions.

The overall aim of this thesis is to explore the functioning of submarine channels as conduits through which sediment is transferred and distributed by turbidity currents across the ocean floor. To this end it is essential to elucidate the link between flow properties of turbidity currents and the morphology as well as the deposit architecture and facies. Specific research objectives that are addressed in the thesis are:

1. Find the conditions where flume experiments produce channels displaying the full suite of erosion and deposition patterns inferred to occur in natural systems;
2. Identify the mechanism by which a submarine channel is initiated on an unchannelised submarine slope;
3. Relate the volume and grain-size distribution of overbank deposition to the grain-size- and density-stratification of channelised turbidity currents;
4. Determine the role that slope channel confinement plays in the partitioning of sediment facies and volume by turbidity currents;
5. Quantify the effect of flow strength on the vertical segregation of grain sizes in turbidity currents;
6. Develop a method to reconstruct turbidity-current flow properties and sediment transfer from ancient submarine channel deposits.

1.10 Overview of this thesis

A combination of different approaches is used to realise the research objectives. Flume experiments are used in Chapter 2, 3 and 4 to show the mutual interaction between turbidity currents and (evolving) submarine channels. An under-water slope is created for the purpose of the experiments within the Eurotank, a 6 m wide, 11 m long, 1.2 m deep tank. An analytical model to simulate suspension dynamics is introduced in Chapter 5. The model is validated by comparing the simulations to experiments in a rectangular flume. The model is applied in an outcrop study in Chapter 6.

Appropriate scaling of sediment suspension is essential to capture the morphodynamics of submarine channels in experiments. **Chapter 2** describes a new scaling approach for turbidity-current experiments that focuses on the ability of turbidity currents to keep sediment in suspension and to re-entrain sediment from the bed. This approach is named Shields Scaling. The experiments show the inception of a leveed channel on an unchannelised slope. Measurements of the sediment surface between sequential turbidity currents show the stepwise evolution of the channel through a combination of levee deposition and variable thalweg erosion and deposition. Velocity measurements show how the flow becomes gradually more confined as the channel evolves.

Chapter 3 uses the same set of experiments as Chapter 2 to investigate the effects of grain-size and density stratification in the experimental turbidity currents on channel-levee evolution. It is shown that the upward decrease in grain size in the levee reflects the upward decrease in grain size in the flow. Additionally, the turbidity-current concentration profile is used to show that the lateral transition from sediment bypass in the channel thalweg to deposition on the levees is related to lateral differences in the sediment transport capacity.

Chapter 4 analyses submarine channels in a mass-balance framework. This analysis tracks the extraction of sediment from a sediment transport system due to deposition. Depending on the channel dimensions relative to the flow size, a certain fraction of the sediment is exchanged due to deposition and erosion by turbidity currents in the channel section. Experiments with pre-formed channels with varying dimensions are used to quantify the partitioning of sediment volume and grain sizes between levees, channel fill and lobe. Flow-velocity measurements are used to identify the mechanisms by which channel dimensions affect structure of the channelised flow. The results of the experiments are compared to a number of natural deep-water systems for which reliable volume estimates have been published.

Grain-size and density stratification are identified as important controls on the volume and grain-size distribution of sediment deposited on the levees of submarine channels in Chapters 3 & 4. Therefore, a simple model is developed in **Chapter 5** to predict stratification in turbidity currents with poorly sorted sediment. Suspended sediment measurements in flume experiments are used to validate the model. Model and experiments produce the same trends where grain-size stratification increases with decreasing shear velocity of the turbidity current.

The model developed in Chapter 5 is used in **Chapter 6** to reconstruct flow properties in an outcropping submarine channel fill. The channel fill is part of the deep-water foreland basin fill of Late Cretaceous age (~70-80 Ma) in the Magallanes Basin in Southern Chile. Samples from different components of the channel fill were analysed to reconstruct the change in grain-size distribution with height in the flow. The stratification model is used to reconstruct the flow parameters that are consistent with the sample characteristics. The results from the model are used to reconstruct the grain-size distribution of the sediment that was transferred through the channel.

Chapter 7 summarises the main conclusions of the thesis and provides perspectives for further research.

Chapter 2

Morphodynamics of submarine channel inception revealed by new experimental approach

ABSTRACT

Submarine channels are ubiquitous on the sea floor and their inception and evolution is a result of dynamic interaction between turbidity currents and the evolving sea floor. However, the morphodynamic links between channel inception and flow dynamics have not yet been monitored in experiments and only in one instance on the modern sea floor. Previous experimental flows did not show channel inception because flow conditions were not appropriately scaled to sustain suspended sediment transport. Here we introduce and apply new scaling constraints for similarity between natural and experimental turbidity currents. The scaled currents initiate a leveed channel from an initially featureless slope. Channelisation commences with deposition of levees in some slope segments and erosion of a conduit in other segments. Channel relief and flow confinement increase progressively during subsequent flows. This morphodynamic evolution determines the architecture of submarine channel deposits in the stratigraphic record and efficiency of sediment bypass to the basin floor.

Based on

Morphodynamics of submarine channel inception revealed by new experimental approach. By: Jan de Leeuw, Joris T. Eggenhuisen, Matthieu J.B. Cartigny, *Nature Communications*, 2016, doi:10.1038/ncomms10886.

2.1 Introduction

Extensive channelised seascapes have been revealed by sea-floor surveys (Damuth et al., 1983; Hay, 1987; Talling et al., 2007; Maier et al., 2011). The channels are characterized by a continuous thalweg along which sediment-laden turbidity flows dominantly bypass sediment (Stevenson et al., 2015). Submarine channels can be up to several kilometers wide and hundreds of kilometers long, and provide the transport pathways for large quantities of sediment, nutrients and carbon into the deeps of the world's ocean (Galy et al., 2007; Talling et al., 2007), where the material is collected in basin-floor fans that form the largest sediment accumulations on the planet.

Sea floor and outcrop evidence demonstrates that channels are associated with erosion into underlying deposits (Clark and Pickering, 1996) as well as aggradation of deposits in levees, channel-fills and splays (Morris et al., 2014). Fundamentally different causalities have been suggested in the spatial and temporal relations between erosive and depositional changes to the submarine landscape. Some studies (Fildani et al., 2013; Maier et al., 2013) envision an evolution where: "only after an initial erosional phase and channel establishment, are turbidity currents able to construct aggrading levees" (Fildani et al., 2013). This contrasts with suggestions that genetically linked precursor lobe morphologies may form an initial depositional template for subsequent channel incision (Eggenhuisen et al., 2011; Sun et al., 2011; Morris et al., 2014; Ortiz-Karpf et al., 2015) and that channels may be entirely depositional both outside and inside the confining conduit (Clark and Pickering, 1996; Stevenson et al., 2013).

Subsurface and outcrop observations on channel morphology and channel deposits are static. Similarly, the presently available direct observations of active submarine channels (Hay, 1987; Xu et al., 2004; Xu, 2010; Hughes Clarke et al., 2011; Cooper et al., 2013) do not span enough time to study morphodynamics of channel inception and evolution. Recently, the extension of a submarine channel has been monitored in a quickly evolving system (Clarke et al., 2015). However, the dataset did not provide direct information about the flow conditions during this morphological evolution. Therefore, modelling studies remain important in the investigation of the morphodynamic interplay between channel form and turbidity currents.

A limited number of experiments successfully produced subaqueous channels using a saline flow over a mobile substrate (Metivier et al., 2005; Hoyal et al., 2008; Weill et al., 2014). However, these flows could not produce depositional morphologies as there was no suspended sediment load, which is vital for levee formation (Weill et al., 2014). Therefore, these experiments provide limited insight into contributions of deposition and erosion during channel inception. Rowland et al. (Rowland et al., 2010) reviewed the full range of published numerical and physical experiments that have tried to achieve self-channelisation (Imran et al., 1998; Baas et al., 2004; Yu et al., 2006) by sediment-laden flows and concluded that channelisation was not achieved in any of the cases.

We present experiments that for the first time capture self-channelisation by turbidity currents. This was achieved by scaling sediment suspension in the experimental turbidity currents to the real world systems. This new scaling approach is called Shields scaling and focuses on two scaling parameters that regulate sediment suspension: 1) the Shields parameter, and 2) a Reynolds scale of the sediment grains. The observed morphodynamic channel evolution establishes that channel inception can either commence with deposition of confining morphology by turbidity currents or erosion of a channel conduit. Thus, channel inception is not exclusively possible following erosion.

2.2 Methods

2.2.1 Description of the set-up

The experiments were conducted in the Eurotank flume laboratory. The Eurotank measures 6x11 m in planform and was filled with water up to a level of 1.2 m above the horizontal floor (Supplementary Figure 2.1). The bathymetry at the bottom of the tank consisted of a slope of 11 degrees and a horizontal basin floor at the base of this slope. The slope was covered with a 10 cm thick layer of loose sand that had the same grain-size distribution as the turbidity currents. A wooden duct was present at the top of the slope to resemble a non-erodible canyon setting at the top of the slope. At the other end of the slope a 10 cm high ridge was placed in order to provide down-dip accommodation for the sediment that reached the base of the slope.

2.2.2 Sediment suspensions

Prior to each experiment, the sediment mixture was prepared outside the tank in a 1.1 m³ mixing tank, with two propellers designed to homogenise sediment-water mixtures up to 30% volumetric sediment concentrations. The quartz sand used to make the suspensions had a median grain size (D_{50}) of 141 μm , a D_{10} of 44 μm , a D_{90} of 199 μm (Supplementary Figure 2.2) and had a specific density of 2650 kg m⁻³. The grain size was analysed using a laser particle sizer (Malvern Mastersizer).

2.2.3 Data collection

During the experiments, a slurry pump was used to supply the suspension to the set-up. A discharge meter (Krohne Optiflux 2300) was mounted in the supply pipe. A Labview control system was used that adjusted the discharge was regulated by a Labview control system that adjusted the pump speed whenever the measured discharge deviated from a set reference value. The discharge during each of the experiments presented here was 30 m³ h⁻¹. The experiments lasted approximately 2 minutes before the mixing tank was drained. Four Ultrasonic Doppler Velocity Profiler probes (*UVP Duo MX; 1 MHz probes*) were installed on an aluminium frame to monitor the flow field during the experiments. These probes were set up at around 0.15 m above the erodible basin floor, with their beam pointing diagonally down into the flow at an angle of 60° relative to the initial local slope of the flume floor. The planview location of the probes is indicated in Figure 2.2. Each of these probes measured a full profile of bed-parallel flow in the direction of the probe orientation. The profiles had a spatial resolution of 0.64 mm and the measurement frequency was 1.81 Hz. Individual velocity profiles have a spikey appearance due to the turbulent nature of the flows. Therefore, time-averaging was applied to create smoother profiles as presented in Figure 2.3A. After each experimental run, the basin was drained to expose the deposit. Then, a digital elevation model (DEM) with a horizontal resolution of 2x2 mm was created using a laser scanner. By subtracting the DEM of the experimental deposits and a DEM of the sediment bed prior to the experiments, a map of deposition and erosion was created for each experiment.

2.2.4 Calculations of flow conditions

The following flow parameters were required to determine the position of each reviewed experiment on the Shields diagram (Fig. 2.1):

Grain size (d): here the median grain-size of the initial sediment mixture in each study was used (D_{50}).

Kinematic viscosity (ν): here the viscosity of clear water at 20 degrees is used ($1 \cdot 10^{-6}$).

Shear velocity (u^*): when estimates are supplied in experimental studies then they are followed. Elsewise the shear velocities are calculated as (Kneller and Mccaffrey, 2003):

$$u^* = \sqrt{g'hS} \quad (2.1)$$

For the present experiments the shear velocity is estimated using (van Rijn, 1993):

$$u^* = U_{max}\kappa \left[\ln \left(\frac{h_{max}}{0.1 D_{90}} \right) \right]^{-1} \quad (2.2)$$

in which h_{max} is the height of the velocity maximum and U_{max} is the maximum velocity.

Reduced gravity (g'): $g(\Delta\rho/\rho)$ in which ρ is the density of the suspension and $\Delta\rho$ is the excess density of the sediment submerged in the ambient fluid. In order to calculate the density of the suspension it is assumed that the density of the sediment concentration is equal to the concentration of the initial mix.

Flow height up to the velocity maximum (h): when only the total flow thickness is given it is assumed that the height of the velocity maximum is at $\frac{1}{4}$ of the total flow thickness.

Bed slope, S : $\sin(\text{bed slope in degrees})$.

We also estimated the flow conditions for turbidity currents in the Monterey Canyon reported by (Xu, 2010). A representative median grain size for the turbidity currents was estimated from sediment cores of the Monterey canyon floor. Core data from Paull et al. (2010) shows that a broad range of grain sizes (ranging from silt to boulders) was deposited on the canyon floor. Middle sand (diameter of $350 \mu\text{m}$) was chosen as a representative grain size because it was the most common grain-size in the cores. The D_{90} was estimated at $500 \mu\text{m}$.

2.3 Results

2.3.1 Scaling approach

Classical turbidity current experiments (Middleton, 1966; Luthi, 1981; Garcia and Parker, 1989; Baas et al., 2004; Mohrig and Buttles, 2007; Alexander et al., 2008; Straub et al., 2008; Kane et al., 2008; Rowland et al., 2010; Cantelli et al., 2011; Eggenhuisen and McCaffrey, 2012) have focused on two non-dimensional scaling characterizations of the fluid flow: the Froude number (Fr), which is the ratio between momentum and gravitational forces of the flow; and the Reynolds number (Re), characterizing the ratio between the momentum and the viscous forces that determine the turbulent state of the flow. As it is not possible to keep both Fr and Re equal to the natural analogues while scaling down flow size, it is common to keep the Froude number similar to natural values and to only require a Reynolds number above the laminar-turbulent threshold (Peakall et al., 1996; Parsons and Garcia, 1998). This Froude-scaling approach has proven to be valuable in understanding the flow dynamics of turbidity currents but it does not guarantee that flows are able to transport sediment in suspension.

| Experimental conditions | |
|-------------------------|----------------------|
| Slope | 11° |
| Discharge | 30 m ³ /h |
| Median grain size | 140 μm |

Table 2.1.: *Boundary conditions of the experiments.*

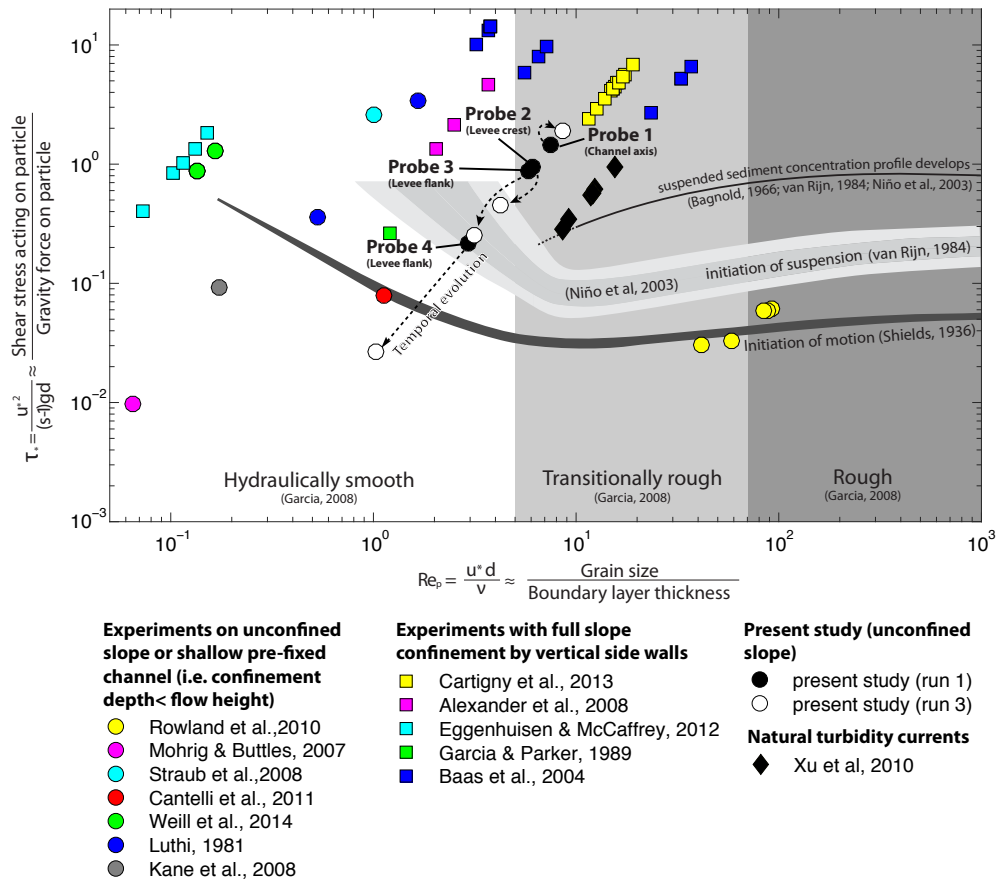


Figure 2.1: Regime diagram for sediment transport. Shields mobility diagram giving an overview of experimental conditions in previous studies (Luthi, 1981; Garcia and Parker, 1989; Baas et al., 2004; Mohrig and Buttlers, 2007; Alexander et al., 2008; Straub et al., 2008; Kane et al., 2008; Rowland et al., 2010; Cantelli et al., 2011; Eggenhuisen and McCaffrey, 2012; Weill et al., 2014; Cartigny et al., 2013), natural flows (Xu, 2010) and the experiments presented in this study. Regime boundaries based on: Shields (1936), Bagnold (1966), van Rijn (1984), Niño et al. (2003) and Garcia (2008).

Many Froude-scaled experiments displayed rapid sediment depletion and were therefore limited in clarifying patterns of deposition and erosion. Depletive flows rapidly lose their complete sediment load because they do not have enough turbulent mixing to compensate for settling of sediment from suspension. In order to predict whether currents are able to entrain and transport sediment in suspension it is important to consider the force ratios acting on the sediment grains. This leads to two additional constraints: the Shields parameter, being the ratio between the turbulent shear, as expressed by the shear velocity, and the gravity-induced settling (Shields, 1936); and the particle Reynolds number, which is the ratio of grain size to the boundary layer thickness (van Rijn, 1993). The former is more commonly quoted in turbidity current studies (Straub et al., 2008) as the ratio between the shear velocity (u_*) and the settling velocity (w_s), but is here expressed as the Shields parameter. The latter is a Reynolds scale with significance

for particle suspension near the bed. It describes the roughness of the sediment surface, which determines whether flow at the boundary is smooth and dominated by viscous forces, or rough and dominated by turbulent forces and shedding of turbulent eddies from particles at the bed surface (Garcia, 2008). If the boundary is smooth, a thin layer of laminar flow protects the bed, and grains that settle into this near-bed boundary layer will no longer interact with suspending turbulent structures and are likely to remain deposited. In the transitionally rough regime there is interaction of turbulent eddies with the bed but viscous forces also play a significant role. As experiments on channel inception are dependent on realistic turbulence-sediment interactions, both in the boundary layer as well in suspension, it follows that such Shields scaling constrains must be satisfied.

The Shields scaling approach mirrors Froude scaling of the flow dynamics in the sense that one scale, namely the ratio of turbulent forces and gravity forces acting on the particle (the Shields parameter), is kept equal to real world values, whereas the other scale (the Reynolds particle scale) is relaxed, as long as rough to transitionally-rough boundary layer conditions are maintained in order to keep a realistic turbulent near-bed regime and aid sediment pick-up into suspension. These two scales form the axes of the classic Shields mobility diagram (Fig. 2.1), which enables a comparison between the present experiments, natural turbidity current conditions, and previous experimental studies.

2.3.2 Comparison with natural currents and previous experiments

In-situ measurements of turbidity currents in the Monterey Canyon (Xu et al., 2004; Xu, 2010) are used to estimate the position of a representative natural turbidity current on the Shields diagram (Supplementary Table 2.1 and Methods). The flows had a transitionally rough boundary and the Shields parameter plots above the suspension threshold (Fig. 2.1). Similarly, the boundary layer was transitionally rough in the present experiments and shear stresses were sufficiently high to support sustained suspension transport. As a result, these currents were sediment-bypass dominated along a significant part of the experimental domain. The experiments presented in this paper were performed under Shields scaling conditions that are representative for the natural environment. Some previous confined slope experiments (Baas et al., 2004; Cartigny et al., 2013) also plot in the natural turbidity current regime. The experiments presented here are, however, the first to satisfy both Froude and Shields scaling (Fig. 2.1) on an unconfined and erodible slope, making them suitable to study flow-substrate interactions during channel inception.

It emerges that many previous studies violated the proposed Shields scaling requirements because the flows had smooth boundary layers, and/or had shear stresses that were below the threshold for initiation of suspension. In the cases where flows had a smooth boundary layer as well as a low Shields parameter (Mohrig and Buttle, 2007; Kane et al., 2008; Cantelli et al., 2011; Eggenhuisen and McCaffrey, 2012) flows were always depositional. Flows in other experiments (Luthi, 1981; Alexander et al., 2008; Straub et al., 2008) had a higher Shields parameter but still a smooth boundary layer. Finally, the experiments of Rowland et al. (Rowland et al., 2010) fulfilled the roughness requirement; however, there the Shields parameter was only approximately equal to the critical value for initiation of bedload motion (Fig. 2.1). None of these experiments led to channelisation morphodynamics.

2.3.3 Morphological evolution

Three turbidity currents with the same characteristics were released successively on a constant and initially featureless sand slope (Boundary conditions in Table 2.1; Set-up shown in Supplementary

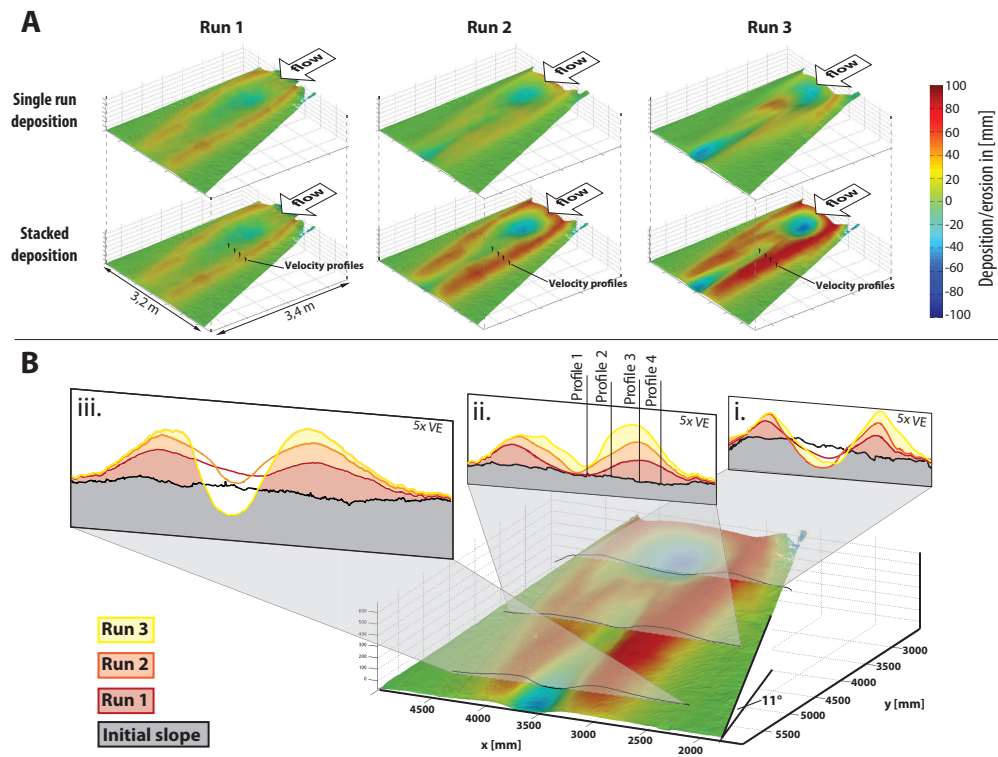


Figure 2.2: Maps of deposition and erosion. (A) Digital elevation models of the deposits formed by sandy turbidity currents. Colours indicate the thickness of the deposits/depth of erosion. Both the cumulative erosion/deposition and the erosion/deposition after each single run are shown. (B) DEM of the final deposit with cross-sections at the lower, middle and upper slope. Cross-sections have 5 times vertical exaggeration. Positions of the probes that measured down-stream velocity profiles are indicated on cross-section ii.

Figure 2.1). The first turbidity current deposited two sub-parallel ridges while the flow largely bypassed in between the two ridges (Fig. 2.2). This pattern of deposition resulted in a morphology that confined the subsequent flows. The relief of this confinement was increased during the subsequent second and third run due to continued deposition on the ridges. A circular scour with a diameter of 70 cm and a final depth of 8 cm is created in between the levees on the upper slope domain throughout the three runs. This contributes to the channel relief in that reach. On the lower slope, erosion in between the ridges was only initiated during the second run. The ridges are built of layers of sediment deposited by successive turbidity currents that each taper away from the channel axis and thus they can be qualified as levees (Kane and Hodgson, 2011).

The cross-sectional geometry of the experimental channel compares well with submarine channels on the modern sea floor that have remained unfilled. The depth:width ratio of the Lucia Chica channel (Fig. 2.3) is 1:12 whereas the aspect ratio formed in the experiment varies between 1:9 and 1:23.

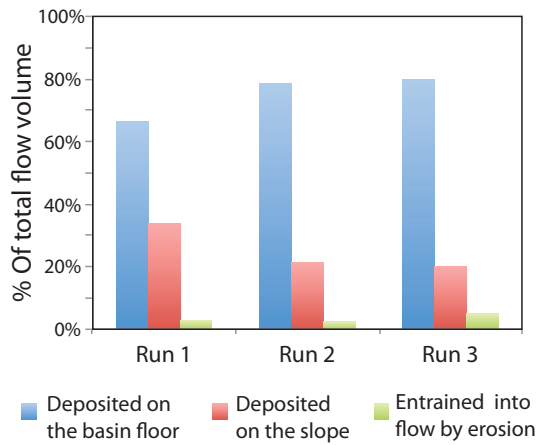


Figure 2.3: Volume of deposits on the slope. Fractions of the total sediment load of the flow deposited and eroded on the slope and on the basin floor. The volume of sediment supplied to the experiments is equal for each of the runs.

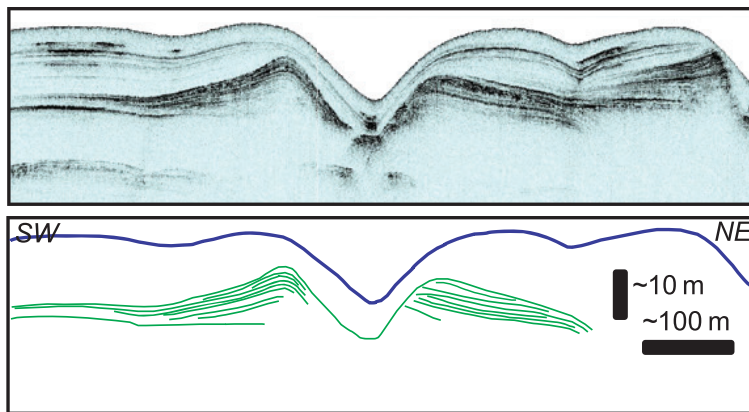


Figure 2.4: Example of a submarine channel on the modern sea floor. Chirp profile through a submarine channel that is part of the Lucia Chica channel system offshore central California (Maier et al., 2013). The green lines indicate the turbidity current deposits. Compare this figure with the cross-sections of the experimental deposits in Figure 2.2b. The blue line indicates the top of the hemipelagic drape. (Figure reprinted with permission from the publisher.)

The amount of sediment bypass on the slope increases in each run as is indicated by an increasing fraction of the sediment reaching the base of slope. The fraction of sediment that reaches the base of slope increases from 66% in Run 1 to 80% in Run 3 (Fig. 2.4).

2.3.4 Evolution of the flow field

The effect of the evolving topography on the flow field is shown by velocity profiles along a slope-perpendicular section (Fig. 2.5A). At the beginning of Run 1, when the slope was not yet modified, there was little across-flow variation in the downstream velocity profile. The confining morphology established by the end of Run 1 resulted in an increase in flow velocity inside the

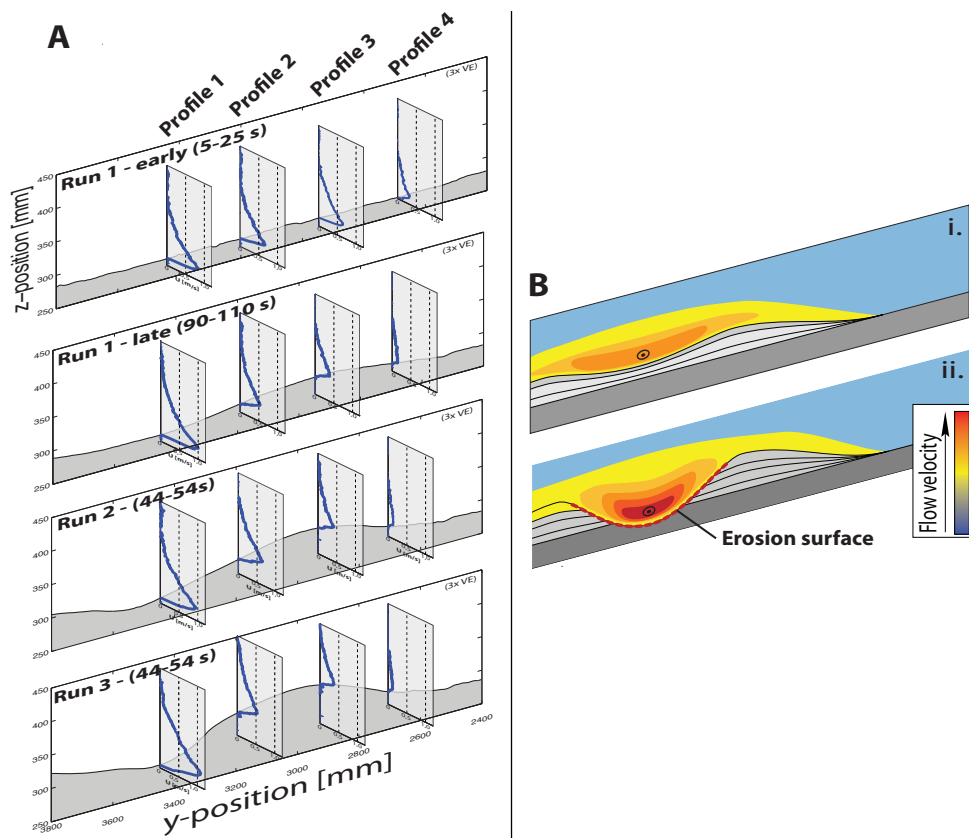


Figure 2.5: (A) Topographic profiles with time averaged velocity profiles measured along the same transect at different time-intervals (early Run 1 (5–25 s), late Run 1 (90–110 s), middle Run 2 (44–54 s), middle Run 3 (44–54 s)). Note that there is three times vertical exaggeration in the topographic profiles. (B) A model for the co-evolution of the flow field and the topography derived from the experiments: i. Broad and unconfined flows build a subtle depositional confinement because deposition rates are slightly lower in the axis. ii. A threshold at which incision starts is reached causing a rapid increase in the confinement relief. Note that the erosion of the channel floor was only observed downstream of the location of Profile 1.

confinement (U_{\max} increases from 0.83 to 1.00 m s⁻¹ at velocity profile 1; Height of U_{\max} was 1.2 cm) and a decrease in flow velocity outside of the confinement (U_{\max} decreases from 0.64 to 0.38 m s⁻¹ at velocity Profile 3). Note that the change in the flow field during Run 1 was caused by a channel with a depth ($h_{U_{\max}}=2.6$ cm) that was only a fraction of the flow height ($h=7.3$ cm). The increase in channel depth during Runs 2 and 3, does not result in a systematic change in flow velocity at any of the profiling locations. These results confirm previous pre-fixed channel experiments (Mohrig and Buttles, 2007), which showed that a flow is already effectively confined within a conduit once the channel depth is greater than the height of the velocity maximum.

The spatial and temporal variations in flow velocity affected the ability of the flows to transport their sediment, and these changes can be tracked within the Shields diagram (Fig. 2.1).

The flow along the centreline of the slope (Fig. 2.5A, velocity Profile 1) has a transitionally rough boundary layer and is able to bypass/erode sediment until the base of the slope. Flow at the off-axis locations of velocity Profile 2 and 3 plot near the boundary between smooth and transitionally rough flow during Run 1. The position of these points shifts towards a field in the hydraulically smooth regime and below the suspension initiation threshold during Run 3. Thus, the conditions at the locations of velocity Profiles 2 and 3 are at or below the conditions for sediment bypass and thus there is continuous deposition at these localities. The flow furthest away from the axis (Fig. 2.5A: Velocity Profile 4) plots within the field where flows have a smooth boundary layer and are below the boundary for suspended sediment transport during all runs. This indicates that flows that carry suspended load are highly depletive in these realms.

The temporal increase in axial flow velocity, which is caused by the progressively increasing confinement, causes an increase in the Shields parameter (Fig. 2.1). The resulting small shift on the Shields diagram of the position of the flow at Profile 1 appears to have little effect on the ability of the flow to transport sediment at this locality because little deposition or erosion is observed here throughout the three runs. Although axial flow velocity was not monitored in the lower channel section, a larger shift on the Shields diagram can be inferred there because of the observed transition from deposition on the channel floor during Run 1 to erosion on the channel floor during Run 2 and 3 (Fig. 2.2b; cross-section iii.). The axial erosion is a further contributor to flow confinement in a dynamic feedback and consequently increases the rates of erosion.

Contrastingly, the flow conditions at the off-axis locations (Velocity Profiles 2,3 and 4), are shifting in the Shields mobility diagram towards positions below the suspension initiation threshold, and indeed there is continuous deposition at these localities.

In summary, spatial and temporal variation in the ability to transport sediment is predicted from the velocity measurements. The relative positions and temporal evolution on the Shields diagram predict the deposition of levees alongside a fairway dominated by sediment bypass and reflects progressive confinement increase during channel inception (Fig. 2.5B).

2.4 Discussion

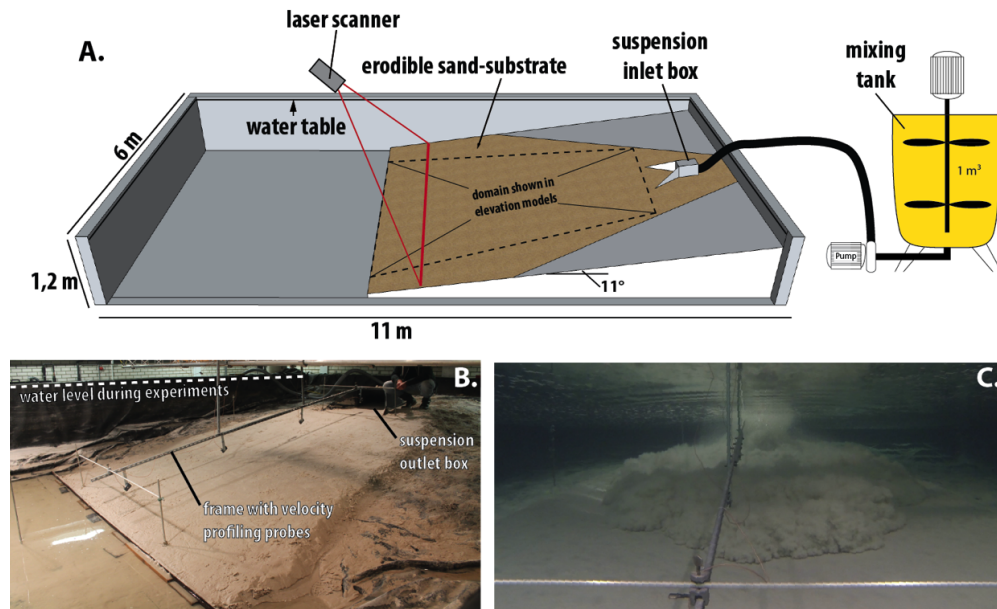
Significant debate has surrounded the nature of the relief that is created during the initial phase of channel formation. It has been argued formationeated during initial phase of of channelization t this locality.diment load by the time that they reach this locality that initial relief that turbidity currents create at a site of repeated activity is likely erosional (Fildani et al., 2013; Maier et al., 2013), which implies that levees commonly form from overspill after formation of an entrenched channel confinement. Trains of erosional scours are widely observed on the floors of channels on the modern ocean floor (Fildani et al., 2006, 2013; Heinio and Davies, 2009; Maier et al., 2011; Covault et al., 2014) and are indeed a likely initial feature of channelisation in many cases. Similarly, the scour in front of the outlet in the present experiments contributes to the initial confinement on the upper slope. However, the initial confinement along the middle and lower slope is created purely by depositional patterns arising from low deposition rates below the flow axis compared to the flow margins. Thus, the incipient levees formed by lateral variations in sediment transport processes and not by overspill from an already established channel. This morphodynamic development confirms the role that depositional templates may play in initial confinement (Eggenhuisen et al., 2011; Morris et al., 2014; Ortiz-Karpf et al., 2015), and the experimental deposit cross-sections are strongly reminiscent of classic observational suggestions of depositional channel architecture (Mutti and Normark, 1987; Clark and Pickering, 1996).

Channel axis erosion caused by initial depositional confinement represents transition from depositional channelisation to erosional channelisation (Fig. 2.5B). This is a confirmation of a “channelisation threshold” at which a subtle confinement created by small depositional gradients causes incision, followed by a channelisation feedback (Eggenhuisen et al., 2011). It emerges that channelisation of turbidity currents can arise from both depositional and erosive sculpting of the sea floor, and may transition from depositional to erosive confinement. These flows thus have various intrinsic tendencies for channelisation, which explains the ubiquitous presence of channels on submarine slopes.

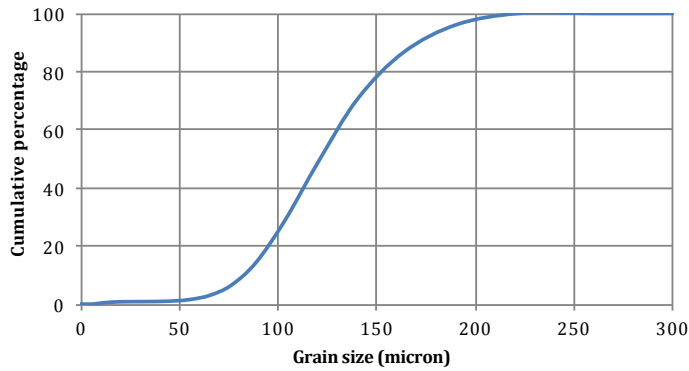
The channel inception debate is just one of many aspects of sea-floor morphodynamics that can now be subjected to thorough testing in the laboratory environment. Previously, this was not possible because experimental turbidity currents did not show realistic patterns of deposition and erosion as a result of inadequate scaling of the suspended sediment transport.

We conclude that confinement can progressively evolve from a depositional or erosional template, promoting gradual enhancement of sediment bypass on the slope. The increase in sediment bypass during the early phase of channel evolution will result in autogenic progradation of the system and deposits with according stacking patterns. Coarse-grained deposits can be expected at the base of finer-grained levees, such coupled stratigraphic bodies can be explained with a single genetic sequence of progressive channel inception, without the need to invoke changes in external mechanisms.

2.5 Supplementary materials



Supplementary Figure 2.1: *Experimental set-up details. (A) Schematic overview of the experimental set-up. (B) Drained set-up prior to an experiment. (C) Underwater view showing a turbidity current flowing downslope during an experiment.*



Supplementary Figure 2.2: Grain-size distribution of the sediment used.

| Author + year | Run # | Volume concentration of sediment [-] | Specific density of sediment | Submerged gravity g' [m/s ²] | Hydraulic radius R [m] | Slope S [-] | Relative density s [-] | Median grain size d [m] | Shear velocity u^* [m/s] | Shields parameter τ^* [-] | Particle Reynolds number Re_p^* [-] |
|--------------------|-----------|--------------------------------------|------------------------------|--|------------------------|-------------|--------------------------|-------------------------|----------------------------|--------------------------------|---------------------------------------|
| Rowland 2010 | 3 | (saline currents) | 1200 | 7.00E-02 | 1.67E-02 | 0.006 | 1.2 | 4.20E-03 | 2.20E-02 | 5.88E-02 | 9.20E+01 |
| Rowland 2010 | 4 | (saline currents) | 1200 | 1.80E-01 | 1.67E-02 | 0.006 | 1.2 | 4.20E-03 | 2.10E-02 | 5.82E-02 | 8.78E+01 |
| Rowland 2010 | 5 | (saline currents) | 1200 | 3.40E-01 | 1.67E-02 | 0.006 | 1.2 | 4.20E-03 | 2.00E-02 | 5.85E-02 | 8.37E+01 |
| Rowland 2010 | 6 | (saline currents) | 1200 | 5.50E-01 | 1.67E-02 | 0.006 | 1.2 | 4.20E-03 | 1.40E-02 | 3.26E-02 | 5.86E+01 |
| Rowland 2010 | 7 | (saline currents) | 1200 | 1.20E+00 | 1.67E-02 | 0.006 | 1.2 | 4.20E-03 | 1.00E-02 | 3.04E-02 | 4.18E+01 |
| Cartigny 2014 | C09-S09-A | 0.09 | 2650 | 1.46E+00 | 2.57E-02 | 0.156 | 2.65 | 1.50E-04 | 7.66E-02 | 2.42E+00 | 1.14E+01 |
| Cartigny 2014 | C09-S11-A | 0.09 | 2650 | 1.46E+00 | 2.59E-02 | 0.191 | 2.65 | 1.50E-04 | 8.49E-02 | 2.97E+00 | 1.27E+01 |
| Cartigny 2014 | C13-S11-A | 0.13 | 2650 | 2.10E+00 | 2.47E-02 | 0.191 | 2.65 | 1.50E-04 | 9.96E-02 | 4.09E+00 | 1.49E+01 |
| Cartigny 2014 | C13-S12-N | 0.13 | 2650 | 2.10E+00 | 2.43E-02 | 0.208 | 2.65 | 1.50E-04 | 1.03E-01 | 4.39E+00 | 1.54E+01 |
| Cartigny 2014 | C15-S10-A | 0.15 | 2650 | 2.43E+00 | 2.46E-02 | 0.174 | 2.65 | 1.50E-04 | 1.02E-01 | 4.28E+00 | 1.52E+01 |
| Cartigny 2014 | C15-S11-N | 0.15 | 2650 | 2.43E+00 | 2.50E-02 | 0.191 | 2.65 | 1.50E-04 | 1.08E-01 | 4.77E+00 | 1.61E+01 |
| Cartigny 2014 | C17-S07-A | 0.17 | 2650 | 2.75E+00 | 2.56E-02 | 0.122 | 2.65 | 1.50E-04 | 9.27E-02 | 3.55E+00 | 1.39E+01 |
| Cartigny 2014 | C17-S09-N | 0.17 | 2650 | 2.75E+00 | 2.43E-02 | 0.156 | 2.65 | 1.50E-04 | 1.02E-01 | 4.30E+00 | 1.53E+01 |
| Cartigny 2014 | C21-S08-A | 0.21 | 2650 | 3.40E+00 | 2.52E-02 | 0.139 | 2.65 | 1.50E-04 | 1.09E-01 | 4.92E+00 | 1.63E+01 |
| Cartigny 2014 | C21-S09-N | 0.21 | 2650 | 3.40E+00 | 2.53E-02 | 0.156 | 2.65 | 1.50E-04 | 1.16E-01 | 5.54E+00 | 1.73E+01 |
| Cartigny 2014 | C26-S07-A | 0.26 | 2650 | 4.21E+00 | 2.58E-02 | 0.122 | 2.65 | 1.50E-04 | 1.15E-01 | 5.45E+00 | 1.72E+01 |
| Cartigny 2014 | C26-S09-N | 0.26 | 2650 | 4.21E+00 | 2.51E-02 | 0.156 | 2.65 | 1.50E-04 | 1.29E-01 | 6.82E+00 | 1.92E+01 |
| Alexander 2008 | H0306 | 0.012 | 2500 | 1.77E-01 | 6.38E-02 | 0.105 | 2.5 | 5.90E-05 | 3.44E-02 | 1.37E+00 | 2.02E+00 |
| Alexander 2008 | H0909 | 0.012 | 2500 | 1.77E-01 | 6.70E-02 | 0.156 | 2.5 | 5.90E-05 | 4.30E-02 | 2.13E+00 | 2.53E+00 |
| Alexander 2008 | H0620 | 0.012 | 2500 | 1.77E-01 | 6.54E-02 | 0.364 | 2.5 | 5.90E-05 | 6.48E-02 | 4.85E+00 | 3.81E+00 |
| Eggenhuisen 2012 | 1 | 0.0121 | 2650 | 8.93E-02 | 1.40E-01 | 0.017 | 2.65 | 9.30E-06 | 7.80E-03 | 4.05E-01 | 7.23E-02 |
| Eggenhuisen 2012 | 2 | 0.0242 | 2650 | 1.28E-01 | 1.10E-01 | 0.017 | 2.65 | 9.30E-06 | 1.12E-02 | 8.34E-01 | 1.04E-01 |
| Eggenhuisen 2012 | 3 | 0.0485 | 2650 | 1.88E-01 | 8.00E-02 | 0.017 | 2.65 | 9.30E-06 | 1.24E-02 | 1.02E+00 | 1.04E-01 |
| Eggenhuisen 2012 | 4 | 0.0364 | 2650 | 2.71E-01 | 7.00E-02 | 0.017 | 2.65 | 9.30E-06 | 1.42E-02 | 1.34E+00 | 1.32E-01 |
| Eggenhuisen 2012 | 5 | 0.0606 | 2650 | 3.01E-01 | 1.00E-01 | 0.017 | 2.65 | 9.30E-06 | 1.65E-02 | 1.81E+00 | 1.53E-01 |
| Mohrig 2007 | 1 | 0.008 | 2650 | 1.29E-01 | 1.50E-02 | 0.002 | 2.65 | 3.00E-05 | 2.16E-03 | 9.61E-03 | 6.45E-02 |
| Straub et al. 2008 | 1 | 0.00424 | 2650 | 1.96E-01 | 1.00E-01 | 0 | 2.65 | 2.90E-05 | 1.40E-02 | 4.18E-01 | 4.04E-01 |
| Cantelli 2011 | | 0.02 | 2650 | 3.24E-01 | 5.00E-03 | 0.08 | 2.65 | 1.00E-04 | 1.14E-02 | 8.01E-02 | 1.13E+00 |
| Weill, 2014 | 5 | (saline currents) | 1040 | 7.41E-01 | 2.00E-04 | 0.139 | 1.08 | 3.00E-05 | 4.54E-03 | 8.77E-01 | 1.36E-01 |
| Weill, 2014 | 6 | (saline currents) | 1040 | 7.41E-01 | 2.00E-04 | 0.139 | 1.08 | 3.00E-05 | 4.54E-03 | 8.77E-01 | 1.36E-01 |
| Weill, 2014 | 7 | (saline currents) | 1040 | 7.41E-01 | 2.00E-04 | 0.139 | 1.08 | 3.00E-05 | 4.54E-03 | 8.77E-01 | 1.36E-01 |
| Weill, 2014 | 10 | (saline currents) | 1040 | 7.41E-01 | 2.00E-04 | 0.208 | 1.08 | 3.00E-05 | 5.55E-03 | 1.31E+00 | 1.66E-01 |
| Weill, 2014 | 11 | (saline currents) | 1040 | 7.41E-01 | 2.00E-04 | 0.208 | 1.08 | 3.00E-05 | 5.55E-03 | 1.31E+00 | 1.66E-01 |
| Luthi, 1981 | 1 | 0.00424 | 2650 | 6.48E-02 | 3.75E-02 | 0.087 | 2.65 | 3.70E-05 | 1.46E-02 | 3.54E-01 | 5.36E-01 |
| Luthi, 1981 | 3 | 0.04061 | 2650 | 6.20E-01 | 3.75E-02 | 0.087 | 2.65 | 3.70E-05 | 4.50E-02 | 3.39E+00 | 1.66E+00 |
| kane, 2008 | | 0.05 | 2650 | 8.09E-01 | 7.49E-02 | 0 | 2.65 | 2.73E-05 | 6.38E-03 | 9.21E-02 | 1.73E-01 |

| | | | | | | | | | | | |
|----------------------|--------------|-------------------|------|----------|----------|-------|------|----------|----------|----------|----------|
| Garcia, 1993 | T3 | (saline currents) | 1350 | 1.50E-01 | 2.50E-02 | 0.08 | 1.35 | 1.00E-04 | 1.55E-03 | 7.00E-03 | 1.54E-01 |
| Garcia, 1993 | A1 | (saline currents) | 1350 | 1.50E-01 | 2.50E-02 | 0.08 | 1.35 | 1.00E-04 | 1.81E-03 | 9.55E-03 | 1.80E-01 |
| Garcia, 1993 | A2 | (saline currents) | 1350 | 1.50E-01 | 2.50E-02 | 0.08 | 1.35 | 1.00E-04 | 1.61E-03 | 7.56E-03 | 1.60E-01 |
| Garcia, 1993 | A3 | (saline currents) | 1350 | 1.70E-01 | 2.50E-02 | 0.08 | 1.35 | 1.00E-04 | 1.61E-03 | 7.56E-03 | 1.60E-01 |
| Garcia, 1993 | A4 | (saline currents) | 1350 | 2.50E-01 | 2.50E-02 | 0.08 | 1.35 | 1.00E-04 | 2.08E-03 | 1.26E-02 | 2.07E-01 |
| Garcia, 1993 | B2 | (saline currents) | 1350 | 2.50E-01 | 2.50E-02 | 0.08 | 1.35 | 1.80E-04 | 2.27E-03 | 8.35E-03 | 4.07E-01 |
| Garcia, 1993 | B3 | (saline currents) | 1350 | 2.10E-01 | 2.50E-02 | 0.08 | 1.35 | 1.80E-04 | 1.84E-03 | 5.48E-03 | 3.30E-01 |
| Garcia, 1993 | B5 | (saline currents) | 1350 | 2.50E-01 | 2.50E-02 | 0.08 | 1.35 | 1.80E-04 | 2.26E-03 | 8.27E-03 | 4.05E-01 |
| Garcia, 1993 | B6 | (saline currents) | 1350 | 2.10E-01 | 2.50E-02 | 0.08 | 1.35 | 1.80E-04 | 2.04E-03 | 6.74E-03 | 3.66E-01 |
| Garcia, 1993 | C1 | (saline currents) | 1350 | 2.20E-01 | 2.50E-02 | 0.08 | 1.35 | 1.80E-04 | 2.07E-03 | 6.94E-03 | 3.71E-01 |
| Garcia, 1993 | C3 | (saline currents) | 1350 | 2.00E-01 | 2.50E-02 | 0.08 | 1.35 | 1.80E-04 | 1.94E-03 | 6.10E-03 | 3.48E-01 |
| Garcia, 1993 | D1 | (saline currents) | 1350 | 1.70E-01 | 2.50E-02 | 0.08 | 1.35 | 1.80E-04 | 1.83E-03 | 5.42E-03 | 3.28E-01 |
| present experiments | R49 probe 1 | 0.11 | 2650 | 1.78E+00 | 7.00E-02 | 0.191 | 2.65 | 1.35E-04 | 4.52E-02 | 9.34E-01 | 6.07E+00 |
| present experiments | R49 probe 2 | 0.11 | 2650 | 1.78E+00 | 7.00E-02 | 0.191 | 2.65 | 1.35E-04 | 5.59E-02 | 1.43E+00 | 7.51E+00 |
| present experiments | R49 probe 3 | 0.11 | 2650 | 1.78E+00 | 7.00E-02 | 0.191 | 2.65 | 1.35E-04 | 4.34E-02 | 8.63E-01 | 5.84E+00 |
| present experiments | R49 probe 4 | 0.11 | 2650 | 1.78E+00 | 7.00E-02 | 0.191 | 2.65 | 1.35E-04 | 2.17E-02 | 2.15E-01 | 2.91E+00 |
| present experiments | R51 probe 1 | 0.11 | 2650 | 1.78E+00 | 7.00E-02 | 0.191 | 2.65 | 1.35E-04 | 3.14E-02 | 4.51E-01 | 4.22E+00 |
| present experiments | R51 probe 2 | 0.11 | 2650 | 1.78E+00 | 7.00E-02 | 0.191 | 2.65 | 1.35E-04 | 6.39E-02 | 1.87E+00 | 8.59E+00 |
| present experiments | R51 probe 3 | 0.11 | 2650 | 1.78E+00 | 7.00E-02 | 0.191 | 2.65 | 1.35E-04 | 2.35E-02 | 2.52E-01 | 3.16E+00 |
| present experiments | R51 probe 4 | 0.11 | 2650 | 1.78E+00 | 7.00E-02 | 0.191 | 2.65 | 1.35E-04 | 7.62E-03 | 2.66E-02 | 1.02E+00 |
| Baas, 2004 | 1 | 0.27 | 2650 | 4.37E+00 | 5.50E-02 | 0.15 | 2.65 | 2.35E-04 | 1.90E-01 | 9.46E+00 | 4.44E+01 |
| Baas, 2004 | 2 | 0.27 | 2650 | 4.37E+00 | 5.50E-02 | 0.15 | 2.65 | 2.35E-04 | 1.90E-01 | 9.46E+00 | 4.44E+01 |
| Baas, 2004 | 3 | 0.35 | 2650 | 5.67E+00 | 5.50E-02 | 0.15 | 2.65 | 2.35E-04 | 2.16E-01 | 1.23E+01 | 5.05E+01 |
| Baas, 2004 | 4 | 0.14 | 2650 | 2.27E+00 | 5.50E-02 | 0.15 | 2.65 | 2.35E-04 | 1.37E-01 | 4.90E+00 | 3.20E+01 |
| Baas, 2004 | 7 | 0.27 | 2650 | 4.37E+00 | 5.50E-02 | 0.065 | 2.65 | 4.00E-05 | 1.25E-01 | 2.40E+01 | 4.96E+00 |
| Baas, 2004 | 8 | 0.21 | 2650 | 3.40E+00 | 5.50E-02 | 0.065 | 2.65 | 4.00E-05 | 1.10E-01 | 1.87E+01 | 4.38E+00 |
| Baas, 2004 | 9 | 0.29 | 2650 | 4.69E+00 | 5.50E-02 | 0.065 | 2.65 | 4.00E-05 | 1.29E-01 | 2.58E+01 | 5.14E+00 |
| Baas, 2004 | 10 | 0.29 | 2650 | 4.69E+00 | 5.50E-02 | 0.065 | 2.65 | 4.00E-05 | 1.29E-01 | 2.58E+01 | 5.14E+00 |
| Baas, 2004 | 11 | 0.29 | 2650 | 4.69E+00 | 5.50E-02 | 0.065 | 2.65 | 4.00E-05 | 1.29E-01 | 2.58E+01 | 5.14E+00 |
| Baas, 2004 | 12 | 0.29 | 2650 | 4.69E+00 | 5.50E-02 | 0.065 | 2.65 | 6.90E-05 | 1.29E-01 | 1.49E+01 | 8.87E+00 |
| Baas, 2004 | 13 | 0.35 | 2650 | 5.67E+00 | 5.50E-02 | 0.065 | 2.65 | 6.90E-05 | 1.42E-01 | 1.80E+01 | 9.75E+00 |
| Baas, 2004 | 14 | 0.21 | 2650 | 3.40E+00 | 5.50E-02 | 0.065 | 2.65 | 6.90E-05 | 1.10E-01 | 1.08E+01 | 7.55E+00 |
| Garcia, 1989 | min | | | 2.00E-02 | 2.50E-02 | 0.08 | 2.5 | 5.00E-06 | 6.33E-03 | 5.46E-01 | 3.15E-02 |
| Garcia, 1989 | max | 0.01 | 2650 | 0.15 | 2.50E-02 | 0.08 | 2.65 | 7.00E-05 | 1.73E-02 | 2.66E-01 | 1.21E+00 |
| Gray, 2005 | 3 deg slope | 0.01 | 2500 | 1.47E-01 | 2.00E-02 | 0.052 | 2.5 | 7.10E-05 | 1.24E-02 | 1.48E-01 | 8.78E-01 |
| Gray, 2005 | 6 deg slope | 0.01 | 2500 | 1.47E-01 | 2.00E-02 | 0.105 | 2.5 | 7.10E-05 | 1.75E-02 | 2.95E-01 | 1.24E+00 |
| Gray, 2005 | 9 deg slope | 0.01 | 2500 | 1.47E-01 | 2.00E-02 | 0.156 | 2.5 | 7.10E-05 | 2.15E-02 | 4.41E-01 | 1.52E+00 |
| yu, 2011 | silica 1 | 0.02 | 2650 | 3.24E-01 | 1.00E-02 | 0.191 | 2.65 | 5.00E-05 | 2.49E-02 | 7.64E-01 | 1.24E+00 |
| yu, 2011 | silica 2 | 0.02 | 2650 | 3.24E-01 | 1.00E-02 | 0.122 | 2.65 | 2.00E-05 | 1.99E-02 | 1.22E+00 | 3.96E-01 |
| yu, 2011 | silica 3 | 0.02 | 2650 | 3.24E-01 | 1.00E-02 | 0.061 | 2.65 | 8.30E-06 | 1.41E-02 | 1.47E+00 | 1.16E-01 |
| Felix, 2005 | kaolin | 0.14 | 2650 | 2.27E+00 | 3.75E-02 | 0.087 | 2.65 | 9.00E-06 | 8.61E-02 | 5.09E+01 | 7.71E-01 |
| Felix, 2005 | silica flour | 0.28 | 2650 | 4.53E+00 | 3.75E-02 | 0.087 | 2.65 | 6.00E-06 | 1.22E-01 | 1.53E+02 | 7.27E-01 |
| Straub & Mohrig 2008 | | | | | | | 2.65 | 2.90E-05 | 3.50E-02 | 2.61E+00 | 1.01E+00 |
| Xu et al., 2010 | 2 @ 820 m | | | | | | 2.65 | 3.50E-04 | 4.83E-02 | 4.12E-01 | 1.68E+01 |
| Xu et al., 2010 | 2 @ 1020 m | | | | | | 2.65 | 2.50E-04 | 4.71E-02 | 5.49E-01 | 1.17E+01 |
| Xu et al., 2010 | 2 @ 1445 m | | | | | | 2.65 | 2.50E-04 | 6.17E-02 | 9.43E-01 | 1.54E+01 |
| Xu et al., 2010 | 3 @ 820 m | | | | | | 2.65 | 2.50E-04 | 4.97E-02 | 6.11E-01 | 1.24E+01 |
| Xu et al., 2010 | 3 @ 1020 m | | | | | | 2.65 | 2.50E-04 | 3.41E-02 | 2.88E-01 | 8.49E+00 |
| Xu et al., 2010 | 4 @ 1020 m | | | | | | 2.65 | 2.50E-04 | 4.83E-02 | 5.76E-01 | 1.20E+01 |
| Xu et al., 2010 | 4 @ 1445 m | | | | | | 2.65 | 2.50E-04 | 3.71E-02 | 3.41E-01 | 9.25E+00 |

Supplementary Table 2.1: Parametrisations of the Shields parameter and particle Reynolds number in experimental and real world turbidity currents as they are plotted in Figure 2.1.

Chapter 3

Linking submarine channel-levee facies and architecture to flow structure of turbidity currents; insights from flume tank experiments.

ABSTRACT

Submarine leveed channels are sculpted by turbidity currents that are commonly highly stratified. Both the concentration and the grain-size decrease upward in the flow and this is a fundamental factor that affects the location and grain-size of deposits around a channel. This study presents laboratory experiments that link the morphological evolution of a progressively developing leveed channel to the suspended sediment structure of the turbidity currents. Previously it was difficult to link turbidity current structure to channel-levee development because observations from natural systems were limited to the depositional products while experiments did not show realistic morphodynamics due to scaling issues related to the sediment transport. Here we use a novel experimental approach to overcome scaling issues, which results in channel inception and evolution on an initially featureless slope. Depth of the channel increased continuously as a result of levee aggradation combined with varying rates of channel floor aggradation and degradation. The resulting levees are fining upward and the grain-size trend in the levee matches the upward decrease in grain-size in the flow. Thus it is shown that such deposit trends can result from internal channel dynamics and do not have to reflect upstream forcing. The suspended sediment structure can also be linked to the lateral transition from sediment bypass in the channel thalweg to sediment deposition on the levees. The transition occurs because the sediment concentration is below the flow capacity in the channel thalweg while higher up on the channel walls the concentration exceeds capacity resulting in deposition of the inner levee. Thus, a framework is provided to predict the growth-pattern and facies of a levee from the suspended sediment structure in a turbidity current.

Based on

Linking submarine channel-levee facies and architecture to flow structure of turbidity currents; insights from flume tank experiments., by Jan de Leeuw, Joris T. Eggenhuisen, Matthieu J.B. Cartigny, *Sedimentology* (in revision)

3.1 Introduction

Submarine channel-levee systems allow turbidity currents to transport sediment over large distances into oceanic basins (Posamentier & Kolla, 2003). These channels are highly dynamic features that can progressively deepen (Hodgson et al., 2016) and extend (Morris et al., 2014), thereby increasing sediment bypass (*sensu* Stevenson et al., 2015) in the more proximal submarine fan region. The build-up of levees does not only contribute to channel confinement but the levees also form sediment bodies in their own right, which constitute a significant portion of submarine fan stratigraphy (Sylvester et al., 2012; Prather et al., 2016). Levees form by overspill processes because turbidity current thickness commonly exceeds channel depth. (Peakall et al., 2000; Pirmez & Imran, 2003; Mohrig & Buttle 2007; Straub et al., 2008; Hansen et al., 2015). An upward decrease in grain size and sediment concentration has been measured in turbidity currents in experiments (Garcia, 1994; Kneller & Buckee, 2000; Baas et al., 2005), field measurements (Xu et al., 2014), and has been reconstructed from deposits around channels and canyons (Migeon et al., 2012; Symons et al., 2017). Therefore, overspill will be more dilute and finer-grained than the flow confined in the channel (Pirmez and Imran, 2003; Spinewine et al., 2011) (Fig. 3.1A). Upward bed thinning and fining have been observed widely in levee sequences and is often attributed to progressive increase of channel depth and thus levee height allowing only the upper part of the turbidity current to overspill (Hess and Normark, 1976; Pirmez and Imran, 2003; Dennielou et al., 2006). Conversely, thickening and coarsening trends have also been recorded (Kane et al., 2007; Kane and Hodgson, 2011) and result when channel floor deposition exceeds levee growth causing coarser grained parts of the turbidity current to overspill (Kane et al., 2007). It is, however, hard to test these mechanisms because beds can rarely be correlated between channel fill deposits and levees, and any control on relative timing of channel and levee deposition is generally absent. Additionally, similar thickening, thinning, coarsening and fining trends can be achieved by changes in flow magnitude and composition (Beaubouef, 2004) possibly forced by sea-level and sediment supply variations due to climate change. Thus, the grain-size trends in levee sequences reflect a combination of morphological evolution of the channel, grain-size sorting in turbidity currents and possible allogenic forcing (Normark and Damuth, 1997; Pirmez and Imran, 2003; Dennielou et al., 2006) (Fig. 3.1B).

To show the effect of different internal and external controls unequivocally it is required that the morphological evolution of the channel and the flow properties are monitored simultaneously, which is difficult to achieve. Outcrop and subsurface datasets provide no direct information on flow processes and monitoring of presently active systems rarely covers sufficient time to monitor the co-evolution of turbidity currents and channel morphology (Xu et al., 2004, 2014; Hughes Clarke, 2016). Geological models of channel-levee evolution have relied on numerical models (Imran et al., 1998; Abd El-Gawad et al., 2012; Janocko et al., 2013; Basani et al., 2014) and laboratory experiments (Mohrig and Buttle, 2007; Islam et al., 2008; Straub et al., 2008; Straub and Mohrig, 2008; Kane et al., 2010b; Ezz et al., 2013), which have provided important insights in the flow dynamics of channelised turbidity currents. However, turbidity currents in previous experiments were strongly depositional and aggradation rates in the channel exceeded aggradation rates on the levees. These experiments were therefore less suitable to test the relation between flow structure, channel-depth evolution and levee grain-size trends. De Leeuw et al. (2016) have recently shown that submarine channel morphodynamics can be accurately captured in Shields-scaled turbidity current experiments. The relevant scaling parameters are the Shields parameter and the particle Reynolds number, which rely on shear velocity of the flow and particle size and density of the suspended sediment. A channel thalweg that is dominated by bypass and erosion

is a key component of natural submarine channel morphodynamics. Bypass and erosion are only possible when suspended sediment transport is vigorously sustained. The shear velocity in channel morphodynamics experiments should therefore be sufficiently high relative to the settling velocity to generate experimental flows that resemble natural channel behaviour.

The Shield-scaled experiments discussed in this paper show the inception and evolution of a channel on an underwater slope where the currents can expand (3D experiments). Turbidity current grain size and concentration profiles are measured in a separate experiment in a rectangular flume tank which is more suitable for this type of measurements (2D experiment; see Methods below). The objectives of this work are to: (i) relate the grain-size stratification in turbidity currents to levee grain-size trends; (ii) determine the role of flow competence and capacity on sediment bypass in the channel axis and contemporaneous deposition on the levees. In general, the results show how grain-size and density stratification in turbidity currents relates to the geometry and facies of levees.

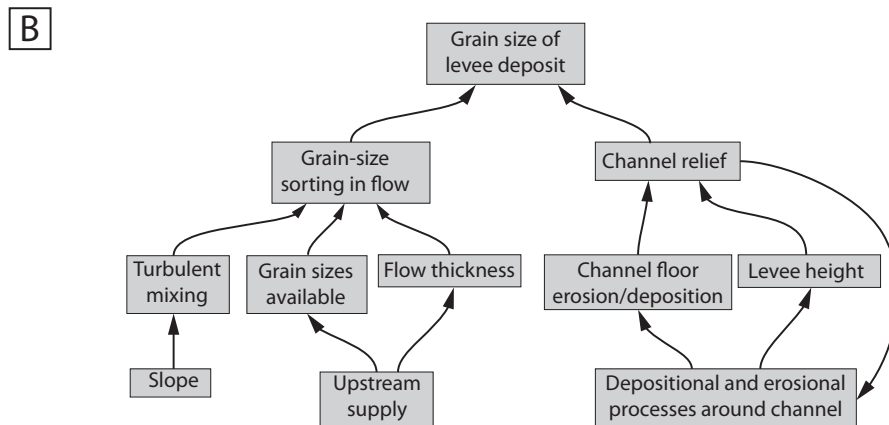
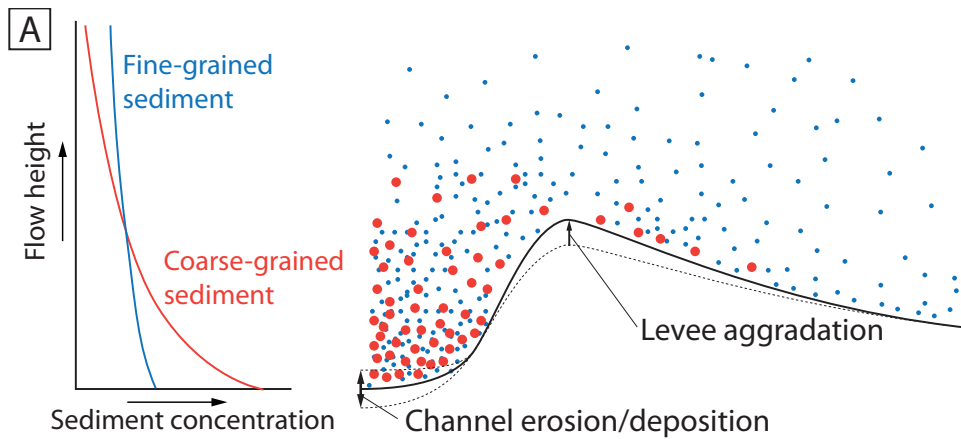


Figure 3.1: (A) Schematic representation of the distribution of fine and coarse suspended sediment in a turbidity current in a leveed channel (modified after Hansen et al., 2015). (B) Diagram illustrating controls on the grain-size distribution of overspill.

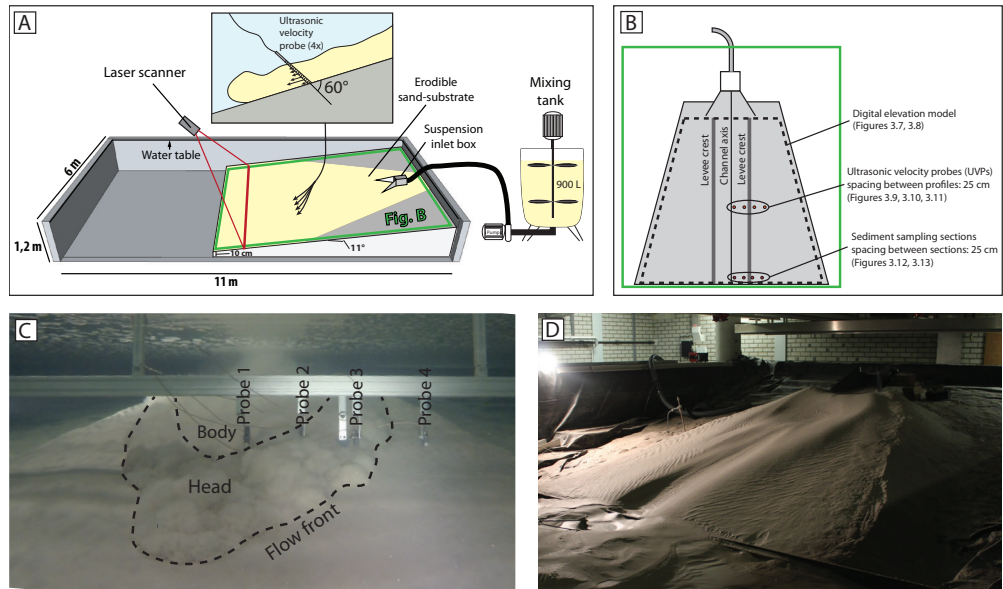


Figure 3.2: (A) Schematic overview of the 3D experimental set-up. (B) Locations of the measurements: velocity profilers, sediment samples, elevation model. (C) Underwater view of the front of the turbidity current in Run 2. (D) Drained tank with deposits from three turbidity currents after Run 3.

3.2 Methods

The 3D experiments presented here are designed to co-measure the progressive evolution of channel relief and the changing velocity field of the turbidity currents forming the channel-levee. Velocity measurements can be performed non-intrusively, and they will not affect the pattern of erosion and deposition of the experiment. Suspended sediment concentration and grain-size stratification are key additional variables to constrain to understand the flow-channel evolution fully. Unfortunately, non-intrusive measurement techniques for these variables are not available for these types of flows. The most reliable measurement technique is to collect samples from the flow with siphon tubes. These tubes need to be inserted into the flow, perturbing the flow structure, and close to the bed, where they affect the pattern of deposition and erosion in the experiment. Additionally, the erodible bed in the 3D experiment would be scoured around the siphoning tubes and the elevation of the siphoning tubes to the bed would therefore vary in an unconstrained fashion. Therefore, two types of experiments are presented here: (i) experiments where a flow was able to expand laterally on a slope and erode and deposit to build channel-levee stratigraphy (3D experiments) and (ii) an experiment in a rectangular flume tank wherein suspended sediment samples were collected with siphon tubes to obtain concentration and grain-size profiles (2D experiments).

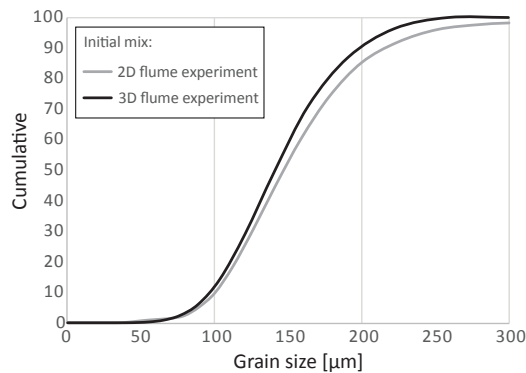


Figure 3.3: Grain-size distribution of the sediment used in the 2D and 3D experiments.

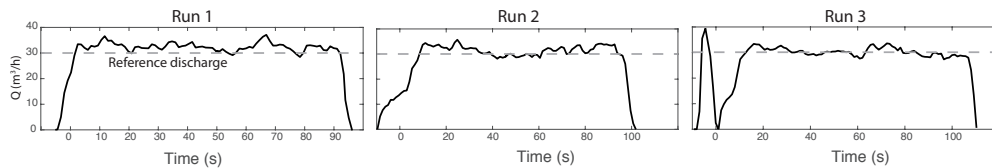


Figure 3.4: Discharge over time throughout Run 1, 2 and 3.

3.2.1 3D channel formation experiments

Set-up

The experiments were performed in the Eurotank flume laboratory in Utrecht. The basin used for the main experiments measures 6 by 11 metres, is 1.2 metres deep and was entirely filled with water during the experiments (Fig. 3.2). The basin floor consisted of an 11 degrees slope ending in a vertical drop of 10 cm. The slope was covered with unconsolidated sand that had the same grain-size distribution as the suspended sediment in the turbidity currents in the 3D experiments (Fig. 3.3). The flow (discharge, concentration) and set-up (slope) parameters were chosen in such a way that Shield – scaled turbidity currents were able to by-pass sediments (de Leeuw et al., 2016) and thereby to resemble a natural slope system on which channels function as a conduit for sediment bypass for the majority of the time. The flows were allowed to spread laterally on the slope, and the substrate on the slope consisted of unconsolidated material which allowed the currents to build topography by deposition as well as by erosion.

Procedure and measurements

Three successive turbidity currents were released from the inlet at the top of the slope (Fig. 3.2). The initial current flowed on a featureless slope whereas subsequent currents interacted with topography created by previous currents. Prior to each run a sediment suspension was prepared in an external mixing tank. The volume of the suspension was 900L and the sediment concentration was 17% by volume. The quartz sand (*Sibelco BR-37*), which was used to make the suspensions had a median grain-size (D_{50}) of 141 μm , a D_{10} of 44 μm , a D_{90} of 199 μm and had a specific density of 2650 kg/m^3 (Fig. 3.3). The grain-size was analysed using a Malvern Mastersizer particle sizer. The mixture was supplied to the main set-up with a centrifugal pump. The supply rate was monitored with a discharge meter (Krohne Optiflux 2300) and the pump speed was adjusted

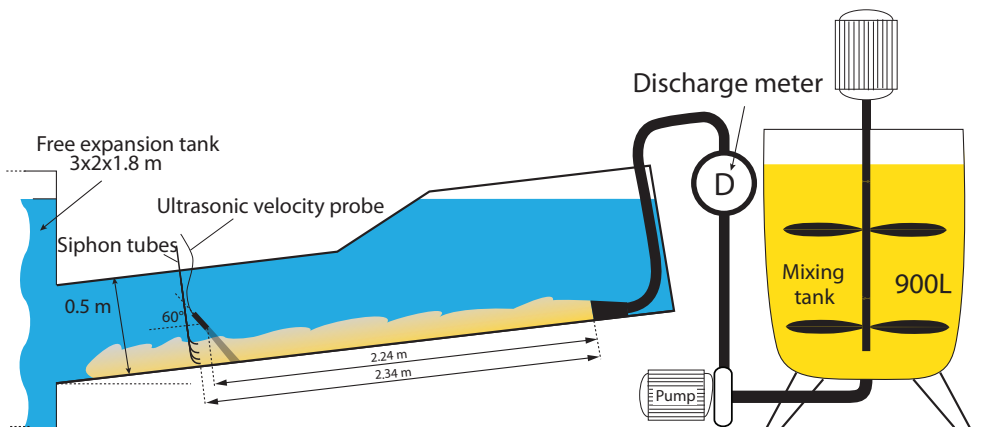


Figure 3.5: Schematic overview of the set-up for the 2D experiments (modified after Cartigny et al., 2014).

when the discharge deviated from the reference value of 8,3 L/s. The discharge during each run was recorded with a Labview control system (Fig. 3.4). The maximum discharge was reached after 5-10 seconds in each run. During Run 3, there was a short interruption of the supply early in the run. Velocity profiles of the turbidity current were collected at four locations using Ultrasonic Doppler Velocity Profiler probes (*UVP Duo MX, 1 MHz*). These probes were installed at a vertical distance of 0.15 m above the bed. The distance between the probes was 0.25 m and their locations are indicated in Figure 3.2B. The probes were oriented parallel to the dip direction of the slope and pointed diagonally down with an angle of 60 degrees relative to the initial slope. The vertical resolution of the velocity profile is 0.74 mm.

The basin was drained to expose the deposit after each experimental run. Then, a digital elevation model (DEM) with a horizontal resolution of 2x2 mm was created using a laser scanner. Maps of deposition and erosion were created for each experiment by subtracting the DEM of the experimental deposits and a DEM of the sediment bed prior to the experiments. In addition, after the final run sediment samples were collected for grain-size analysis.

3.2.2 2D flow sampling experiments

Set-up

The concentration and grain-size distribution of the turbidity currents were measured in a separate experimental set-up. The 2D set-up consists of a 4 m long, 0.5 m deep and 0.1 m wide rectangular flume that terminates in a run-out tank (Fig. 3.5) and is largely similar to the set-up presented by Cartigny et al. (2013). The slope angle of the flume tank floor is 9 degrees.

Procedure and measurements

The sediment was supplied from the mixing tank that also was used for the 3D experiments. The sediment used in the experiment was from a different batch and had a slightly larger median grain-size (146 μm) than the sediment used in the 3D experiment (140 μm) (Fig. 3.3). The volume of the mix is 900 L and the volume concentration of sediment is 17%. The discharge during the experiment was 3.5 L/s. Flow velocity and sediment concentration were measured at 2.24 m and

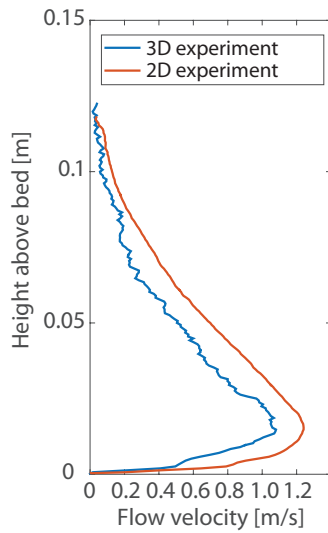


Figure 3.6: Comparison between a representative velocity profile from the 2D run and a velocity profile from the 3D run. The shown velocity profile from the 3D run uses the velocity data from Probe 1 from the interval 30–50 seconds of Run 3.

| Experiment type | Flow thickness (m) | Maximum velocity (m/s) | Depth-averaged velocity (m/s) | Shear velocity (m/s) | Shear velocity/Settling velocity (-) |
|-----------------|--------------------|------------------------|-------------------------------|----------------------|--------------------------------------|
| 2D | 0.73 | 1.25 | 0.92 | 0.079 | 5.5 |
| 3D | 0.77 | 1.05 | 0.66 | 0.062 | 4.7 |

Table 3.1: Turbidity current flow parameters in the 2D and 3D experiment. The velocity profiles used to determine these flow parameters are shown in Fig. 3.6.

2.34 m from the inlet, respectively (Fig. 3.5). A UVP probe was used to measure the flow velocity profile and siphoning tubes measured the sediment concentration and grain-size at different elevations in the flow. The siphoning tubes had an inner diameter of 8 mm and were centred at 1, 2, 4 and 8 cm above the inclined bed. The flow was completely bypassing such that the bed did not aggrade and the distance between the siphoning tubes and the bed remained constant.

3.2.3 Integration of the results from the 2D and 3D experiments

The concentration and grain-size measurements from the 2D experiments are to be applied in the interpretation of the deposits formed in the 3D experiments. The differences in physical configuration between the 2D flume and the 3D experiment make it difficult to reproduce a flow with exactly the same velocity, concentration, and grain-size profile in both experiments. At similar boundary conditions (slope, discharge), turbidity currents in 2D experiments tend to have a higher flow velocity compared to 3D experiments. This is likely to be a result of the lateral spreading of the flow in the 3D experiments. The boundary conditions in the 2D experiment were adjusted to create a flow with a thickness and velocity that is approximately similar to those measured in the 3D experiments. Two measures were taken: (1) discharge is lowered from 8.3 L/s in the 3D experiments to 3.5 L/s in the 2D experiment and (2) the slope is lowered from 11° in the

3D experiments to 9° in the 2D experiment. Representative velocity profiles of the flows in both experiments are shown in Figure 3.6. These profiles show that the flows in both experiments have similar thickness and velocity, although the velocity of the flow in the 2D experiment is ~ 0.15 m/s higher. There are three smaller differences between the boundary conditions in both flumes. Firstly, the grain-size distribution of the sediment used in the 2D experiment has a median grain-size which is $6 \mu\text{m}$ coarser than the sediment used in the 3D experiment (Fig. 3.3). Secondly, the sediment samples from the flow have been collected in the 2D experiment at 2.34 m from the inlet whereas the deposit samples in the 3D experiments have been collected at 3.4 m from the inlet. Thus, the flow in the 3D experiment evolved over a longer distance before it reached the location where it deposited the sediment that was later sampled. Thirdly, the turbidity current in the 2D experiment by-passed all sediment, while the turbidity current in the 3D experiment deposited part of the sediment upslope of the location where measurements were taken.

Despite the geometrical differences between the set-ups, the grain-size and concentration structure of the currents are fairly similar. One indication that the currents in both types of experiments have similar characteristics is the similarity of their velocity profiles (Fig. 3.6). Flow parameters from both experiments are shown in Table 1 and make the comparison quantitative. Compared to the 3D experiment, the flow in the 2D experiment is characterised by a higher maximum velocity, depth-averaged velocity and shear velocity. A critical parameter that controls the shape of the concentration profile is the ratio between the shear velocity (u^*) and the settling velocity (W_s). A higher u^*/W_s ratio results in a concentration profile that is more uniform (Rouse, 1937). A characteristic settling velocity is obtained for each of the experiments from the median grain size of the sediment used. The 2D experiment had a slightly higher u^*/W_s ratio compared to the 3D experiment (Table 3.1). This implies that the turbidity current in the 3D experiment was slightly less homogenised and more stratified in terms of density and grain size. However, previous theoretical work (Rouse, 1937) has shown variations u^*/W_s ratio between 4.7 and 5.5 do not result in a large difference in the shape of the sediment concentration profile. Additionally, variations in suspension dynamics (u^*/W_s) between the 2D and 3D experiments are much smaller than the range of values that will be presented within the 3D channel-levee system below.

3.3 Results

3.3.1 3D experiments

Morphological development

Deposition and erosion maps for the three subsequent runs were created (Fig. 3.7). The turbidity current in Run 1 deposited two sub-parallel ridges and caused limited erosion between the ridges on the upper slope. The ridges are confining the core of the flow, have a tapering geometry away from the ridge-crest, and can therefore be qualified as levees. The resulting topography provided confinement on the slope for the subsequent turbidity currents. The turbidity current in Run 2 deposited additional sediment on the levees. Furthermore, the current eroded sediment between the levees on the lower and upper segments of the slope (Fig. 3.7). The gradient along the centreline of the confinement became irregular because the erosion in the centre of the channel did not occur along the whole length of the slope. During Run 3 the turbidity current deposited more sediment on the levees. The left levee aggraded less than the right levee during this run. This is likely to be related to the shift of the channel axis toward the right levee. It is not clear why this shift of the channel axis occurred. Erosion of the channel floor continued along the lower and

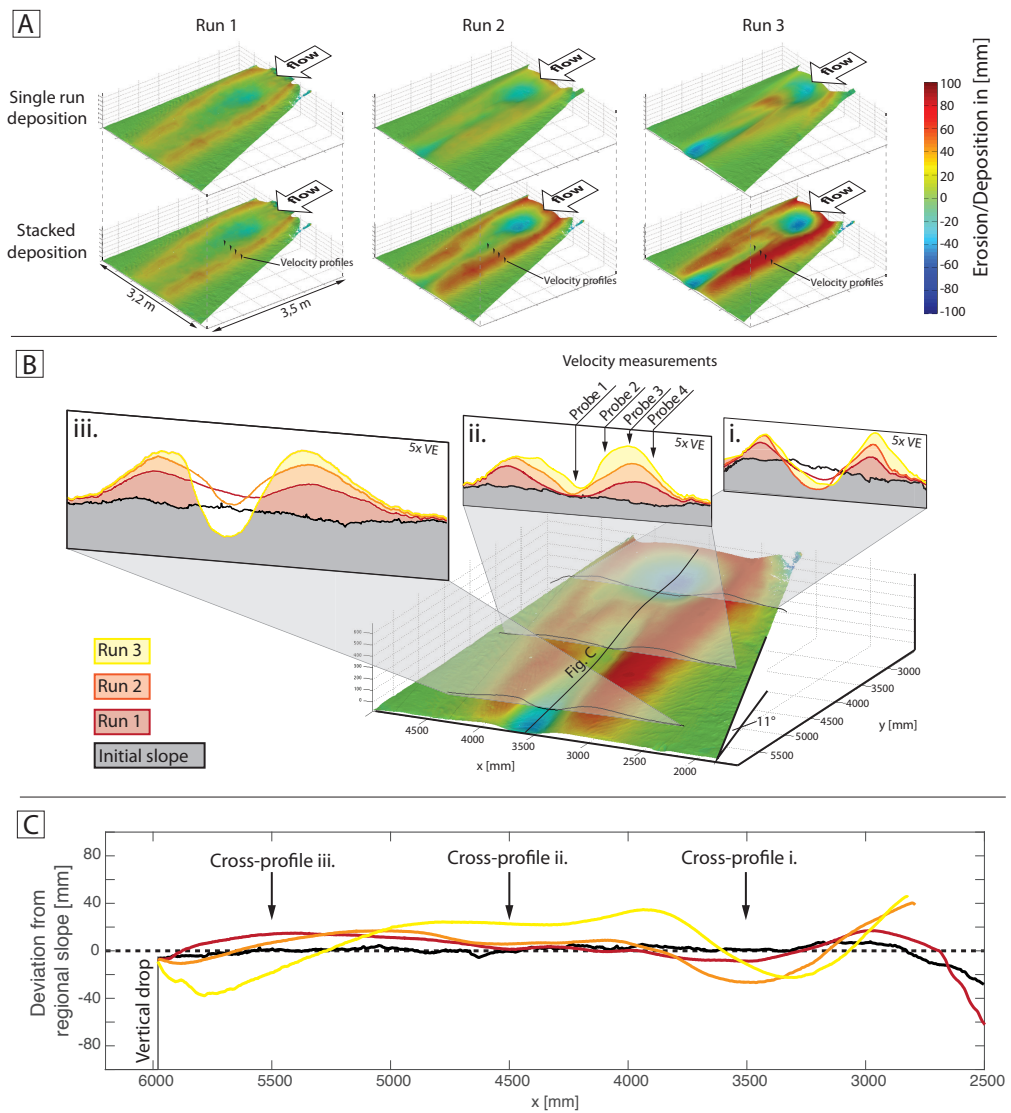


Figure 3.7: (A) Elevation models with colours indicating the thickness of the deposits after each run. Figures in the upper row show the deposition from each run separately. Figures in the lower row show the cumulative deposition after each run. (B) Cross-sections extracted from the elevation models illustrate the step-wise evolution of the slope channel. (C) Cross-section along the channel thalweg. (adapted from de Leeuw et al. (2016))

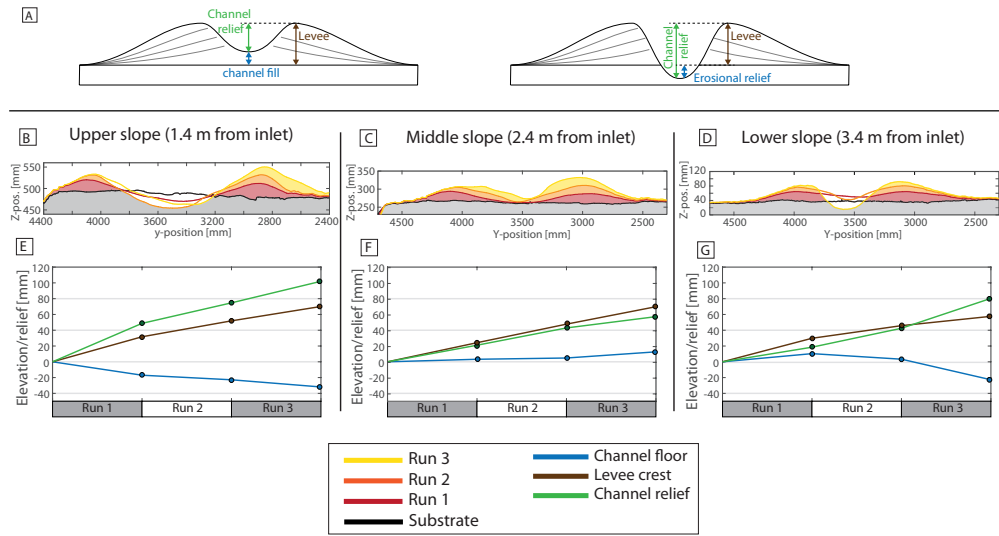


Figure 3.8: (A) Cartoon illustrating the relation between levee height, channel thalweg position and channel relief. Cross-sections of the channel on the upper (B), middle (C) and lower (D) slope. Locations of the cross-sections are the same as in Figure 3.7A. Aggradation/degradation of the channel floor and levees and the resulting channel depth are shown for the channel cross-sections on the upper (E), middle (F) and lower (G) slope. Note that the levee aggradation is similar in each of the cross-sections but the channel floor aggradation/degradation differs in timing and amplitude between the cross-sections. The channel relief evolution does therefore also differ between the cross-sections.

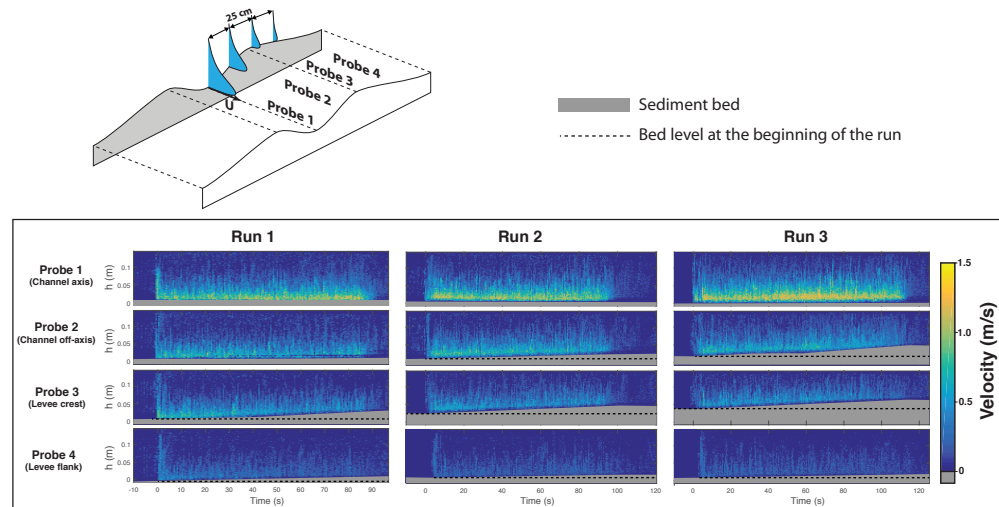


Figure 3.9: Downslope velocity of the turbidity current at each probe location and during each run. The locations of the probes are indicated in Figure 3.2.

upper segments of the slope while deposition on the channel floor took place on the middle slope segment.

Channel relief is defined here as the difference in elevation between the channel thalweg and the levee crest (Fig. 3.8A). During each of the runs the levee grows due to deposition while the channel thalweg is subject to variable degrees of deposition and erosion. Figure 3.8 shows the evolution of the channel relief for three cross-sections of the channel. In the cross-sections through the upper and lower slope (Fig. 3.8B, D, E, G), erosion occurs on the channel floor as well as deposition on the levees. The total channel relief is larger than the thickness of the levees in these cross-sections. Conversely, on the middle segment of the slope (Fig. 3.8C, F), there is no deposition or erosion on the channel floor during Run 1 and 2 and some deposition on the channel floor during Run 3. As a result, the final channel relief is smaller than the thickness of the levee. Overall, channel depth showed a monotonic increase through all runs in all locations. This was primarily the result of significant levee aggradation, which outweighed the variability in channel floor erosion and aggradation along the slope.

Development of the velocity field

The time-series of the velocity measurements collected during the three experiments at four probe locations are shown in Figure 3.9. Velocity measurements show the spatial and temporal variation in the flow in response to morphological evolution. The flow velocity in the thalweg of the slope channel (Probe 1) was systematically higher than away from the axis and the contrast increased as the channel confinement was building up. The height change of the bed at each of the four probe locations can be traced in the velocity data (Figure 3.9). The sediment bed equates to the point where the velocity goes to zero (grey). The bed is stationary at the location of Probe 1 while the bed aggrades continuously at the locations of Probes 2-4.

Velocity measurements from different time intervals show how the velocity field responds to the evolution of topography (Fig. 3.10). For each probe, time-averaged velocity profiles were obtained for 15s intervals (Fig. 3.10). The heads and tails (defined here as the first and last five seconds of the current) were not included in these intervals. During the first run (Fig. 3.10A, D, G, J), the maximum velocity increased along the channel axis while it decreased at the other localities. During the subsequent second (Fig. 3.10B, E, H, K) and third (Fig. 3.10C, F, I, L) run there was no further increase in the axial flow velocity (Probe 1) but there was a further decrease in the flow velocity at the off-axis locations (Probe 2-4). The continued decrease of the maximum velocity at Probes 2-4 is closely correlated with the aggradation of the bed at these locations.

Figure 3.11A shows the velocity profiles from all four probes combined in one plot. The profiles do each represent the average velocity over the interval 5-20 seconds of Run 3. This illustrates the velocity structure across the channel. The velocity profiles inside the confinement (Probes 1-3) do collapse above their respective velocity maxima. This part of the velocity profile is called the mixing layer and is defined as the domain above the velocity maximum, where the suspension mixes with the ambient fluid, and the velocity decreases upwards to 0 m/s. This collapse of the velocity profiles implies that the mixing layer is laterally uniform inside the channel. Figure 3.11B shows the same velocity profiles as shown in Figure 3.11A with the context of the contemporaneous channel topography. Contours of equal velocity are interpolated between the velocity profiles. This illustrates the uniformity of the mixing layer across the channel and the flat top of the current.

The velocity profile outside of the channel confinement (i.e. measured by Probe 4) deviates from the flat top seen within the channel. Thus, the velocity structure outside of the channel

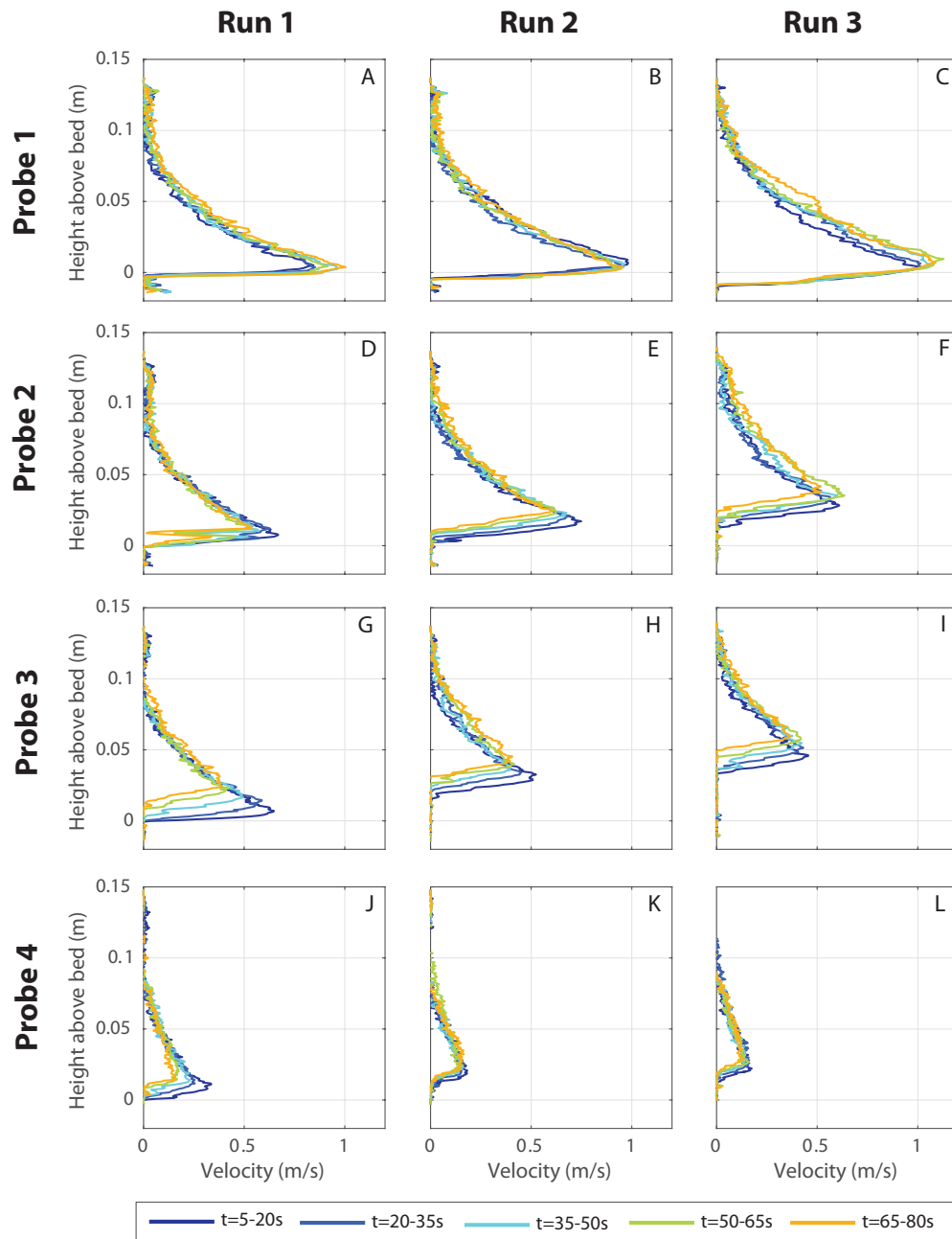


Figure 3.10: Temporal changes in flow velocity illustrated by time-averaged velocity profiles. (A,B,C) Probe 1. (D,E,F) Probe 2. (G,H,I) Probe 3. (J,K,L) Probe 4. Each velocity profile represents the average velocity over a 15 seconds interval. The locations of the probes are indicated in Figure. 3.2. The reference level in each of the plots is the bed at the start of Run 1.

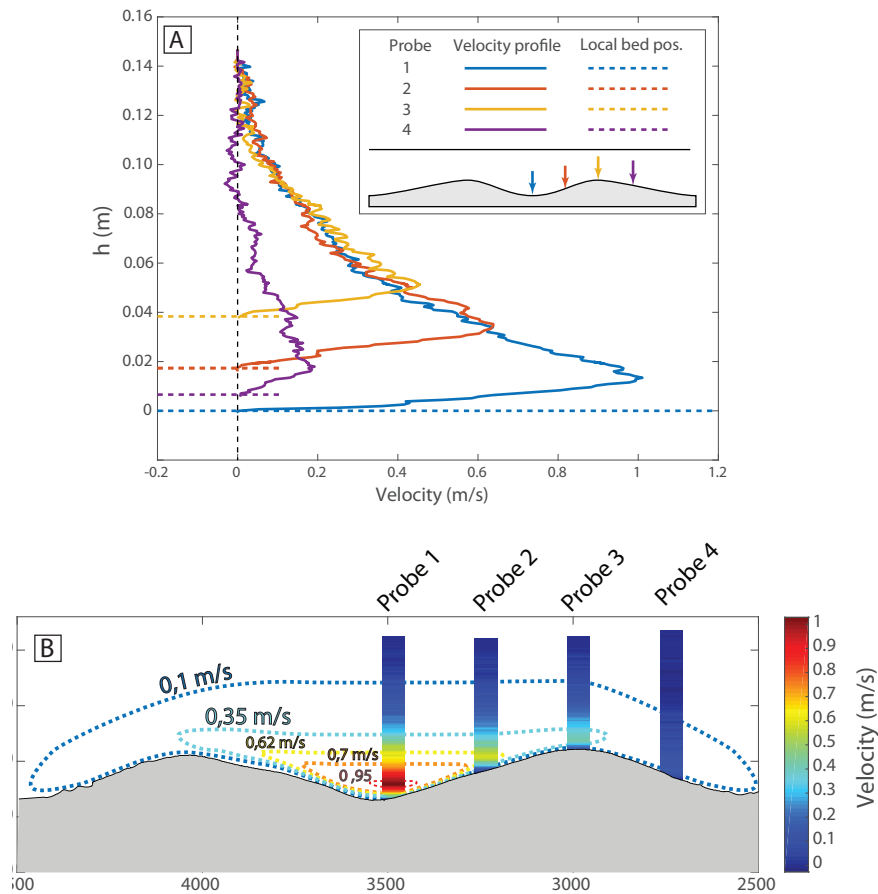


Figure 3.11: (A) Time-averaged velocity profiles from Probes 1 to 4 from the same time interval (5–20 s, Run 3) combined in one plot. Note that the mixing layer of the velocity profile inside the channel (1–3) collapses. (B) Velocity profiles from the same time interval plotted on the channel cross-section. Dashed lines indicate interpreted velocity contours.

was decoupled from the velocity structure inside of the channel. This leads to the important observation that the high-velocity core of the flow was contained within the channel and was not blanketing the entire slope.

Grain-size of the experimental levee deposits

Samples from the deposits were collected along four vertical sections (Fig. 3.2B) through the right levee on the lower slope. The median grain size of each of the samples is shown in Figure 3.12. The lowermost 2–3 samples from each of the vertical sections contain sediment from the substrate rather than sediment deposited by the turbidity currents. The median grain-size of the substrate is $\sim 150 \mu\text{m}$, slightly coarser than the grain size of any of the turbidity current deposits in the sections. Sections 2, 3 and 4 contain deposits of turbidity currents. The grain-size is decreasing upward in Section 2 and 3 whereas Section 4 is first coarsening and then fining upward. In Section 3 (Fig. 3.13A,B), it was found that a more coarse-grained sample was taken around the boundaries

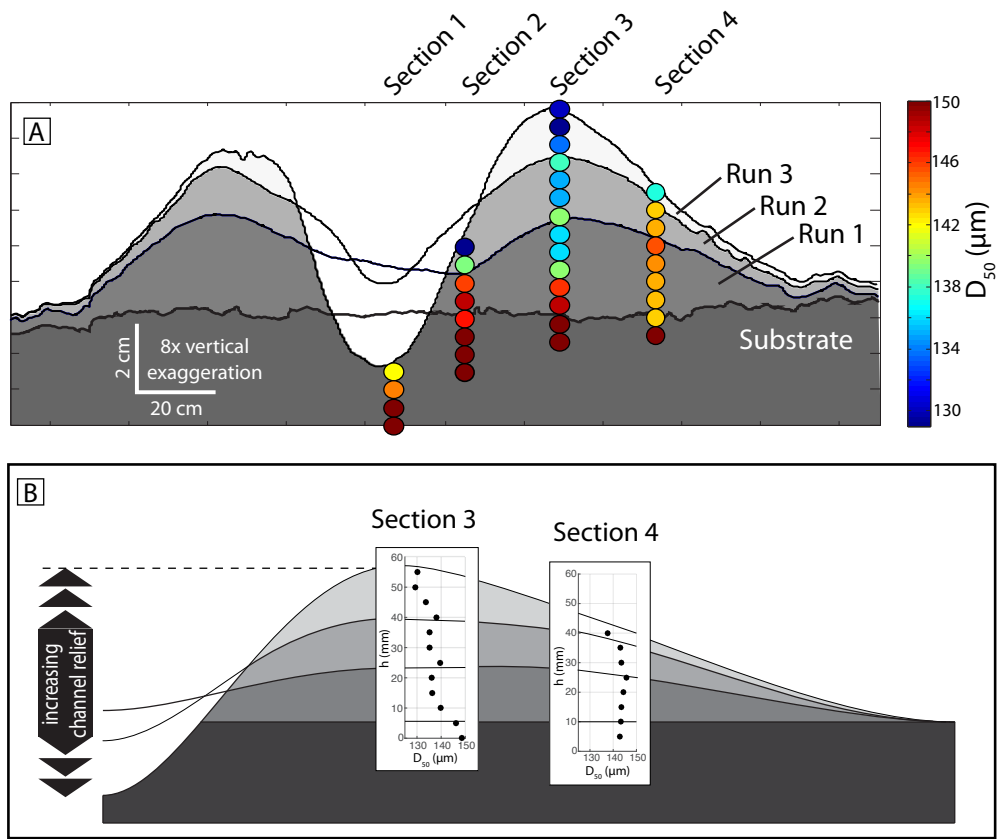


Figure 3.12: (A) Cross-section of one levee on the lower slope from which deposit samples were collected. Colour of dots indicate the median grain size of each sample. (B) Schematic representation of the levee stratigraphy and the grain-size trends in the sections with samples. Figure 3.2 provides a birds-eye view of the experimental domain with sample locations.

between the deposits of subsequent runs. Uncertainties in correlations between the DEM and the deposit stratigraphy prevent the unambiguous attribution of these relatively coarse samples to the top or base of sedimentation units. However, it is likely that the coarse samples correspond to the base of sediment units, because this would be consistent with the intuitive interpretation that sedimentation units are fining upward.

Figure 3.13 displays the median levee grain size of samples from the levee-crest section (Section 3), not plotted against stratigraphic position as in Figure 3.12, but against channel relief at the moment of deposition. Channel relief is the difference in elevation between the levee crest and the channel thalweg, which are both changing as the channel evolves (Fig. 3.8). The grain-size of the levee deposits decreases with increasing channel depth (Fig. 3.13). The steepest grain-size gradient occurs in the lowermost centimetre of the channel relief.

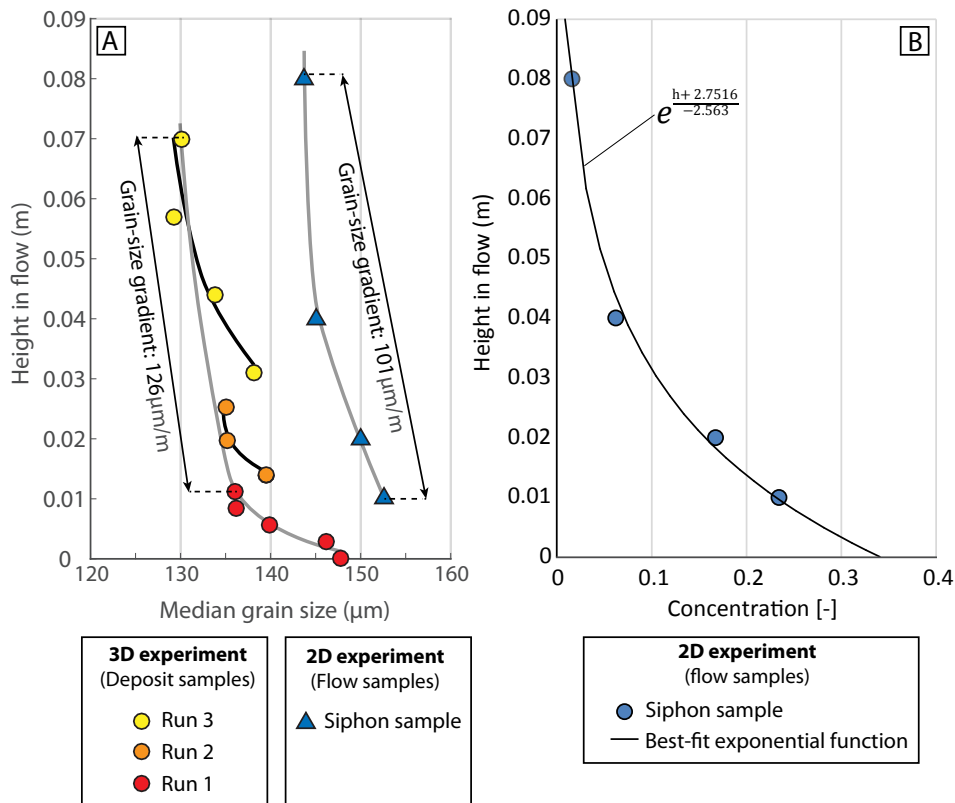


Figure 3.13: (A) Comparison between the grain-size trend in the levee deposit section (Section 3; Fig. 3.12) and the vertical change in grain size in an experimental turbidity current. The levee deposit samples are from the 3D experiments while the turbidity current samples were collected in a separate 2D experiment. Note that the deposit and flow profile have a similar grain-size gradient. (B) Suspended sediment concentration profile measured in the 2D experiment.

3.3.2 2D experiments

Grain-size stratification

The concentration and grain-size distribution in the sandy turbidity currents were measured during a single run in the 2D set-up. The siphoning tubes provide samples of the flow at 1, 2, 4 and 8 cm above the bed. The median grain-size of the suspended sediment decreases upward in the flow (Figure 3.13A). The grain-size gradient is largest between 1 and 4 centimetres above the bed and smaller between 4 and 8 centimetres above the bed. Averaged over the interval between 1 and 8 cm above the bed grain size decrease is 104 μm per metre elevation gain above the bed. The grain-size trend in the levee crest section (Fig. 3.13A, Section 3) has been calculated for a similar elevation interval. The decrease in grain-size between 0.8 and 7 cm above the channel thalweg is 126 μm per metre elevation gain. Overall, a very similar grain-size gradient is observed in the flow and the levee deposits. However, the absolute grain-sizes in the deposits are finer than those measured in the two-dimensional flow.

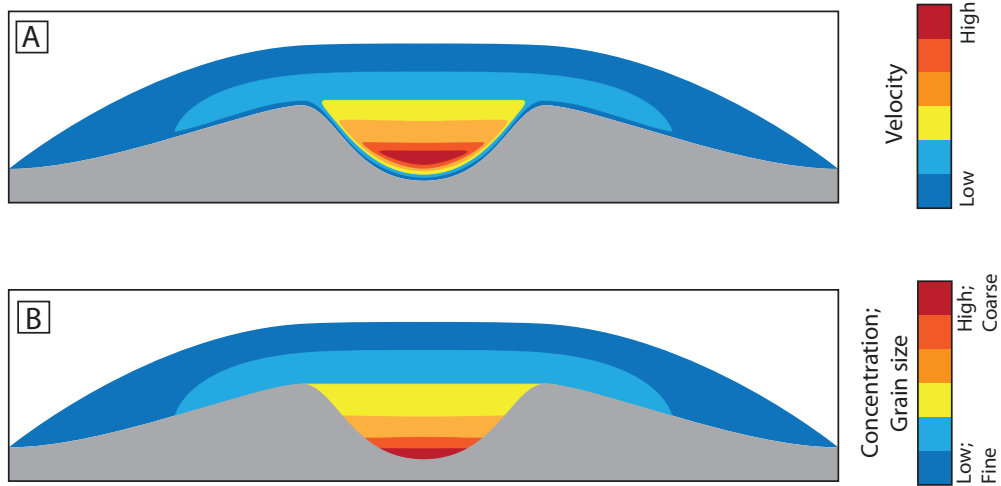


Figure 3.14: (A) Schematic representation of the velocity structure around the channel. (B) Schematic representation of distribution of suspended sediment concentration and grain size.

Density stratification

The suspended sediment concentration in the experimental turbidity current decreased sharply upward in the flow (Fig. 3.13B). A sediment concentration of 23% by volume was measured at 1 cm above the bed while the concentration at 8 cm above the bed was only 1.6%. An exponential function gives a good fit with the concentration data points and is used to interpolate and extrapolate the suspended sediment concentration profile.

3.4 Discussion

3.4.1 Flow structure in the channel

Velocity structure

The measurements in the 3D experiments provide unique constraints on the velocity structure, and allow us to draw a data-driven cross-section of the velocity field of a turbidity current in a leveed channel (Fig. 3.11). It appears that mixing-layer velocities inside the channel confinement are laterally uniform. Outside the confinement (i.e. on the levee flanks), the velocity structure is decoupled from the velocity structure inside the channel and the velocity decreases away from the levee crest. A schematic representation of the velocity structure is provided in Figure 3.14A. Many previous workers have schematically drawn a similar velocity structure for leveed submarine channels (Kane et al., 2010b; Peakall et al., 2000; Pirmez and Imran, 2003) where the velocity field in the channel is laterally uniform and the overbank flow is decoupled from the channelised flow. Here this assumption is confirmed for the first time by velocity measurements inside and outside the channel.

The probes are oriented parallel to the dip-direction of the slope. Therefore, they can only measure the downstream component of the velocity, which may be significantly lower than the true magnitude of the velocity when the flow direction diverges from this orientation. Turbidity current flow on levees is commonly divergent from the channel and flow direction may rotate

as the overbank fluid wedge develops (Kane et al., 2010a; Peakall et al., 2000). Current ripples on the experimental levee flanks indicate a flow at an angle of 35-40 degrees away from the channel (assuming that palaeoflow was perpendicular to ripple crests). With this angle between the direction of the flow and the orientation of Probe 4 (which is located above the levee flank), the downstream component of the velocity is 18-23% percent smaller than the true magnitude of the velocity. It is possible to correct the velocity data for this deviation but this would not fundamentally change the image of the velocity field across the channel such as shown in Figure 3.11.

Suspended sediment distribution

The grain-size and concentration structure of the turbidity currents have only been measured in the 2D experiment. It is assumed here that the concentration and grain-size are laterally uniform inside the channel (Fig. 3.14B), thereby resembling the velocity structure. A similar concentration structure was also found in 3D numerical modelling by Abd El-Gawad et al. (2012). The concentration and grain size of the suspended sediment outside the confinement, on the levee flank, are less well constrained in the present experiments. Generally, levee bed thickness and grain size decrease with distance away from the channel thalweg (Dykstra et al., 2012; Hansen et al., 2015). This indicates that concentration and grain size in the flow gradually decrease as turbidity currents run out on the levee flank.

3.4.2 Relating vertical sorting in turbidity currents to fining-upward levees

Fining upward levees are commonly observed in outcrops (Beaubouef, 2004) and cores from the sea floor (Normark and Damuth, 1997; Pirmez and Imran, 2003; Dennielou et al., 2006). The upward fining is often related to increasing channel depth. However, previously it remained difficult to test this depositional model. Firstly, changes in bed thickness and grain size within a levee sequence can both be a result of changes in channel depth and changes in flow size (Dennielou et al., 2006; Kane et al., 2011). From the depositional record it is rarely possible to distinguish between the two types of forcing that can both have the same effect. Secondly, it is difficult to constrain the relative timing of levee build-up and channel cutting and filling. Finally, there are no direct measurements from natural systems available of the grain-size sorting within the turbidity current structure. The present dataset provides constraints on the flow properties and deposit properties as well as on the morphological evolution of the channel. The dataset can thus be used to test the effect of grain-size sorting combined with channel deepening on levee deposit grain-size.

The levee deposits generated in the experiments are fining upward and the upward fining sequence is deposited by a series of turbidity currents that are equal in discharge and sediment composition. Thus, upstream forcing does not play a role and the grain-size trend of the deposits is purely the result of evolving channel morphology and associated overspill from progressively higher and more fine-grained divisions of the turbidity current.

Comparison between flow and deposit grain-size trend

Pirmez and Imran (2003) describe a method to invert grain-size sorting in turbidity currents from upward fining in levee sequences. Therein, it is assumed that the levee deposits are representative of the grain size in the current at the level that corresponds to the channel depth at time of deposition. The present experiments allow to evaluate this approach. The method holds up well for the present experiments because the decrease of levee grain size with channel depth has a gradient

that is similar to the decrease in grain-size with height in the turbidity current (Fig. 3.13). The gradient is somewhat smaller in the 2D experiment and this may be a result of the stronger vertical mixing due to its higher velocity (Fig. 3.6). Although the deposit and flow profile have a similar gradient there is a difference in absolute grain size as is shown by the flow samples from the 2D experiment which are consistently coarser than the deposit samples from the 3D experiment. Presumably, this is caused by: 1) the difference in grain-size distribution of the sediment used in both experiments, 2) deposition of coarser sediment upslope of the measuring location in the 3D experiments.

Superimposed on the fining-upward trend in the deposits there are also shorter cycles of more rapid fining within the basal section of individual event beds. This is particularly apparent from the relatively coarse deposit samples that coincide with the base of event beds from Runs 2 and 3. The fining cycles within individual flows are not likely to be related to waning flow because the discharge of the turbidity current remained constant throughout the runs. Therefore, it is proposed that the coarse sediment at the base of event beds is deposited by the heads of turbidity currents. The head of a turbidity current typically has strong turbulent mixing and therefore transports coarse sediment relatively high in the flow. Baas et al. (2005) have previously shown this experimentally. Therefore, the overspilling current from the head of the flow will contain coarser sediment. Fining upward beds, consisting of sand/mud couplets, have been observed widely in levees and channel terraces (e.g. Kane et al., 2007; Hubbard et al., 2014; Hansen et al., 2015). However, the difference in the mixing structure of turbidity current heads and bodies has not previously been considered a factor that could influence the grain-size of overspilling currents.

The deposits from each of the three turbidity currents display a lateral coarsening trend from the levee crest away from the channel (Fig. 3.12A; compare Sections 3 and 4). Such a trend is surprising and is not commonly observed in natural systems. Dykstra et al. (2012) for example, record a gradual decrease in grain size from proximal to distal levee in outcrop.

Depth-evolution of the channel

Levee building and channel incision are the two fundamental processes that govern the depth evolution of a channel but the relative timing and magnitude of these processes may differ between channels. Channels may start as purely aggradational and develop an erosive component later (Hodgson et al., 2016), or they may start with erosion and develop levees after that (Fildani et al., 2013). In natural systems it is rarely possible to constrain the movement of the channel floor contemporaneous with the aggradation of the levee (Kane et al., 2007). Thus in order to reconstruct the grain-size sorting in turbidity currents workers have previously assumed that the depth of the channel was equal to the height of the levee at each point in time (cf. Pirmez and Imran, 2003; Dennielou et al., 2006). The present experiments illustrate that this can lead to major over- and underestimations of the channel relief. In the channel segment on the lower slope where the sediment samples were collected the channel floor was initially aggrading and then degrading (Fig. 3.8C). The growth of channel relief did therefore increase during each subsequent run. The graph which shows deposit grain-size as a function of channel depth (Fig. 3.13A) would have looked significantly different if the vertical change of the channel floor would not have been taken into account. Specifically, the concavity of the curve would have been much lower. Concluding, the grain-size sorting in the turbidity currents cannot be accurately reconstructed when the height in the levee sequence is simply related to the basis of the channel.

Grain-size segregation in natural turbidity currents

The present experiments confirm that grain-size stratification in the flow is an important control on the vertical grain-size changes in the levee sequence. Thus, it is important to improve our understanding of vertical grain-size sorting in natural turbidity currents to provide constraints on the variability in grain-size of overspilling currents. Most information about concentration and grain-size distribution in turbidity currents comes from laboratory experiments (Garcia, 1994; Niño et al., 2003) and numerical models (Stacey and Bowen, 1988). Similar to our experiments, these authors show a gradual decrease of concentration and grain-size with height above the bed. Sediment properties of turbidity currents in the field have only been measured by Xu et al. (2014) using sediment traps. They found that sand was suspended in turbidity currents in the Monterey Canyon to a height of at least 70 metres above the canyon floor. The paucity of field measurements is a result of technical challenges. Due to the destructive nature of turbidity currents, measuring the sediment in the flow has proven to be even more challenging than measuring the velocity. This gap in our current knowledge highlights the importance of future sea-floor monitoring studies (Talling et al. 2015). However, even with improved sea-floor monitoring techniques, it is unlikely that the build-up of a complete levee sequence and the associated flow structures can be monitored because of the long time scales involved. Conclusive evidence that fining-upward levees can form purely as a result of increasing channel depth must therefore come from experiments such as the present ones.

3.4.3 Is deposition on the levees driven by competence or near-bed capacity?

The turbidity currents in the channel are primarily bypassing and eroding sediment along the channel axis while they are depositing sediment on the levees at the same time. The transition from bypass in the channel to deposition on the channel margins can either be caused by limited flow capacity or limited flow competence (Hiscott, 1994), where capacity-driven deposition is related to the amount of sediment in suspension independent of the grain-size, while competence-driven deposition is grain-size driven as the coarser grains settle due to a reduction in the flow competence. It is important to distinguish these two depositional mechanisms as in outcrop they are linked to different facies, which could form another opportunity to link deposits and flow structure. Capacity-driven deposits tend to be more poorly sorted because suspended sediment of all grain-sizes available in the flow is deposited (Hiscott, 1994). The present dataset provides constraints on the depositional behaviour, flow velocity, flow concentration and flow composition and can therefore be used to assess which mechanism was controlling the balance between bypass and deposition in a channelised setting.

Capacity-driven deposition

Firstly, the possibility that limited flow capacity is driving deposition is explored. Deposit and flow data from the early stage of Run 3 (interval 5–20s) are used for this analysis. The capacity to transport sediment in suspension decreases with decreasing u^* for two reasons. Firstly, the concentration profile becomes more concave and this implies that less suspended sediment can be supported in the water column (Hiscott, 1994). This aspect of capacity will here be called suspension capacity. Secondly, the maximum near-bed concentration goes down with decreasing u^* (Smith and Mclean, 1977; van Rijn, 1984; Cantero et al., 2011; Eggenhuisen et al., 2017). This aspect of capacity will here be called near-bed capacity. The focus is here on the near-bed capacity because it has the most direct implications for deposition from suspension. The near-bed capacity is determined at the location of each velocity probe inside of the confinement (i.e. Probe 1 to

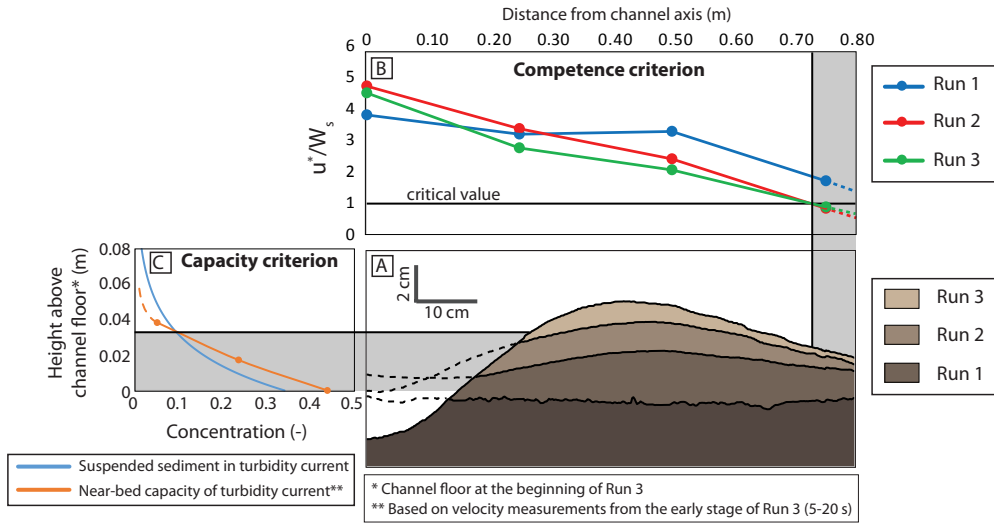


Figure 3.15: (A) Channel cross-section on the lower slope. (B) Ratio between shear velocity and settling velocity as a function of distance from the channel axis. This is a competence criterion. (C) Sediment-concentration profile and near-bed capacity as a function of height above the channel floor. The ratio between the near-bed capacity and the actual concentration is a capacity criterion.

3) and is compared to the suspended sediment concentration (Fig. 3.13B) at the corresponding height in the flow (Fig. 3.15C). The near-bed capacity criterion of Eggenhuisen et al. (2017) is used to determine the near-bed concentration at which the flow is saturated:

$$C_{sat} = \frac{u^*{}^3 \rho_f}{140\nu g(\rho_s - \rho_f)} \quad (3.1)$$

with ρ_f being the density of water, ρ_s the density of the suspended sediment, the kinematic viscosity of water, u^* the shear velocity, and C_{sat} the maximum near bed concentration. Shear velocities are here estimated using (Kneller, 2003):

$$u^* = \sqrt{g \frac{\Delta\rho}{\rho} h S} \quad (3.2)$$

where $\Delta\rho$ is the density difference between the suspension and the ambient fluid of density ρ . $\Delta\rho$ is calculated for the depth-interval from the bed to the velocity maximum (see supplementary information for details). h is the height of the flow from the bed to the velocity maximum and S is the tangent of the slope. Capacity-driven deposition will occur when the near-bed concentration (C_b) exceeds the saturation concentration at the bed (C_{sat}).

The basal flow concentration is determined using the assumption that the flow concentration at each height is uniform across the width of the channel (Fig. 3.14). Thus, the basal concentration on the channel walls is a function of the elevation above the channel floor.

In the channel thalweg the suspension capacity exceeds the actual concentration and the flow is thus undersaturated (Fig. 3.15). Thus, no deposition driven by capacity is expected at this locality and the elevation models (Fig. 3.4) show that the bed does indeed not aggrade at this locality during Run 3. The calculated suspension capacity on the channel wall and on the levee crest is lower than the measured sediment concentrations at those heights in the flow (Fig. 3.15C).

This implies that the near-bed flow on the channel wall and on the levee is oversaturated with suspended sediment and should be aggrading as a result of capacity-driven deposition, which is confirmed by the elevation models.

Competence-driven deposition

Limited flow competence is a potential additional driver for deposition. It is assumed here that a flow has sufficient competence to keep sediment in suspension when:

$$u^*/W_s > 1 \quad (3.3)$$

where u^* is the shear velocity and W_s is the settling velocity of the median grain-size (Bagnold, 1966). The critical ratio of 1 does not indicate a sharp transition from bypass to competence-driven deposition because the onset of suspension is a qualitative phenomenon that cannot be captured by a discrete threshold value of any physical parameter (van Rijn, 1984; Niño et al., 2003). Nevertheless, it has proven to be a useful estimator of suspension competence. The settling velocity (W_s) used here is the settling velocity of the median grain-size of the flow at the inlet. The settling velocity is calculated from the grain size using the relation of Ferguson and Church (2004). The shear velocity is here estimated using (Middleton and Southard, 1984):

$$u^* = U_{max} \kappa \left[\ln \left(\frac{h_{max}}{0.1 D_{90}} \right) \right] \quad (3.4)$$

where h_{max} is the height of the velocity maximum, U_{max} is the maximum velocity and κ is the von Kármán constant. The method used to estimate the shear velocity differs from the method used in the flow competence analysis. The method used in the competency analysis requires information about the suspended sediment concentration. However, the sediment concentration outside of the confinement is poorly constrained. Therefore, an alternative method is used here that only requires information about the shape of the velocity profile. This allows to estimate the u^*/W_s ratios inside as well as outside of the confinement. Further details on the shear velocity estimates are provided in the supplementary information.

u^*/W_s ratios are determined for each velocity-profiling location (locations shown in Figure 3.2) and for each run (Run 1 to 3). In the centre of the channel u^*/W_s was generally ranging from 4-5 throughout all runs (Fig. 3.15B). The u^*/W_s ratio systematically decreases away from the channel axis mainly due to the outward decrease in flow velocity (Fig. 3.15). The u^*/W_s ratio drops below 1 at a distance of 70-80 cm away from the channel axis, but still ranges between 2-3.5 on the proximal levee and levee crest. This implies that there was potential for competence-driven deposition on the distal levee while it was less likely that lack of suspension competence was driving deposition on the proximal levee and levee crest. There is an increase through time in the u^*/W_s ratio inside the channel and a decrease in u^*/W_s ratio outside of the channel as the flow becomes increasingly more confined by the evolving channel relief throughout Runs 1-3 (Fig. 3.11B). It is here tentatively suggested that the transition from capacity to competence-driven deposition could explain the lateral coarsening trend observed in the experimental deposits. Competence-driven deposition selectively deposits the coarser grains whereas deposition driven by capacity drops all the grains that are suspended near the bed. The deposits from the same turbidity current will therefore be more coarse-grained and better sorted when deposition is driven by competence..

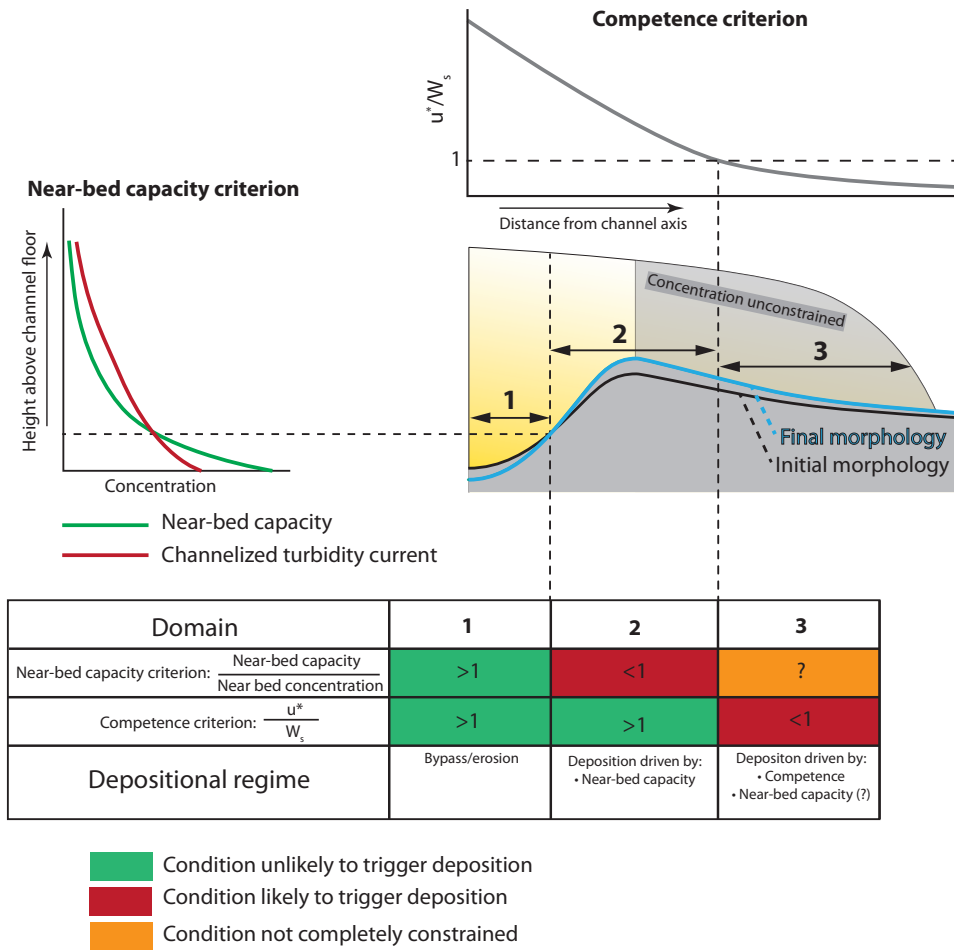


Figure 3.16: Cartoon illustrating the depositional regimes in the channel-levee system. The depositional regime is controlled by two factors: the near-bed capacity and the flow competence

3.4.4 Predicting the morphological evolution of the channel from the density structure of the flow

Different depositional regimes do thus occur laterally in the experimental channel-levee system (Fig. 3.16). The channel axis (Domain 1) is a zone of bypass because the flow is neither at capacity or at its competence limit. The channel margins and proximal levees (Domain 2) are characterized by sufficient flow competence to keep the sediment in suspension but a basal concentration that exceeds near-bed capacity. The deposition in this region is thus likely to be driven by near-bed capacity. Finally, on the distal levee (Domain 3), the deposition is competence-driven because the competence limit is exceeded. In addition, the near-bed capacity may be exceeded here. However, it is not possible to constrain this because there are no flow concentration measurements available in this region.

A fundamental control on the morphological evolution of submarine channels is the position of the lateral transition from sediment bypass around the channel axis (Domain 1) to sediment

deposition on the levees (Domain 2). In the experiments this transition appears to be controlled by the onset of capacity-driven deposition on the margins. Whether capacity-driven deposition does also occur on the proximal part of natural levees is not clear. Much of the deposition on natural levees is likely to be competence-driven because massive poorly sorted sand that is typical for capacity-driven suspension sedimentation (Hiscott, 1994) is sparse in levee deposits (Kane et al., 2010a). However, the inner levees of incipient channels are probably poorly preserved in many cases because they are reworked by subsequent flows as the channel evolves further.

The transition from bypass conditions to competence-driven deposition on the margin is marked by the crossing of the concentration profile with the near-bed capacity profile (Figs 15C, 16). Deposition on the channel margin starts at the height above the channel thalweg that corresponds to this crossing. It is thus shown how the concept of suspension capacity can be used to predict morphological evolution in the context of a channel where the bed intersects with different divisions of a current that is strongly density stratified. This provides a useful framework that can be used to predict the morphological evolution of a channel from the flow structure of a turbidity current. Previously, Straub & Mohrig (2008) presented a model for levee growth controlled by the density structure of channelised turbidity currents. Such a model for levee growth can in the future be combined with the present model, which also describes processes inside the channel. This can result in a comprehensive model for forward and inverse modelling of the stratigraphic record of submarine channel evolution.

3.5 Conclusions

- Grain-size stratification in turbidity currents combined with increasing channel relief results in fining-upward levee deposits. The grain-size trend in the levee is in good agreement with the grain-size trend in the flow. This provides verification of previous conceptual models. The channel relief evolution is not a simple function of levee growth. Contemporaneous deposition or erosion on the channel floor also have a significant influence on the evolution of channel relief.
- Channel-relief evolution is not a simple function of levee growth. Contemporaneous deposition or erosion on the channel floor also have a significant influence on the evolution of channel relief.
- Vigorous mixing in the head of turbidity currents reduces grain-size stratification in turbidity currents. This leads to relatively coarse-grained overspill during the early stage of each flow.
- The depositional and erosional behaviour of turbidity currents in the experimental channel-levee system can be predicted using competence and capacity criteria. The transition from bypass in the channel thalweg to deposition on the channel margin is a result controlled by flow capacity rather than flow competence.
- The concepts of competence and capacity can thus be used to predict the morphological evolution and resulting stratigraphic architecture of submarine channels.

Chapter 4

Sediment volume and grain-size partitioning between submarine channel-levee systems and lobes: An experimental study

ABSTRACT

The downstream extraction of mass from sediment transport systems has been recognised as an important control on the stratigraphic architecture in alluvial systems. A similar importance can be expected in clastic deep-water systems. Unique in deep-water systems is the continuous overspill from submarine channels. These channels are the main pathways for turbidity currents travelling towards the basin floor and their dimensions are inferred to act as an important control on the amount of overspill. However, the partitioning of sediment by individual turbidity currents as a function of channel dimensions has not been investigated previously.

We present a series of physical experiments studying the link between channel dimensions and the resulting partitioning of sediment volume and grain size between sub-environments. The experimental set-up consists of a slope (11°) with a straight pre-formed channel and a horizontal basin floor. An identical flow was released repeatedly into channels with different dimensions, resulting in various styles of overspill, erosion and deposition under varying degrees of channel confinement.

Our results show how channel dimensions control the partitioning of sediment volume and grain sizes. Generally, low aspect-ratio channels are more efficient and can transport up to 89% of the volume to the basin floor, whereas high aspect-ratio channels are less efficient and funnel about 67% of the sediment volume to the basin floor. The efficiency of the channel also affected the grain-size distribution of the sediment that was extracted from the flow. With increasing channel efficiency, the volume of levees relative to channel fills increases and the grain size of the sediment retained on the slope decreases.

This study demonstrates the value of the analysis of deep-water systems in a mass-balance framework as it provides significant insights in the interplay between the downstream evolution of turbidity currents due to mass extraction and the morphological evolution of submarine channels. This is important because it can contribute to the prediction of facies and volumes of deep-water architectural elements and the unravelling of internal and external controls from the stratigraphic record.

Based on

Sediment volume and grain-size partitioning between submarine channel-levee systems and lobes: An experimental study. By: Jan de Leeuw, Joris T. Eggenhuisen, Yvonne T. Spychala, Maarten Heijnen, Florian Pohl, Matthieu J.B. Cartigny, *in preparation*.

4.1 Introduction

Turbidity currents transport large volumes of sediment from the shelf edge into oceanic basins. Their runout distance can be 10s to 1000s of kilometres (Heezen and Ewing, 1952; Damuth and Kumar, 1975; Talling et al., 2012; Stevenson et al., 2013; Dorrell et al., 2014; Kneller et al., 2016). Much of this distance is usually covered while the currents are contained in submarine leveed channels. These currents can transfer sediment over large distances without exchanging any sediment by deposition or erosion (Stevenson et al., 2013). Typically, however, as the flow travels down its tract, two first-order parameters are changing: Volume and composition of sediment transported in suspension.

Turbidity currents in leveed submarine channels can exchange sediment with their surroundings in various ways. Firstly, overspilling flows preferentially deposit fine-grained sediment on the levees (Hiscott et al., 1997; Kane et al., 2007; Hansen et al., 2015). Secondly, deposition in the channel axis occurs when channels are aggradational and this results in the extraction of the coarser grained sediment fraction from the flow (Normark, 1978; Clark and Pickering, 1996). Relative volumes of sediment partitioned into the levees and channel fill were estimated by Straub et al. (2012) for a channel system on the continental slope offshore Brunei (Fig. 4.1A,B). It appears that levees form the largest sediment volume (89%) of the channel-levee system stratigraphy on this particular submarine slope.

The remaining sediment in turbidity currents that reaches the downstream end of a channel is deposited as lobes. The transition from channels to lobes occurs at different degrees of mass extraction. In many basins, lobes only form a minor portion of the total submarine fan volume (Paola and Martin, 2012; Picot et al., 2016). Paola & Martin (2012) showed that, in an intraslope basin in the Gulf of Mexico, the channel-lobe transition occurred at 60-80% mass extraction (Fig. 4.1C). The highest proportion of sand in this small system is found around the channel-lobe transition (Fig. 4.1D). Similarly, the highest sand content in many other deep-water systems does also occur around the base-of-slope (Prather et al., 2016). Grain-size partitioning in deep-water systems does therefore differ fundamentally from fluvial systems where deposition selectively extracts the coarse sediment fraction (Strong et al., 2005). At present, it is not entirely clear what is causing the contrasting styles of sediment grain-size partitioning in deep-water systems and in fluvial systems.

One unique feature of submarine channels is the continuous overflow of the dilute and fine-grained, supra-channel portion of the flow (Posamentier and Kolla, 2003). The volume and grain size of mass extracted, primarily depend on channel depth relative to flow height (Mohrig & Buttles, 2007). Typically, after channel inception, confinement increases progressively due to levee build-up and/or channel incision and this increases their efficiency (i.e. their ability to transport sediment basinwards (Hodgson et al., 2016). The increased efficiency may cause the channel to extend or to deliver more sediment to terminal lobes.

To sum up, the relation between turbidity current flow characteristics (thickness, stratification) and channel dimensions is widely recognised as the key control on sediment partitioning in deep water systems, yet no study has systematically and quantitatively explored the parameter set.

The analysis of sediment routing systems in a mass-balance framework has proven to be a viable method to unravel the forcing mechanisms that control stratigraphic facies and architecture. Such an approach has already been applied to alluvial-coastal systems such as the Cretaceous infill of the Western Interior Basin (Hampson et al., 2014), the Eocene infill of the

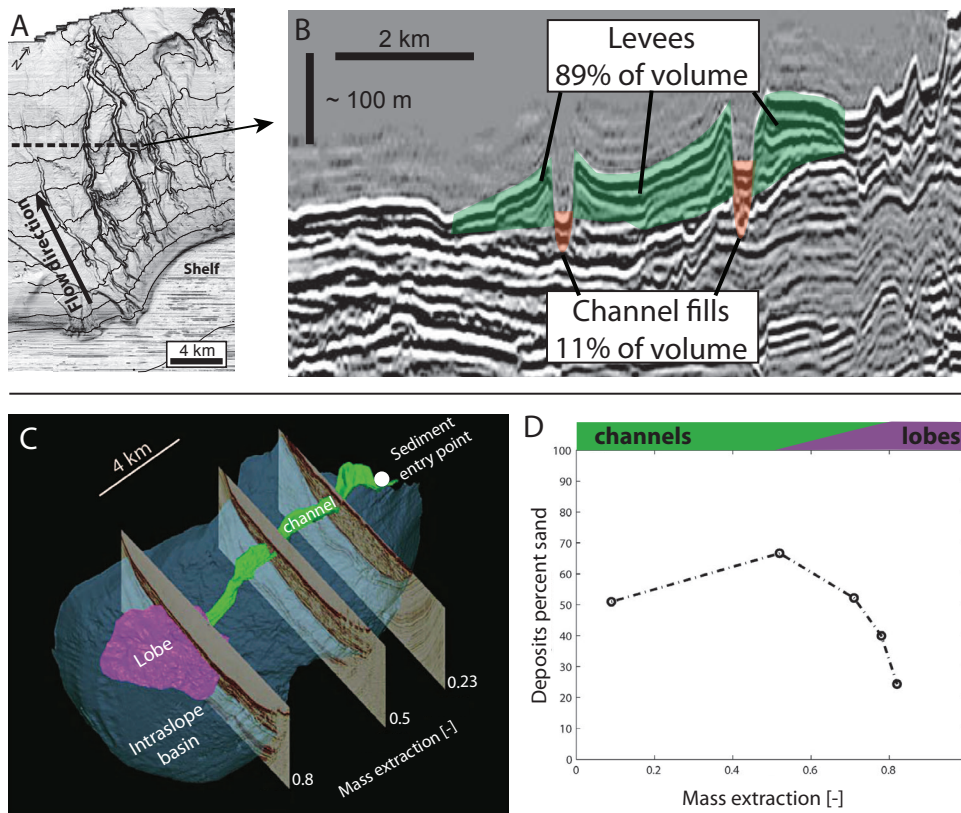


Figure 4.1: Volume estimates of depositional elements in deep-water systems. (A,B) Partitioning of sediment volumes between channel fills, levees and levees for a channel network on the continental slope offshore Brunei Darussalam (NW Borneo). Levees constitute a much greater volume than channel fills in this system. Figure modified after Straub et al. (2012). (C) Partitioning of sediment volumes between channel-related deposits and lobe deposits in an intraslope mini basin that is part of the Brazos-Trinity system in the Gulf of Mexico. Figure modified after Paola & Martin (2012). (D) Partitioning of sediment grain sizes in the same mini basin. Sand content of the deposits increases downstream in the channelised section of the basin. Sand content of the deposits decreases downstream in the section of the basin where lobes dominate.

South Pyrenees Foreland Basin (Michael et al., 2014) and also to experimental fluvial systems (Strong et al., 2005).

We apply a mass-balance approach to an experimental deep-water system consisting of a slope channel segment and a horizontal basin floor. Physical experiments have the advantage that the sediment input is precisely constrained and it is possible to track the distribution of deposits from individual currents. The aims of this study are to: (1) investigate the partitioning of sediment volumes and grain sizes between levees, channel fills and lobes as a function of channel width and depth (together termed channel dimensions throughout this paper) in a controlled laboratory setting; (2) reconstruct the flow evolution from the documented deposits; (3) review

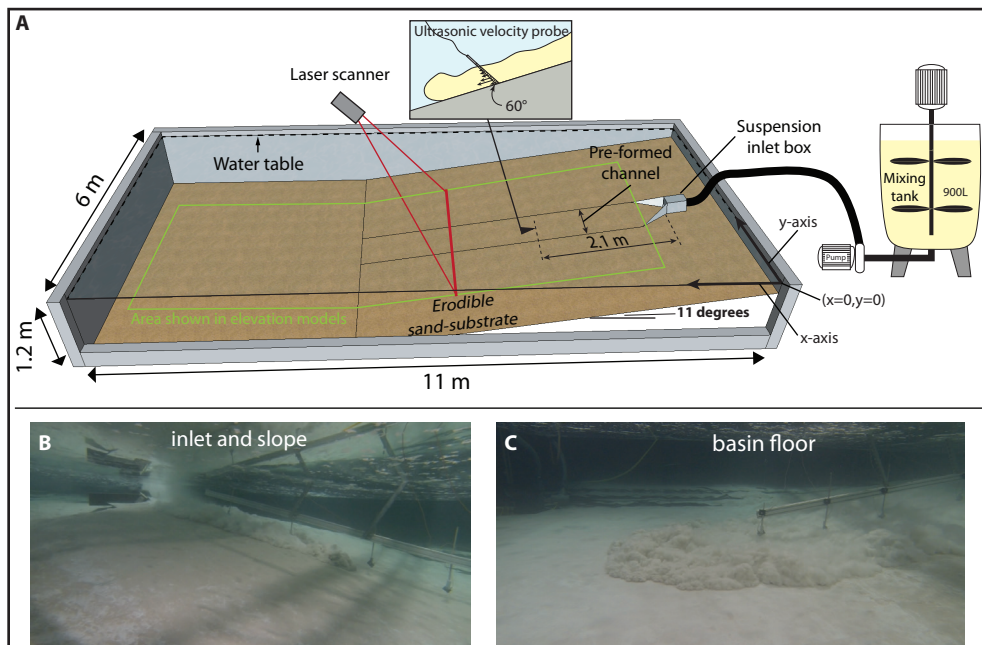


Figure 4.2: (A) Set-up for flume experiments. A mixture of sediment and water is sourced from an external mixing tank. In the basin, the turbidity current flows over a slope with a pre-formed channel. The substrate is erodible. Current velocity is monitored with an ultrasonic velocity probe in the centre of the channel at 2.1 m from the inlet. (B,C) Images taken by underwater cameras taken from different viewpoints.

published estimates of volume and grain-size partitioning in deep-water systems; and to (4) discuss the applications of our results towards stratigraphic prediction and interpretation.

4.2 Methods

4.2.1 Set-up, procedure and measurements

The experiments were performed in a 11 m long, 6 m wide and 1.2 m deep tank (Fig. 4.2A). The basin contained a slope of 11° with a horizontal section at its base. Boundary conditions that were kept constant for all experiments are summarized in Table 4.1. Both the slope and the basin floor were covered with a layer of erodible sand. A channel was carved in the slope before each experiment. Depth and width of the pre-formed channels were varied between the experiments (Table 4.2). These dimensions were chosen based on the dimensions of a self-formed channel created in earlier experiments with similar boundary conditions (de Leeuw et al., 2016/Chapter 2 of this thesis). The same procedure was followed during each of the experiments. First, the basin was entirely filled with water. The suspension for the turbidity current was prepared in an external mixing tank. Underwater cameras recorded the turbidity current on the slope and the basin floor (Fig. 4.2B, C). The sediment used consisted predominantly of fine sand with a fraction of silt ($D_{10} = 25 \mu\text{m}$, $D_{50} = 131 \mu\text{m}$, $D_{90} = 223 \mu\text{m}$; Fig. 4.3). The substrate in the tank is made of sand with the same grain-size distribution. Any entrainment of substrate did therefore add the same






| Run | Width [m] | Depth [m] | (3x vertical exaggeration) |
|-----|-----------|-----------|--|
| 1 | 0.8 | 0.08 |  |
| 2 | 1.2 | 0.03 |  |
| 3 | 0.53 | 0.05 |  |
| 4 | 0.8 | 0.05 |  |
| 5 | 0.8 | 0.03 |  |

Table 4.2: *Dimensions of the pre-formed channel for the experiments*

| Boundary conditions during the experiments | |
|---|-----|
| Suspension tank volume [L] | 900 |
| Initial sediment concentration [% vol.] | 17 |
| Discharge [L/s] | 8.3 |
| Slope angle [°] | 11 |
| Basin floor angle [°] | 0 |

Table 4.1: *Boundary conditions that were identical for all of the experiments*

material to the flow as supplied at the inlet. The suspension from the mixing tank was supplied to the set-up with a centrifugal pump. A Krohne Optiflux 2300 was used to monitor the discharge during the experiments. The turbidity current entered the set-up through an inlet box. This box consisted of a 1 m section with a non-erodible substrate and gradually expanding side walls. An ultrasonic velocity probe (UVP) was used to measure the flow velocity profile in the centre of the channel during each run. Digital elevation models of the sediment surface were made before and after each run. The difference between these elevation models indicates where the flow deposited and eroded sediment. Sediment samples were collected close to the sediment surface. The ~1 mm-thick silt drape that covered the deposits after each experiment was scraped away before the sample was collected. A laser particle sizer (Malvern Mastersizer) was used to determine the grain-size distribution of each sediment sample.

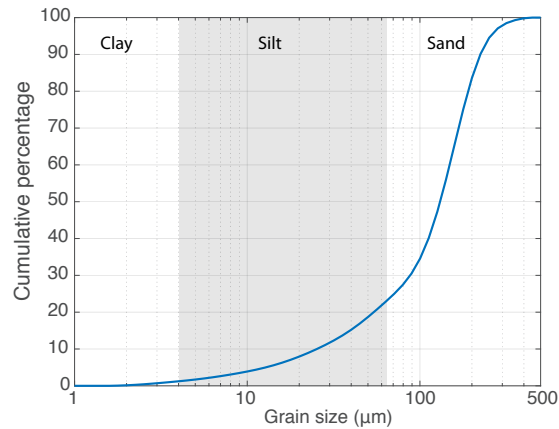


Figure 4.3: *Grain-size distribution of the sediment used in the experiments.*

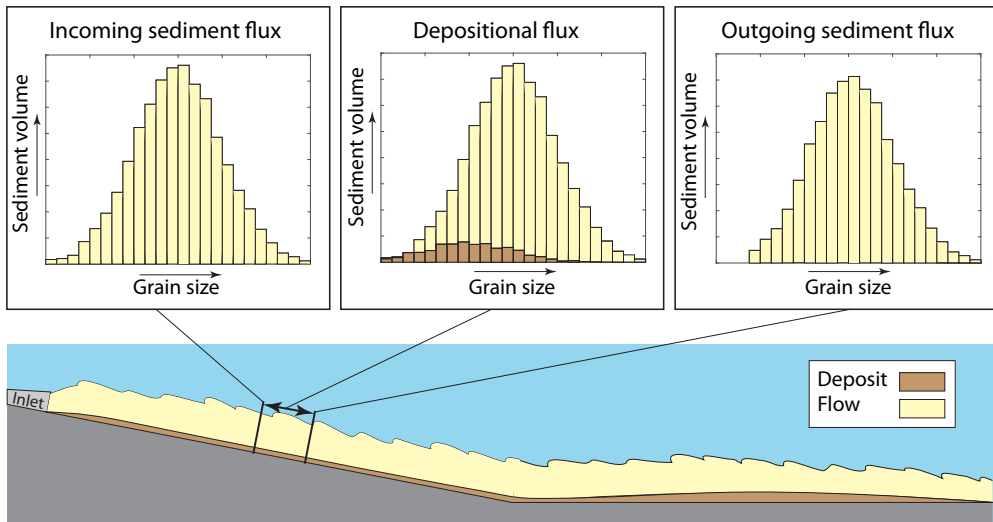
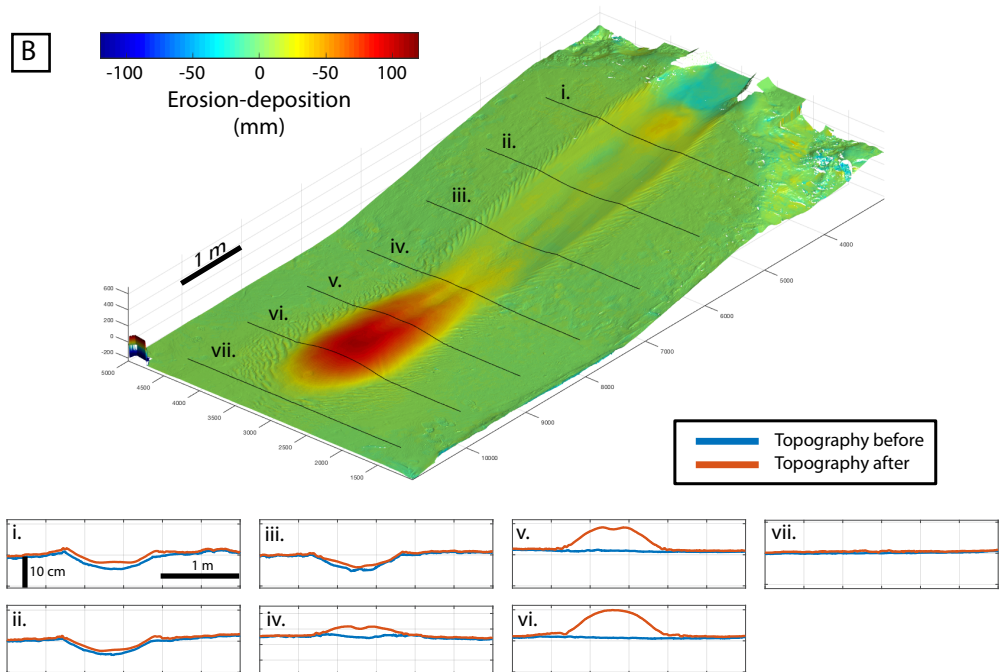
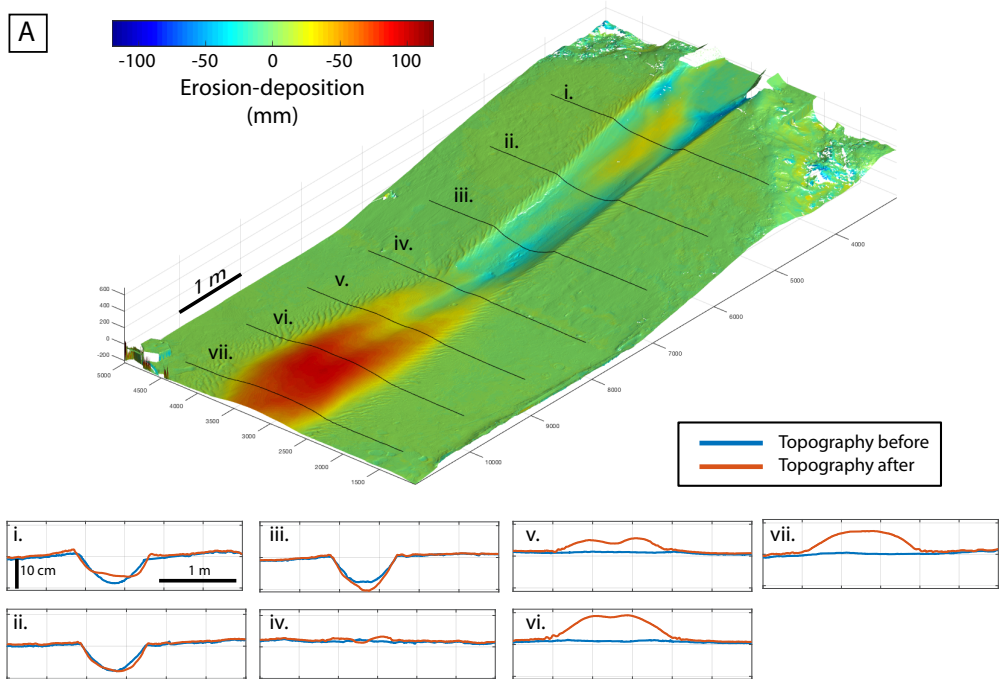
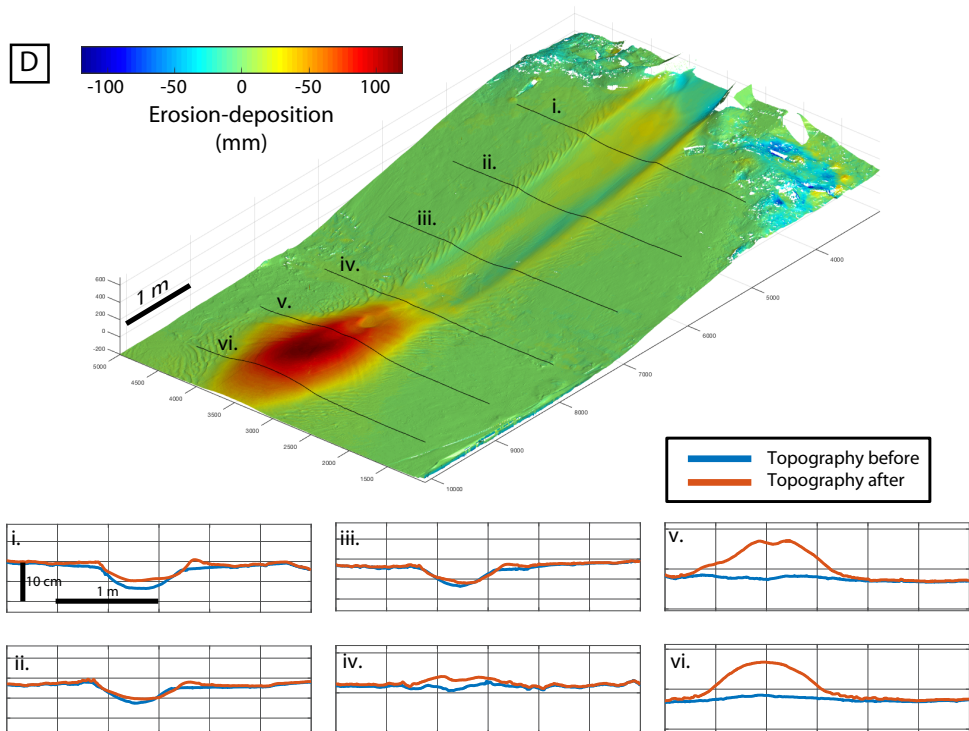
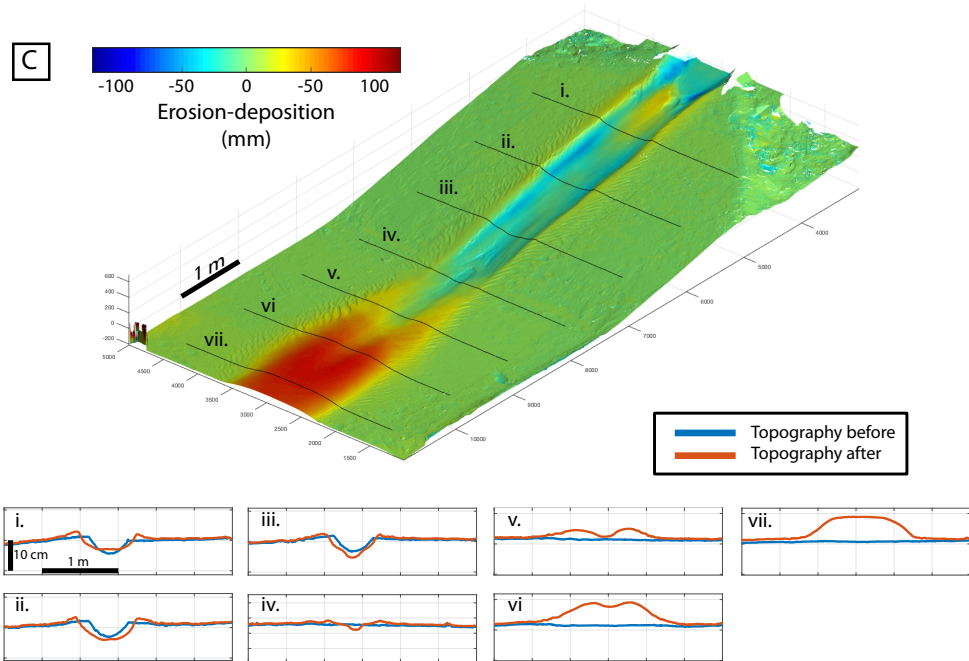


Figure 4.4: *Sketch illustrating the reconstruction of downstream mass extraction. The sediment deposited in each section of slope slope is subtracted from the initial sediment volume in the turbidity current. Deposition typically results in the selective extraction of a certain grain-size fraction. The suspended sediment volume and grain-size distribution thus change downstream.*

4.2.2 Mass-balance analysis

Deposit volume and grain size were used to reconstruct the downstream change in transported sediment volume and grain size by turbidity currents as they ran out on the slope and basin floor. The initial state of the turbidity current is defined by the suspension in the mixing tank. Volume and grain-size distribution of the suspended sediment at each point in the system was reconstructed by subtracting the sediment that was deposited upstream of that point (Fig. 4.4). The deposit volumes are derived from the difference between the elevation models before and after the experiments. It is assumed that the grain-size distribution of each volume of deposit is





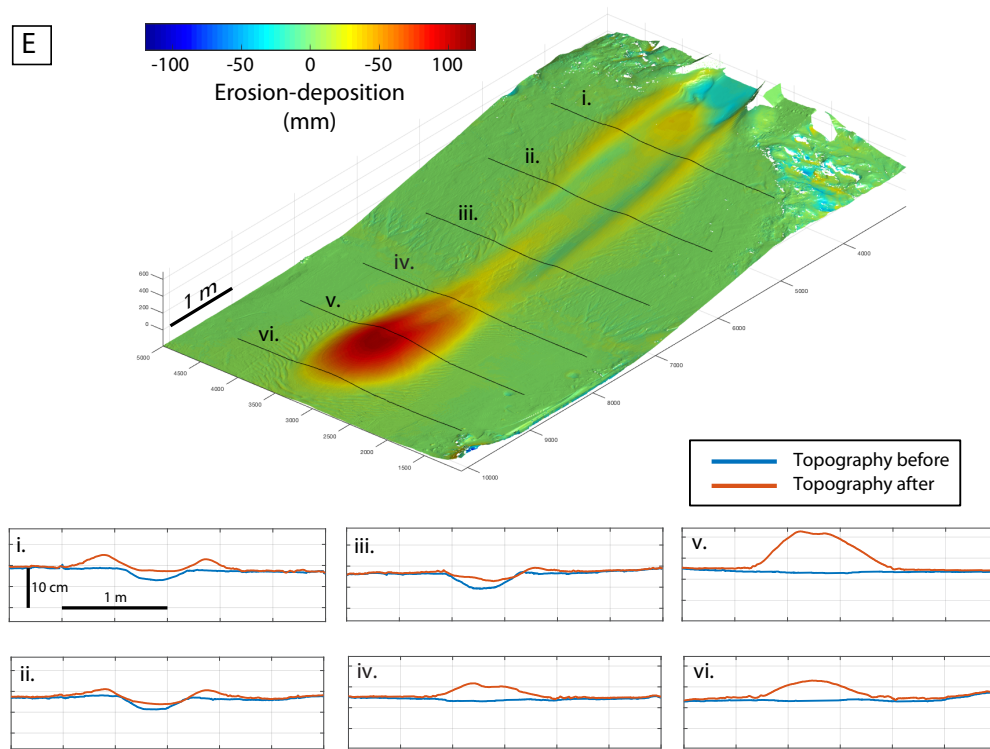


Figure 4.5: Maps of deposition and erosion with cross-sections of the channel and lobe at a 1-metre interval. (A) Results from Run 1 in which the initial channel depth was 8 cm and the channel width 80 cm. (B) Run 2 (Depth: 5 cm, Width: 120 cm) (C) Run 3 (Depth: 5 cm, Width: 53 cm) (D) Run 4 (Depth: 5 cm, Width: 80 cm) (E) (Depth: 3 cm, Width: 80 cm)

equal to the grain-size distribution of the nearest sediment sample. The bin width of the grain-size classes is 0.16ϕ . The phi-scale is a logarithmic sediment grain-size scale that was introduced by Krumbein and Aberdeen (1937).

4.3 Results

4.3.1 Deposit volume distribution

Five experiments were conducted during which the duration of the turbidity current, sediment grain-size distribution and discharge were the same. During each experiment the turbidity current deposited part of its sediment load on the slope section, while the remainder of its sediment formed a lobe on the horizontal basin floor. Figure 4.5 shows maps of deposition and erosion of the five experiments. During Runs 2, 4 and 5 (Fig. 4.5B, D, E) deposition on the slope was both inside the channel, as channel fill, and outside of the channel, by the formation of levees. During Runs 1 and 3 (Fig. 4.5A, C) the turbidity current deposited sediment outside the channel, whereas inside of the channel there was a mix of erosion and deposition.

Initial channel dimensions had a significant effect on the partitioning of sediment volumes between the slope and the basin floor. The fraction of sediment deposited on the slope was

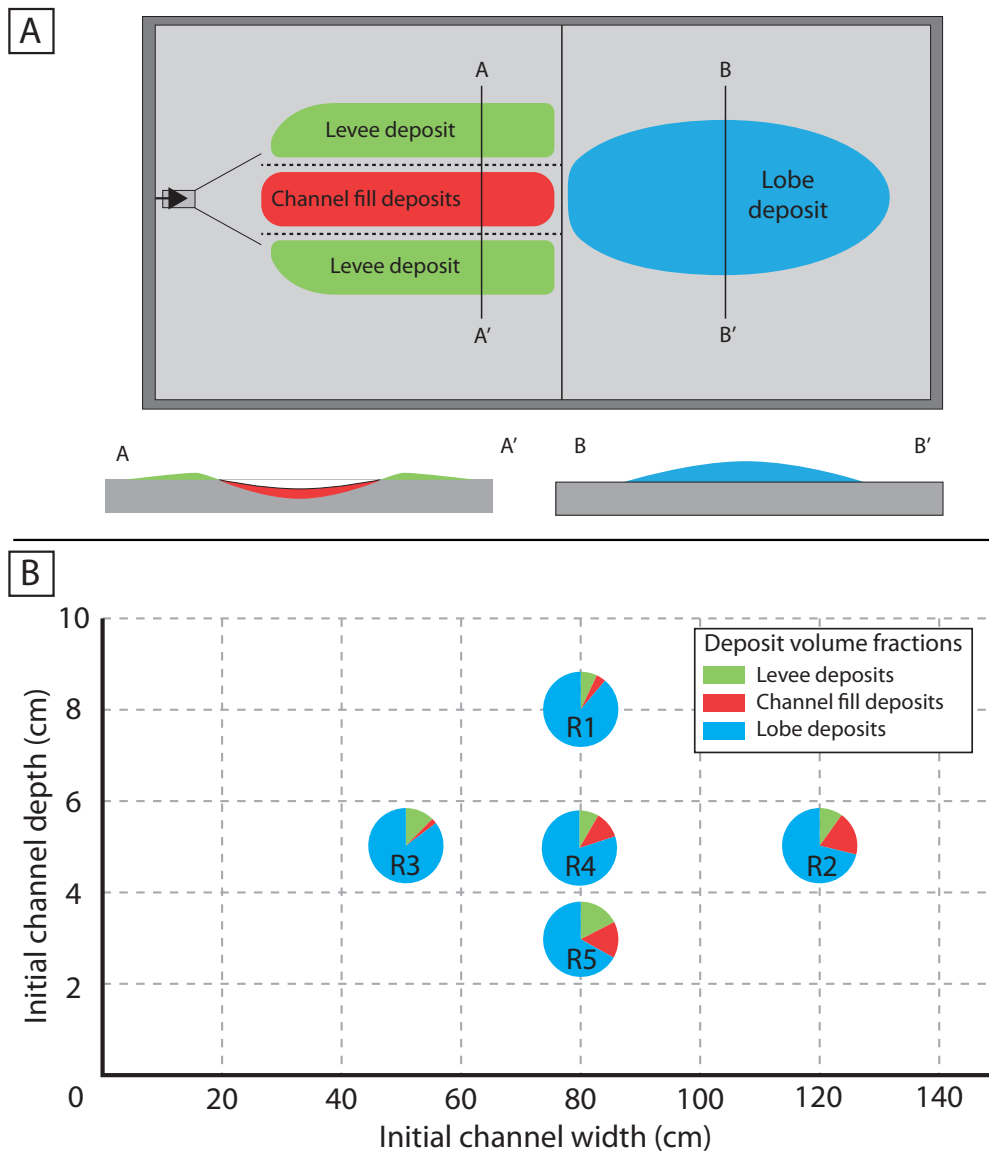


Figure 4.6: (A) Sediment bodies distinguished in the experiments. (B) Partitioning of sediment volumes between channel, levees and lobes in experiments with different initial channel dimensions.

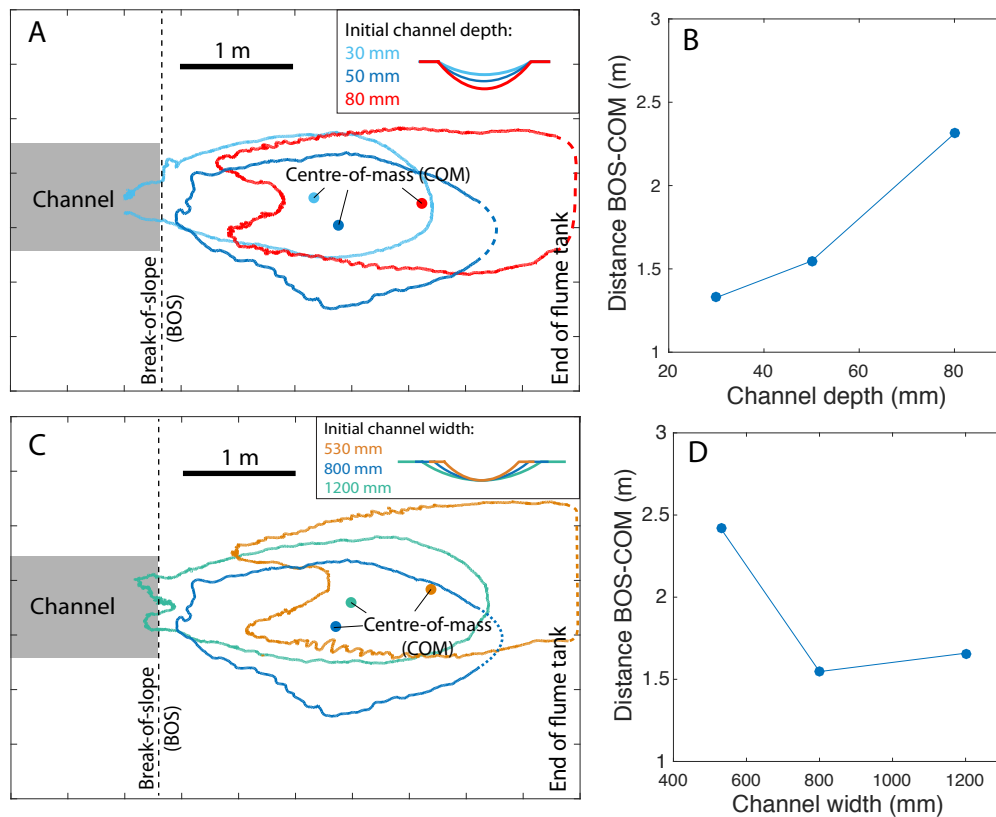


Figure 4.7: Effect of channel dimensions on the geometry of the lobe formed on the basin floor. The 25 mm thickness contour of each lobe is shown. (A) Lobe geometry as a function of channel depth. A shallow channel results in a broad lobe that overlaps onto the slope. Deeper channels result in slope-detached sedimentation of more elongate lobes. (B) The centre-of-mass of the lobe is located farther into the basin when the channel is deeper. (C) Lobe geometry as a function of channel width. Wider channels result in wider lobes with depocentres close to the break of slope (BOS). Narrow channels result in slope-detached sedimentation and more elongate lobe deposits with depocentres farther into the basin. (D) The centre-of-mass of the lobes shifts basinwards with increasing channel depth.

smallest when the channel had a small width and/or a large depth. For example, in Run 5 (channel width: 0.8m, depth: 0.03m), the percentage of sediment that reached the basin floor was 67% (Fig. 4.6). Run 1 with a deeper channel (width: 0.8m, depth: 0.08m) delivered 89% of the sediment to the basin-floor lobe (Fig. 4.6). The channel in Run 1 can thus be classified as *efficient* because it delivers the largest fraction of sediment to the basin floor.

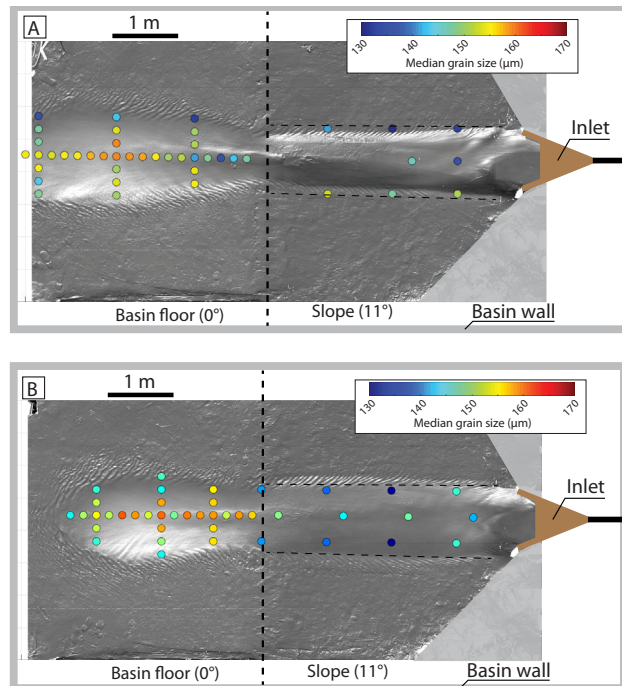
Also, the partitioning of sediment volume on the slope between the channel fill and the levees differed between the experiments. The runs with the smallest channel width (Run 3, channel width 0.53m, depth: 0.08m) experienced the least deposition in the channel relative to levee deposition ($V_{\text{levee}}:V_{\text{channel}} = 85:15$). The run with the largest channel width (Run 2, channel width 1.2m, depth: 0.03m) experienced the most deposition in the channel relative to deposition on the levee ($V_{\text{levee}}:V_{\text{channel}} = 34:66$).

The dimensions of the channel also affected the geometry of the lobe that formed on the basin floor. Figure 4.7 shows the 25 mm thickness contours of the lobe formed in each of the experiments. Lobes that are sourced by a channel with a larger depth (Fig. 4.7A) or a smaller width (Fig. 4.7C) are more elongated and reach farther into the basin. Lobes that are sourced by more efficient channels (i.e. small width or large depth) are also farther detached from the slope. This means that significant deposition does not start immediately at the break-of-slope. Rather, there is a zone of shallow scouring and minor deposition directly downstream of the break-of-slope. A good example of this erosional type of channel-lobe transition zone is provided by profile D in Figure 4.5C.

4.3.2 Grain size of deposits

Maps of median grain size of the deposits in each experiment are shown in Figure 4.8A-E. Each dot indicates the location of a sediment sample and its colour indicates the median grain size. Two patterns that are persistent between the runs appear. Firstly, the lobes are relatively coarse-grained compared to the slope deposits. Secondly, the maximum grain size on the lobes is found in the central part and not at the most proximal part of the lobe.

The median grain size of the slope deposits ranges from ~130-160 μm and the median grain size of the lobe deposits ranges from ~150-175 μm . The deposits are thereby consistently coarser than the initial composition of the turbidity current at the inlet ($D_{50} = 131 \mu\text{m}$). This is primarily a result of bypass of the silt fraction in the flow. This fine sediment fraction remains in suspension, is not incorporated in the deposits, and settles slowly as a thin drape long after the turbidity current supply at the inlet has stopped.



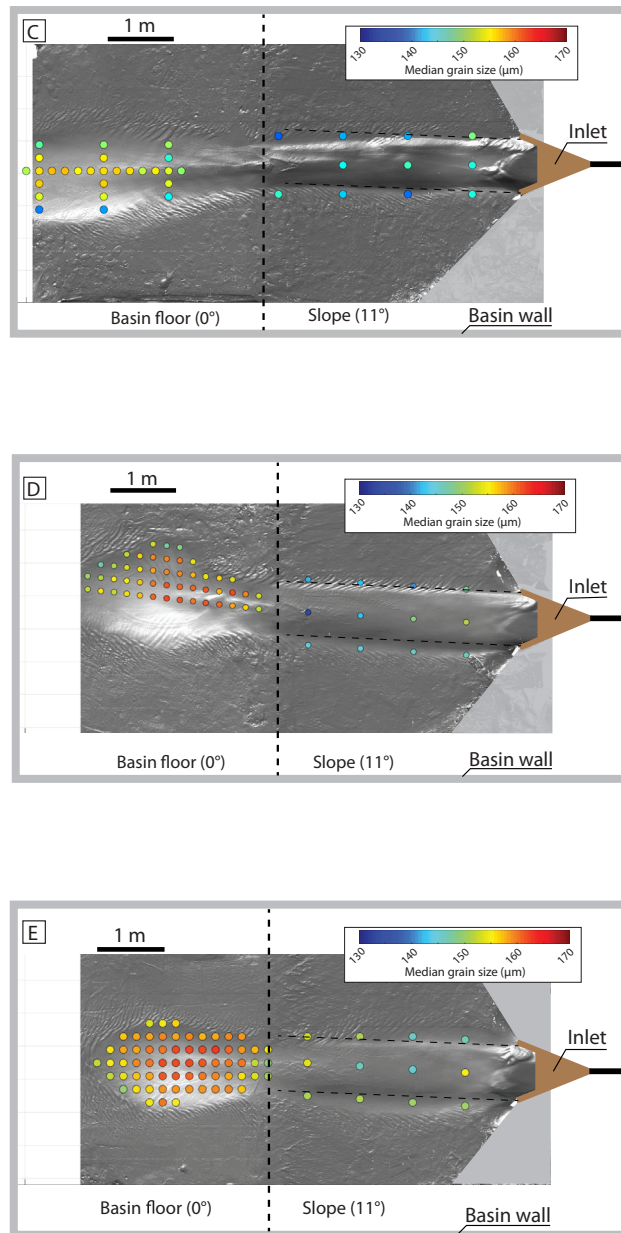


Figure 4.8: Maps with median grain size of deposit samples collected after each experiment. (A) Results from Run 1 in which the initial channel depth was 8 cm and the channel width 80 cm. (B) Run 2 (Depth: 5 cm, Width: 120 cm) (C) Run 3 (Depth: 5 cm, Width: 53 cm) (D) Run 4 (Depth: 5 cm, Width: 80 cm) (E) (Depth: 3 cm, Width: 80 cm)

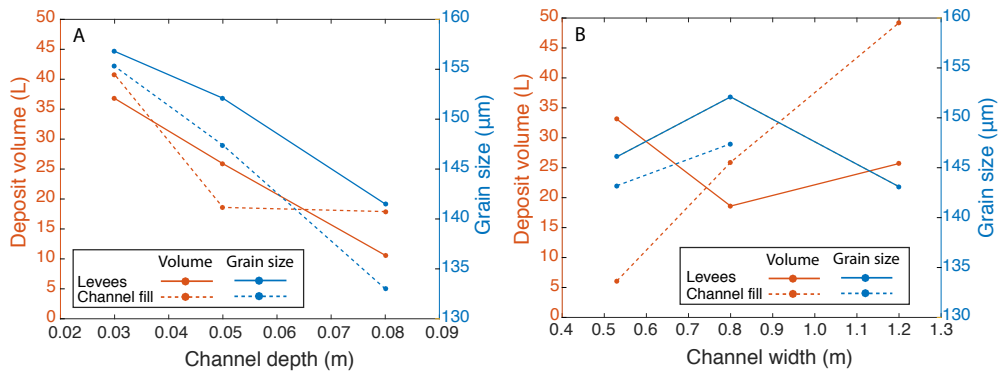


Figure 4.9: Effect of channel dimensions on grain-size- and volume-partitioning between levees and channel fill. (A) Effects of channel depth. An increase in channel depth results in a decrease in the volume and grain size of sediment deposited as levees and channel fill. (B) Effects of channel width. An increase in channel width results in an increase in channel-fill volume. Levee volume and deposit grain size do not show a clear relation with channel width.

Grain size of levee and channel-fill deposits show a clear relation with channel depth. Representative values for levee and channel-fill grain size are obtained by taking the average of all the deposit samples from these two environments. Figure 4.9A shows that both the channel fill and the levee deposits become more fine-grained with increasing channel depth. A clear relation between the channel width and the grain size of the deposits is not found (Fig. 4.9B).

4.3.3 Velocity structure of channelised turbidity currents

The velocity profile was measured in the centre of the channel at equal distance from the inlet during Run 1, 2, 4 and 5. No velocity measurements were obtained during Run 3. The time-averaged (interval 10–30 s) velocity profiles for different runs are compared in Figure 4.10. The velocity profiles show that the maximum flow velocity was 0.9–1 m/s at 1–1.5 cm above the bed (Fig. 4.10). The flow velocity at 10 cm above the bed was 10–20% of the maximum flow velocity. The exact current thickness is hard to define but video footage combined with the velocity profiles suggest that the current thickness is of the order of 0.1 m. The turbidity currents were only partially confined in the channels during the experiments because the current thickness exceeded the channel depth (0.03–0.08 m). Flow velocity at the level that corresponds to the top of the confinement varies between 0.15 m/s (Run 1, channel depth 8 cm) and 0.7 m/s (Run 5, channel depth 3 cm). The geometry of the channel has a significant impact on the velocity structure of the turbidity current. Figure 4.10A shows that the current in a shallow channel (Run 5) is flattened compared to a current in a channel of equal width and a larger depth (Run 1). Figure 4.10B shows that the turbidity current in a wide channel is flatter than the current in a channel of equal depth and a smaller width.

4.3.4 Reconstruction of turbidity current runout

Sediment grain-size- and volume-partitioning was reconstructed for three experiments (Runs 1, 4 and 5). The pre-formed channels in Runs 1, 4 and 5 were 8, 5 and 3 cm deep, respectively, while the channel depth was 80 cm in each of these runs. The volume of transported sediment in the turbidity currents decreased downstream as a result of deposition (Fig. 4.11A). A deeper channel

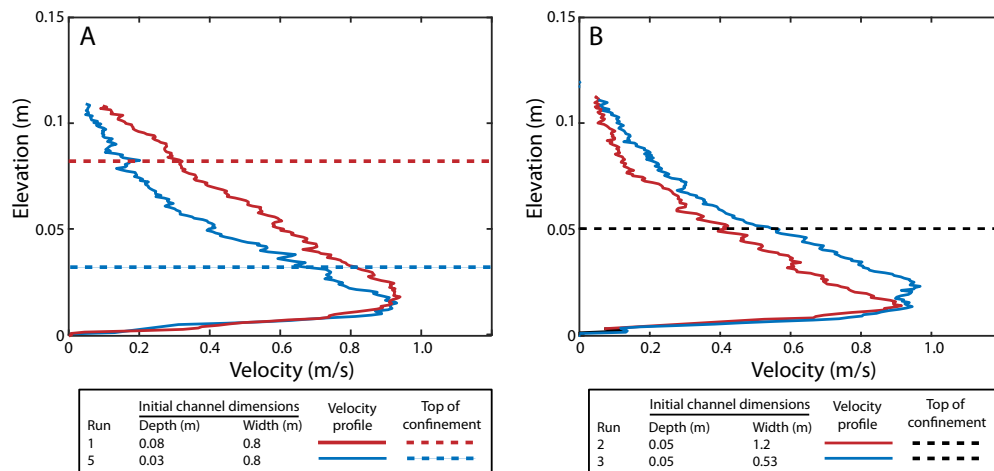


Figure 4.10: Velocity profiles of turbidity currents measured in the centre of each channel. (A) A turbidity current in a deep channel has a larger thickness than a turbidity current in a shallow channel. (B) A turbidity current in a narrow channel has a larger thickness and velocity maximum than a turbidity current in a wide channel.

resulted in less deposition on the slope and a larger proportion of sediment reaching the break-of-slope. Beyond the break-of-slope, on the horizontal basin floor, the deposition rate increased. The flow that exited the shallowest channel (Run 5) responded to the change in slope more abruptly and the maximum deposition rate was reached at ~ 1.5 m downstream of the break-of-slope. The turbidity current in the deepest channel (Run 1) transported sediment farther out onto the basin floor and a peak in deposition rate occurred farther out into the basin, at ~ 2.5 m from the break-of-slope. Downstream change of median grain size of the flows and the deposits are shown in Figure 4.11B. The median grain size of the sediment in the flow decreases slowly on the slope and much faster on the basin floor in each of the experiments. The flows that are sourced by deeper channels cover a larger distance before the grain size of the suspended sediment drops steeply.

For Run 5, the reconstruction of downstream flow evolution is presented in additional detail (Fig. 4.12). Grain-size distribution of the flow and the deposits are compared at different positions in the system (Fig. 4.12A). Silt-sized sediment becomes more abundant in the flow farther downstream in the system as the sand-sized sediment fraction is lost by deposition. The downstream change in sediment volume per grain-size class is shown in Figure 4.12C. This figure illustrates that sediment finer than ~ 80 μm completely bypasses. During the experiments it was observed that the dilute suspension cloud with fine-grained sediment reflected against the back of the flume tank and slowly settled in the minutes after the run to form a 1-2 mm thick drape over the flume tank. This silt fraction would have been deposited further downstream in a natural system.

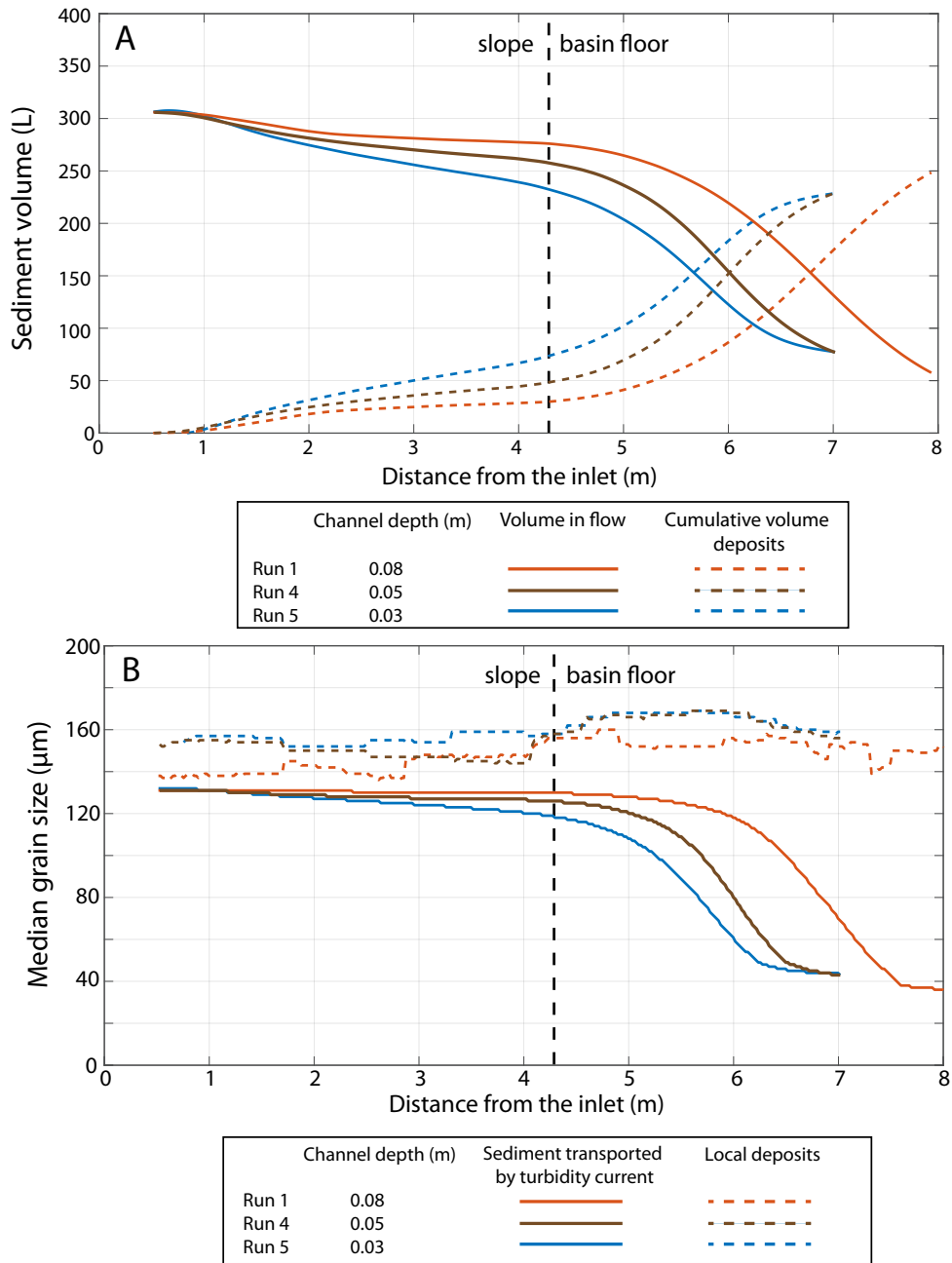


Figure 4.11: Downstream changes in flow size and composition. Results are shown for Run 1 (channel depth = 8 cm, width = 80 cm), Run 4 (channel depth = 5 cm, width = 80 cm) and Run 5 (channel depth = 3 cm, width = 80 cm) (A) Downstream change in transported and deposited sediment volume. (B) Downstream change in transported and deposited sediment grain size.

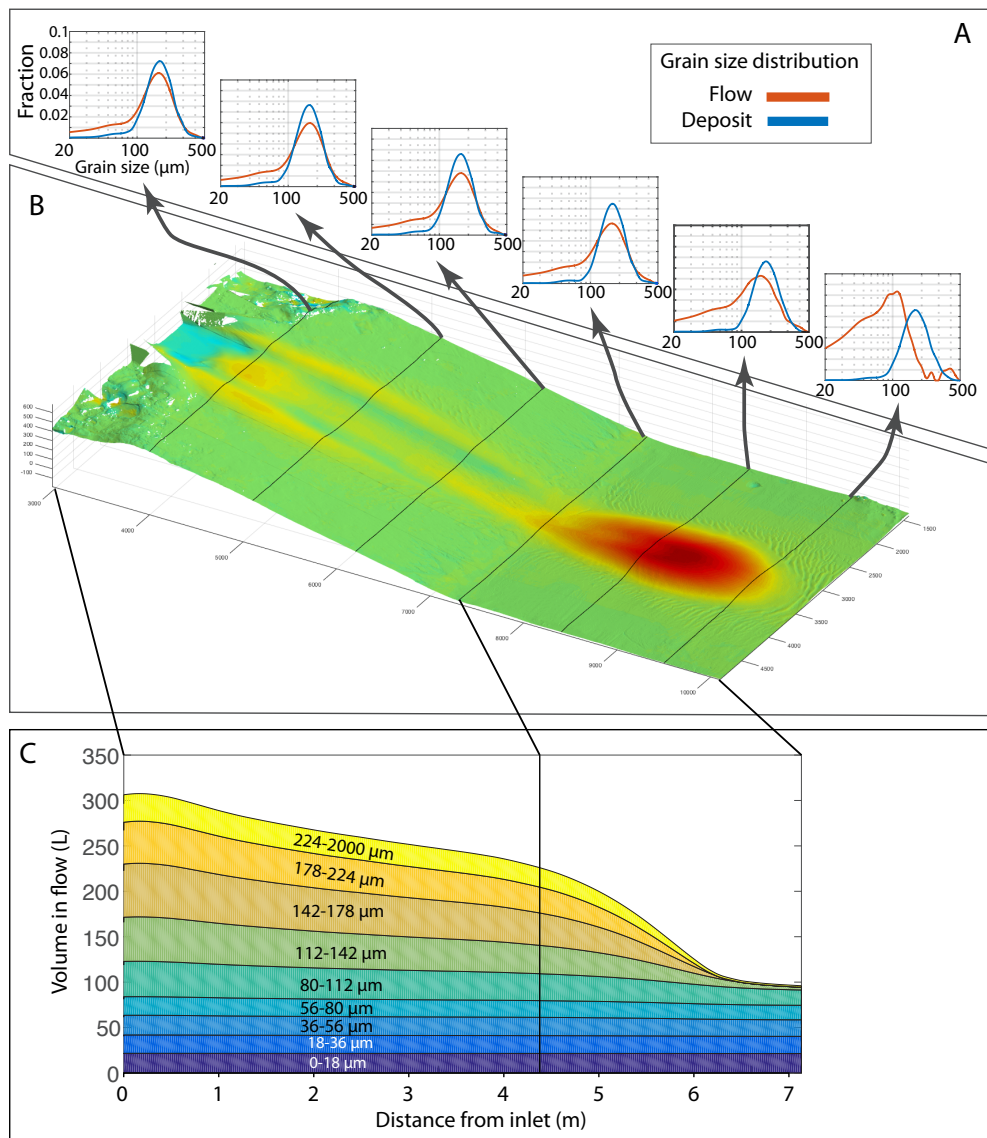


Figure 4.12: Representations of the downstream extraction of mass in Run 5 (channel depth = 3 cm, width = 80 cm). (A) The grain-size distribution of the sediment in the flow and deposits are shown at multiple positions in the system. (B) Map of deposition and erosion. The same colour scale as in Fig. 4.5 is used. (C) Volume of sediment transported in the flow for different sediment grain-size classes. Note that sediment coarser than $\sim 80 \mu\text{m}$ is extracted from the flow while sediment finer than $\sim 80 \mu\text{m}$ is nearly completely bypassed to the downstream end of the system.

4.4 Discussion

4.4.1 Channel geometry and sediment partitioning

Volume partitioning

The volume of sediment that reaches the downstream end of a channel section depends on the initial sediment load of the turbidity current and the fraction that is extracted on the slope. The experiments show that sediment is partitioned into channel fill and levees on the slope in variable volume fractions depending on the channel geometry. These results are in line with previous experiments that showed that channel efficiency (i.e. the fraction of sediment that bypasses the channel section) increases with channel depth (Kane et al., 2008; de Leeuw et al., 2016). Progressive changes in channel confinement occur in most submarine channels (Maier et al., 2013; Ortiz-Karpf et al., 2015; Pemberton et al., 2016) and this has important implications for the stratigraphic evolution of deep-water systems (Hodgson et al., 2016). Here, the influence of channel depth and width on sediment volume and grain-size partitioning in deep-water systems is assessed.

Shallow channels are associated with a larger levee volume (Fig. 4.9A) because the supra-channel portion of the current is larger (Fig. 4.10A), which increases the sediment flux to the overbank area (Straub and Mohrig, 2008). The relation between channel width and levee volume is more complicated. When comparing three runs with equal depth and different channel widths (Runs 2,3 and 4), the run with the narrowest channel (Run 3) is associated with the largest levee volume (Fig. 4.9B). This is interpreted to be the result of the effect of channel width on current thickness. A larger volume of overspill occurs because the current in the narrow channel has a larger thickness than the current in the wider channel. The difference in current thickness between the current in the narrow and wide channel is evident from the velocity data (Fig 4.10B). The current in the wide channel is relatively thin due to lateral spreading of the current inside the channel. However, levee volume associated with the run with the widest channel (Run 2) is larger than the levee volume associated with the intermediate channel. This may be due to the large volume of channel floor deposition in the wide channel, which results in an effective decrease in channel depth, which promotes overspill from the channel.

The volume of channel floor deposition decreases with channel depth and increases with channel width (Figs 4.6 and 4.9). These changes are interpreted to be the result of differences in shear velocity. Flows in a narrow or deep channels show limited lateral spreading. This results in a larger flow thickness and subsequently a higher shear velocity. This allows the currents to keep more sediment in suspension and therefore limits deposition on the channel floor.

Lobes that are sourced by different types of channels have distinctively different geometries (Fig. 4.7). This illustrates that the channel dimensions do not only affect the deposition patterns locally, but that the effect is also transferred downstream. The effects of channel dimensions can be transferred in different ways. Firstly, the channel geometry controls the efficiency and thereby the volume of sediment that reaches the basin floor. If the current that reaches the downstream end of the channel has a relative larger sediment load, it will have a longer runout. In the experiments, the percentage of sediment that reaches the downstream end of the channel ranges from 67% for a low-efficiency, shallow channel (Run 5) to 89% for a high-efficiency deep channel (Run 1). In addition, the channel geometry sets the velocity structure in the channel. The experiments illustrate that a high-efficiency channel (i.e. large depth or small width) results in a flow with a higher velocity and larger thickness (Fig. 4.10). The thicker and faster flow reaches farther into

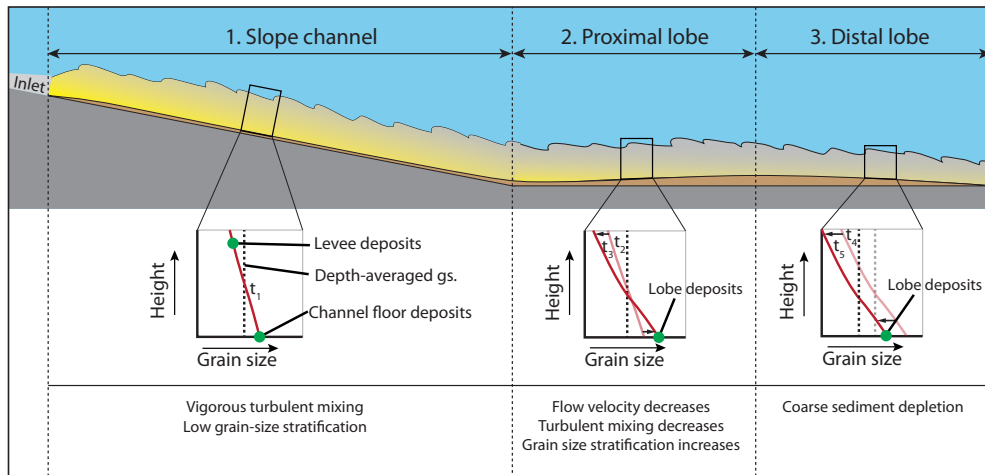


Figure 4.13: *Simplified reconstruction of the runout of a turbidity current in an experiment. Three main zones are recognised along the sediment routing system: (1) The turbidity current in the slope channel has little vertical variation in grain size due to vigorous turbulent mixing. (2) Turbulent mixing decreases on the lobe located on the horizontal basin floor. The grain size at the base of the flow increases downstream as a result. (3) Farther out on the basin floor the flow gets depleted in coarse sediment, which results in a decrease in the grain size of the deposits.*

the basin, because it takes longer before spreading and deceleration have resulted in deposition of the full sediment load in the flow. Process mechanisms that link channel dimensions with channel efficiency are thus identified in the experiments.

Grain-size partitioning

Generally, the levee and channel fill deposits are finer grained than the deposits of the basin-floor lobe (Fig. 4.8). We identify two main factors that control the grain-size distribution of sediment deposited from turbidity currents: (1) the vertical sorting of sediment in the flow and (2) the grain-size spectrum available in the flow.

Vertical sediment segregation in the flow controls grain-size distribution of the sediment that is deposited at the base of the flow and the sediment in the overspilling portion of the current that escapes from the channel (Fig. 4.13). An upward decrease in grain size in turbidity currents has been measured directly in small experimental turbidity currents (e.g. Garcia, 1994; Baas et al., 2005) and has been reconstructed from submarine channel deposits (e.g. Jobe et al., 2017; Symons et al., 2017). Previous experiments (Chapter 3 of this thesis) with similar boundary conditions (sediment grain size, discharge and slope) have shown that an upward decrease in grain size also occurs in these small-scale currents. In the present experiments, the levee grain size decreases as channel depth increases (Fig. 4.9A). We interpret this to be the result of grain-size stratification. Deposits derived from the basis of turbidity currents (channel fill and lobe) are expected to be coarser grained than the levee deposits. Lobe deposits indeed have a larger median grain size than levees in each of the experiments. However, channel floor deposits formed in the experiments are finer grained than the levees (Fig. 4.9A). This pattern is dissimilar from most natural systems and may indicate that at least some of the channel fill was deposited during the waning phase of flow

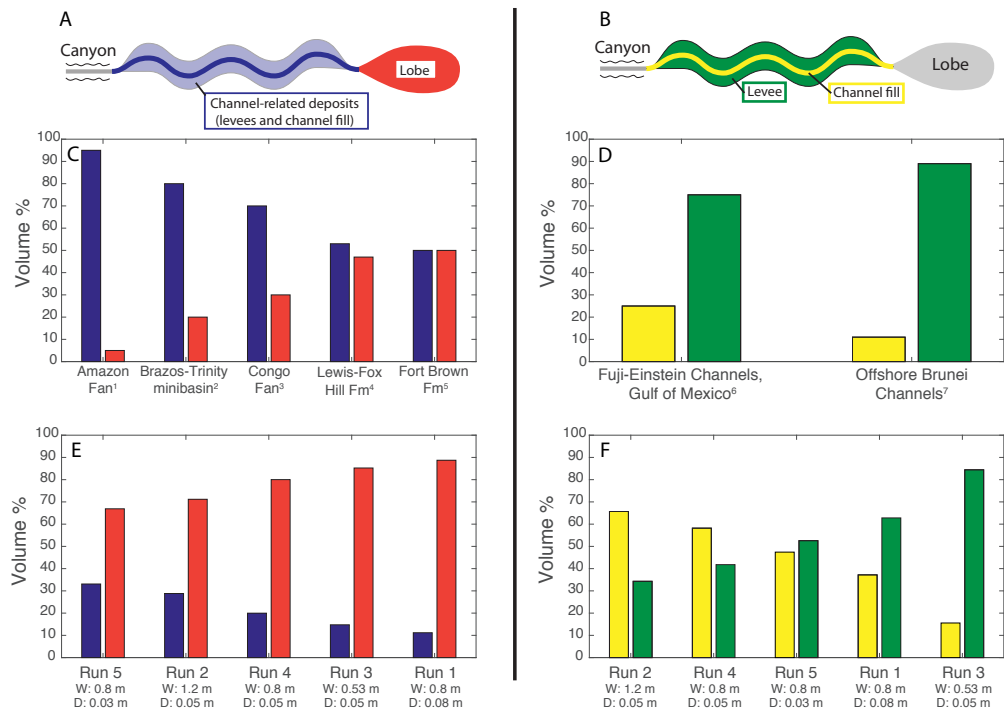


Figure 4.14: Volume partitioning in deep-water systems. (A) Partitioning in experiments between slope-channel deposits (levees and channel fills; in blue) and lobe deposits (in red). (B) Partitioning in experiments between channel-fill deposits (in yellow) and levee deposits (in green) (C) Partitioning in natural systems between slope channels and lobes. (D) Partitioning in natural systems between channel fills and levees. (E) Partitioning in experiments between slope channels and lobes. (F) Partitioning in experiments between channel fills and levees. ¹Jegou et al., 2008 and Pirmez & Imran, 2003; ²Paola & Martin, 2003; ³Picot et al., 2016; ⁴Carjaval & Steel, 2012; ⁵van der Merwe et al., 2014; ⁶Sylvester et al., 2012; ⁷Straub et al., 2012.

near the end of the experiments when the sediment that was still in transport was relatively fine-grained.

The grain-size spectrum in the flow is a second major control on the deposit grain size. Flow reconstructions from the present experiments (Figs 4.11, 4.12) show that flows get depleted in coarse sediment towards the distal end of the system. This explains the decrease in median grain size from the centre of the lobe to the distal lobe in the experiments (Fig. 4.8).

A downstream coarsening trend occurs in each of the experiments from the break-of-slope to the centre of the lobe. Such a facies trend is not normally expected in lobes. Recently, however, downstream coarsening of turbidity current deposits has been recognised in flume experiments and in outcrops of the Fort Brown Formation in the Karoo (Pohl and Eggenhuisen, 2016). A depositional model is developed based on these observations in which the downstream coarsening is attributed to increasing grain-size stratification in decelerating turbidity currents which increases the grain size at the base of the flow. The downstream coarsening observed on the proximal lobe in the present experiments is likely to be a result of this process as well (Fig. 4.13).

4.4.2 Sediment partitioning in natural systems compared with experiments

Volume partitioning

Estimates of sediment volumes in different components of deep-water systems (levees, channel fills, lobes) become increasingly available through outcrop and subsurface studies. Some datasets with volume estimates cover both the channel and lobe segments of deep-water systems (Fig. 4.14A,C; Jegou et al., 2008; Carvajal and Steel, 2012; Paola and Martin, 2012; Van der Merwe et al., 2014; Picot et al., 2016), while other datasets cover the channel-levee system and the partitioning between channel fills and levees therein (Fig. 4.14B,D; Straub et al., 2012; Sylvester et al., 2012).

Partitioning between channel-related deposits (levees, channel fills) and lobes was documented for the Congo Fan (Picot et al., 2016), the Amazon Fan (Pirmez and Imran, 2003; Jegou et al., 2008), the Lewix-Fox Hill Formation in the Washakie Basin in Wyoming (Carvajal and Steel, 2012), and the Fort Brown Formation in the Karoo Basin (Van der Merwe et al., 2014). Relative volumes of channel-related deposits and lobes vary greatly between these deep-water systems (Fig. 4.14C). The lobes associated with the Amazon Fan only constitute a minor volume compared to the channel-related deposits while in the Fort Brown Formation the channel-related deposits and lobes are comparable in volume. In general, it seems that for large, mud-rich fan systems on continental margins, such as the Amazon Fan and Congo Fan, lobes form a comparatively small fraction of the total fan volume. For systems such as the Washakie and Karoo Basin, the lobes form a larger volume fraction. These systems were located in intracontinental basins and had a higher portion of sand and a smaller slope length than the Amazon Fan. Thus, the characteristic transition in deep-water systems from channels to lobes is not tied to a certain degree of mass extraction. It has previously been hypothesized that in any sediment routing system similar deposit characteristics are likely to occur at similar degrees of mass extraction from the source into a basin if the basin characteristics and sediment supply are similar (Strong et al., 2005; Paola and Martin, 2012). The deep-water systems that are compared in this study are vastly different in terms of basin configuration and calibre of sediment supplied and it should thus be no surprise that the channel-lobe transition is not tied to a specific degree of mass extraction. The comparatively small lobes in the more mud-prone systems, such as the Amazon Fan, may be explained as follows: a condition of self-channelisation can be maintained as long as sufficient mud and silt are available in the flow to build up levees (Posamentier and Kolla, 2003). A loss of confinement due to depletion of mud and silt-sized sediment will only occur at a high degree of mass extraction because a large volume of silt and mud were available initially in mud-rich systems. Systems with a more sand-prone sediment supply will be depleted in mud at a lower degree of mass extraction and have lobes that form a larger volume fraction of the sediment load. Such an interpretation implies that there may be a critical sand:mud ratio at which a channel transition will occur. This should be a topic of future investigation.

In the experimental systems (Fig. 4.14E) a much larger fraction of sediment is partitioned into the lobe (67-89%) than in any of the natural systems considered here (3-50%) (Fig. 4.14C). This is largely the result of the geometry of the set-up where a short section of slope is followed by a horizontal basin floor where the flow becomes depletive to form a lobe. Such a profile with a sharp break occurs on some active margins where the slope is affected by faults, but more commonly slope profiles are graded (Kneller, 2003). A larger fraction of sediment would probably be partitioned into the channel fill and levees in the experiments if the slope section would be longer.

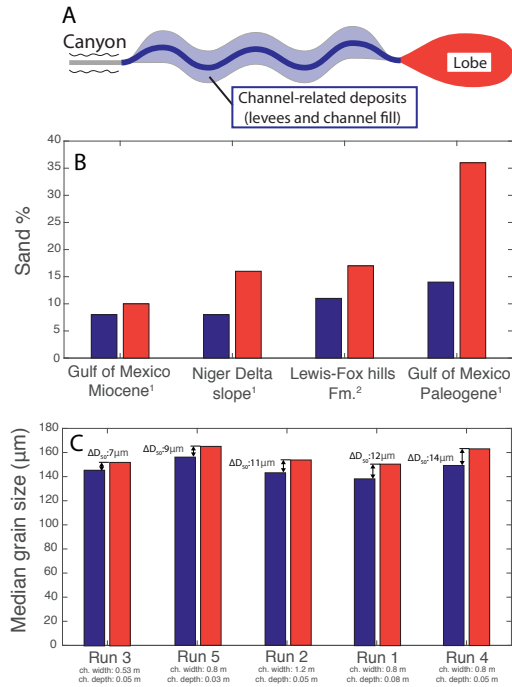


Figure 4.15: Partitioning of grain-size fractions in deep-water systems. (A) Partitioning in experiments between channel-related deposits (levees and channel fills, in blue) and lobe deposits (in red). (B) Partitioning in natural systems between channel-related deposits and lobes. (C) Partitioning in experiments between channel-related deposits and lobes. ¹Carjaval & Steel, 2012; ²Prather et al., 2016.

Partitioning of sediment volumes between channel fills and levees has been documented for a channel network on the continental slope offshore Brunei (Fig. 4.1B, Straub et al., 2012) and for the Fuji-Einstein system in the Gulf of Mexico (Sylvester et al., 2012). Levee volumes are significantly larger than channel fill volumes in these systems (Fig. 4.14D). It should be noted, however, that the volume partitioning in a certain stratigraphic interval may not be representative for individual turbidity currents. It may well be possible, for example, that initial flows were depositing on the levees and bypassed in the channel axis while later turbidity currents mainly deposited in the channel.

The experiments show highly variable sediment volume partitioning between levees and lobes (Fig. 4.14F). Channel fill volumes relative to levee volumes are small in some experiments (Runs 1,3,5) while channel fill volumes exceed the levee volume in other experiments (Runs 2,4). This raises the question what is driving the volume partitioning between levees and channel fills. Runs 1 and 3 have the largest levee volume relative to channel fill volume (Fig. 4.14F) Meanwhile, the volume of channel-related deposits (levees and channel fills combined) was low for these runs, which means that the channel was very efficient (Fig. 4.14E). Thus, the experiments show that optimisation of channel dimensions reduces channel-floor deposition more effectively than levee

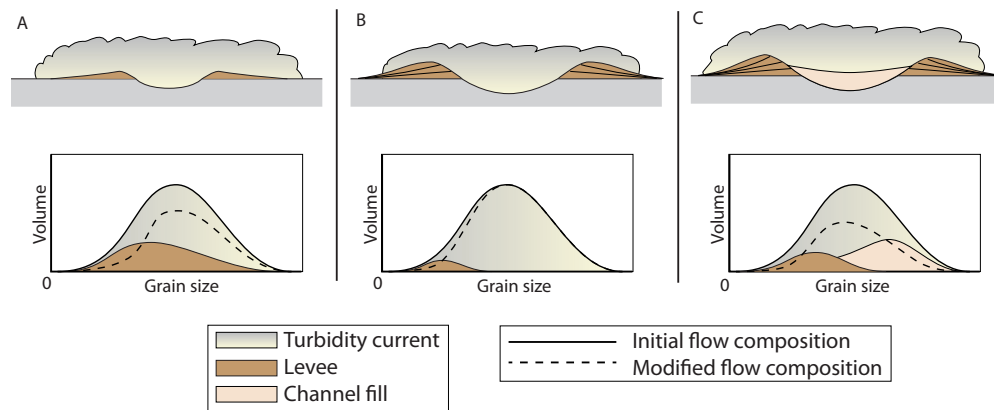


Figure 4.16: Schematic illustration of the effect of channel evolution on sediment partitioning. (A) An immature channel has little relief. The turbidity current is relatively inefficient because a large volume of sediment is lost to overspill from the channel. The overspilling current has a broad grain-size distribution (B) A mature channel has a greater depth due to further growth of the levees and incision in the channel thalweg. The turbidity current is efficient because only a small fraction of sediment is lost due to overspill. The overspill is very fine-grained. (C) During the late stages of channel evolution the channel gets filled with sediment. The turbidity current deposits sediment both on the channel floor and on the levees. Deposition on the levees preferentially extracts fine sediment from the flow while deposition on the channel floor preferentially extracts coarse sediment from the flow.

deposition. Some degree of current overspill onto levees will nearly always occur unless turbidity currents are confined in a deep canyon.

Grain-size partitioning

Partitioning of sediment grain-size fractions between submarine slopes, where channel-levee systems dominate, and basin floors, where lobes dominate, has been documented for the Lewis-Fox Hills Formation in the Washakie Basin (Carjaval & Steel, 2012). Additionally, Prather et al. (2016) report sand percentages for the Miocene and Paleogene deep-water deposits in the Gulf of Mexico and for the Niger delta slope. In each of these cases the highest sand percentage is found on the basin floor (Fig. 4.15B). Similarly, other basin-wide studies have qualitatively shown that most of the sand transported by turbidity currents accumulates on the lower slope and basin floor (Hubbard et al., 2011; van der Merwe et al., 2014). The Miocene deposits in the Gulf of Mexico show relatively little difference in sand percentage between the slope and basin floor. This is thought to be a result of the stepped slope profile that enhances capturing of sand in minibasins on the slope (Prather et al., 2016).

An increase in deposit grain size from the slope to the basin floor is also found in the experiments. The contrast in grain size is relatively small as compared to natural systems (Fig. 4.15C) partially because the sediment available in the experiments is mostly sand-sized while the range can be much broader in natural systems. Nevertheless, the comparison illustrates that the same patterns of grain-size partitioning are produced by experimental flows which are two to three orders of magnitude smaller than their natural counterparts.

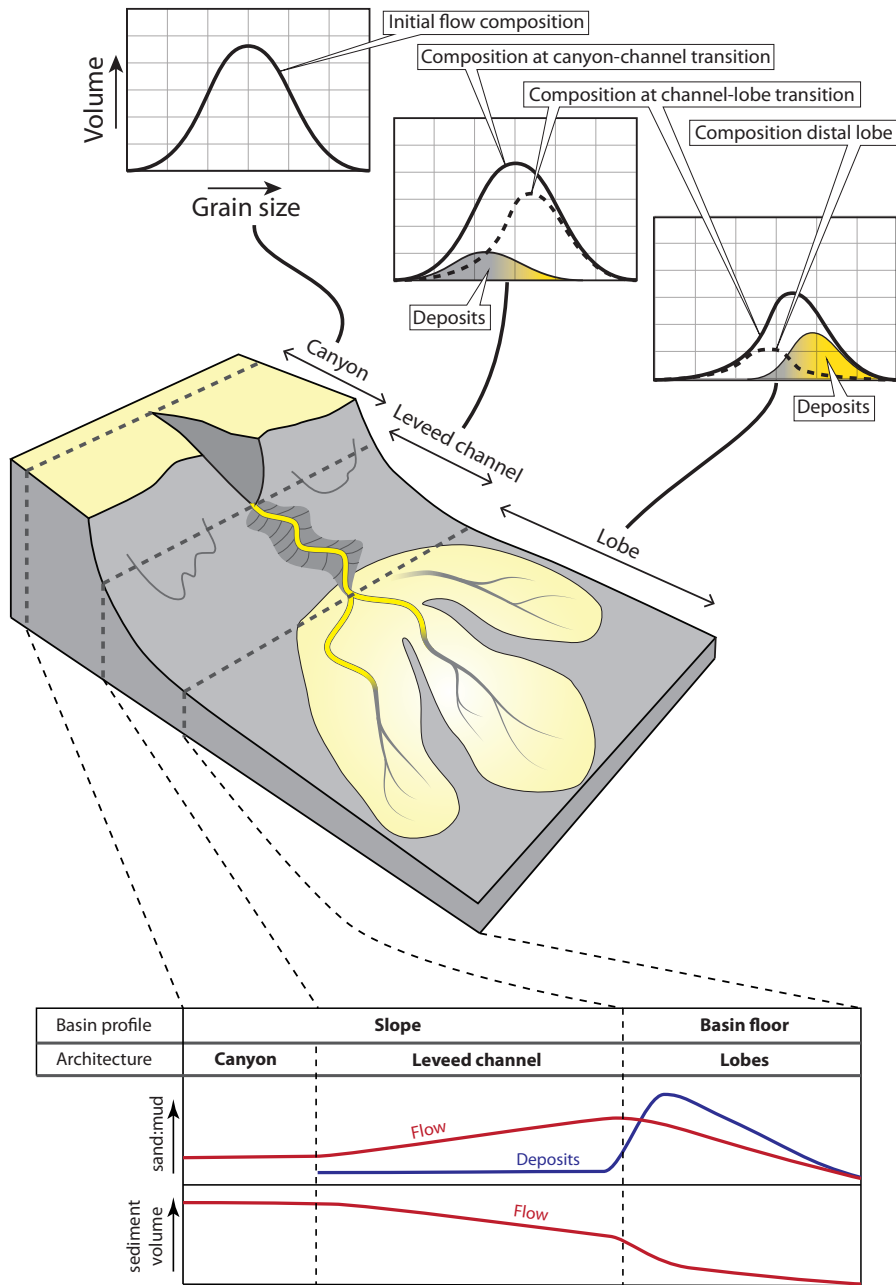


Figure 4.17: Summary figure illustrating the partitioning of sediment in a deep-water system consisting of a canyon section, a leveed channel and a lobe. Lower panel shows the downstream evolution of flow composition (sand:mud ratio) and size as a result of downstream mass extraction due to deposition. (Figure inspired on Posamentier & Kolla (2003) and SEPM course notes by P. Haughton)

The efficient bypass of sand on the slope is closely linked to the density structure of turbidity currents: sand is generally concentrated in the lower divisions of the flow and will therefore not be lost to overspill from slope channels. Once the flow transits from the channel onto the lobe, sand deposition is no longer inhibited because the entire flow becomes unconfined, expands laterally and decelerates.

4.4.3 Deep-water systems in a mass-balance framework

The present study highlights that the functioning of channels as a sediment filter is strongly dependent on the channel dimensions. Each of the experiments can be considered to represent a different phase in the evolution of a channel. The dimensions of submarine channels evolve progressively during their evolution (Maier et al., 2013; Hodgson et al., 2016). During the incipient phases of channel formation, the confinement width and depth are likely small compared to the flow size. The channel subsequently allows a large sediment volume with a broad range of grain sizes to escape from a channel. This situation is similar to Run 5. The flow that reaches the downstream end of the channel will therefore be significantly altered relative to the input composition (Fig. 4.16A). As the degree of confinement increases due to levee build-up (Hodgson et al., 2016), the volume of sediment deposited on the levees decreases (Fig. 4.16B). The grain size of the sediment that is deposited on the levees becomes restricted to the finer end of the spectrum. This situation may be represented by Run 1. During the later stages of channel evolution, a channel typically shallows and widens as extensive deposition on the channel floor takes place (e.g. Hubbard et al., 2014; Fig. 4.16C). Deposition on the channel floor extracts relatively coarse sediment from the flow. In addition, the deposition on the channel floor reduces channel relief and this increases overspill. The remaining flow at the downstream end of the channel section is significantly reduced in volume and the grain-size distribution is changed according to the components that are extracted. This phase of channel evolution may be represented by Run 2.

Figure 4.17 provides a schematic representation of a deep-water system and the downstream extraction of mass from turbidity currents. Unique in deep-water systems is the selective extraction of the fine-grained sediment in the channelled section of the system (Posamentier & Martinsen, 2003). In fluvial systems, on the contrary, the coarse sediment fraction is often preferentially extracted from the sediment supply (Strong et al., 2005). Experiments have shown to be a valuable tool to study the effect of downstream mass extraction on the sedimentary architecture of alluvial basins (Strong et al., 2005). The present experiments show that a mass-balance analysis can also be applied to clastic deep-water systems. There, the mass-balance analysis has the potential to provide similar insights in controls on sedimentary architecture.

Full dynamical scaling is not always necessary nor possible in geomorphological experiments (Paola et al., 2009). However, some key processes need to be captured in experiments to study downstream mass extraction from turbidity currents: (1) the turbidity currents needs to be stratified in grain size and (2) deposition in the channel section needs to be dominated by overspill and not by filling of the channel. Experiments that fulfil these conditions can be analysed in a mass-balance framework to answer a range of questions related to the stratigraphic evolution of deep-water systems. Examples of such questions include: (1) does the channel-lobe transition occur at a critical degree of mass extraction or a critical sand:mud ratio in the flow? (2) How is the sand:mud ratio at the sediment supply related to the sand:mud ratio of the different depositional components of the system (i.e. levees, channel fills and lobes)?

4.5 Conclusions

Experiments were conducted in which turbidity currents flowed through submarine channels with various dimensions. Monitoring of the flows during the experiments and mapping of the deposits after the experiments allowed to identify the effects of confinement on flow processes and the partitioning of sediment volume and grain size fractions by turbidity currents.

- The geometry of slope confinement is a major factor influencing the fraction of the initial supply and calibre of sediment delivered to the basin floor. Channels with a large depth and/or a small width show the highest degree of sediment bypass to the basin floor. The fraction of sediment that reaches the basin floor in the experiments varies between 67% and 89% depending on the channel geometry.
- Flow velocity measurements elucidate the mechanisms that control channel efficiency. Flow thickness relative to channel depth controls the amount of overspill. Flow thinning due to lateral spreading in a wide channel increases deposition inside the channel.
- A mass-balance reconstruction, where deposits are subtracted from the initial sediment flux, shows that suspended sediment volume as well as grain size decrease downstream in the system due to preferential extraction of the coarse sediment fraction. The sediment that is extracted from the flow on the slope represents a finer part of the grain size spectrum than the deposits on the lobe.
- Most of the sediment volume and grain-size partitioning produced in the experiments are comparable to natural systems. Similar to most natural systems, the experiments show that slope deposits are fine-grained compared to the basin floor deposits.
- The different channel dimensions between the experiments and the associated sediment partitioning patterns can be considered as snapshots from different phases of channel evolution. An incipient channel has a small depth and width. This results in a low efficiency due to the large volume of overspill. A mature channel has a larger depth. This results in a higher efficiency. A channel in the latest stage of its evolution has a large width and a small depth. This results in a low efficiency reflected in the large volume of deposition inside and outside the channel.
- It is suggested here that analysing deep-water systems in a mass-balance framework can aid stratigraphic interpretation and prediction. Future work should apply this analysis to physical experiments as well as to field and subsurface datasets. It may, for example, be possible that the channel-lobe transition can be linked to a certain degree of mass extraction or to a critical sand:mud ratio in the flow.

Chapter 5

Turbulent diffusion modelling of grain-size segregation in polydisperse turbidity currents; an experimental validation and possibilities for application

ABSTRACT

The grain size of turbidity-current deposits typically decreases with height above the thalweg of submarine canyons and channels. This vertical change in deposit grain size reflects the grain-size stratification in polydisperse turbidity currents. The grain-size stratification is, in turn, related to the intensity of turbulent mixing because turbulence homogenises the current and reduces grain-size stratification. However, a comprehensive approach to relate the stratification implied from the deposits to reconstruct turbidity current flow properties from deposit characteristics is currently not available. A simple analytical diffusion model, based on the Rouse equation, is presented to calculate grain-size gradients in turbidity currents. The model predicts the vertical change in concentration of every grain-size class suspended in the current above a near-bed reference level. Fine sediment is distributed more homogeneously than coarse sediment and fine sediment therefore becomes relatively more abundant upwards in the flow. This results in a decrease in median grain size upwards in the flow. Flume experiments are used to test the model. Sandy turbidity currents were run in a rectangular flume tank and sampled with siphoning tubes at four elevations above the bed. Flume slope angles of 4 and 8 degrees were used. The turbidity current on the steeper slope has a higher turbulence intensity and is therefore less stratified in terms of grain size. The vertical gradient in grain size and concentration measured in the experiments are in reasonable agreement with the model results. The possibilities to use the model to interpret submarine channel deposits are discussed. An approach is suggested where the model is repeated with different turbulence intensities until the modelled grain-size stratification matches the deposits. Significant insights in the properties of past turbidity currents in a submarine channel can thereby be obtained.

Based on

Turbulent diffusion modelling of grain-size segregation in polydisperse turbidity currents; an experimental validation and possibilities for application. By: Jan de Leeuw, Joris T. Eggenhuisen, Florian Pohl, Matthieu J.B. Cartigny, *in preparation*.

5.1 Introduction

Grain-size stratification is a common feature of turbidity currents (Straub and Mohrig, 2008; Kane and Hodgson, 2011; Hansen et al., 2015). Sand-prone channel fills and clay-rich levees of submarine channels can therefore be deposited by the same flows (Hiscott et al., 1997). Vertical grain-size gradients in turbidity currents have directly been measured in flume experiments (Garcia, 1994; Baas et al., 2005; Straub and Mohrig, 2008; Straub et al., 2011), and modelled with numerical models (Stacey and Bowen, 1988; Huang et al., 2007; Abd El-Gawad et al., 2012a; Abd El-Gawad et al., 2012b). These vertical trends in the flow have also been reconstructed by analysing deposits from different elevations above the thalweg of channels and canyons (Hiscott et al., 1997; Pirmez and Imran, 2003; Dennielou et al., 2006; Babonneau et al., 2010; Paull et al., 2010; Migeon et al., 2012; Hubbard et al., 2014; Jobe et al., 2017). Figure 5.1 shows the deposit grain size versus height above the thalweg in a number of natural channel systems. Between these systems there are differences in flow thickness and the range of sediment grain sizes available but they all show a systematic decrease of deposit grain size with height above the thalweg of the channel or canyon. Also in settings where turbidity currents are not confined within a channel, it is inferred that sand was only transported in the lower portions of the flow because the sandy portions of turbidite beds only drape a limited amount of topography (Stevenson et al., 2014; Spychala et al., 2017).

Grain-size gradients are the result of differences in vertical mixing between coarse and fine sediment fractions. In a current with a polydisperse sediment load (i.e. multiple sediment grain sizes), the coarse sediment fraction is concentrated near the base of the current while finer sediment fraction is more homogeneously distributed over the height of the current (Garcia, 1994; Kneller and Buckee, 2000; Baas et al., 2005; Hansen et al., 2015; Tilston et al., 2015) (Fig. 5.2A). Intense turbulence will homogenise sediment of all grain sizes and will therefore reduce the vertical variation in grain size in turbidity currents (Baas et al., 2005; Fig. 5.2B). The grain-size gradient in a turbidity current, measured either directly or reconstructed from deposits, thus reflects important current properties. However, a method to reconstruct the flow structure from the vertical change in grain size is currently not available. This requires a model that describes the concentration profile for each grain-size class in suspension.

The vertical distribution of mono- and polydisperse sediment within a turbulent flow is often approximated with turbulent diffusion models (Rouse, 1937; Vanoni, 1946; Graf, 1971; van Rijn, 1993; Vanoni, 2006; Garcia, 2008; Dorrell et al., 2013). In this approach, sediment particles are considered to be mixed by turbulence in analogy to heat, momentum, and dissolved matter. An equilibrium concentration profile is reached when there is a balance between the turbulent mixing, which homogenises the current, and the sediment settling, which pulls the sediment towards the bed. The Rouse equation (Rouse, 1937) is an analytical solution for the equilibrium concentration profile applicable to fluvial flow structures. The concentration profiles predicted by the Rouse equation are more stratified as the ratio between the shear velocity and the settling velocity becomes smaller, where the shear velocity is a flow parameter that can be used as a measure for the intensity of turbulent mixing.

The Rouse equation has also been applied directly as an analytical framework for sediment stratification in turbidity currents (Hiscott, 1994; Hiscott et al., 1997; Straub and Mohrig, 2008; Bolla Pittaluga and Imran, 2014). This approach in turbidity current modelling has led to consistent results in relating flow structure to geological deposit characteristics (Hiscott et al., 1997; Jobe et al. 2017). This is a good result given the obvious differences between the flow structure of turbidity currents and the flow structure of open channel flows for which the Rouse

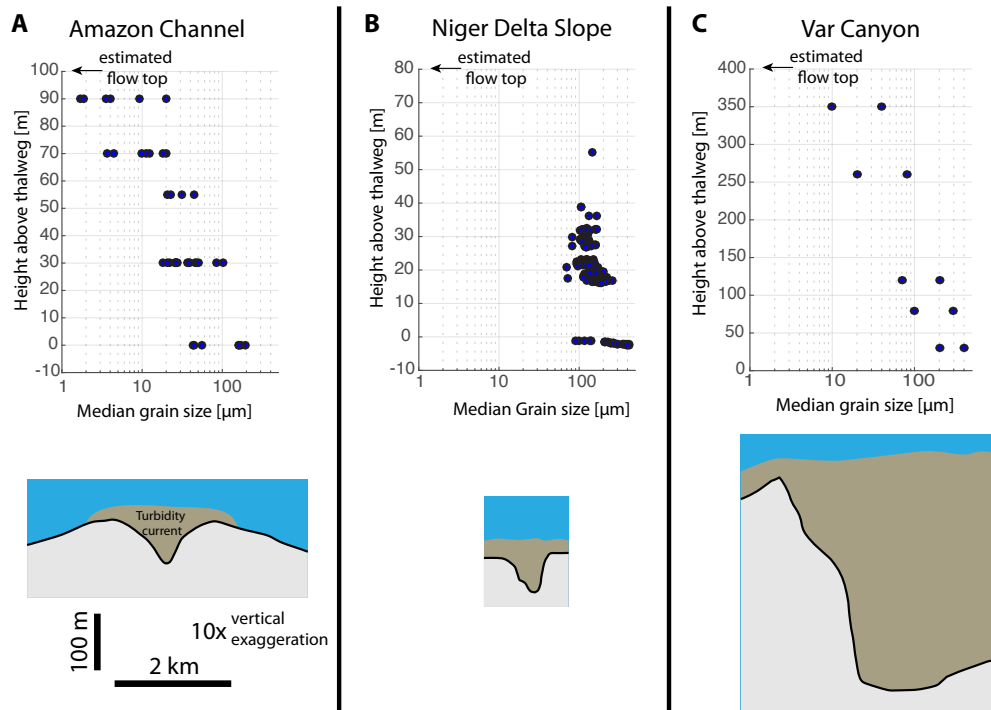


Figure 5.1: Change in deposit grain size as a function of height above the channel thalweg for a number of natural submarine channels. (A) Amazon Channel (Hiscott et al., 1997; Pirmez et al., 2003) (B) Niger Delta slope channels (Jobe et al. 2017). (C) Var Canyon (Migeon et al., 2012). A representative channel/canyon cross-section is shown for each of the systems. These cross-sections each have the same scale.

equation is derived. However, the applicability of the Rouse equation to turbidity currents has not been validated against field or measurements of sediment-laden turbidity currents in experiments.

In this study we present turbidity current flume experiments in which grain-size stratification in turbidity currents is measured. The results of these experiments are compared to an analytical model based on the Rouse equation. The specific objectives are: to (1) determine the fit of the analytical model with the experiment data, (2) to quantify how grain-size stratification changes with shear velocity, and (3) to explore how the analytical modelling approach may be applied to reconstruct turbulence intensity and the associated stratification structure of past turbidity currents from a grain size profile that is reconstructed from deposits.

5.2 Methods

5.2.1 Grain-size stratification model

The purpose of the model is to predict the upward change in grain size and concentration from a near-bed reference level. The model presented here requires four inputs: (1) grain-size distribution of the suspended sediment at one reference level, (2) sediment concentration at the same reference level, (3) thickness of the flow and (4) the shear velocity of the flow. The reference level can in principle be located at any level in the flow where flow conditions are fully constrained. The concentration profile for sediment of each individual grain-size class is calculated using the Rouse

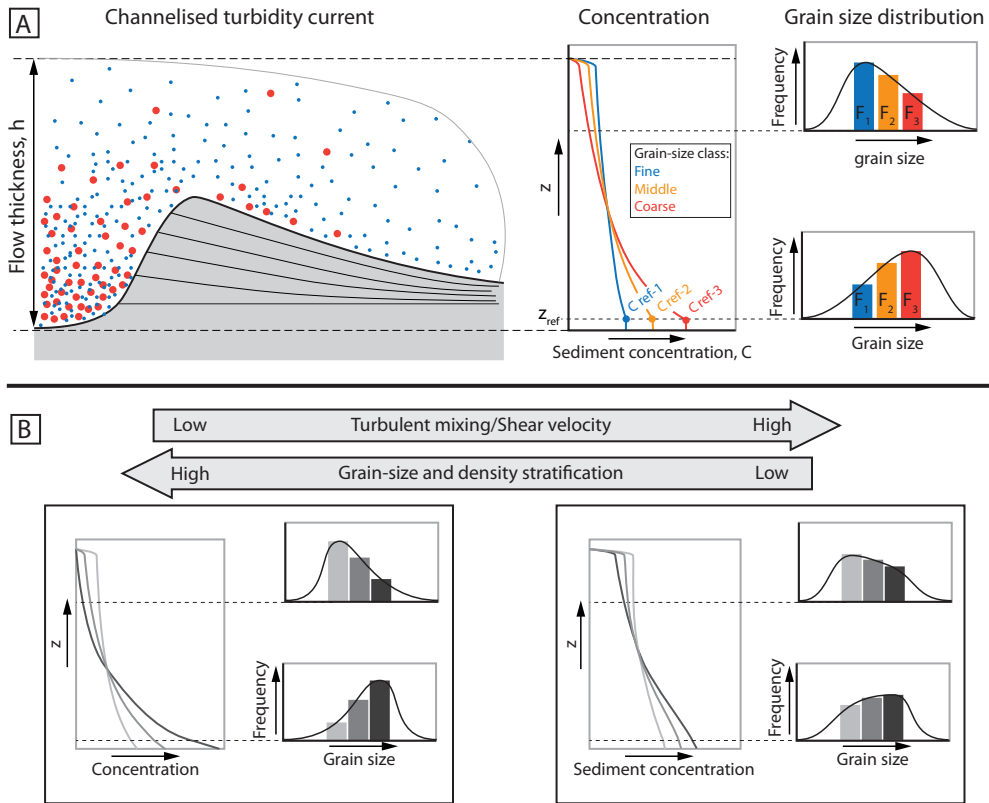


Figure 5.2: Conceptual model of grain-size stratification in channelised turbidity currents. (A) Left: schematic representation of a leveed channel. Middle: concentration profiles for different grain-size classes. Right: grain-size distribution of suspended sediment at two levels in the flow. The coarse sediment fraction is concentrated near the base of the flow whereas the fine sediment fraction is more homogeneously mixed. The fine sediment fraction is therefore relatively more abundant in the upper part of the flow. (B) Turbidity currents become more stratified in grain size and density as the turbulent mixing intensity decreases.

equation (Eq. 1). This equation is originally meant for the prediction of sediment concentration profiles of open channel flows with a free surface at the top. Turbidity currents are affected by shear at the top surface with ambient the water and this likely affects the shape of the concentration profile. However, a modified version of the Rouse equation for turbidity currents is currently not available. Nevertheless, the Rouse equation and slightly modified versions of it have previously been used as a useful first-order approximation for the concentration profile in turbidity currents (Hiscott, 1994; Hiscott et al., 1997; Straub and Mohrig, 2008; Bolla Pittaluga and Imran, 2014).

The Rouse equation gives the concentration profile of sediment in the grain-size class i as (Rouse, 1937; see Garcia, 2008 for a modern treatment of the derivation):

$$C_i(z) = C_{refi} \left(\frac{H-z}{z} \left(\frac{z_{ref}}{H-z_{ref}} \right) \right)^{\frac{v_{si}}{k\omega^*}} \quad (5.1)$$

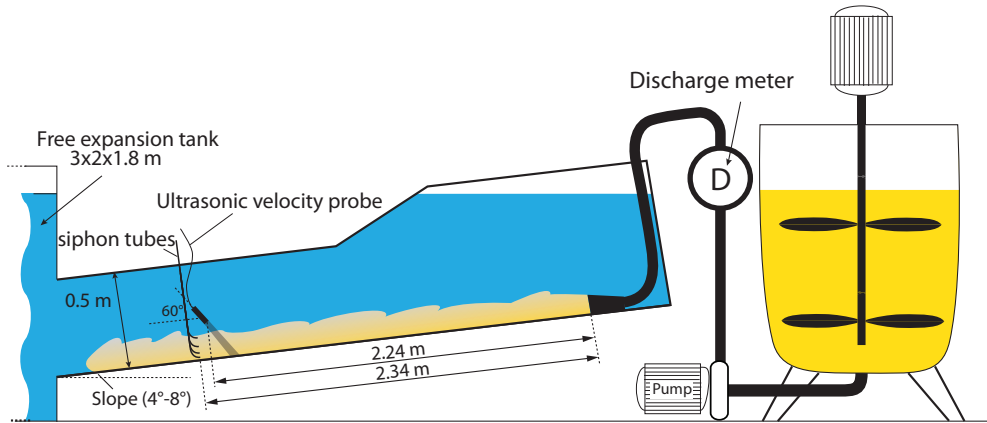


Figure 5.3: Sketch of the experiment set-up. A mixture of sand and water is prepared in an external mixing tank. A pump supplies the suspension to the set-up. Flume width is 10 cm. The pump speed is regulated in order to keep the discharge constant. Velocity of the turbidity current in the flume tank is measured with an ultrasonic velocity probe. Suspended sediment concentration and grain-size distribution are measured from samples collected with siphon tubes at 1, 2, 4 and 8 cm above the bed.

where c_{refi} is the volume concentration of sediment [-] in grain-size class i at the reference level, H is the thickness of the flow [m], z is the height above the bed [m], z_{ref} is the height of the reference level [m], v_{si} is the settling velocity of the sediment in grain-size class i [m/s], κ is the von Karman constant (0.4) and u^* is the shear velocity [m/s]. Figure 5.2A shows a schematic concentration profile in which H , z , z_{ref} and C_{refi} are annotated for clarification of these parameters. C_{refi} is obtained using:

$$C_{refi} = C_{ref} F_{refi} \quad (5.2)$$

where C_{ref} is the total volumetric sediment concentration at the reference level, F_{refi} is the fraction of the sediment volume at the reference level in grain-size class i . C_{ref} is only known a priori if direct concentration measurements are available. C_{ref} is set at 1 when concentration measurements are not available. F_{refi} is obtained from the grain-size analysis of a sediment sample from the reference level (Fig. 5.2A).

The total sediment concentration profile is obtained by summation of the concentration profiles for the individual grain-size classes:

$$C(z) = \sum_i C_i(z) \quad (5.3)$$

The fraction of sediment in grain-size class i at an elevation z in the flow is obtained by dividing the concentration of sediment in class i by the total concentration:

$$F_i(z) = \frac{C_i(z)}{C(z)} \quad (5.4)$$

The fraction of sediment in each grain-size class (F_i) is used to construct the grain-size distribution histogram of the suspended sediment at each height in the flow (Fig. 5.2A). The grain-size distribution histograms are used to determine the 10th, 50th and 90th percentile of the grain-size distribution (D_{10} , D_{50} and D_{90}) at each height in the flow.

| Run | Slope (tangent; degrees) | Initial sediment concentration (% vol.) | Discharge (dm ³ /s) | Duration (s) | Depositional/ Non- depositional | Flow thickness (m) |
|-----|--------------------------------|--|-----------------------------------|-----------------|---------------------------------------|--------------------------|
| 1 | 0.14; 8 | 17% | 3.5 | 115 | Non- depositional | 0.073 |
| 2 | 0.070; 4 | 17% | 3.5 | 115 | Depositional | 0.077 |

Table 5.1: Boundary conditions and flow parameters during the flume experiments.

5.2.2 Experiment procedure

The analytical model is validated by comparing the outcomes to the vertical change in the suspended sediment grain-size distribution of two experimental turbidity currents. The two flows were ran in a rectangular flume tank (Fig. 5.3) with flume-floor slopes of 4° and 8°. Suspended sediment grain size and concentration in the flow were measured using suspension samples that were collected with siphoning tubes at 0.01, 0.02, 0.04 and 0.08 m above the bed. Grain-size analysis of the collected sediment was performed using a laser particle-size analyser (Malvern Mastersizer). The suspended sediment grain size and concentration were thus constrained at four elevations in the flow. Additionally, a velocity profile was measured during each experiment using an ultrasonic velocity probe (*MetFlow UVP duo*). Measurements of flow velocity and suspended sediment were made after the head of the current had passed and when the discharge was constant.

5.2.3 Inputs from experiments for the analytical model

The conditions during the experiments (Table 5.1) are used as inputs for the analytical model. This way we can assess how well the model reproduces the grain-size stratification that has been measured in the flume experiments. The first two inputs required for the model are the grain-size distribution and sediment concentration at some reference level (z_{ref}) in the flow. The lowermost siphoning tube at 0.01 m above the flume floor is chosen as the reference level.

The third input required is the thickness of the flow, which is here obtained from velocity profiles using the integral method of Ellison and Turner, (1959):

$$UH = \int_0^{\infty} u dz \quad (5.5)$$

$$U^2 H = \int_0^{\infty} u^2 dz \quad (5.6)$$

$$U = \frac{U^2 H}{UH} \quad H = \frac{UH}{U} \quad (5.7)$$

where U is the depth-averaged velocity [m/s], H is the thickness of the flow [m] and u is the velocity [m/s] as a function of height above the bed. The fourth input required is the shear velocity of the flow. The shear velocity for both runs are obtained from (Kneller, 2003):

$$u^* = \sqrt{g \frac{\Delta \rho}{\rho} H_{umax} S} \quad (5.8)$$

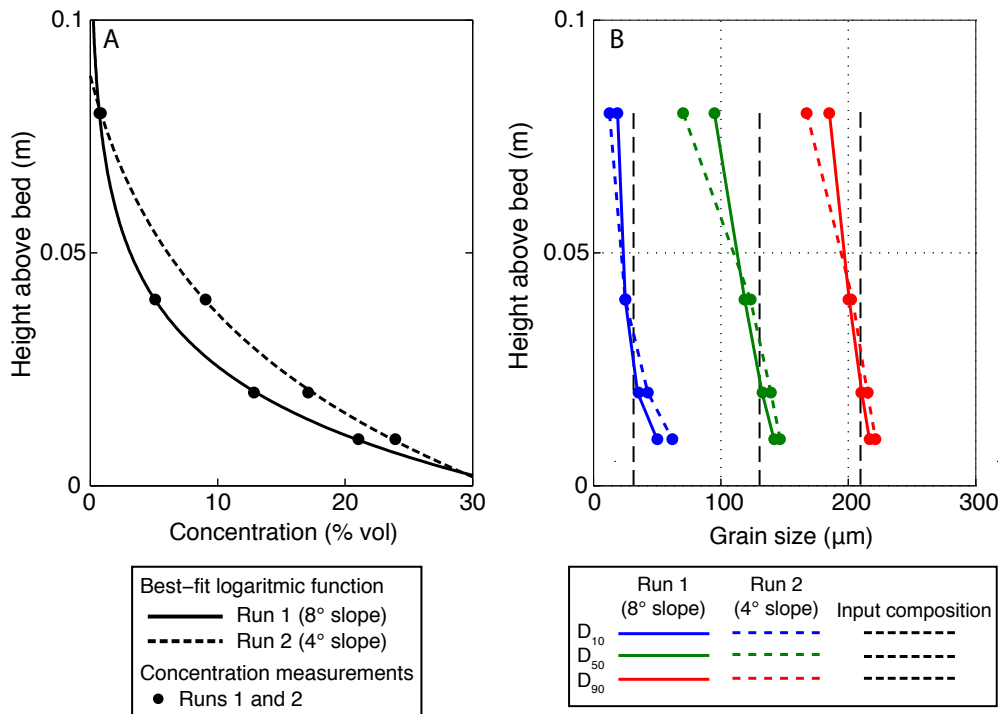


Figure 5.4: (A) Sediment concentration profiles of Run 1 (8° flume-floor slope) and Run 2 (4° flume-floor slope). (B) Grain-size profiles of Run 1 and 2. Note that a steeper flume floor slope is associated with less vertical variation in grain size.

where $\Delta\rho$ is the density difference between the suspension and the ambient fluid of density ρ [kg/m^3]. $\Delta\rho$ is calculated for the depth interval from the bed to the velocity maximum, H_{umax} is the height of the velocity maximum [m], and S is the tangent of the slope [-].

The shear velocity provides one measure for the intensity of turbulent mixing. Another measure for this flow property that is commonly used is the magnitude of velocity fluctuations. Deviations from the time-averaged velocity at each point in time can be calculated as (Eggenhuisen and McCaffrey, 2012):

$$v' = v - \bar{v} \quad (5.9)$$

where v is the instantaneous velocity and \bar{v} is the time-averaged velocity [m/s]. The turbulence intensity can be obtained from a time series of velocity measurements (e.g. Kneller et al., 1999):

$$I = \sqrt{\frac{\sum_{i=1}^N (v'_i)^2}{N}} \quad (5.10)$$

where I is the turbulence intensity [m/s] and N equals the number of data points in the velocity time-series.

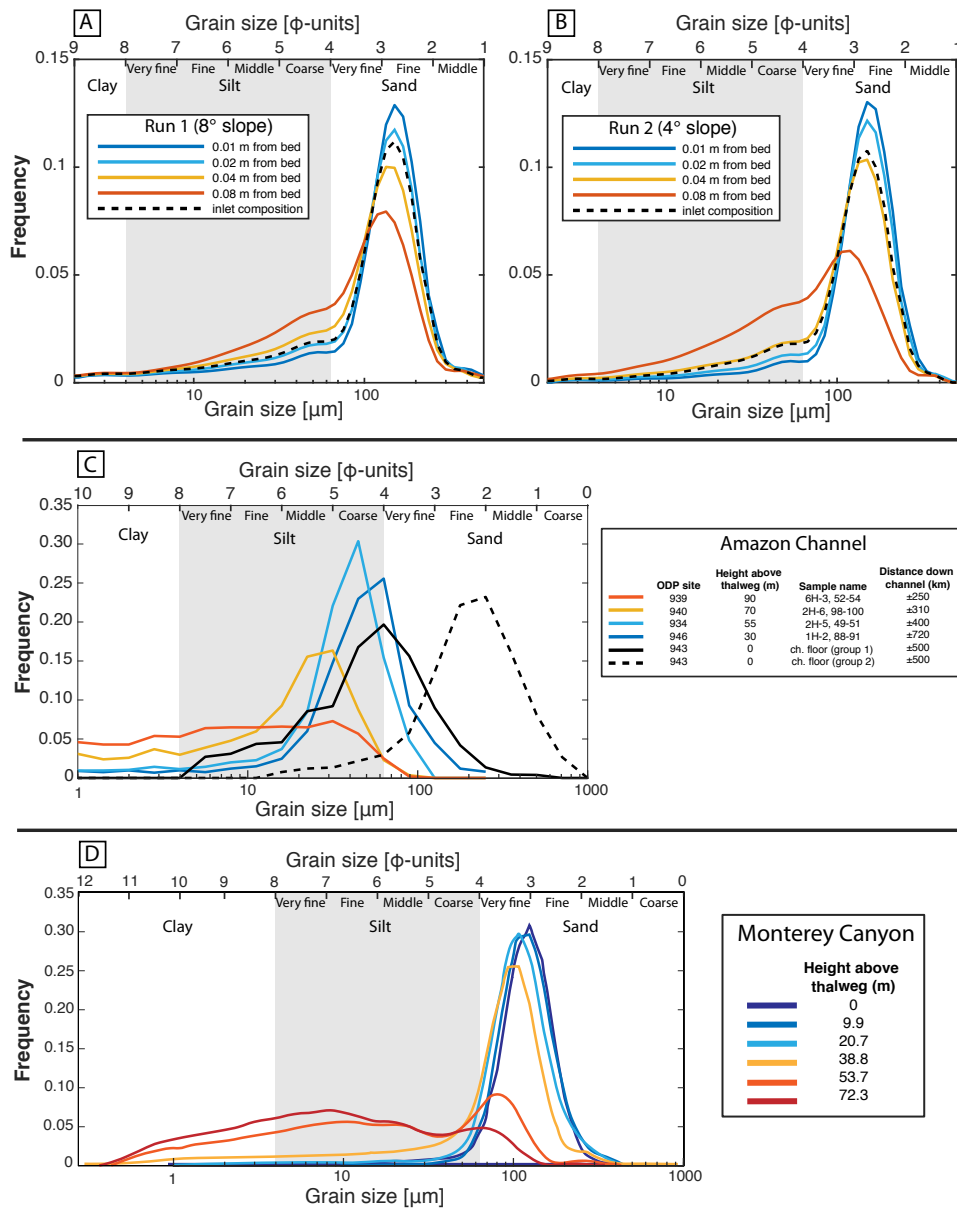


Figure 5.5: (A,B) Grain-size distribution of suspended sediment samples collected with siphon tubes at different elevations above the bed in experimental turbidity currents. (A) Suspended sediment samples from Run 1 (8° slope) (B) Suspension samples collected during Run 2 (4° slope). (C) Grain-size distribution of deposit samples from the Amazon Channel (Hiscott et al., 1997; Manley et al., 1997). (D) Grain-size distribution of deposit samples from the canyon wall of the Monterey Canyon (Symons et al., 2017). Note that the shift in grain-size distribution with height above the thalweg shows a similar pattern in the natural systems and in the experiments.

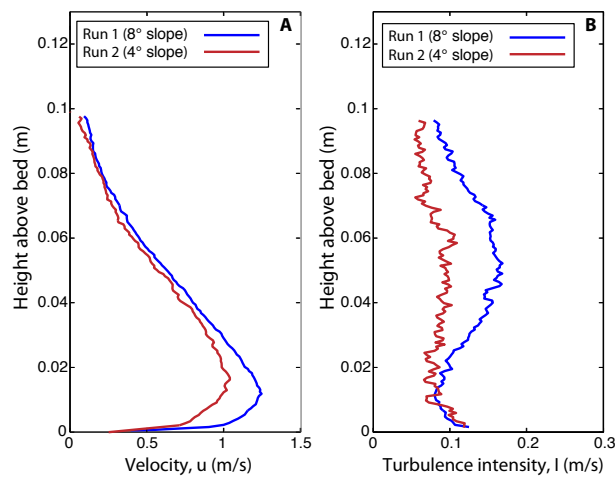


Figure 5.6: (A) Time-averaged velocity profiles of Run 1 and 2 (B) Turbulence-intensity profiles from Runs 1 and 2. Note that the turbidity current on the steeper slope (Run 1) has a higher flow velocity and higher turbulence intensity.

5.3 Results

5.3.1 Flume experiments

Suspension samples

Flow conditions during the two runs are shown in Table 5.1. The turbidity current on the low slope was depositional while the current on the steep slope displayed complete bypass (*sensu* Stevenson et al., 2015). Measurements of flow velocity and suspended sediment were made after the head of the current had passed and the flow was quasi-steady. Both runs have a concave concentration profile (Fig. 5.4A). The high-slope run (Run 1) displays a more rapid upward decrease in concentration than the low-slope run (Run 2). In addition, the grain size decreases upwards in the flow in both runs (Fig. 5.4B). The vertical change in grain size was largest in the low-slope run.

Figure 5.5 (A, B) shows the full grain-size distribution of each of the suspended sediment samples collected with the siphoning tubes. The samples from the lower two siphoning tubes (0.01 and 0.02 m above the bed) are enriched in coarse-grained sediment and depleted in fine-grained sediment relative to the composition of the sediment supplied at the inlet. Contrastingly, the samples from the upper two siphoning tubes (0.04 and 0.08 m above the bed) are enriched in fine sediment and depleted in the coarser sediment compared to the sediment at the input.

Flow velocity and turbulence

Velocity and turbulence intensity profiles are shown in Figure 5.6. Time-averaged velocity profiles (Fig. 5.6A) illustrate that current velocity increases with slope. The velocity maximum of the low-slope run is 1.0 m/s while the velocity maximum of turbidity current in the high-slope run is 1.2 m/s. The turbulence intensity profile (Fig. 5.6B) of the high-slope run displays a turbulence minimum around the velocity maximum similar to observations in previous experimental turbidity current studies (Kneller et al., 1999; Eggenhuisen and McCaffrey, 2012; Cartigny et al., 2013). The

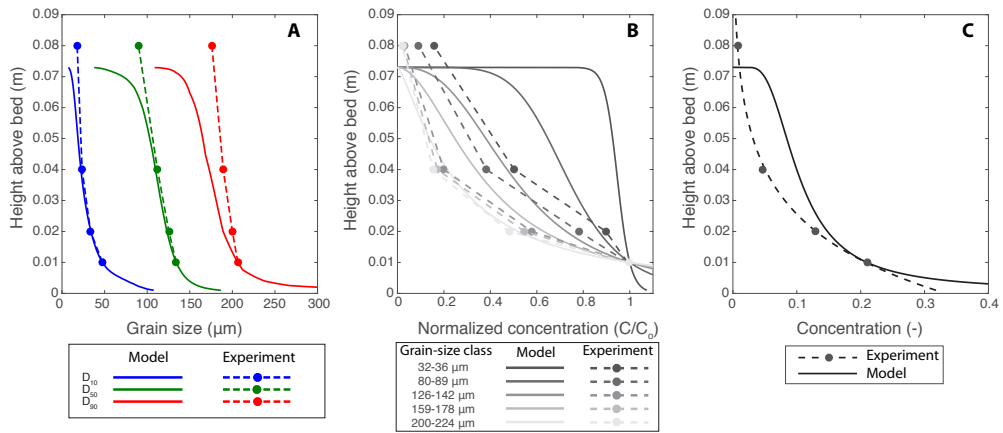


Figure 5.7: Comparison between results from an experiment (Run 1; 8° slope) and the results from the analytical model. (A) D_{10} , D_{50} and D_{90} profiles (B) Normalised concentration profiles by grain-size class.

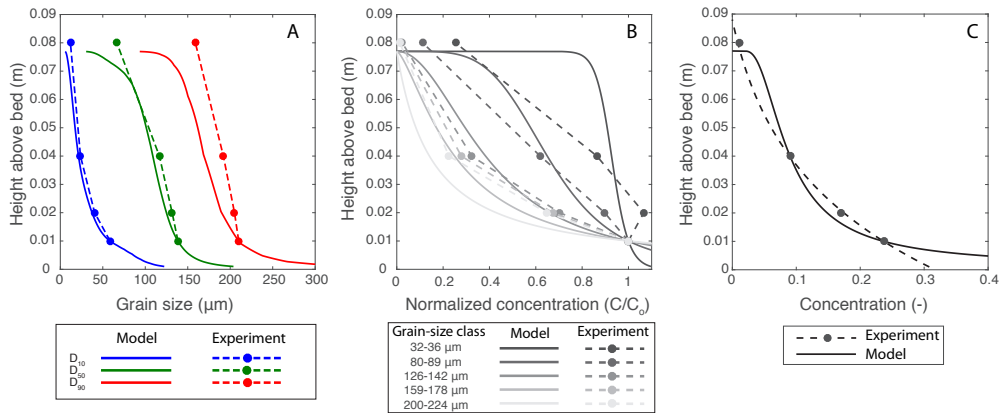


Figure 5.8: Comparison between results from an experiment (Run 2; 4° slope) and the results from the analytical model. (A) D_{10} , D_{50} and D_{90} profiles. (B) Normalised concentration profiles by grain-size class. (C) Concentration profile.

low-slope turbidity current shows little vertical variation in turbulence intensity and has a lower turbulence intensity in general.

5.3.2 Comparison of model results and experiments

Comparison between model and experiments

Figures 5.7 and 5.8 show the experimental and analytical modelling results of the high- and low-slope run, respectively. Grain-size trends (Figs 5.7A, 5.8A) produced by the model are in good agreement with the experiments. Goodness of fit depends on the statistical parameter considered. The gradients of the median grain size (D_{50}) and 10th size percentile (D_{10}) measured

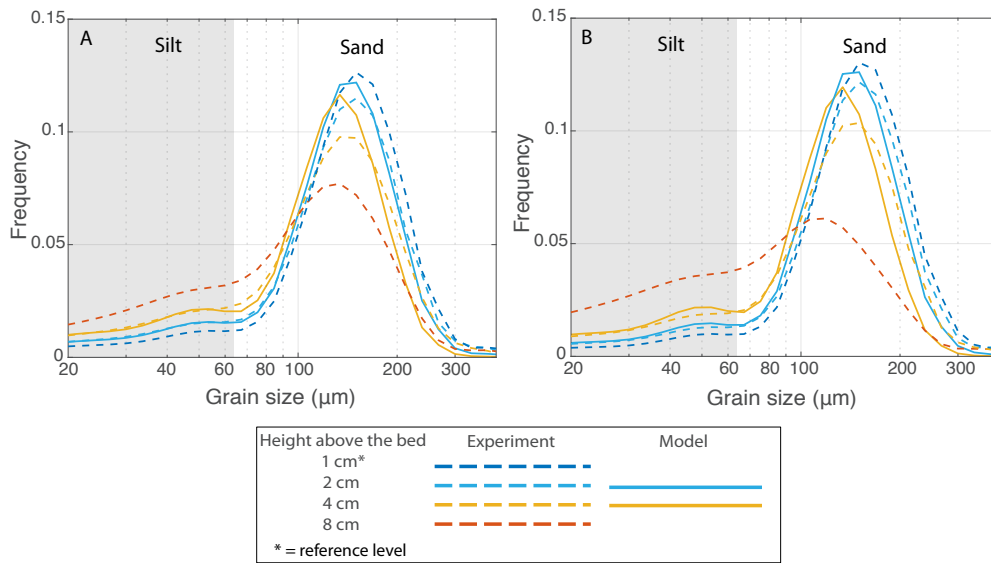


Figure 5.9: Grain-size distribution of the suspended sediment at different elevations in the flow. Comparison between results from experiments and analytical model results. (A) Run 1 (8° slope). (B) Run 2 (4° slope).

in the experiments closely resemble the model results, whereas the model clearly over-predicts the gradient in the 90th size percentile (D_{90}).

Normalised concentration profiles for different sediment grain-size classes are presented in Figures 5.7B and 5.8B. Both model and experiments show that the fine sediment grain-size classes are more uniformly distributed over the height of the flow than the coarse sediment grain-size classes. However, the fit between the model and the experiments is not equally good for the concentration profiles of all grain-size classes. The measured concentration profiles for the coarse sediment grain-size classes (126–142 μm , 159–178 μm , 200–224 μm) are in reasonable agreement with the model. However, the upward decrease of concentration for the finest grain-size class that is plotted (32–36 μm) is severely under predicted by the model. In the high-slope run (Run 1), for example, the model predicts that sediment in the 32–36 μm class is nearly homogeneously distributed over the height of the flow (Fig. 5.7B) while the experimental measurements show a significant upward decrease in concentration.

Concentration profiles produced by the model are also in reasonable agreement with experimental measurements (Figs 5.7C, 5.8C), although some differences occur. The concentration profiles predicted by the model are more concave than the measured concentration profiles. Also the model predicts relatively high concentrations in the upper part of the flow, which is not in agreement with the exponential decay that characterises the measured concentration profile.

Figure 5.9 shows a comparison between the simulated and measured grain-size distributions at different levels in the flows. The general trends are reproduced well by the model: both experiments and the model show that the finer sediment fractions (i.e. below $\pm 100 \mu\text{m}$) become relatively more abundant upwards in the flow, while the coarse sediment becomes relatively less abundant. A precise match between the simulated and measured grain-size distribution curves is not achieved however. The measured grain-size distribution at 0.01 m above the bed serves as a

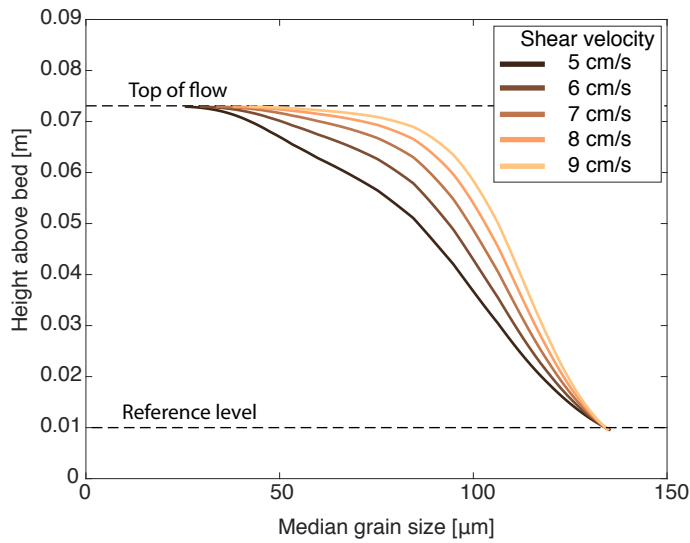


Figure 5.10: Median grain-size gradient predicted by the analytical model for five different shear velocities. Note that the vertical variation in grain size decreases with increasing shear velocity.

reference level for the model and therefore there is necessarily a match between the model and the experiment here. At 0.02 and 0.04 m above the bed, significant differences occur between grain-size distribution predicted by the model and measurements in the experiment. At 0.08 m above the bed, the model predicts no sediment in suspension while the measurements show that sediment is in suspension at this height, albeit the concentration is comparatively low (1% vol. in both runs) (Figs 5.7C, 5.8C).

Effect of shear velocity on grain-size stratification

Both the model results and the experiments show that the grain-size gradient decreases with increasing shear velocity, which is a measure of turbulent mixing. Figure 5.4B shows the median grain-size profiles of the high- and low-slope experiment. The low-slope run with the lower shear velocity (6.4 cm/s) has a larger vertical change in grain size than the high-slope run in which the shear velocity of the turbidity current was higher (8.2 cm/s).

The model runs show a similar relation between shear velocity and grain-size stratification. Repeated model runs with 5 different shear velocities were performed to illustrate the effect of shear velocity on the grain-size gradient. The other boundary conditions (flow thickness, composition at the reference level) during these model runs were equal to the high-slope run (Run 1). Figure 5.10 shows the upward change in simulated median grain size as a function of shear velocity. In analogy with the experiments, the vertical change in grain size decreases with increasing shear velocity.

5.4 Discussion

5.4.1 Origin of similarities and differences between model and experiments

The model and experiments show the same general trends: (1) a gradual decrease in sediment grain size and concentration with height in the flow and (2) an increase in grain-size stratification

with decreasing shear velocity. Thus, a simple turbulent diffusion model is able to quantify the main characteristics of a turbidity current in terms of grain-size and density stratification. However, there are also significant differences between the model and the experimental results. For example, the decrease in D_{90} is overestimated by the model (Figs 5.7A, 5.8A). Furthermore, the concentration profiles predicted by the model are more concave than the concentration profiles measured in the experiments (Figs 5.7C, 5.8C). Multiple factors could have contributed to the deviations between the model results and the experiments.

Firstly, the Rouse equation is valid under a free surface at the top of the flow. Turbidity currents, however, are affected by shear at the top of the flow due to friction with the overlying ambient water. This results in a different vertical distribution of turbulent mixing in turbidity currents compared to open channel flows and this will, in turn, affect the vertical distribution of sediment. We anticipate that the fit between turbidity current experiments and results from analytical or numerical diffusion models will improve when the effects of interaction with ambient water at the top of currents are taken into account.

In addition, shear velocity, which is required as an input for a Rouse-type equation, can be estimated using various methods which all come with significant uncertainties (Kneller, 2003). The uncertainty is particularly large because the methods that is used to estimate shear velocity have not originally been designed with the turbidity current flow structure in mind. Shear velocity serves as a measure for the intensity of turbulent mixing. Measurements of velocity fluctuations in the present experiments (Fig. 5.6B) provide an independent constraint on the intensity of turbulent mixing. These measurements show that the high-slope run with the highest estimated shear velocity indeed has a higher turbulence intensity. These results qualitatively show that shear velocity estimates obtained in this study are indeed a usable proxy for the intensity of turbulent mixing.

Furthermore, entrainment of ambient water at the top of turbidity currents lowers the sediment concentration in the upper part of the flow. The dilution by ambient water has an equal effect on the concentration of all sediment grain sizes that are present in the upper portion of the flow. This may partially explain why even the finest sediment fraction is not homogenized by turbulence in the experimental turbidity currents.

Finally, one of the assumptions behind the Rouse equation is that the sediment distribution in the flow has reached an equilibrium. This assumption may not be valid for the flume experiments because there was only a limited amount of time available between the inlet point and the position where the flow samples were collected. Given a distance of 2.35 m and a depth-averaged flow velocity of ~ 0.7 m/s, the time available for stratification to develop was about 3.5 seconds. This may not have been enough time to establish an equilibrium profile for all grain-size classes. Using an analytical model, Dorrell and Hogg (2012) have shown that the time-scale of response of suspensions to changing flow conditions are grain-size dependent and the response time is longer for smaller grain sizes. Further work is needed to establish whether the concentration profiles in the present experiments represent an equilibrium or transient state.

5.4.2 Controls on grain-size gradient in turbidity currents

Two primary controls on the grain-size gradient of turbidity currents are identified: (1) the grain-size distribution of the sediment supplied at the source and (2) the intensity of turbulent mixing in the flow.

The grain-size distribution of the sediment is important because grain size can only vary vertically in turbidity currents when a range of grain sizes is available. The potential for vertical

variation in grain size is larger when a large range of sizes is suspended. The grain size of the suspended sediment in the present flume experiment ranges from $\sim 19 \mu\text{m}$ (5th percentile) to $\sim 236 \mu\text{m}$ (95th percentile). Theoretically, the median grain size at the base of the flow could be very close to the largest size available in the flow while the median grain size near the top of the flow could be very close to the smallest grain size available in the flow. However, the median grain size at the base of the flow can never be quite as large as the maximum grain size available because sediment of the coarsest grain-size class may be very concentrated at the base of the flow but is still accompanied by sediment of other grain-size classes. The grain-size range available in a system does thus provide a theoretical upper limit on the maximal vertical variation in grain size in turbidity currents. In practice the vertical shift in median grain size will be much smaller. The range of median grain sizes measured in the present experiments ranges from $70 \mu\text{m}$ at 0.08 m above the bed to $146 \mu\text{m}$ at 0.01 m above the bed (in the low-slope experiment), which is a much smaller range than the grain size spectrum available ($19\text{--}236 \mu\text{m}$).

A second control on the grain-size gradient in turbidity currents is the shear velocity which serves as a measure for the intensity of turbulent mixing. Sediment of all sizes will be more homogeneously distributed over the height of the flow when the intensity of turbulent mixing is higher. The vertical variation in median grain size therefore decreases with increasing shear velocity. The present experiments confirm that turbidity currents with a high shear velocity do indeed have less vertical variation in grain size (Fig. 5.4B). Shear velocity changes as a function of slope, flow thickness and flow density (Kneller, 2003). It is therefore anticipated that, for example, a decrease in slope will be associated with flows that are more stratified in terms of grain size and density. The simple model presented here can thus be used to quantify the effect of changes in slope, for example along a channel section, on changes in stratification.

Other factors that are not directly related to the shear velocity may also affect grain-size and density stratification. Bottom roughness can enhance turbulent mixing in turbidity currents and act to mix sediment upwards as was shown with numerical models (Arfaie et al., 2014) and experiments (Eggenhuisen and McCaffrey, 2012). Additionally, bends in submarine channels can increase vertical mixing and thereby decrease stratification (Straub et al., 2011).

5.4.3 Vertical change in grain size distribution in experiments compared to natural systems

The experimental turbidity currents show a gradual change in suspended sediment grain-size distribution upwards in the flow (Fig. 5.5A, B). The coarse sediment fraction becomes gradually less abundant while the fine sediment fraction gradually becomes more abundant with height. Similar direct measurements of suspension composition at multiple elevations above the bed are currently not available for natural turbidity currents. As a substitute, deposit samples from different elevations above the thalweg of a canyon or channel can be used. Grain-size distributions of deposit samples are available for the levees of the Amazon Channel (Fig. 5.5C) (Hiscott et al., 1997; Manley et al., 1997; Pirmez and Imran, 2003) and for the walls of the Monterey Canyon (Fig. 5.5D) (Symons et al., 2017).

Deposits around the Amazon Channel were collected during an ODP cruise (ODP Leg 155). Samples were collected from the channel floor, channel terraces and levee flanks at different distances down channel. Channel relief differed between the locations and samples do thus represent channel overspill from different elevations above the channel thalweg (Hiscott et al., 1997). Figure 5.5C shows one representative grain-size distribution from each core location. Apart from the channel floor samples, the samples are all dominated by silt-sized sediment. The change in grain-size distribution of the Amazon samples shows a pattern that is similar to the

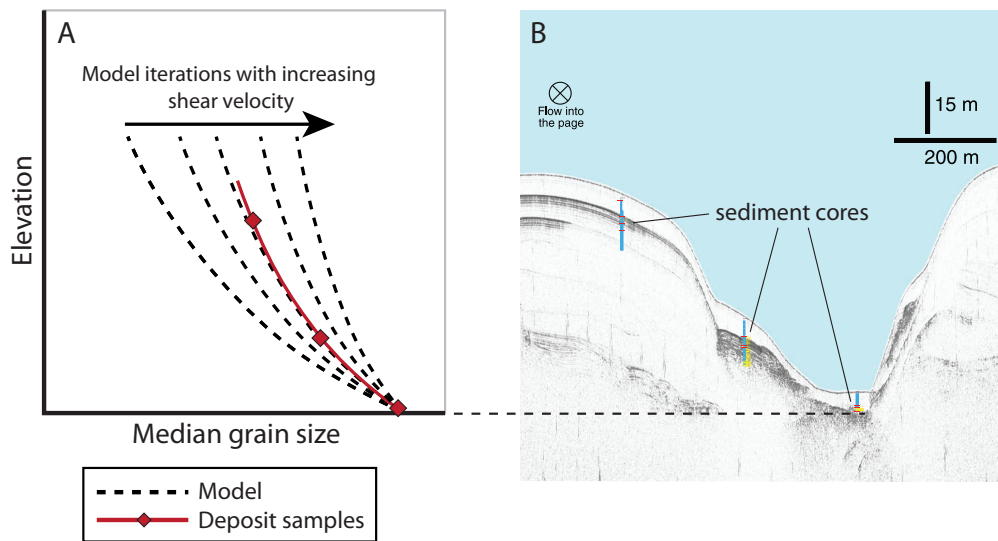


Figure 5.11: (A) Cartoon illustrating the approach that can be followed to reconstruct turbidity current flow properties from deposits. The vertical change in grain size that is obtained from deposit samples is matched with the analytical model by repeating the model with different shear velocities until a match with the grain size gradient from the deposits is obtained. (B) Example of a submarine channel from the Niger Delta slope with sediment cores collected at different elevations above the channel thalweg (Jobe et al., 2017).

experiments (Fig. 5.5A, B). The distribution curves are largely overlapping but the fine sediment fraction becomes relatively more abundant with height above the base of the flow while the coarse sediment fraction becomes relatively less abundant.

Samples in the Monterey Canyon were collected at different heights on the canyon wall and are dominated by sand-sized sediment. Figure 5.5D shows grain-size distribution of each of the cores. Again, a gradual shift towards the finer sediment grain-size classes with height above the thalweg is observed. Thus, the same general pattern of gradually shifting grain-size distribution is observed in experiments and in natural systems. This suggests that the grain-size stratification works in a similar way in experimental turbidity currents and in natural currents which are orders of magnitude larger.

5.4.4 Reconstructing turbidity current flow properties from the rock record

We presented an analytical model that predicts grain-size stratification in turbidity currents and validated this model with experimental data. The experiments and analytical model results demonstrate that grain-size and density gradients in turbidity currents are a function of the turbulent mixing intensity. Jobe et al. (2017) proposed that an important application of stratification modelling can be the prediction of grain size and bed thickness of levee and terrace deposits around submarine channels. This can, for example, be relevant for hydrocarbon reservoir quality prediction in areas where data on the deposit properties are limited. Here we propose an inverse approach that can be used in areas where the characteristics of deposits are well constrained but little is known about the properties of past turbidity currents. A number of issues arise when

channel morphology and deposit facies are used as inputs to reconstruct turbidity current flow properties.

Firstly, in natural field-scale turbidity currents the grain-size profile has never been measured directly and therefore it has to be inferred from the composition of the deposits. One has to assume that the deposits at a certain height above the channel thalweg are representative of the composition of the suspension at the corresponding height. Dennielou et al. (2006), Migeon et al. (2012) and Jobe et al. (2017) worked with this assumption previously. Symons et al. (2017) compared flow samples from a sediment trap with cores from the Canyon walls in the Monterey Canyon and they confirmed that flow and deposit grain size at equivalent height are indeed similar. In addition, in experiments (Chapter 3) it was shown that the grain-size trend in a levee sequence of a submarine channel compares well with grain-size stratification in the turbidity current inside the channel. This also attests to the similarity of deposit and flow grain size at each height above the base of the flow.

Secondly, it is difficult to determine the height of deposit samples above the original base of the flow. Sediment samples from the modern sea floor still have the context of the original channel bathymetry. In such cases the height of levee and terrace deposits above the thalweg is a useful measure of relief at time of deposition. However, there may still be an error because the thalweg of the channel may have aggraded or degraded since the time of deposition (Pirmez and Imran, 2003). Reconstructing the elevation of deposits above the channel thalweg is much more challenging in outcropping channel-levee systems where bounding surfaces related to channels are commonly composite in nature and cannot easily be related to the original morphology (Hubbard et al., 2014).

Finally, the model requires flow conditions as input (flow thickness and shear velocity), and these measurements are only available for a few channel and canyon systems that are presently active such as the Monterey Canyon (Xu et al., 2004; Xu et al., 2013). For inactive systems on the sea floor and systems in the stratigraphic record it is never possible to obtain these measurements. In fact, we set out a workflow by which reconstruction of flow conditions is the objective to be pursued.

Employing the analytical model to reconstruct past flow conditions requires three main steps. First, the vertical change in grain size in the turbidity current needs to be reconstructed from deposit samples. Suitable sets of deposit samples for these reconstructions are already available for several systems on the modern sea floor such as the Amazon Channel (Fig. 5.5C) and the Monterey Canyon (Fig. 5.5D). Second, the thickness of the flow needs to be estimated from the geological record without making use of direct measurements of flow properties. As a first-order approximation it would be reasonable to assume that the flow thickness is comparable to the depth of the channel. Oversized flows, which are much thicker than the channel depth, tend to reduce in size rapidly due to excessive overspill and are therefore unlikely to occur at a large distance downstream of the origin of a submarine channel (Mohrig and Buttle, 2007; Straub et al., 2011; Hodgson et al., 2016; Kane et al., 2016). This leaves the shear velocity as the final unknown. To obtain a value for this parameter the model was run multiple times at different shear velocities. The grain-size gradient predicted by each model realisation is then compared to the grain-size gradient reconstructed from deposit samples (Fig. 5.11). A goodness-of-fit match between the model results and the deposit data indicates the optimal shear velocity and the associated stratification structure of the turbidity current.

Summarising, modelling of grain-size stratification can be used to reconstruct flow properties of past turbidity currents from deposit data. The only input required is the grain-size gradient of

the flow, which can be reconstructed using a minimum of two deposit samples from different levels above the channel or canyon thalweg. Such samples are relatively easily obtained from modern and ancient systems and the approach presented can therefore be widely applied. The results of model will show how sediment of different grain-sizes is distributed vertically in the flow and this result can be used to reconstruct the volume and composition of the sediment transferred through a channel. Such sediment budget reconstructions will have uncertainties that are related to the limitations of the simplified approach set out in this paper.

5.5 Conclusions

We used flume experiments and an analytical model to test the effect of flow conditions on grain-size and density stratification in turbidity currents. Results show that:

- A simple analytical diffusion model can reproduce the general grain-size and density stratification trends in experimental polydisperse turbidity currents.
- Modelling and experiments show that grain-size stratification increases with decreasing shear velocity. The model can be used to quantify the change in stratification due to a change in boundary conditions (e.g. a change in channel slope which results in a change in shear velocity).
- An approach is set out to use the model to reconstruct past flow conditions from deposits. Flow conditions are found by iteration of the model at different shear velocities until a grain-size gradient is found that matches with the grain-size gradient implied from deposits. Due to the simplicity of the model and the small number of inputs required it has the potential to be applied to a large number of channels and canyons both on the modern ocean floor and in the stratigraphic record.

Chapter 6

Reconstructing turbidity current flow properties from submarine channel deposits using stratification modelling; Application to the Gabriela Channel fill, Tres Pasos Formation, Chile

ABSTRACT

Submarine channel-fills and channel-related deposits such as levees and deposits on terraces commonly show a decrease in grain size as a function of height above the channel thalweg. This indicates that the channelised turbidity currents were stratified in terms of grain size. Here, an approach is presented to invert grain-size and density stratification and associated palaeoflow conditions from channel fills in the stratigraphic record. This approach is applied to outcrop data from deep-water deposits from the Tres Pasos Formation in the Magallanes Basin in Chile. The focus is on one channel fill in this formation (the Gabriela Channel), which shows an intra-channel transition from coarse-grained axial fill to finer grained deposits at the elevated channel margins. Previous workers estimated that the relief between channel axis and margin was only a few metres when turbidity currents filled the channel. Grain-size analysis was performed on thin sections of channel-axis and margin deposits. The difference in median grain size between the channel-axis and margin samples was 1-3 ϕ -units and the samples from the two environments form two distinctly different groups, although overlap of the distributions is observed. A diffusion-based model is employed to find a grain-size stratification structure that is consistent with the deposit samples. A match is achieved by iterating the model at different shear velocities. It is concluded that different types of turbidity currents occurred in the channel with shear velocities ranging from 0.8 to 5.8 cm/s. The model prediction for the grain-size stratification is used to reconstruct the sediment transfer through the channel. The bulk sediment transfer appears to be much more silt-rich (16-41% silt) than the axial channel fill (4-5% silt). This result is useful as a predictor for the composition of downstream lobes. The approach has the potential to be applied to many other deep-water systems.

Based on

Reconstructing turbidity current flow properties from submarine channel deposits using stratification modelling; Application to the Gabriela Channel fill, Tres Pasos Formation, Chile. By: Jan de Leeuw, Joris T. Eggenhuisen, Yvonne T. Spychala, Florian Pohl, *in preparation*.

6.1 Introduction

Turbidity currents are typically laden with a mix of clay, silt and sand (Garcia, 1994; Hiscott et al., 1997). Each sediment grain size class has its own concentration profile (Garcia, 1994). Coarse sediment is concentrated near the base of the current while fine sediment fractions are more homogeneously distributed. These differences in vertical distribution between the sediment grain-size classes control the volume of each grain size that can be transferred downstream through channels. Quantifying the sediment transfer in submarine channels, including the relative volumes of clay, silt and sand, is an important aim in deep-water sedimentology.

A gradual decrease in deposit grain size with height above the thalweg has been observed in numerous submarine channels and canyons on the modern ocean floor (Pirmez and Imran, 2003; Dennielou et al., 2006; Migeon et al., 2012; Jobe et al., 2017; Symons et al., 2017). Similar observations can be made in submarine channels from outcrop. Hubbard et al. (2014) studied the Gabriela Channel of the Tres Pasos Formation in Chile and noted that: “Turbidity-current stratification is implied from the rapid, lateral intrachannel transition from sand-sized to finer-grained facies despite a limited amount of interpreted relief on the channel base between the axis and margin”. Potentially, the stratification implied from the deposits can be used to quantify the turbidity current density and grain-size stratification as well as flow parameters such as the shear velocity, which is a measure of the intensity of turbulent mixing. This would shed light on the characteristics of currents that shaped ancient submarine channels and on the volume of sediment that was transported through these channels. Hiscott et al. (1997) made a preliminary attempt to relate stratification implied from deposits to flow properties. For the Amazon Channel they documented that sediment with a diameter of $\sim 250 \mu\text{m}$ (2ϕ -units) is present on the channel floor but absent on a terrace at 55 m above the channel thalweg. This implies that sediment with a diameter of 2ϕ -units and coarser was only suspended in the lower part of the flow and this is consistent with the stratification produced at a shear velocity of $\sim 7 \text{ cm/s}$. A first-order estimate of the shear velocity was thus obtained from the maximum grain size that occurs in the higher portion of the flow. Recently, Jobe et al. (2017) used a core data set from a submarine channel on the Niger Delta slope to reconstruct the change in bed thickness and grain size with height above the channel thalweg. A simple numerical model was used to predict the change in bed thickness and grain size under realistic flow conditions, and model results show a good match with field data.

However, it has not previously been attempted to invert flow structure and turbulent mixing from exhumed submarine channel deposits. A key difference between channels on the modern sea floor and channel fills in the stratigraphic record is that in the former the bathymetry is observable, while in the latter the bathymetry has to be reconstructed from compound stratigraphic surfaces (Hubbard et al., 2014; Hodgson et al., 2016). Stratigraphic surfaces are often diachronous and do not represent the landscape at any point in time (Strong and Paola, 2008). This poses a major challenge as it is therefore hard to constrain what the vertical position of different components of a channel fill was with respect to the thalweg at the time of deposition. One notable exception is an outcrop study of Hubbard et al. (2014) in which a detailed reconstruction of the morphological evolution of a channel was made based on outcrop data. The study focussed on a channel fill contained in the Tres Pasos Formation in Chile, named the Gabriela Channel. The authors inferred from the outcrop architecture that sea-floor relief between the channel axis and margin was of the order of 3-6 metres and thereby much smaller than the thickness of the channel fill ($\sim 25 \text{ m}$).

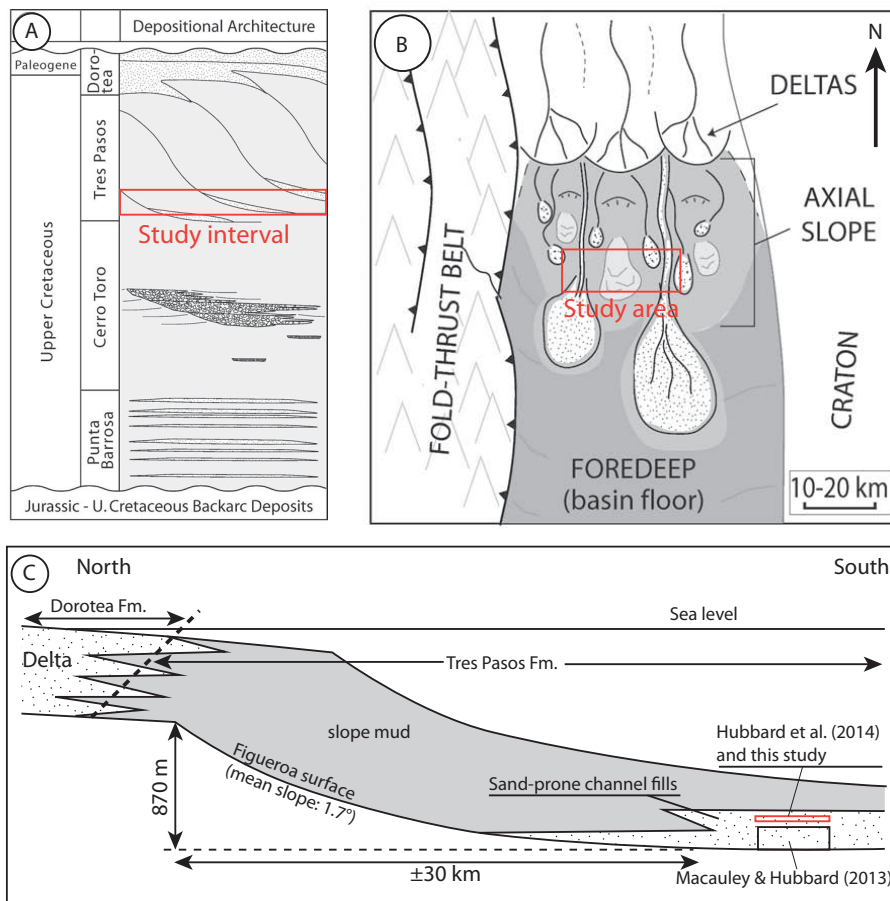


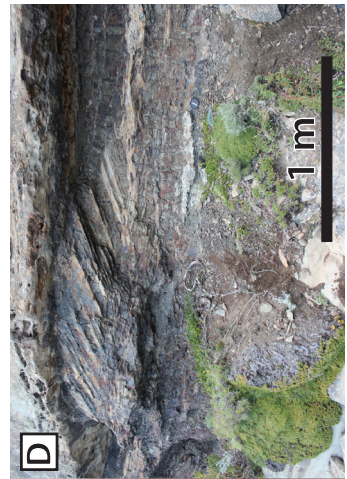
Figure 6.1: Overview of the study area. (A) Stratigraphy of the Magallanes Basin infill. This study focusses on the lower slope deposits of the Tres Pasos Formation. (B) Palaeogeography during the deposition of the Tres Pasos Formation. (C) Location of the Gabriela Channel fill within the context of the Tres Pasos Formation basin fill. Note that most sand accumulated on the lower slope and basin floor. Figure adapted from Hubbard et al. (2010).

This study aims to reconstruct turbidity currents in the Gabriela Channel using the interpreted sea-floor morphology of Hubbard et al. (2014) as a framework. The objectives of this study are to: (1) determine the difference in grain-size distribution between channel-axis and channel-margin deposits using thin-section analysis; (2) to find the range of shear velocities and associated grain-size stratification structures that conform with the stratification that is implied from the deposits; and (3) to estimate the grain-size distribution of the sediment that has bypassed through the studied channel cross-section to the basin-floor.

Amalgamated sandstone (AS facies)



Chaotic mudstone (CM facies)



Thinly interbedded sand-mud (thinIB facies)



Thick interbedded sand-mud (thickIB facies)



Figure 6.2: Facies observed in the outcrop belt. The amalgamated sandstone facies (AS-facies) is characterised by: (A) Continuous successions of sandstone that are up to 25 m thick, (B) occasional occurrence of dish structures and (C) mud clasts that occur both in isolations and in bands. The chaotic mudstone facies (CM-facies) is characterised by: (D) transported blocks, (E) injections of sand between mudstone and (F) intense bioturbation. The mud-prone interbedded facies (MPI-facies) association is characterised by: (G) 1–20 cm thick beds of fine to very fine sandstone alternated with mudstone and (H,I) parallel and cross-lamination in the sandstone beds. The sand-prone interbedded facies (SPI-facies) is characterised by: (J) fine to middle-sandstone alternated with mudstone that makes up less than 20% of the succession, (K) interbedded mud that has been locally eroded and (L) Load structures.

6.2 Description of the Gabriela Channel outcrop

6.2.1 Geological setting

The Magallanes Basin has been interpreted as a retroarc foreland basin (Macellari et al., 1989; Hubbard et al., 2010; Romans et al., 2011). The basin is filled with Cretaceous deep-water deposits and Late Cretaceous to Paleogene deltaic deposits. This study focusses on the Tres Pasos Formation, which is the youngest deep-water formation in the basin (Fig. 6.1A). During the time of its formation, sediment was sourced from the north and was transported southwards along the basin axis (Fig. 6.1B). The clinoform relief from the shelf edge to the basin floor was estimated at 700-900 m and the slope gradient at 1.5-2 degrees (Hubbard et al., 2010). The Figueroa Surface defines one of the clinoforms within the Tres Pasos Formation and the estimated uncompacted palaeorelief along this surface is 870 m (Fig. 6.1C). Directly overlying this surface, around the base of the slope, is a 300 m thick sequence of sand-prone channel fills. Macauley and Hubbard (2013) studied the lower 170 metres of this succession and identified at least 18 channel fills. Each of the channels had a similar SSW orientation and a low sinuosity (1.01-1.1). Thickness of these channel elements varies between 6-15 m and their width is approximately 300 m. Hubbard et al. (2014) focussed on a single channel from the upper part of the 300 m thick succession of channel fills, the Gabriela Channel. This channel element is unique due to its three-dimensional exposures that allow for a detailed interpretation of its stratigraphic evolution.

6.2.2 Facies descriptions

The sedimentological facies of the Tres Pasos Formation has been described in detail by several authors (Hubbard et al., 2010; Macauley and Hubbard, 2013; Hubbard et al., 2014). Here, brief descriptions of the facies in the Gabriela Channel fill are provided:

Amalgamated sandstone facies (AS-facies)

This facies consists of thick-bedded (0.2-5 m) fine- to medium-grained sandstone which is mostly structureless. Beds are amalgamated and form intervals up to 25 m thick (Fig. 6.2A). Some bed interfaces may go unnoticed due to lack of grain-size contrast. Sedimentary structures are occasionally observed near bed tops and include parallel and cross-lamination. Dish structures (Fig. 6.2B) and dispersed mudstone clasts (Fig. 6.2C) are also observed in some beds. Some beds are rich in mudstone clasts at their base.

The structureless sandstones are interpreted as deposits from high-density turbidity currents (Arnott and Hand, 1989; Kneller and Branney, 1995; Leclair and Arnott, 2005; Talling et al., 2012; Cartigny et al., 2013). The laminated bed tops represent the less energetic tails of these currents. Amalgamation surfaces and mudstone clasts indicate that the flows were able to rework the substrate.

Chaotic mudstone facies (CM-facies)

This facies is characterised by mudstone and sandy mudstone interbedded with discontinuous thin-beds (<10 cm) of fine- to coarse-grained sandstone (Fig. 6.2D). Numerous internal scour surfaces are present. Locally, the deposits are highly injected by sandstone (Fig. 6.2E). Bioturbation is moderate to intense (Fig. 6.2F).

The presence of scour surfaces and the injected sand indicate the bypass of energetic flows (Stevenson et al., 2015). Bioturbation indicates prolonged exposure at the sea bed.

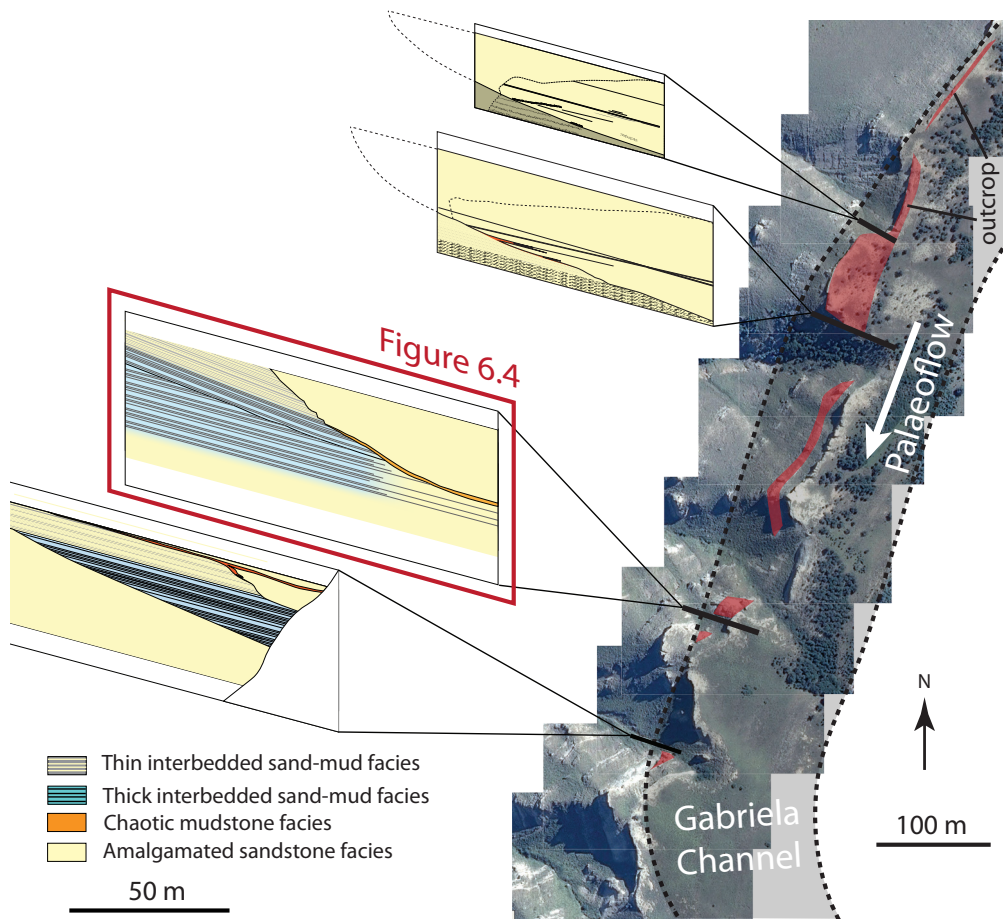


Figure 6.3: Outcrop belt of the Gabriela Channel. The channel makes a slight bend and crops out over a length of ~1.5 km. Four hillslope gullies provide cross-sectional exposure of the Gabriela Channel. The panel in the red box is shown in more detail in Figure 6.5. Figure adapted from Hubbard et al. (2014).

Thinly interbedded facies (thinIB-facies)

Fine- to very fine-grained sandstone beds (1-20 cm thick) are intercalated with mudstone (Fig. 6.2G). Sedimentary structures are abundant and include planar and cross-lamination (Fig. 6.2H, I). Mudstones and sandstones have similar thicknesses and form similar proportions of the succession. Bioturbation is observed in some beds.

The sandstones are interpreted as deposits from low-density turbidity currents (Talling et al., 2012). Planar and cross-lamination were produced by reworking of the sediment through dilute flows along the bed (Allen, 1982; Southard, 1991; Best and Bridge, 1992). Mudstones were deposited by turbidity current tails.

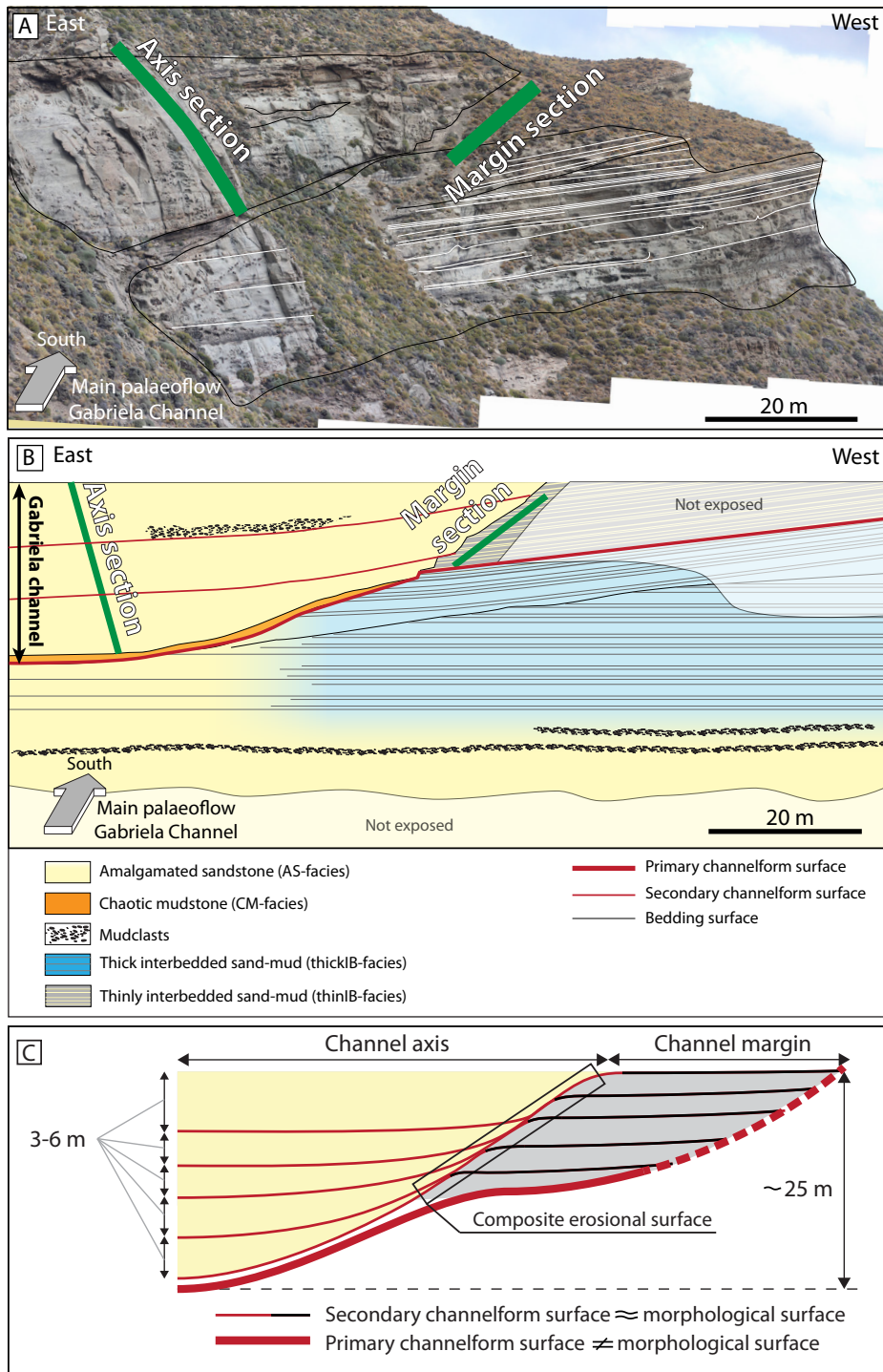


Figure 6.4 (previous page): Cross-section of the Gabriela Channel in one of the slope gullies. Location of the outcrop is shown in Figure 6.3. (A) Photograph with locations of the sample intervals. (B) Panel showing the distribution of sedimentary facies. (C) Schematic representation of the Gabriela Channel fill. Note that multiple secondary channelform surfaces coalesce to form a composite erosional surface.

Thick interbedded facies (thickIB-facies)

Fine- to medium-grained sandstone beds with a thickness of 2 to 100 cm alternated with mudstones that are relatively thinner (1-5 cm thick; Fig. 6.2J). Most beds are dominantly structureless and have planar laminated tops. Some of the interbedded mudstones are discontinuous due to erosion (Fig. 6.2K). Load structures occur at the base of some sandstone beds (Fig. 6.2L).

6.2.3 Architecture of Gabriela Channel outcrop

In the study area near Laguna Figueroa, the Gabriela Channel fill is exposed over a distance of ~1.5 km. The channel makes a slight bend towards the east along the outcrop belt and this leads to variable exposure of the western margin and the centre of the channel (Fig. 6.3). In this study, the focus is on a cross-sectional channel exposure in one of the hillslope gullies (Fig. 6.4).

The primary channelform surface that defines the base and the margins of the Gabriela Channel fill has a relief of ~25 m (Hubbard et al., 2014). In the centre of the channel this surface is overlain by a layer of chaotic mudstone (CM-facies) that is up to 1 m thick (Fig. 6.4B). The channel fill consists of amalgamated sandstone (AS-facies) and thinly interbedded sand and mud (thinIB-facies). The amalgamated sandstone is interpreted as the result of deposition in the channel axis/thalweg whereas the thin interbedded sandstone and mudstone is interpreted as deposits that formed on elevated terraces on the channel margin. An erosional contact separates the two different facies. This erosional surface is interpreted to be composite in nature and formed during multiple stages of cutting and filling of the channel (Fig. 6.4C). Each of the phases of channel cutting created relief on internal channelform surfaces. Hubbard et al. (2014) refer to these internal surfaces as *secondary channelform surfaces* and estimate that the erosional relief on these surfaces is 3-6 m. The authors also suggest that these secondary channelform surfaces represent the morphology of the channel conduit as it was present on the palaeo-seafloor during the channel-filling stage. This implies that a vertical offset of 3-6 m between the channel axis and margin was sufficient to form deposits with distinctively different facies.

6.3 Grain-size distribution of channel axis and margin samples

6.3.1 Methodology: sample collection and thin section grain-size analysis

Two sections with turbidite sandstones were selected for sampling. The location of these sections is shown in Figure 6.4. One section contained thick-bedded (>1 m) sandstones (AS-facies), interpreted as channel axis deposits, and the other section contains thin-bedded (<30 cm) sandstones alternating with mudstones (thinIB-facies) that was interpreted as channel margin deposits (Fig. 6.4). The amalgamated sandstone beds were sampled at three positions: 20 cm above their base, in the middle of the bed, and 20 cm below the bed top. The thin-bedded sandstones were sampled in the middle of the beds. Samples were collected using a geological hammer. Strike and dip were indicated on a smooth surface of the sample. Thin sections were cut perpendicular to the bedding and parallel to the mean local palaeoflow direction of 200° (SSE). The oriented thin sections were photographed under a Leica optical microscope that automatically stitched

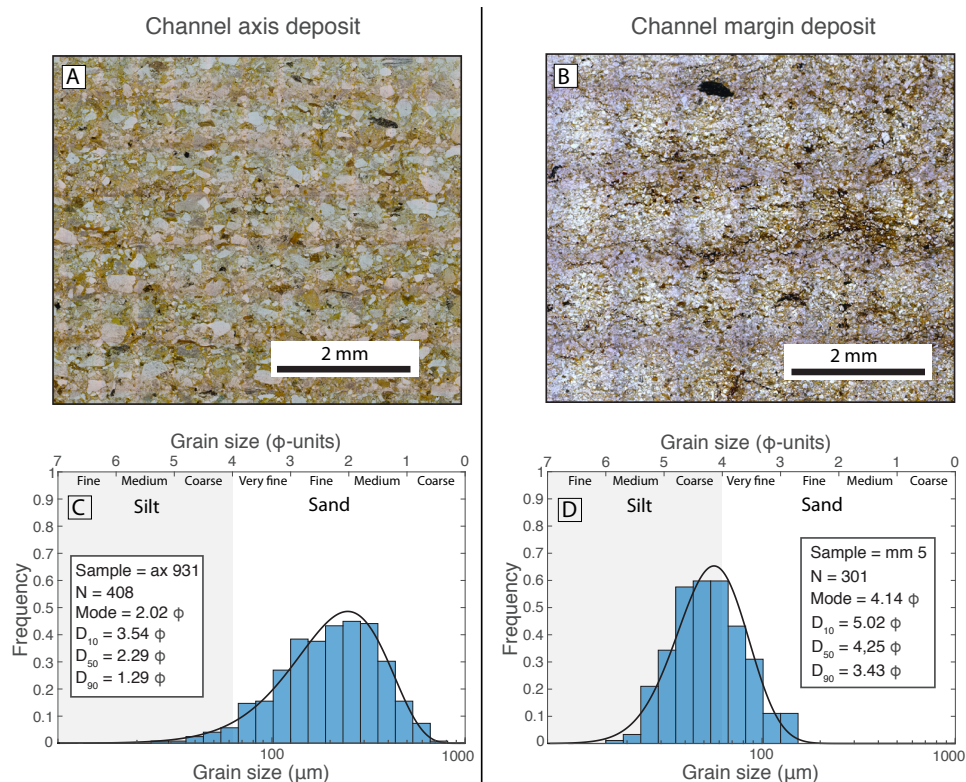


Figure 6.5: Thin-section images of a channel-axis sample (A) and a channel-margin sample (B). (C,D) Grain-size distributions are determined from these thin sections. A gamma distribution is fitted to the data.

the individual images to make a high-resolution image of the entire thin section. The result is an image that covers an area of at least 1.5x2 cm and has a resolution of 1.841 μm per pixel (examples are shown in Fig. 6.5A, B). A grid with a regular spacing was added as an overlay to the image. The image was then loaded in the image processing software ImageJ. A standard grid counting technique was used (see Sylvester and Lowe, 2004) where only the grains that coincided with regularly spaced points from the grid overlay were measured. The outline of each grain was selected manually. Using the outlines, the software determined the dimensions (length of long axis and short axis) and orientation of the long axis. The number of measured grains was at least 300 per thin section. The smallest grain size that could be reliably measured with the present method is 20 μm (medium silt). This lower limit is a consequence of the resolution of the thin section image and the thickness of the thin section (30 μm). Grains with a diameter much smaller than the thin-section thickness are difficult to identify. Sylvester & Lowe (2004) also quote 20 μm as the smallest grain size that can still be measured in thin section with an optical microscope. Further steps are needed to convert the long and short axes measured in the thin sections into the true nominal diameter of each grain. The diameter of a grain is underestimated in a thin section in most cases because the grain is rarely cut through its centre (Johnson, 1994). The following equation (Johnson, 1994) was used to correct for this sectioning effect and obtain the true nominal diameter:

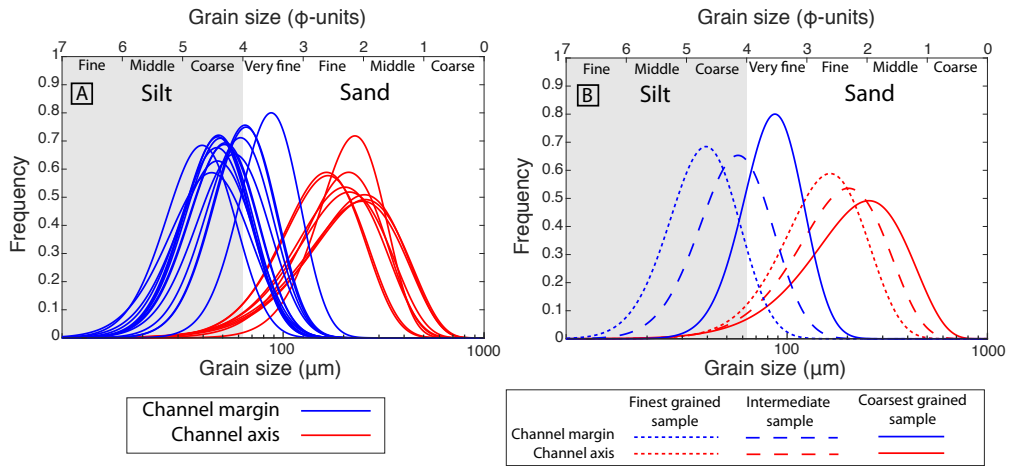


Figure 6.6: (A) Grain-size distribution of all sediment samples from the channel axis and margin. (B) Three samples were selected from the channel-axis and margin samples: the coarsest grained sample, a representative intermediate sample and the finest grained sample.

$$D_{mm} = d'_{mm} + 0.4(a'_{mm} - d'_{mm})^2 \quad (6.1),$$

where d' is equal to $(a'b')^{1/2}$, and a' and b' are the measured long and short axis of the grain. The size obtained for each grain is converted to the ϕ -scale (*sensu* Krumbein and Sloss, 1963):

$$\phi = -\log_2 \frac{D}{D_0} \quad (6.2),$$

where D_0 is a reference diameter of 1 mm and D is the diameter of the particle in mm.

The next step is the conversion of individual grain measurements to a full grain-size distribution. Grain dimensions have been measured at regularly spaced sampling points in each thin section. In this case the number frequency of each grain size is equivalent to the volume percentage of the grain size in the sample volume (Johnson, 1994). Finally, a histogram of the grain-size distribution is plotted (Fig. 6.5C, D) and a gamma probability distribution is fitted to the histogram. This distribution function is chosen because it accommodates for the skewness of the histograms. The plotted gamma probability density function is scaled such that the total area under the curve is equal to 1, so that the distributions from samples with different sample sizes can be compared.

6.3.2 Results: grain-size distribution of channel axis and margin deposits

Figure 6.6A shows the grain-size distributions of the 9 channel axis samples and 13 channel-margin samples that were analysed. Grain-size analysis shows that the channel axis samples are consistently coarser than the channel-margin samples (Fig. 6.6A). Modal grain size of the channel axis samples is 1-3 ϕ -units coarser than the margin samples. Thin section images from a representative channel-axis sample (Fig. 6.5A) and a channel margin sample (Fig. 6.5B) illustrate the difference in texture between these types of samples. Despite the distinctly different grain-size distributions of the channel-axis and margin samples, there still is a significant overlap between

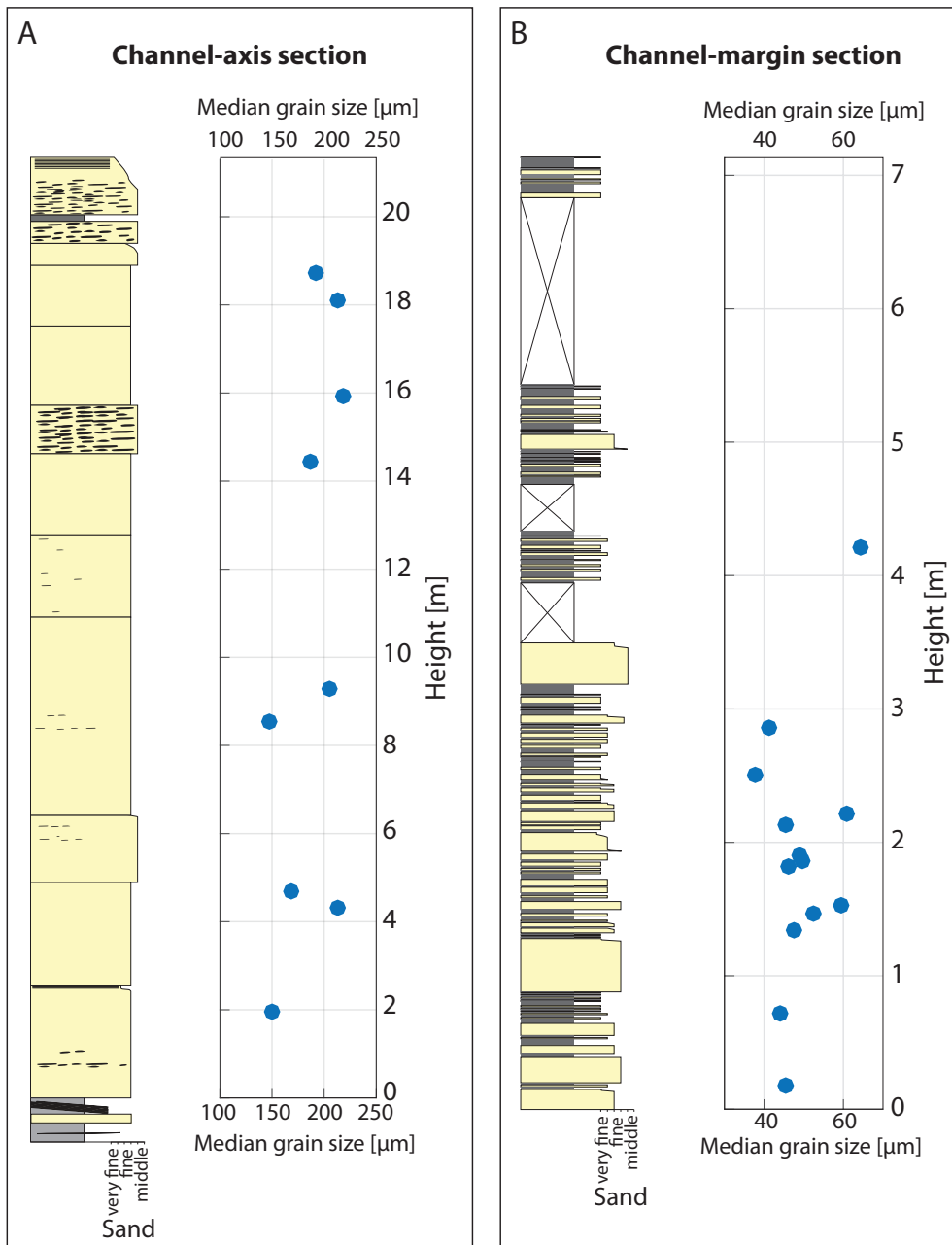


Figure 6.7: Sedimentary sections from the channel axis (A) and margin (B) with median grain size of each of the sediment samples. Note that the grain size of the sediment samples does not vary systematically with height in either of the sections. Locations of the sections are shown in Figure 6.4.

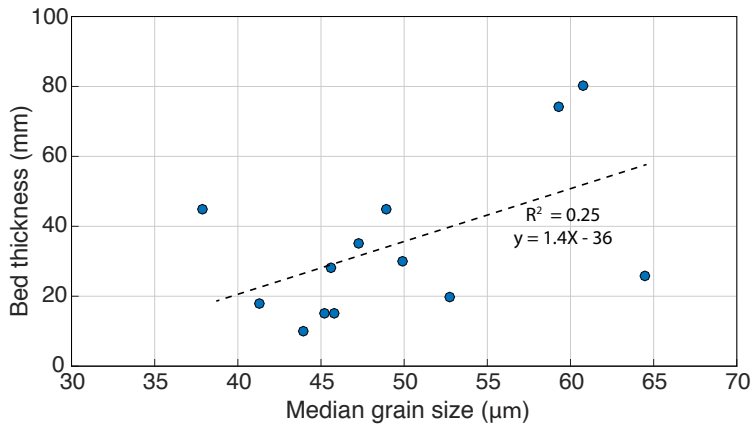


Figure 6.8: Median grain size of sediment samples from the channel margin section (Fig. 6.7B) plotted against bed thickness. A weak correlation ($R^2 = 0.25$) between bed thickness and grain size is found.

the distribution curves. Sediment with a size of 5-2 ϕ -units (coarse silt- upper-fine sand) is abundantly present in most of the channel axis as well as margin samples. Sediment with a size between 2-0.5 ϕ -units (middle to coarse sand) is almost exclusively present in the channel-axis samples. Channel-axis samples are relatively more poorly sorted than the channel margin samples as indicated by a wider distribution curve with a lower peak.

The grain size of the samples does not change systematically with position in the sedimentary sections (Fig. 6.7). In fact, the variation seems to be random, although a higher sampling density may be needed to identify any cyclical variation in grain size throughout the sections. Grain size of the channel-margin beds is weakly correlated ($R^2 = 0.25$) with bed thickness (Fig. 6.8), where thicker beds are coarser grained.

6.4 Modelling of grain-size stratification

6.4.1 Model approach

A model based on the Rouse Equation (Rouse, 1937) is used to predict the relative vertical change in concentration of every sediment-grain-size class. The model is described in detail in Chapter 5. A validation of the model with experimental results is also presented there.

The inputs required for the model are: (1) flow thickness, (2) grain-size distribution at a reference level and (3) the shear velocity of the flow. A first-order estimate of flow thickness is derived from the depth of the channel by assuming that channel depth and flow thickness were equal. The grain-size distribution of a sample from the channel axis/thalweg is used as a reference for the suspended sediment grain-size distribution at the base of the flow. Thus, it is assumed that no segregation took place during sediment deposition and that all grain sizes are transferred equally from the base of the flow to the deposit. This assumption is valid for capacity-driven deposition from suspension (Hiscott, 1994). It is assumed that the suspension composition is constant from the channel thalweg to 5% of the flow depth because the type of modelling presented here necessitates a reference level above the bed. A reference level at 5% of the flow depth is a standard value in this type of modelling (Altinakar et al., 1996; Garcia, 2008; Bolla Pittaluga and Imran, 2014). The shear velocity of the flow is not constrained *a priori*. Instead, a

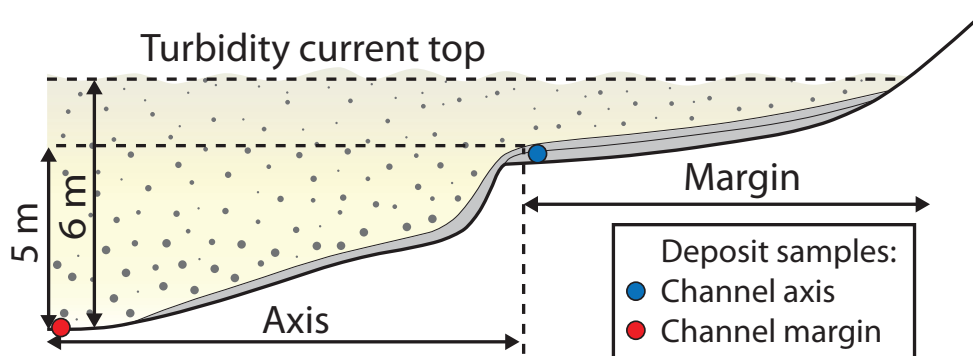


Figure 6.9: Channel geometry and flow thickness used in the model application. The relief between the channel thalweg and margin is set at 5 metres. The flow thickness is 6 metres and the flow structure is laterally uniform. Figure adapted from Hubbard et al. (2014).

| | | Channel axis samples | | |
|------------------------|-------------------------|-----------------------|---------------------|-------------------------|
| | | Finest grained sample | Intermediate sample | Coarsest grained sample |
| Channel margin samples | Finest grained sample | Run 1 | Run 2 | Run 3 |
| | Intermediate sample | Run 4 | Run 5 | Run 6 |
| | Coarsest grained sample | Run 7 | Run 8 | Run 9 |

Table 6.1: Sediment samples used as inputs for different model runs. Grain-size distributions of these samples are shown in Figure 6.6B.

shear velocity estimate is obtained by iteration of the model with different shear velocities until the vertical change in grain size that is reconstructed from the deposits matches with the results of the model. The grain-size distributions of the channel margin sample and the suspension grain-size distribution at the equivalent level in the flow are considered to match when the distributions have the same mode.

6.4.2 Interpreted channel morphology and flow thickness

Channel morphology and flow thickness cannot be observed directly in outcrop, yet estimates of these parameters are needed as model inputs. The interpreted relief between the channel axis and margin during the channel filling stage was only a fraction of the stratigraphic thickness (~25 m) of the channel element (Hubbard et al., 2014). Secondary channelform surfaces with an erosional relief of 3–6 m are interpreted to be more similar to morphological surfaces by these authors. Therefore, we choose a representative value of 5 m for the axis-margin relief (Fig. 6.9). Flow thickness must be larger than the axis-margin relief to allow for any deposition on the channel margin. The flow thickness is therefore set at 6 m in the model. Neither the axis-margin relief

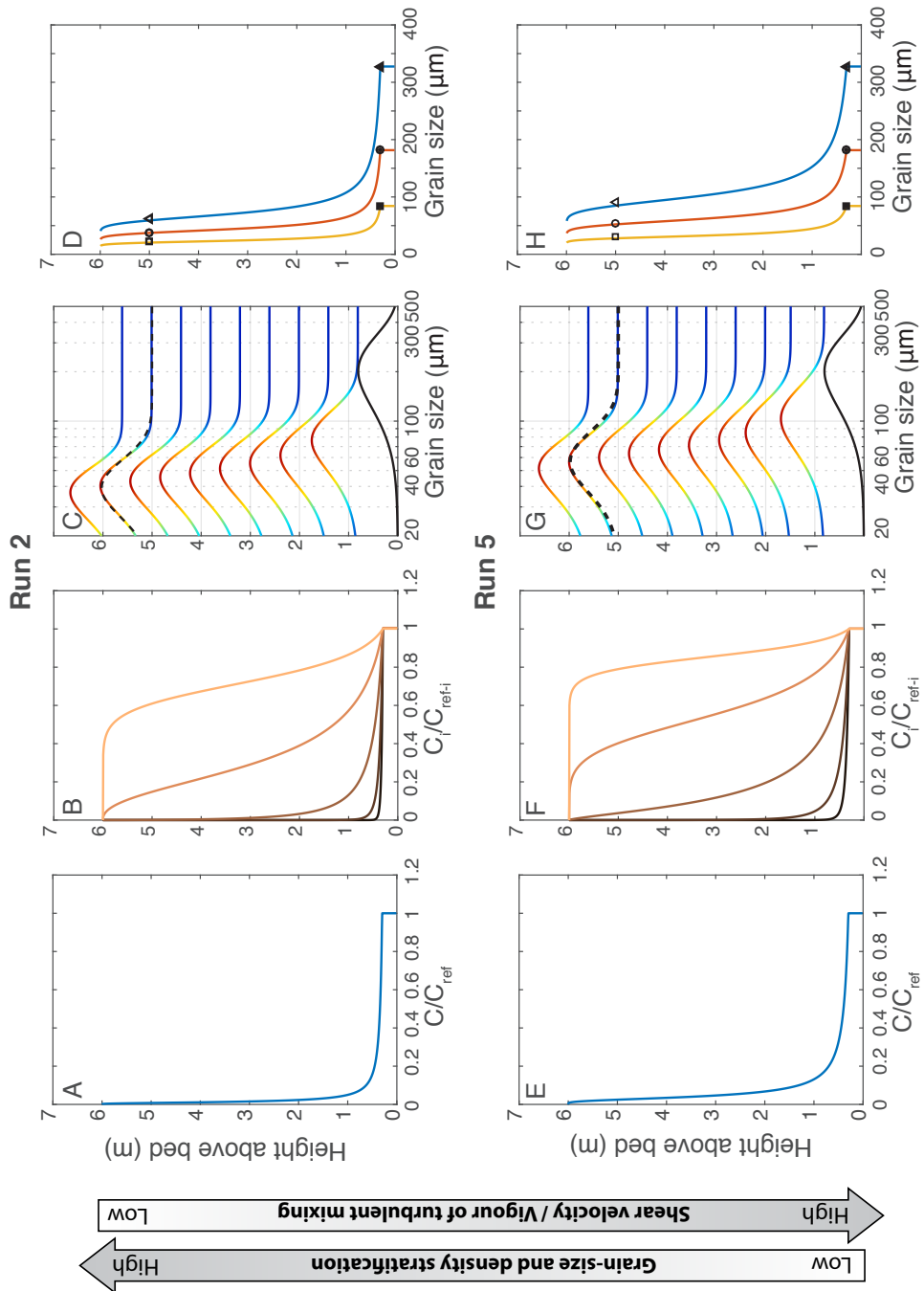
| | | Channel axis samples | | |
|------------------------|-------------------------|---|---|---|
| | | Coarsest grained sample | Intermediate sample | Finest grained sample |
| Channel margin samples | Finest grained sample | Run 1 $u^*=0.8$ cm/s ($u^*/W_s=0.3$) | Run 2 $u^*=1.0$ cm/s ($u^*/W_s=0.5$) | Run 3 $u^*=1.1$ cm/s ($u^*/W_s=0.73$) |
| | Intermediate sample | Run 4 $u^*=1.8$ cm/s ($u^*/W_s=0.67$) | Run 5 $u^*=2.1$ cm/s ($u^*/W_s=1.05$) | Run 6 $u^*=2.3$ cm/s ($u^*/W_s=1.53$) |
| | Coarsest grained sample | Run 7 $u^*=5.3$ cm/s ($u^*/W_s=2.0$) | Run 8 $u^*=5.4$ cm/s ($u^*/W_s=2.7$) | Run 9 $u^*=5.8$ cm/s ($u^*/W_s=3.8$) |

Table 6.2: Shear velocity estimates obtained with grain-size stratification modelling. u^*/W_s ratios based on the median grain size of the axis deposits are indicated between brackets. Modelling results of Runs 2, 5 and 8 (in the grey box) are presented in detail in Figure 6.10.

nor the flow thickness are constrained very precisely. Should the current be thicker or the relief between the channel axis and margin be smaller, then the channel margin would be located in a relatively lower level of the flow. This would mean that the flow is more stratified in grain size because the change in grain size between the channel axis and the channel margin occurs over a smaller portion of current. A more stratified flow would, in turn, yield a lower shear velocity as a modelling result.

6.4.3 Grain-size stratification from deposits

The vertical change in grain size from the channel axis to the elevated channel margin depends on the samples that are selected. It is not immediately clear which axis and margin samples were deposited by the same flows because bed-scale correlation is not possible between channel axis and terrace environments (Fig. 6.4). It is actually quite common to find that axial channel fill is no longer stratigraphically connected to levees or terrace deposits because the transition is eroded (Kane and Hodgson, 2011). Therefore, it is assumed that various combinations of coarse and fine-grained axis and margin samples were deposited by the same flows. From each of the two depositional environments, three samples were selected: the coarsest grained sample, a representative intermediate sample and the finest grained sample (Fig. 6.6B). This leads to 9 possible combinations of axis and margin samples that are used as inputs for model runs (Table 6.1). The difference in grain size between the samples is largest when the finest grained sample from the channel margin and the coarsest grained sample from the channel axis are selected for the reconstruction of the grain-size gradient (Run 3). Run 7 represents the other endmember with the smallest difference in grain size between the channel axis and margin which implies the least stratified flow.



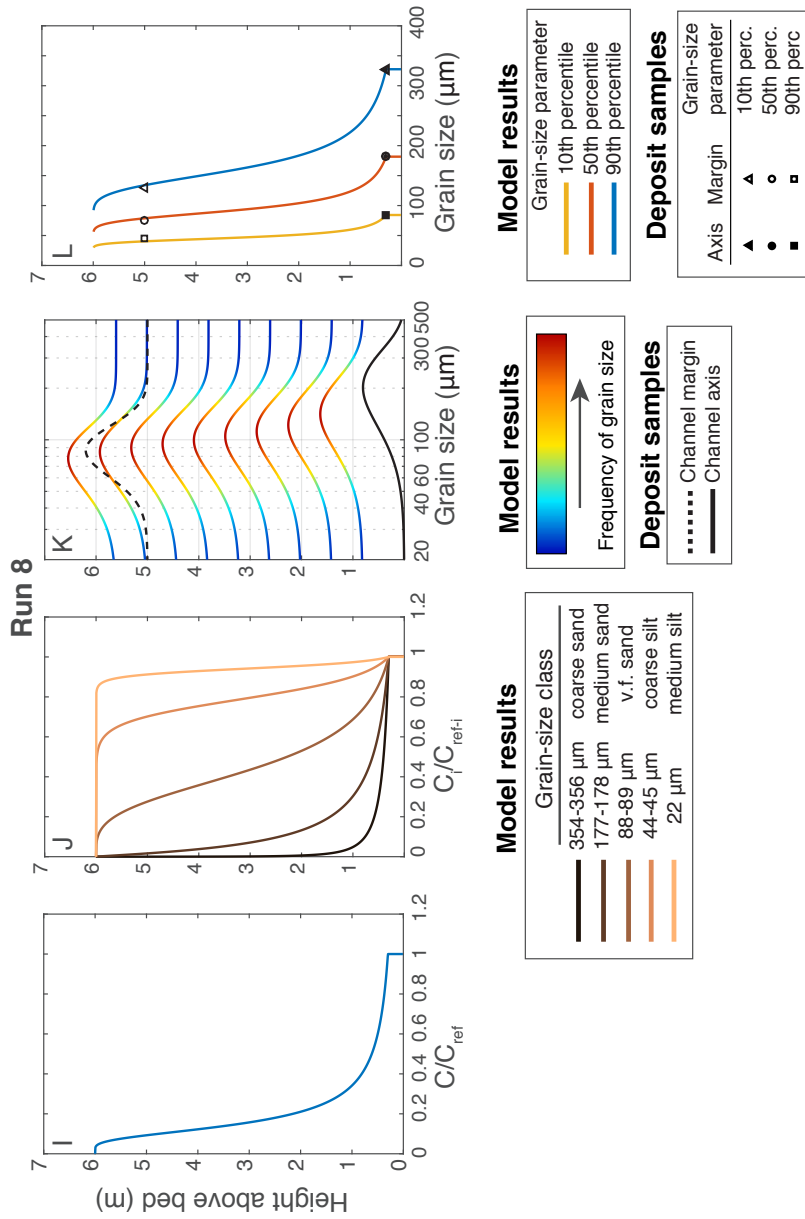


Figure 6.10: Modelling results for Runs 2, 5 and 8. Panels A-D show results from Run 2, Panels E-H show results from Run 5 and Panels I-L show results from Run 8. Different types of model results are shown: Panels A, E and I show concentration profiles. Panels B, F and J show normalised concentration profiles for sediment grain-size classes. Panels C, G and K show the grain-size distribution of the suspended sediment at different elevations in the flow. Grain-size distributions of the channel axis and margin deposit samples are plotted in black. Panels D, H an L show the vertical change in the 10th, 50th and 90th percentile of the grain size distribution. Note that the shear-velocity/turbulent-mixing intensity was lowest in Run 2. This resulted in a flow that was highly stratified in density and grain size.

6.4.4 Matching deposit data with the model to reconstruct flow properties

Model runs were performed to obtain the flow conditions that match the stratification implied of different combinations of deposit samples (Table 6.1). Figure 6.10 shows the turbidity-current flow structure for Runs 2, 5 and 8. The model demonstrates that the turbidity-current concentration, grain-size profile (Fig. 6.10) and shear velocity (Table 6.2) are heavily influenced by the samples that are used as model inputs.

Depending on the model inputs, shear velocity estimates range from 0.8 cm/s to 5.8 cm/s. The shear velocity obtained with the modelling depends mainly on the grain-size distribution of the channel-margin sample (Table 6.2). Runs 7, 8 and 9 use the most coarse-grained channel margin sample as a reference for the flow composition at 5 m above the thalweg, and have the highest shear velocity (5.3-5.8 cm/s). This relatively high shear velocity is needed to suspend the coarser sediment fraction in the higher portion of the current that flows onto the terrace. Thus, the model results are sensitive to the grain-size distribution of the channel-margin samples. The grain-size distribution of the channel-axis sample has a smaller effect. A coarser grained channel-axis sample results in a lower shear velocity as a model result. However, the difference in shear velocity is no more than 0.5 cm/s between model runs that use the coarsest grained and finest grained channel-axis samples as model inputs.

Model results from Runs 2, 5 and 8 are analysed in more detail (Fig. 6.10). These three runs cover the full range from model runs with a low shear velocity (Run 2) to model runs with a high shear velocity (Run 8). Normalised concentration profiles for different sediment grain-size classes show that silt-sized sediment ($D < 63 \mu\text{m}$) is relatively homogeneously distributed, while sand-sized sediment ($D > 63 \mu\text{m}$) is more concentrated at the base of the flow (Fig. 6.10 B, F, J). In the model run with the lowest shear velocity (Run 2), the decline in relative concentration upwards in the flow is largest. The suspension of sand-sized sediment is therefore restricted to the lower half of the flow in this run. Run 5 and 8 have a higher shear velocity and this results in a flow that is less stratified in grain size (Fig. 6.10 C, G, K and D, H, L) and density (Fig. 6.10 A, E, I).

A shear velocity estimate is sometimes derived from deposits using a sediment transport competence criterion. A simple criterion for sediment transport competence is provided by the ratio between the shear velocity and the settling velocity. Sediment is believed to be transported in suspension when $u^*/W_s > 1$ (Bagnold, 1966; Middleton, 1966; Kneller and McCaffrey, 1999). To determine the characteristic settling velocity (W_s) a representative grain size is needed. To this end, the median grain size of each channel-axis sample is used. It turns out that some of the shear-velocity estimates obtained with the stratification model yield u^*/W_s ratios that are less than unity. Four of the runs are associated with a u^*/W_s ratio lower than unity (Runs 1, 2, 3 and 4) while five of the runs have a ratio that is higher than unity (Runs 5, 6, 7, 8 and 9).

6.5 Discussion

6.5.1 Synchronicity of channel-axis and margin deposits

An important assumption for the flow reconstruction is that the deposits on the channel axis and margin were deposited contemporaneously by the same turbidity currents (Fig. 6.11, Scenario 1). However, this cannot be proven conclusively because beds cannot be correlated between the axis and the margin. The alternative would be that turbidite beds on the margin were deposited by an initial series of turbidity currents and that the channel-axis deposits formed during a separate, later phase of turbidite deposition that filled the channel conduit (Fig. 6.11; Scenario II). In the latter case the flow reconstruction from axis and margin deposits may not be valid because the

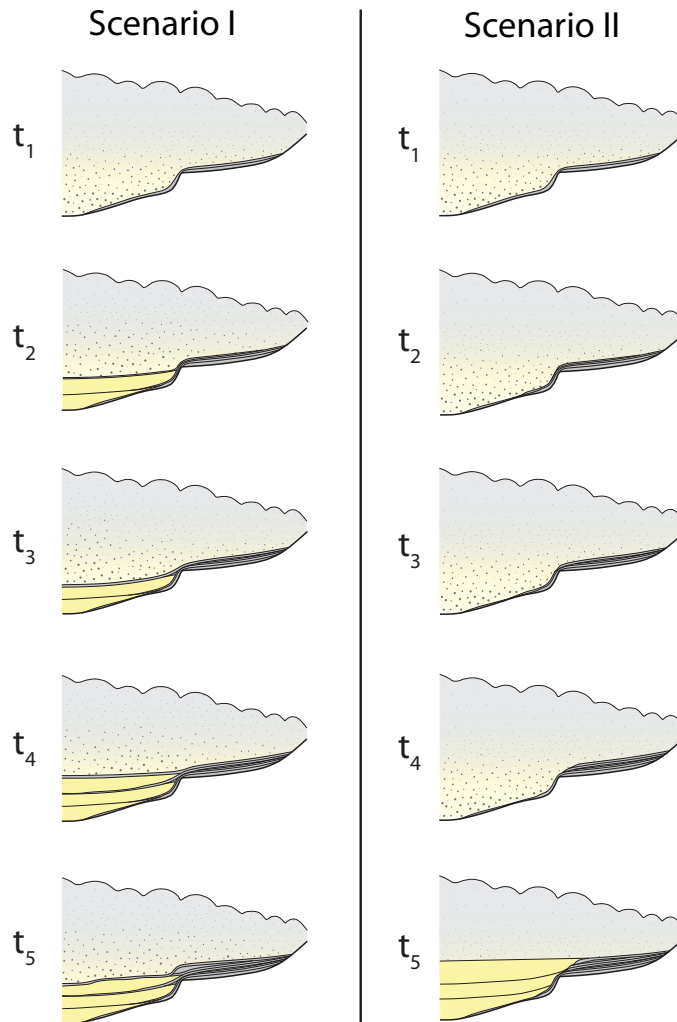


Figure 6.11: Scenarios for the morphological evolution of the submarine channel. In scenario I, deposition in the channel axis is contemporaneous with deposition on the channel margin. This is the model favoured by Hubbard et al. (2014). In scenario II, deposition in the channel axis only occurs during the latest stage of channel evolution. Figure modified after Hubbard et al. (2014)

deposits that are compared represent different phases of channel evolution and the characteristics of turbidity currents during these phases may have been different. However, the preferred interpretation of Hubbard et al. (2014) is that deposition on the axis and margin occurred during the same phase of channel evolution (Scenario I). The reason for this interpretation being that the correlation of sandstone beds from the channel axis into the channel margin was locally preserved in other parts of the outcrop belt. This implies that channel-axis and margin deposit were formed by similar flows and that it is therefore possible to use samples from the two environments to reconstruct a single flow structure.

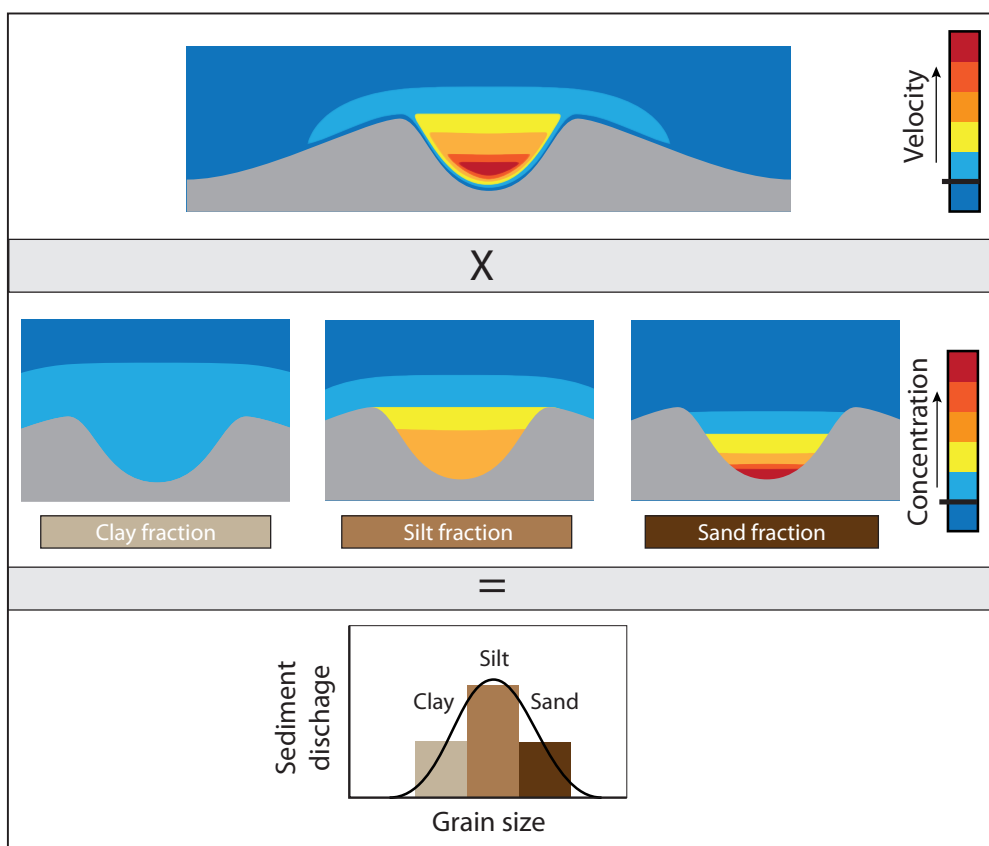


Figure 6.12: The approach to determine the sediment discharge through a submarine channel. It is assumed that the velocity and suspended sediment concentration are laterally uniform in the channel. For every sediment grain-size class, the velocity field is multiplied with the concentration field to determine the discharge of the grain-size class. This gives the volume that every sediment grain-size class contributes to the discharge of the channel. This result is then used to reconstruct the grain-size distribution of the sediment transported by the turbidity current.

6.5.2 Turbidity-current flow properties

The model is able to reproduce grain-size stratification structures that match with deposit samples from the channel axis and the elevated margin. Model results are particularly sensitive to the grain-size distribution of the sediment samples on the channel margin. The range of grain sizes on the channel margin indicates the range of grain sizes that was suspended in the upper portion of the turbidity currents in the channel. The suspended sediment grain-size distribution is, in turn, related to the shear velocity of the flow. Previously, Hiscott et al. (1997) used the maximum grain size at different elevations above the thalweg to estimate grain-size stratification and the associated shear velocity. Here, we improve this approach by using the entire sediment grain-size distribution rather than just the coarsest grains in suspension.

One main outcome of the modelling is that the shear velocity of turbidity currents that filled the channel was in the range from 0.8 cm/s (Run 1) and 5.8 cm/s (Run 9) (Table 6.2). Model

runs within this range of shear velocities are associated with a range of stratification structures. Shear velocities which are on the lower end of the spectrum imply that it is difficult to transport all sediment grain sizes that are present in the axis channel in significant quantities. For example, turbidity currents with a shear velocity of 0.8 cm/s (Run 1) are unlikely to transport the coarsest sediment fraction through the channel axis (~500 μm) in large quantities. The model runs with the lowest shear velocity estimates may therefore represent low-density, silt-prone turbidity currents that caused relatively minor amounts of sediment transport through the channel axis. These turbidity currents alternated with more energetic turbidity currents that deposited relatively coarser material on the channel margin. Flows that deposited coarser sediment onto the channel margin generally also had a higher concentration as is indicated by a positive correlation between bed thickness and grain size (Fig. 6.8). The model results presented here thus place some constraints on the range of flow properties that occurred in the channel. The results indicate that a range of flow types occurred and that there was no unique characteristic flow structure that applicable to all turbidity currents.

Variations in the channel-margin grain size may not only reflect variations in flow properties between turbidity currents but can also reflect variations in channel relief between events. These variations in channel relief may have occurred because the axis and margin did not always aggrade at the same rate. With the present data it is, however, hard to distinguish between the relative contributions of variations in channel relief and flow power to the channel margin facies.

In channels on the modern sea floor that were recently active there is less uncertainty about the channel morphology. With sediment samples it is shown for some modern channels that there is significant scatter in the relation between height above the thalweg and deposit grain size. Notable examples include the Amazon Channel (Hiscott, 1997) and channels on the Niger Delta slope (Jobe et al., 2017). In these cases, it is not feasible that this grain-size variability was due to large fluctuations in channel depth. The scatter in the relation between height above thalweg and grain size must thus reflect the distribution of flow sizes that passed through these channels.

6.5.3 Reconstruction of sediment transfer in the submarine channel

While deposits in the axis of a channel are commonly sand-prone and deposits on elevated channel margins or levees are commonly more silt- or clay-prone, it is not immediately clear in which relative quantities these different calibres of sediment are transported.

The type of modelling presented here can be used to quantify the grain-size distribution of the sediment that is transferred in a submarine channel. Reconstructions of sediment transfer have already been made for fluvial drainage systems by making use of the velocity field and suspended sediment concentration field in a river channel (Lupker et al., 2011). Figure 6.12 illustrates how sediment transfer can be reconstructed. For each sediment grain-size class, the concentration field is multiplied by the velocity field to obtain the sediment discharge:

$$Q_s^i = \int_0^h C^i(h) * W(h) * U(h) dh \quad (6.3),$$

where Q_s^i is the discharge [m^3/s] of sediment in grain-size class i , C_i is the concentration of sediment of grain-size class i , W is the width of the channel [m] as a function of height above the thalweg and U is the velocity profile [m/s] of the turbidity current. It is assumed that the velocity structure in the channel is laterally uniform. In the simplest model application, it is also assumed that the channel is rectangular and that the channel width does not change with height as a result.

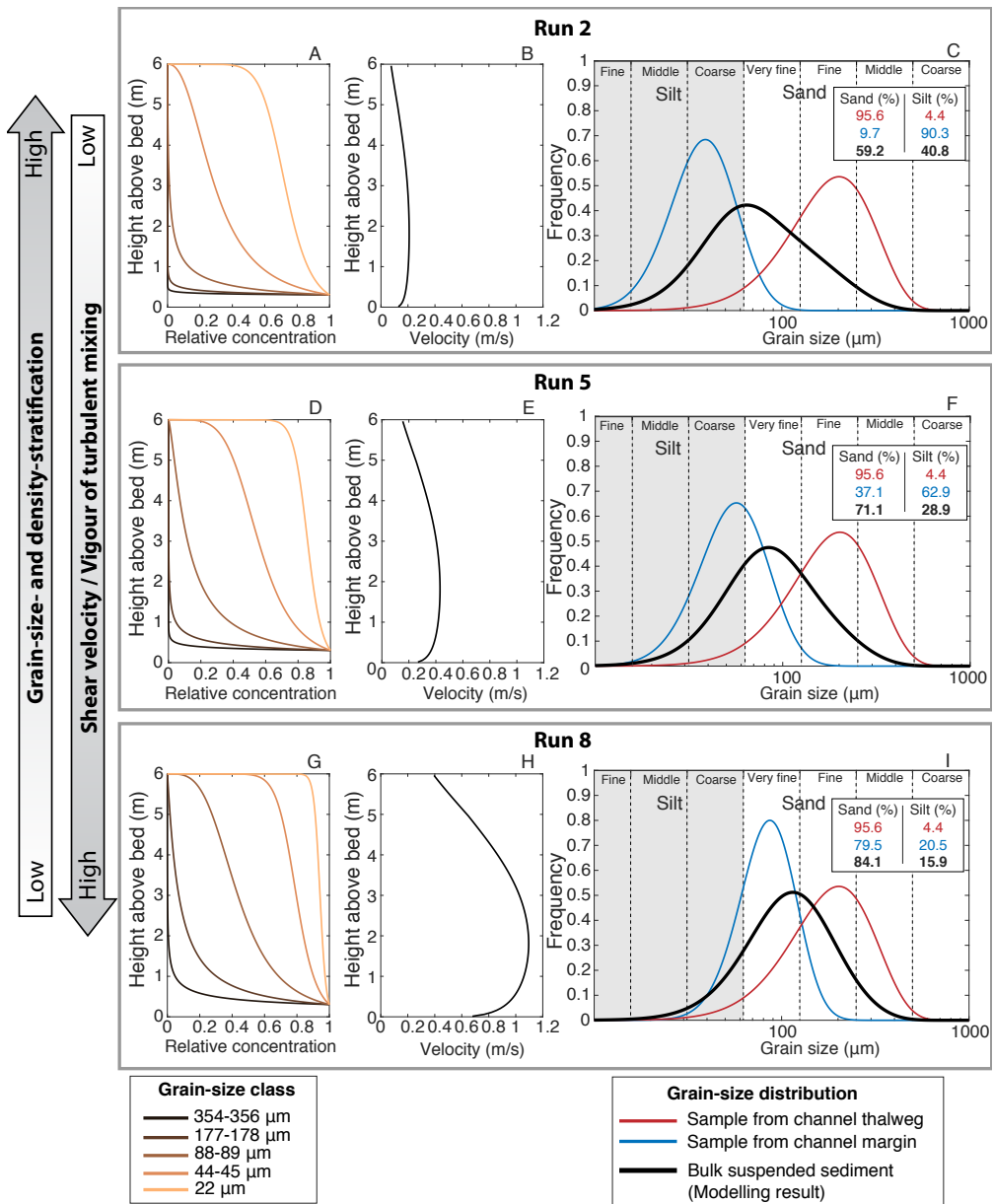


Figure 6.13: Predictions of grain-size distribution of suspended sediment transferred in the Gabriela Channel. Predictions are provided for Run 2 (A-C), Run 5 (D-F) and Run 8 (G-I). Predictions are based on concentration profiles for each grain-size class (A,D,G) that are multiplied with a velocity profile (B,D,H). Note that the bulk suspended sediment transferred in the channel is most silt-prone for Run 2 and most sand-prone for Run 8. Run 2 is associated with the lowest shear velocity while Run 8 is associated with the highest shear velocity.

The results of Runs 2, 5 and 8 are used to reconstruct the grain-size distribution of the sediment that is transferred for these different model realizations. Concentration profiles for each sediment grain-size class are already available from the runs (Fig. 6.10A, E, I). Velocity profiles are obtained using an analytical model for the velocity structure of turbidity currents (Eggenhuisen and van der Grind, 2016; following Kneller et al., 1999). Each of the velocity profiles has the normal bell-shaped turbidity-current velocity profile that is a result of combined shear at the base of the current with the bed and at the top of the current with the ambient water (Kneller et al., 1999). The velocity maximum varies from 0.2 m/s for Run 2 to 1.1 m/s for Run 8 (Fig. 6.13B, D, G).

The sediment-transfer reconstructions for the three runs show that the bulk sediment transferred in the channel is always significantly finer grained and more silt-prone than the channel-axis deposits (Fig. 6.13C, F, I). The percentage of silt in the channel-axis samples in these runs is 4.4% while the percentage of silt in the turbidity currents ranges from 15.9% to 40.8%, according to the simulations, depending on the input conditions. The bulk sediment transfer is most fine-grained and most silt-prone for Run 2 (Fig. 6.13C) and relatively coarsest grained and least silt-prone for Run 8 (Fig. 6.13I). Compared to the channel margin samples, which are representative for the suspension grain-size distribution in the uppermost part of the flow, the bulk sediment transfer is relatively coarser grained.

The present analysis illustrates that it is possible to quantify the grain-size distribution of the sediment transferred in a submarine channel. This type of reconstruction is valuable for prediction of lithologies that can be expected downstream in the remaining slope-channel section and on the basin floor. The approach that is laid out here can be refined further in future studies to improve predictions of sediment-transfer volume and grain-size distribution in modern and ancient submarine channels. For example, the concentration profile can be predicted by diffusion models that are more refined than the Rouse equation. Additionally, a suitable field dataset can be used to validate the model by comparing the predicted and actual deposit character down-dip of a reference channel cross-section. Such a validation is not possible in the Tres Pasos dataset because down dip deposits are not exposed.

6.5.4 Interpretation of the shear velocity to settling velocity ratio

The ratio between the shear velocity and sediment-settling velocity (u^*/W_s) is recognised as an important non-dimensional parameter that characterises the sediment transport capacity and competence (Bagnold, 1966; Hiscott, 1994). The u^*/W_s ratio is often used as a competence criterion, where a ratio greater than 1 indicates that flows are able to transport the sediment. However, for the analysis of the present model runs, this critical ratio has limited use. The characteristic u^*/W_s varies from 0.3 to 3.8 between the model runs (Table 6.2), where W_s is based on the median grain size of the deposits in the channel axis. However, in model runs with a u^*/W_s ratio that is much lower than 1 (e.g. Run 2; Fig. 6.10A-D) the model still predicts suspended sediment transport. In part, this is due to the fact that the sediment available has a wide grain-size distribution and the finer grained fraction is still easily supported in suspension at a low shear velocity. Hence, a single u^*/W_s ratio has limited use as a predictor for the onset and amount of sediment suspension in these polydisperse currents. More importantly, the u^*/W_s ratio determines the shape of the concentration profile for every sediment grain-size class through the Rouse equation. A u^*/W_s ratio smaller than 1 yields a concentration profile that is very concave, while sediment from the finer sediment grain-size classes in the same flow has a higher u^*/W_s ratio and is much more homogeneously distributed. The turbidity currents that are modelled here have a

wide range of suspended sediment grain sizes, resulting in a large spread of concentration profiles for the different grain-size classes (Fig. 6.10). Thus, for a polydisperse suspended sediment current, the u^*/W_s ratio can serve as a transport-capacity predictor. The ratio can be determined for every grain-size class, to then be used as a parameter that predicts the shape of each concentration profile and thereby the relative volume of sediment of each grain-size class that is suspended in the water column.

6.6 Conclusions

This study uses the vertical change in deposit grain size with height above the thalweg of a submarine channel to reconstruct turbidity current flow conditions. As a case study we use an outcropping submarine channel fill that is part of the deep-marine Tres Pasos Formation. Analytical modelling shows that the change in deposit grain size from the channel axis to the channel margin implies that the turbidity current in the submarine channel was highly stratified in terms of density and grain size. Matching of the model and outcrop data places quantitative constraints on the shear velocity of the flow and the degree of grain-size and density stratification.

The analytical model, which is based on the Rouse equation, shows that the vertical change in grain size reflects the vigour of turbulent mixing. Finer grained deposits on the elevated channel margin imply that turbulent mixing was unable to suspend the coarse sediment fraction to the upper part of the flow. Using different combinations of channel axis and margin samples as model inputs, a range of possible flow structures is reconstructed. The shear velocity varied from 0.8 cm/s, when the finest grained channel margin sample was used as a model input to 5.8 cm/s when the coarsest grained margin sample was used as model input.

We use the inverted flow structures to predict the composition of sediment transported through the channel cross-section into the basin. The results highlight that the sand-prone nature of the axial channel fill (95% sand, 5% silt) is not representative for the bypassing flows because a large fraction (16-41 %) of sediment transferred through the channel is actually silt. The modelling approach presented here can thus be used to predict the relative volume of different sediment grain-size classes that can be expected as deposits down dip of a studied channel cross-section.

Chapter 7

Synthesis

This thesis is focused on sediment transfer by turbidity currents through submarine channels, the pathways through which sediment from the continent is redistributed across the sea floor (Chapter 1).

The physical experiments (Chapters 2, 3 and 4) show how turbidity currents interact with submarine channels. Channel dimensions relative to flow size and changes therein are identified as primary controls on sediment transfer efficiency. The vertical distribution of suspended sediment in turbidity currents determines the volume and grain size of sediment that is transported through the channel and the volume and grain size that is lost by overspill. A simple analytical model is developed to predict grain-size and density stratification (Chapter 5). The insights are combined to reconstruct the flow structure of turbidity currents from the stratigraphic record (Chapter 6). Here follows a general discussion of these results.

7.1 Morphodynamics of submarine channels in flume experiments

The inception and evolution of submarine channels can be witnessed in laboratory experiments with appropriate scaling conditions (Chapter 2). New scaling constraints are introduced that ensure that turbidity currents keep sediment in suspension and entrain sediment from the bed. These scaling constraints dictate that the Shields parameter and the particle Reynolds number are within certain ranges. Experiment conditions such as slope, discharge and sediment grain size need to be such that these scaling constraints are met. The experiments demonstrate that these scaling constraints allow to generate sediment-laden turbidity currents in the laboratory that keep the sediment load that is initially imposed upon them in suspension.

The morphodynamics of submarine channel inception are studied in Chapter 2. For the first time, turbidity currents in experiments generated a channel on a previously unchannelised slope. The depth of this channel increased progressively as the subsequent turbidity currents modified the channel morphology (Fig. 2.2 and Fig. 7.1A). Contrastingly, in previous experiments there was a progressive decrease in relief of pre-formed channels because deposition rates along the channel thalweg exceeded deposition rates on the levees (e.g. Kane et al., 2008; Straub et al., 2008; Ezz et al., 2013; Fig. 7.1B). Sediment bypass along the channel axis did not occur in those experiments because the currents could not maintain all sediment in suspension. Previous experiments with sediment-laden, channelised turbidity currents are therefore considered to be representative for the latest stage of channel evolution when channel relief declines due to dominant deposition inside the channel (Peakall & Sumner, 2015). The present experiments demonstrate that the earlier phases of channel evolution can also be captured in experiments. This is significant because it increases the range of questions about submarine channel morphodynamics that can be addressed in laboratory experiments.

For example, it was previously unclear whether the inception of a submarine channel starts with the erosion of a conduit (Fildani et al., 2013) or whether it also can start with deposition (Hodgson et al., 2011). The experiments presented in Chapter 2 demonstrate that a submarine channel can be initiated largely due to the confinement created by levee formation (Fig. 7.1A).

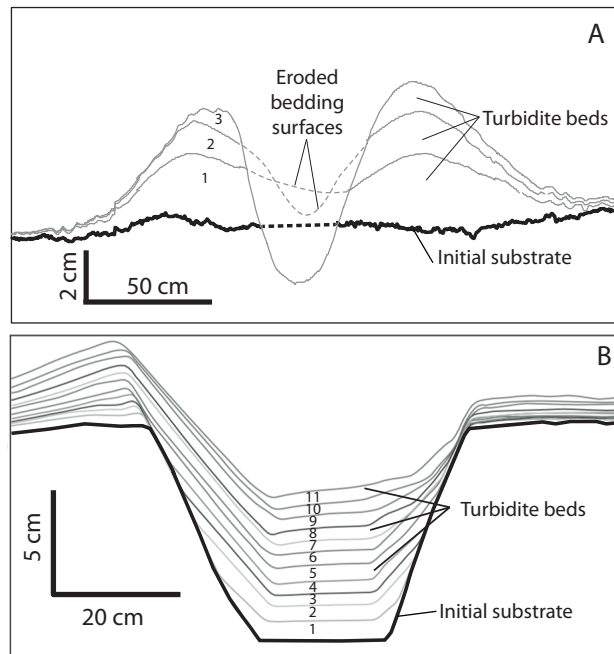


Figure 7.1: Cross-sections of submarine channels in experiments. (A) Channel cross-section from the experiments in Chapters 2 and 3 of this thesis. Three turbidity currents were run on a slope with no initial channel. Note that channel relief increased progressively because deposition on the levees was accompanied with low sedimentation rates or erosion around the channel thalweg. (B) Channel cross-section from experiments from Straub et al. (2008). 11 turbidity currents were run through a pre-formed channel. Note that channel relief decreased progressively because turbidity current deposition inside the channel exceeded deposition on either of the levees.

This does not exclude the possibility of erosional channel inception on the sea floor: the results from the experiments indicate that the relative contribution of deposition and erosion to channel inception are variable.

The self-formed (Chapter 2) and pre-formed (Chapters 3, 4) experimental submarine channels do not have meander bends as many of their natural counterparts because the length of the channel section (3–4 m) is only a few times its width (~ 1 m). Future studies aiming to expand the present work to meandering submarine channels can follow different strategies. One option is to use a much larger laboratory set-up. Another option is to change the boundary conditions of the experiments to reduce the flow size and associated channel size while still complying with the scaling constraints.

Numerical models are not limited by size limitations and would therefore be a suitable alternative. The results of the present experiments can be used to calibrate such models. The morphodynamics of turbidity currents are to a large extent controlled by stratification in these currents (see next paragraph). A numerical model that captures the evolution of submarine channels should thus account for stratification and is less likely to be successful when it works with depth-averaged flow properties.

7.2 Stratification of channelised turbidity currents

Grain-size and density stratification are key characteristics of turbidity currents that control the characteristics of deposits around submarine channels. Levees of submarine channels often show an upward decrease in bed thickness and deposit grain size (Fig. 5.1) and this pattern has been attributed to the increase in height of the deposits above the channel thalweg as the levees grow higher (Pirmez et al., 2003; Dennielou et al., 2006; Hansen et al., 2015). In Chapter 3 the levee deposit grain-size trend is directly compared to the grain-size profile of a turbidity current from a similar experiment. The deposit and flow grain-size profiles have a similar gradient (Fig. 3.13) and this confirms that the vertical trend in levee grain size can indeed be used to reconstruct the turbidity current flow structure. Previously it was not possible to compare vertical trends in the deposit and flow because sediment concentration and grain-size profiles of turbidity currents have never been measured directly in natural submarine channels. Chapter 3 does therefore provide a validation of the assumption used in previous studies.

The rate at which grain size and density decrease with height in a turbidity current reflects the intensity of turbulent mixing. Experiments (Chapter 5) show that vigorous turbulent mixing homogenises a turbidity current and limits vertical variation in grain size while weaker turbulent mixing leads to a more stratified flow (Figs 5.2 and 5.5). The results from the experiments are used to validate a simple analytical model that can predict grain-size and concentration profiles of polydisperse suspensions. The model makes use of the Rouse Equation to predict the concentration profile for every sediment grain-size class in the suspension. The usage of multiple sediment grain-size classes in the model is essential to predict grain-size stratification. The Rouse equation was derived for open-channel flows but the present study confirms that it is also usable as a first-order predictor for the concentration profile of turbidity currents.

A model that predicts stratification in turbidity currents based on turbidity-current flow properties can be used in two different ways. Firstly, such a model can be used to predict grain-size distribution and bed thickness of deposits in and around submarine channels. Such an approach is proposed by Jobe et al. (2017) and can be useful for reservoir quality prediction. However, this approach requires *a priori* assumptions about flow conditions in the channel. Alternatively, when changes in deposit grain-size or bed-thickness with height above the thalweg of a channel are well constrained, the model can be iterated with different flow conditions until model results show a good fit with field data. This approach is followed in Chapter 6 and provides a new method to constrain flow conditions. It is shown that turbidity currents in submarine channels of the deep-marine Tres Pasos Formation (Cretaceous; Chile) were highly stratified in density and grain size (Chapter 6). The simulations show the differentiation in concentration profiles between the sediment grain-size classes, which include both sand- and silt-sized sediment. The amount of sand suspended in the water column was relatively small in the modelled test-case because suspension of sand was largely restricted to the lower portion of the flow while the silt-sized sediment is more homogeneously distributed. This suspension structure forms the basis for a reconstruction of the sediment transfer through the channel (Fig. 6.12). Such a reconstruction can serve to predict the volume and grain-size distribution of the deposits down-slope.

7.3 Submarine channels in a mass-balance perspective

Turbidity currents are able to bypass the coarser sediment fraction (i.e. sand) to the distal end of deep-water systems because this sediment fraction is concentrated in the lower part of the flow which remains fully confined in submarine channels (Posamentier & Kolla, 2003). The upper part of the flow is often lost due to overspill from submarine channels. This leads to a preferential

extraction of the fine sediment fraction, which increases the median grain size and decreases the volume of the remaining flow (Fig. 4.17).

Models for the distribution of sedimentary facies in sedimentary basins are important for the prediction of reservoir potential on a regional scale. Many clastic deep-water systems are characterised by an increase in sand-to-mud ratio in the stratigraphy from the slope to the basin floor (Prather et al., 2016). Similarly, the experiments in Chapter 4 show an increase in deposit grain size in the downstream direction. The most coarse-grained deposits in the experiments occur around the centre of the lobe on the horizontal basin floor.

The experiments described in Chapter 4 indicate that the degree of confinement of turbidity currents in submarine channels and vertical grain-size stratification are important controls on the partitioning of sediment by turbidity currents. The relative thickness of the flow with respect to the channel depth determines the portion of the stratified flow that can be transported inside the channel and the portion that is lost due to overspill. Channel width and depth change continuously as a channel evolves (Chapters 2,3). A newly formed channel has a small depth relative to the thickness of turbidity currents. Turbidity currents in such a channel lose a large portion of the flow due to overspill (Fig. 4.16). Channel depth relative to flow thickness increases as channels become more mature. This restricts the overbank flow to the uppermost portion of the turbidity current, which only contains fine-grained sediment in a low concentration. It has been suggested that deep-water systems can prograde onto the basin floor in the absence of external forcing due to progressive slope confinement (Hodgson et al., 2016). The experiments in Chapter 4 show that basin-floor lobes that are sourced by a deeper channel are indeed more elongate for equal upstream boundary conditions (Fig. 4.7).

Thus, in order to predict the downstream partitioning of sediment by turbidity currents and the associated facies distribution, it is essential to understand two factors: (1) stratification in turbidity currents, and (2) the morphological evolution of submarine channels. This thesis addressed both of these issues. The next step to improve prediction of grain-size and volume partitioning in deep-water systems is further integration of models on turbidity current stratification and on morphological evolution of submarine channels.

References

- Abd El-Gawad, S.M., Cantelli, A., Pirmez, C., Minisini, D., Sylvester, Z., Imran, J., 2012a. Three-dimensional numerical simulation of turbidity currents in a submarine channel on the seafloor of the Niger Delta slope. *Journal of Geophysical Research: Oceans*, **117**, 1–16. doi:10.1029/2011JC007538
- Abd El-Gawad, S.M., Pirmez, C., Cantelli, A., Minisini, D., Sylvester, Z., Imran, J., 2012b. 3-D numerical simulation of turbidity currents in submarine canyons off the Niger Delta. *Marine Geology*, **326**, 55–66. doi:10.1016/j.margeo.2012.06.003
- Alexander, J., McLelland, S.J., Gray, T.E., Vincent, C.E., Leeder, M.R., Ellett, S., 2008. Laboratory sustained turbidity currents form elongate ridges at channel mouths. *Sedimentology*, **55**, 845–868. doi:10.1111/j.1365-3091.2007.00923.x
- Allen, J.R.L., 1982. Sedimentary structures, vol. II, Developments in Sedimentology. Elsevier.
- Arfaie, A., Burns, A.D., Dorrell, R.M., Eggenhuisen, J.T., Ingham, D.B., McCaffrey, W.D., 2014. Optimised mixing and flow resistance during shear flow over a rib roughened boundary. *International Communications in Heat and Mass Transfer*, **58**, 54–62. doi:10.1016/j.icheatmasstransfer.2014.08.005
- Arnott, R.W.C., Hand, B.M., 1989. Bedforms, primary structures and grain fabric in the presence of suspended sediment rain. *Journal of Sedimentary Research*, **59**.
- Baas, J., Kesteren, W. Van, Postma, G., 2004. Deposits of depletive high-density turbidity currents: a flume analogue of bed geometry, structure and texture. *Sedimentology*, **51**, 1053–1088. doi:10.1111/j.1365-3091.2004.00660.x
- Baas, J.H., McCaffrey, W.D., Haughton, P.D.W., Choux, C., 2005. Coupling between suspended sediment distribution and turbulence structure in a laboratory turbidity current. *Journal of Geophysical Research: Oceans*, **110**, 1–20. doi:10.1029/2004JC002668
- Babonneau, N., Savoye, B., Cremer, M., Bez, M., 2010. Sedimentary Architecture in Meanders of a Submarine Channel: Detailed Study of the Present Congo Turbidite Channel (Zaiango Project). *Journal of Sedimentary Research*, **80**, 852–866. doi:10.2110/jsr.2010.078
- Bagnold, R., 1966. An approach to the sediment transport problem from general physics. *Geological Survey Professional Paper*, **422-I**. Geological Survey, Washington, DC.
- Basani, R., Janocko, M., Cartigny, M.J.B., Hansen, E.W.M., Eggenhuisen, J.T., 2014. MassFLOW-3D as a simulation tool for turbidity currents: some preliminary results, in: From Depositional Systems to Sedimentary Successions on the Norwegian Continental Margin. John Wiley and Sons. doi:10.1017/CBO9781107415324.004
- Beaubouef, R.T., 2004. Deep-water leveed-channel complexes of the Cerro Toro Formation, Upper Cretaceous, southern Chile. *AAPG Bulletin*, **88**, 1471–1500. doi:10.1306/06210403130
- Best, J., Bridge, J., 1992. The morphology and dynamics of low amplitude bedwaves upon upper stage plane beds and the preservation of planar laminae. *Sedimentology*, **39**, 737–752.
- Bolla Pittaluga, M., Imran, J., 2014. A simple model for vertical profiles of velocity and suspended sediment concentration in straight and curved submarine channels. *Journal of Geophysical Research: Earth Surface*, **119**, 483–503. doi:10.1002/2013JF002812
- Cantelli, A., Pirmez, C., Johnson, S., Parker, G., 2011. Morphodynamic and Stratigraphic Evolution of Self-Channelized Subaqueous Fans Emplaced by Turbidity Currents. *Journal of Sedimentary Research*, **81**, 233–247. doi:10.2110/jsr.2011.20
- Cantero, M.I., Cantelli, A., Pirmez, C., Balachandar, S., Mohrig, D., Hickson, T.A., Yeh, T., Naruse, H., Parker, G., 2011. Emplacement of massive turbidites linked to extinction of turbulence in turbidity currents. *Nature Geoscience*, **5**, 42–45. doi:10.1038/ngeo1320

- Cartigny, M.J.B., Eggenhuisen, J.T., Hansen, E.W.M., Postma, G., 2013. Concentration-Dependent Flow Stratification In Experimental High-Density Turbidity Currents and Their Relevance To Turbidite Facies Models. *Journal of Sedimentary Research*, **83**, 1047–1065. doi:10.2110/jsr.2013.71
- Carvajal, C., Steel, R., 2012. Source-to-sink sediment volumes within a tectono-stratigraphic model for a Laramide shelf-to-deep-water basin: methods and results, in: *Tectonics of Sedimentary Basins: Recent Advances*. pp. 131–151. doi:10.1002/9781444347166.ch7
- Clark, J.D., Pickering, K.T., 1996. Architectural elements and growth patterns of submarine channels: Application to hydrocarbon exploration. *AAPG Bulletin*, **80**, 194–221.
- Cooper, C., Wood, J., Andrieux, O., 2013. Turbidity current measurements in the Congo Canyon, in: *Offshore Technology Conference 2012 Proceedings*. Houston, Texas.
- Covault, J.A., 2011. Submarine fans and canyon-channel systems: A review of processes, products, and models. *Nature Education Knowledge*, **3**, 1–19.
- Covault, J.A., Kostic, S., Paull, C.K., Ryan, H.F., Fildani, A., 2014. Submarine channel initiation, filling and maintenance from sea-floor geomorphology and morphodynamic modelling of cyclic steps. *Sedimentology*, **61**, 1031–1054. doi:10.1111/sed.12084
- Covault, J. a., Shelef, E., Traer, M., Hubbard, S.M., Romans, B.W., Fildani, a., 2012. Deep-Water Channel Run-Out Length: Insights from Seafloor Geomorphology. *Journal of Sedimentary Research*, **82**, 21–36. doi:10.2110/jsr.2012.2
- Curry, J.R., Emmel, F.J., Moore, D.G., 2002. The Bengal Fan: Morphology, geometry, stratigraphy, history and processes. *Marine and Petroleum Geology*, **19**, 1191–1223. doi:10.1016/S0264-8172(03)00035-7
- Daly, R. a, 1936. Origin of Submarine “Canyons.”, *American Journal of Science*, **31**, 401–420. doi:10.4157/grj.12.841
- Damuth, J.E., Kolla, V., Flood, R.D., Kowsmann, R.O., Monteiro, M.C., Gorini, M.A., Palma, J.J.C., Belderson, R., 1983. Meandering channels meandering and bifurcation patterns on the Amazon deep sea fan as revealed by pong-range side-scan sonar. *Geology*, **11**, 94–98.
- Damuth, J.E., Kumar, N., 1975. Amazon Cone: morphology, sediments, age, and growth pattern. *Geological Society of America Bulletin*, **86**, 863–878.
- De Leeuw, J., Eggenhuisen, J.T., Cartigny, M.J.B., 2016. Morphodynamics of submarine channel inception revealed by new experimental approach. *Nature Communications*, **7**, 10886. doi:10.1038/ncomms10886
- Denniellou, B., Huchon, A., Beaudouin, C., Berné, S., 2006. Vertical grain-size variability within a turbidite levee: Autocyclicity or allocyclicity? A case study from the Rhone neofan, Gulf of Lions, Western Mediterranean. *Marine Geology*, **234**, 191–213. doi:10.1016/j.margeo.2006.09.019
- Dorrell, R.M., Darby, S.E., Peakall, J., Sumner, E.J., Parsons, D.R., Wynn, R.B., 2014. The critical role of stratification in submarine channels: Implications for channelization and long runout of flows. *Journal of Geophysical Research: Oceans*, **119**, 2620–2641. doi:10.1002/2014JC009807
- Dorrell, R.M., Hogg, A.J., 2012. Length and Time Scales of Response of Sediment Suspensions to Changing Flow Conditions. *ASCE Journal of Hydraulic Engineering*, **138**, 430–439. doi:10.1061/(ASCE)HY.1943-7900
- Dorrell, R.M., Hogg, A.J., Pritchard, D., 2013. Polydisperse suspensions: Erosion, deposition, and flow capacity. *Journal of Geophysical Research: Earth Surface*, **118**, 1939–1955. doi:10.1002/jgrf.20129
- Dykstra, M., Kneller, B., Milana, J.P., 2012. Bed-thickness and grain-size trends in a small-scale proglacial channel-levée system; the Carboniferous Jejenes Formation, Western Argentina: Implications for turbidity current flow processes. *Sedimentology*, **59**, 605–622. doi:10.1111/j.1365-3091.2011.01268.x
- Eggenhuisen, J.T., Cartigny, M.J.B., de Leeuw, J., 2017. Physical theory for near-bed turbulent particle suspension capacity. *Earth Surface Dynamics*, **5**, 269–281. doi:10.5194/esurf-5-269-2017
- Eggenhuisen, J.T., McCaffrey, W.D., 2012. The vertical turbulence structure of experimental turbidity currents encountering basal obstructions: implications for vertical suspended sediment distribution in non-equilibrium currents. *Sedimentology*, **59**, 1101–1120. doi:10.1111/j.1365-3091.2011.01297.x

- Eggenhuisen, J.T., McCaffrey, W.D., Haughton, P.D.W., Butler, R.W.H., 2011. Shallow erosion beneath turbidity currents and its impact on the architectural development of turbidite sheet systems. *Sedimentology*, **58**, 936–959. doi:10.1111/j.1365-3091.2010.01190.x
- Eggenhuisen, J.T., van der Grind, G., 2016. The EuroSEDS Sediment Budget Estimator (SBE) App; a predictive tool for turbidity current sediment transport rate., in: Eurotank Studies of Experimental Deepwater Sedimentology (EuroSEDS): Year 2 Report. Utrecht University, pp. 109–122.
- Ellison, T.H., Turner, J.S., 1959. Turbulent entrainment in stratified flows. *Journal of Fluid Mechanics*, **6**, 423–448. doi:10.1017/S0022112059000738
- Ezz, H., Cantelli, A., Imran, J., 2013. Experimental modeling of depositional turbidity currents in a sinuous submarine channel. *Sedimentary Geology*, **290**, 175–187. doi:10.1016/j.sedgeo.2013.03.017
- Ferguson, R.I., Church, M., 2004. A simple universal equation for grain settling velocity. *Journal of Sedimentary Research*, **74**, 933–937. doi:10.1306/051204740933
- Fildani, A., Hubbard, S.M., Covault, J.A., Maier, K.L., Romans, B.W., Traer, M., Rowland, J.C., 2013. Erosion at inception of deep-sea channels. *Marine and Petroleum Geology*, **41**, 48–61. doi:10.1016/j.marpetgeo.2012.03.006
- Fildani, A., Normark, W.R., Kostic, S., Parker, G., 2006. Channel formation by flow stripping: Large-scale scour features along the Monterey East Channel and their relation to sediment waves. *Sedimentology*, **53**, 1265–1287. doi:10.1111/j.1365-3091.2006.00812.x
- Galy, V., France-Lanord, C., Beyssac, O., Faure, P., Kudrass, H., Palhol, F., 2007. Efficient organic carbon burial in the Bengal fan sustained by the Himalayan erosional system. *Nature*, **450**, 407–10. doi:10.1038/nature06273
- Garcia, M., 2008. sedimentation engineering: processes, measurements, modeling, and practise. American Society of Civil Engineers, Rseton, Virginia, USA.
- Garcia, M., Parker, G., 1989. Experiments on hydraulic jumps in turbidity currents near a canyon-fan transition. *Science*, **245**, 393–6. doi:10.1126/science.245.4916.393
- Garcia, M.H., 1994. Depositional Turbidity Currents Laden with Poorly Sorted Sediment. *Journal of Hydraulic Engineering*, **120**, doi:10.1061/(ASCE)0733-9429(1994)120:11(1240)
- Hampson, G.J., Duller, R.A., Petter, A.L., Robinson, R.A.J., Allen, P.A., 2014. Mass-balance constraints on stratigraphic interpretations of linked alluvial–coastal–shelfal deposits from source to sink: Example from the Cretaceous Western Interior Basin, Utah and Colorado, U.S.A. *Journal of Sedimentary Research*, **84**, 935–960. doi:10.2110/jsr.2014.78
- Hansen, L., Janocko, M., Kane, I., Kneller, B., 2017. Submarine channel evolution, terrace development, and preservation of intra-channel thin-bedded turbidites: Mahin and Avon channels, offshore Nigeria. *Marine Geology*, **383**, 146–167. doi:10.1016/j.margeo.2016.11.011
- Hay, A.E., 1987. Turbidity currents and submarine channel formation in Rupert Inlet, British Columbia: 2. The roles of continuous and surge-type flow. *Journal of Geophysical Research: Oceans*, **92**, 2883–2900.
- Heezen, B.C., Ewing, M., 1952. Turbidity currents and submarine slumps, and the 1929 Grand Banks earthquake. *Am. J. Sci*, **250**, 849–873.
- Heinio, P., Davies, R.J., 2009. Trails of depressions and sediment waves along submarine channels on the continental margin of Espirito Santo Basin, Brazil. *Geological Society of America Bulletin*, **121**, 698–711. doi:10.1130/B26190.1
- Hess, G.R., Normark, W.R., 1976. Holocene sedimentation history of the major fan valleys of Monterey fan. *Marine Geology*, **22**, 233–251. doi:10.1016/0025-3227(76)90063-3
- Hiscott, R.N., 1994. Loss of capacity, not competence, as the fundamental process governing deposition from turbidity currents. *Journal of Sedimentary Research*, **A64**, 209–214.
- Hiscott, R.N., Hall, F.R., Pirmez, C., 1997. Turbidity-current overspill from the Amazon Channel: texture of the silt/sand load, paleoflow from anisotropy of magnetic susceptibility, and implications for flow processes. *Proceedings of the ocean drilling program, Scientific results*, **155**, 531–538.

- Hodgson, D., Kane, I., Flint, S., Brunt, R., Ortiz-Karpf, A., 2016. Time transgressive confinement on the slope and the progradation of basin-floor fans: Implications for the sequence stratigraphy of deep-water deposits. *Journal of Sedimentary Research*, **64**, 1236–1273. doi:10.1017/CBO9781107415324.004
- Hoyal, D., Sheets, B.A., Edwards, C.M., Bloch, R.B., 2008. Controls from Channel Formation in Deep Water Distributive Systems. *AAPG Search and Discovery*.
- Huang, H., Imran, J., Pirmez, C., 2007. Numerical modeling of poorly sorted depositional turbidity currents. *Journal of Geophysical Research: Oceans*, **112**, 1–15. doi:10.1029/2006JC003778
- Hubbard, S.M., Covault, J.A., Fildani, A., Romans, B.W., 2014. Sediment transfer and deposition in slope channels: Deciphering the record of enigmatic deep-sea processes from outcrop. *Bulletin of the Geological Society of America*, **126**, 857–871. doi:10.1130/B30996.1
- Hubbard, S.M., Fildani, a., Romans, B.W., Covault, J. a., McHargue, T.R., 2010. High-Relief Slope Clinoform Development: Insights from Outcrop, Magallanes Basin, Chile. *Journal of Sedimentary Research*, **80**, 357–375. doi:10.2110/jsr.2010.042
- Hughes Clarke, J.E., 2016. First wide-angle view of channelized turbidity currents links migrating cyclic steps to flow characteristics. *Nature Communications*, **7**, 11896. doi:10.1038/ncomms11896
- Hughes Clarke, J.E., Conway, K., Talling, P., Cartigny, M., Lintern, G., Hill, P., 2015. Monitoring the Evolution of Submarine Channels on Fjord Prodeltas and Associated Depositional Basins. *AAPG Search and Discovery*, **41678**.
- Imran, J., Parker, G., Katopodes, N., 1998. A numerical model of channel inception on submarine fans. *Journal of Geophysical Research*, **103**, 1219–1238. doi:10.1029/97JC01721
- Islam, M.A., Imran, J., Pirmez, C., Cantelli, A., 2008. Flow splitting modifies the helical motion in submarine channels. *Geophysical Research Letters*, **35**, L22603. doi:10.1029/2008GL034995
- Janocko, M., Cartigny, M.B.J., Nemeč, W., Hansen, E.W.M., 2013. Turbidity current hydraulics and sediment deposition in erodible sinuous channels: Laboratory experiments and numerical simulations. *Marine and Petroleum Geology*, **41**, 222–249. doi:10.1016/j.marpetgeo.2012.08.012
- Jegou, I., Savoye, B., Pirmez, C., Droz, L., 2008. Channel-mouth lobe complex of the recent Amazon Fan: The missing piece. *Marine Geology*, **252**, 62–77. doi:10.1016/j.margeo.2008.03.004
- Jobe, Z., Sylvester, Z., Pittaluga, M.B., Frascati, A., Pirmez, C., 2017. Facies Architecture of Submarine Channel Deposits on the Western Niger Delta Slope : Implications for Grain-size and Density Stratification in Turbidity Currents. *Journal of Geophysical Research: Earth Surface*, **122**, F003903. doi:10.1002/2016JF003903
- Johnson, M., 1994. thin-section grain size analysis revised. *Sedimentology*, **41**, 985–999.
- Kane, I.A., Hodgson, D.M., 2011. Sedimentological criteria to differentiate submarine channel levee subenvironments: Exhumed examples from the Rosario Fm. (Upper Cretaceous) of Baja California, Mexico, and the Fort Brown Fm. (Permian), Karoo Basin, S. Africa. *Marine and Petroleum Geology*, **28**, 807–823. doi:10.1016/j.marpetgeo.2010.05.009
- Kane, I.A., Kneller, B.C., Dykstra, M., Kassem, A., McCaffrey, W.D., 2007. Anatomy of a submarine channel-levee: An example from Upper Cretaceous slope sediments, Rosario Formation, Baja California, Mexico. *Marine and Petroleum Geology*, **24**, 540–563. doi:10.1016/j.marpetgeo.2007.01.003
- Kane, I.A., McCaffrey, W.D., Peakall, J., 2010a. On the Origin of Paleocurrent Complexity Within Deep Marine Channel Levees. *Journal of Sedimentary Research*, **80**, 54–66. doi:10.2110/jsr.2010.003
- Kane, I.A., McCaffrey, W.D., Peakall, J., 2008. Controls on sinuosity evolution within submarine channels. *Geology*, **36**, 287–290. doi:10.1130/G24588A.1
- Kane, I.A., McCaffrey, W.D., Peakall, J., Kneller, B.C., 2010b. Submarine channel levee shape and sediment waves from physical experiments. *Sedimentary Geology*, **223**, 75–85. doi:10.1016/j.sedgeo.2009.11.001

- Kane, I., Pontén, A., Vangdal, B., Eggenhuisen, J., Hodgson, D.M., Sychala, Y.T., 2017. The stratigraphic record and processes of turbidity current transformation across deep-marine lobes. *Sedimentology*, **64**, 1236–1273. doi:10.1111/sed.12346
- Keevil, G.M., Peakall, J., Best, J.L., Amos, K.J., 2006. Flow structure in sinuous submarine channels: Velocity and turbulence structure of an experimental submarine channel. *Marine Geology*, **229**, 241–257. doi:10.1016/j.margeo.2006.03.010
- Kleinhans, M.G., van Dijk, W.M., van de Lageweg, W.I., Hoyal, D.C.J.D., Markies, H., van Maarseveen, M., Roosendaal, C., van Weesep, W., van Breemen, D., Hoendervoogt, R., Cheshier, N., 2014. Quantifiable effectiveness of experimental scaling of river- and delta morphodynamics and stratigraphy. *Earth-Science Reviews*, **133**, 43–61. doi:10.1016/j.earscirev.2014.03.001
- Kneller, B., 2003. The influence of flow parameters on turbidite slope channel architecture. *Marine and Petroleum Geology*, **20**, 901–910. doi:10.1016/j.marpetgeo.2003.03.001
- Kneller, B., Buckee, C., 2000. The structure and fluid mechanics of turbidity currents: a review of some recent studies and their geological implications. *Sedimentology*, **47**, 62–94. doi:10.1046/j.1365-3091.2000.047s1062.x
- Kneller, B., Mccaffrey, W.D., 2003. The interpretation of vertical sequences in turbidite beds: the influence of longitudinal flow. *Journal of Sedimentary Research*, **73**, 706–713.
- Kneller, B.C., Branney, M.J., 1995. Sustained high-density turbidity currents and the deposition of thick massive sands. *Sedimentology*, **42**, 607–616.
- Kneller, B.C., Nasr-Azadani, M., Radhakrishnan, S., Meiburg, E., 2016. Long-range sediment transport in the world's oceans by stably stratified turbidity currents. *Journal of Geophysical Research: Oceans*, **121**, 1–13. doi:10.1002/2016JC011978
- Kneller, C., Bennett, S.J., Mccaffrey, W.D., 1999. Velocity structure, turbulence and fluid stresses in Experimental Gravity Currents. *Journal of Geophysical Research*, **104**, 5381–5391.
- Krumbein, W.C., Aberdeen, E., 1937. The sediments of Barataria Bay. *Journal of Sedimentary Petrology*, **7**, 3–17.
- Krumbein, W.C., Sloss, L.L., 1963. Stratigraphy and sedimentation, Geology series. W. H. Freeman, San Francisco.
- Kuenen, P.H., Migliorini, C.I., 1950. Turbidity currents as a cause of graded bedding. *The Journal of Geology*, **58**, 91–127.
- Luthi, S., 1981. Experiments on non-channelized turbidity currents and their deposits. *Marine Geology*, **40**, 59–68.
- Macauley, R. V., Hubbard, S.M., 2013. Slope channel sedimentary processes and stratigraphic stacking, Cretaceous Tres Pisos Formation slope system, Chilean Patagonia. *Marine and Petroleum Geology*, **41**, 146–162. doi:10.1016/j.marpetgeo.2012.02.004
- Macellari, C.E., Barrio, C.A., Manassero, M.J., 1989. Upper Cretaceous to Paleocene depositional sequences and sandstone petrography of southwestern Patagonia (Argentina and Chile). *Journal of South American Earth Sciences*, **2**, 223–239.
- Maier, K.L., Fildani, A., Paull, C.K., Graham, S.A., McHargue, T.R., Caress, D.W., McGann, M., 2011. The elusive character of discontinuous deep-water channels: New insights from Lucia Chica channel system, offshore California. *Geology*, **39**, 327–330. doi:10.1130/G31589.1
- Maier, K.L., Fildani, A., Paull, C.K., McHargue, T.R., Graham, S. a., Caress, D.W., 2013. Deep-sea channel evolution and stratigraphic architecture from inception to abandonment from high-resolution Autonomous Underwater Vehicle surveys offshore central California. *Sedimentology*, **60**, 935–960. doi:10.1111/j.1365-3091.2012.01371.x
- Manley, P.L., Pirmez, C., Busch, W., Cramp, A., 1997. 3. Grain-size characterization of the Amazon Fan deposits and comparison to seismic facies units. *proceedings of the ocean drilling program, Scientific results*, **155**, 35–52.
- Maslin, M., Knutz, P.C., Ramsay, T., 2006. Millennial-scale sea-level control on avulsion events on the Amazon Fan. *Quaternary Science Reviews*, **25**, 3338–3345. doi:10.1016/j.quascirev.2006.10.012

- Metivier, F., Lajeunesse, E., Marie-Christine, C., 2005. Submarine Canyons in the Bathtub. *Journal of Sedimentary Research*, **75**, 6–11. doi:10.2110/jsr.2005.002
- Michael, N.A., Whittaker, A.C., Carter, A., Allen, P.A., 2014. Volumetric budget and grain-size fractionation of a geological sediment routing system: Eocene Escanilla Formation, south-central Pyrenees. *Bulletin of the Geological Society of America*, **126**, 585–599. doi:10.1130/B30954.1
- Middleton, G., 1966. small-scale models of turbidity currents and the criterion for auto-suspension. *Journal of Sedimentary Petrology*, **36**, 202–208.
- Middleton, G., Southard, J.B., 1984. Mechanics of sediment movement. SEPM short course lecture notes No. 3. Tulsa, OK.
- Migeon, S., Mulder, T., Savoye, B., Sage, F., 2012. Hydrodynamic processes, velocity structure and stratification in natural turbidity currents: Results inferred from field data in the Var Turbidite System. *Sedimentary Geology*, **245–246**, 48–62. doi:10.1016/j.sedgeo.2011.12.007
- Mohrig, D., Buttles, J., 2007. Deep turbidity currents in shallow channels. *Geology*, **35**, 155–158. doi:10.1130/G22716A.1
- Morris, E., Hodgson, D., Flint, S.S., Brunt, R., Butterworth, P., Verhaeghe, J., 2014. Sedimentology, Stratigraphic Architecture, and Depositional Context of Submarine Frontal-Lobe Complexes. *Journal of Sedimentary Research*, **84**, 763–780.
- Niño, Y., Lopez, F., Garcia, M., 2003. Threshold for particle entrainment into suspension. *Sedimentology*, **50**, 247–263.
- Normark, W.R., 1978. Fan valleys, channels, and depositional lobes on modern submarine fans: characters for recognition of sandy turbidite environments. *AAPG Bulletin*, **62**, 912–931.
- Normark, W.R., 1970. Growth patterns of deep-sea fans. *AAPG bulletin*, **54**, 2170–2195.
- Normark, W.R., Damuth, J.E., 1997. sedimentary facies and associated depositional elements. *proceedings of the ocean drilling program, Scientific results*, **155**, 531–538.
- Ortiz-Karpf, A., Hodgson, D.M., McCaffrey, W.D., 2015. The role of mass-transport complexes in controlling channel avulsion and the subsequent sediment dispersal patterns on an active margin: the Magdalena Fan, offshore Colombia. *Marine and Petroleum, Geology*, **64**, 58–75. doi:10.1016/j.marpetgeo.2015.01.005
- Paola, C., Martin, J.M., 2012. Mass-Balance Effects In Depositional Systems. *Journal of Sedimentary Research*, **82**, 435–450. doi:10.2110/jsr.2012.38
- Paola, C., Straub, K., Mohrig, D., Reinhardt, L., 2009. The “unreasonable effectiveness” of stratigraphic and geomorphic experiments. *Earth-Science Reviews*, **97**, 1–43. doi:10.1016/j.earscirev.2009.05.003
- Parsons, J., Garcia, M., 1998. Similarity of gravity current fronts. *Physics of Fluids*, **10**, 1–5.
- Paull, C.K., Ussler III, W., Caress, D.W., Lundsten, E., Covault, J. a., Maier, K.L., Xu, J., Augenstein, S., 2010. Origins of large crescent-shaped bedforms within the axial channel of Monterey Canyon, offshore California. *Geosphere*, **6**, 755–774. doi:10.1130/GES00527.1
- Peakall, J., Ashworth, P., Best, J., 1996. Physical modelling in fluvial geomorphology: principles, applications and unresolved issues, in: Rhoads, B.L. and Thorn, C.E., J. (Ed.), *The Scientific Nature of Geomorphology*. John Wiley and Sons, pp. 221–253.
- Peakall, J., McCaffrey, B., Kneller, B., 2000. A Process Model for the Evolution, Morphology, and Architecture of Sinuous Submarine Channels. *Journal of Sedimentary Research*, **70**, 434–448. doi:10.1306/2DC4091C-0E47-11D7-8643000102C1865D
- Pemberton, E.A.L., Hubbard, S.M., Fildani, A., Romans, B., Stright, L., 2016. The stratigraphic expression of decreasing confinement along a deep-water sediment routing system: Outcrop example from southern Chile. *Geosphere*, **12**, 114–134. doi:10.1130/GES01233.1
- Pettingill, H.S., Weimer, P., 2002. Worldwide deepwater exploration and production: Past, present, and future. *The Leading Edge*, **21**, 371–376.

- Pickering, K., Hiscott, R., 2015. Deep Marine Systems: Processes, Deposits, Environments, Tectonic and Sedimentation. John Wiley & Sons. p. 696
- Picot, M., Droz, L., Marsset, T., Dennielou, B., Bez, M., 2016. Controls on turbidite sedimentation: Insights from a quantitative approach of submarine channel and lobe architecture (Late Quaternary Congo Fan). *Marine and Petroleum Geology*, **72**, 423–446. doi:10.1016/j.marpetgeo.2016.02.004
- Piper, D.J.W., Cochonat, P., Morrison, M.L., 1999. The sequence of events around the epicenter of the 1929 Grand Banks earthquake: Initiation of debris flows and turbidity currents inferred from sidescan sonar. *Sedimentology*, **46**, 79–97.
- Pirmez, C., Beaubouef, R.T., Friedman, S.J., Mohrig, D., 2000. Equilibrium Profile and Baselevel in Submarine Channels: Examples from Late Pleistocene Systems and Implications for the Architecture of Deepwater Reservoirs, in: Global Deep-Water Reservoirs: Gulf Coast Section SEPM Foundation 20th Annual Bob F. Perkins Research Conference. pp. 782–805.
- Pirmez, C., Imran, J., 2003. Reconstruction of turbidity currents in Amazon Channel. *Marine and Petroleum Geology*, **20**, 823–849. doi:10.1016/j.marpetgeo.2003.03.005
- Posamentier, H.W., Kolla, V., 2003. Seismic geomorphology and stratigraphy of depositional deep-water deposits 383. *Journal of Sedimentary Research*, **73**, 367–388. doi:10.1306/111302730367
- Prather, B.E., O'Byrne, C., Pirmez, C., Sylvester, Z., 2016. Sediment partitioning, continentalslopesand base-of-slope systems. *Basin Research*, **29**, 1–23. doi:10.1111/bre.12190
- Romans, B.W., Fildani, a., Hubbard, S.M., Covault, J. a., Fosdick, J.C., Graham, S. a., 2011. Evolution of deep-water stratigraphic architecture, Magallanes Basin, Chile. *Marine and Petroleum Geology*, **28**, 612–628. doi:10.1016/j.marpetgeo.2010.05.002
- Rouse, H., 1937. Modern Conceptions of the Mechanics of Fluid Turbulence. *Transactions of the American Society of Civil Engineers*, **102**, 463–505.
- Rowland, J.C., Hilley, G.E., Fildani, a., 2010. A Test of Initiation of Submarine Leveed Channels by Deposition Alone. *Journal of Sedimentary Research*, **80**, 710–727. doi:10.2110/jsr.2010.067
- Shields, A., 1936. Anwendung der Aehnlichkeitsmechanik und der Turbulenzforschung auf die Geschiebebewegung, Mitteilungen der Preussischen Versuchsanstalt fur Wasserbau und Schiffbau. Berlin, Germany.
- Smith, J.D., Mclean, S.R., 1977. Spatially Averaged Flow Over a Wavy Surface. *Journal of Geophysical Research*, **82**, 1735–1746.
- Sømme, T.O., Jackson, C.A.L., 2013. Source-to-sink analysis of ancient sedimentary systems using a subsurface case study from the Møre-Trøndelag area of southern Norway: Part 2 - sediment dispersal and forcing mechanisms. *Basin Research*, **25**, 512–531. doi:10.1111/bre.12014
- Southard, J.B., 1991. Experimental determination of bed-form stability. *Annual Review of Earth and Planetary Sciences*, **19**, 423–455.
- Spinewine, B., Sun, T., Babonneau, N., Parker, G., 2011. Self-similar long profiles of aggrading submarine leveed channels: Analytical solution and its application to the Amazon channel. *Journal of Geophysical Research: Earth Surface*, **116**, 1–15. doi:10.1029/2010JF001937
- Spychala, Y.T., Hodgson, D.M., Stevenson, C.J., Flint, S.S., 2017. Aggradational lobe fringes: The influence of subtle intrabasinal seabed topography on sediment gravity flow processes and lobe stacking patterns. *Sedimentology*, **64**, 582–608. doi:10.1111/sed.12315
- Stacey, M.W., Bowen, A.J., 1988. The vertical structure of density and turbidity currents: theory and observations. *Journal of Geophysical Research*, **93**, 3528–3542.
- Stevenson, C., Talling, P.J., Sumner, E.J., Masson, D.G., Frenz, M., Wynn, R., 2014. On how thin submarine flows transported large volumes of sand for hundreds of kilometres across a flat basin plain without eroding the sea floor. *Sedimentology*, **61**, 1982–2019. doi:10.1111/sed.12125

- Stevenson, C.J., Jackson, C.A.-L., Hodgson, D.M., Hubbard, S.M., Eggenhuisen, J.T., 2015. Deep-Water Sediment Bypass. *Journal of Sedimentary Research*, **85**, 1058–1081. doi:10.2110/jsr.2015.63
- Stevenson, C.J., Talling, P.J., Wynn, R.B., Masson, D.G., Hunt, J.E., Frenz, M., Akhmetzhanov, A., Cronin, B.T., 2013. The flows that left no trace : Very large-volume turbidity currents that bypassed sediment through submarine channels without eroding the sea floor. *Marine and Petroleum Geology*, **41**, 186–205. doi:10.1016/j.marpetgeo.2012.02.008
- Straub, K.M., Mohrig, D., 2008. Quantifying the morphology and growth of levees in aggrading submarine channels. *Journal of Geophysical Research: Earth Surface*, **113**, 1–20. doi:10.1029/2007JF000896
- Straub, K.M., Mohrig, D., McElroy, B., Buttles, J., Pirmez, C., 2008. Interactions between turbidity currents and topography in aggrading sinuous submarine channels: A laboratory study. *Geological Society of America Bulletin*, **120**, 368–385. doi:10.1130/B25983.1
- Straub, K.M., Mohrig, D., Pirmez, C., 2012. Architecture of an aggradational tributary submarine channel network on the continental slope offshore Brunei Darussalam. *SEPM Special publication*, **99**, 145–161.
- Strong, N., Sheets, B., Hickson, T., Paola, C., 2005. A mass-balance framework for quantifying downstream changes in fluvial architecture, in: Blum, M., Marriott, S., Leclair, S. (Eds.), *Fluvial Sedimentology VII* (Special Publication 35 of the IAS). Blackwell publishing Ltd., pp. 243–253. doi:10.1002/9781444304350.ch14
- Sun, T., Ghayour, K., Hall, B., Miller, J., 2011. Process-Based Modeling of Deep Water Depositional Systems, in: *Proceedings of the 30 Th GCSSEPM Foundation Bob F Perkins Research Conference*.
- Sylvester, Z., Deptuck, M.E., Prather, B.E., Pirmez, C., O'Byrne, C., 2012. Seismic Stratigraphy of a Shelf-Edge Delta and Linked Submarine Channels in the Northeastern Gulf of Mexico. Application of the Principles of Seismic Geomorphology to Continental-Slope and Base-of-Slope Systems: Case Studies from Seafloor and Near-Seafloor Analogues 99, pp. 31–59. doi:10.2110/pec.12.99.0031
- Sylvester, Z., Lowe, D.R., 2004. Textural trends in turbidites and slurry beds from the Oligocene flysch of the East Carpathians, Romania. *Sedimentology*, **51**, 945–972. doi:10.1111/j.1365-3091.2004.00653.x
- Symons, W.O., Sumner, E.J., Paull, C.K., Cartigny, M.J.B., Xu, J.P., Maier, K.L., Lorenson, T.D., Talling, P.J., 2017. A new model for turbidity current behavior based on integration of flow monitoring and precision coring in a submarine canyon. *Geology*, **45**, 367–370. doi:10.1130/G38764.1
- Talling, P.J., Allin, J., Armitage, D.A., Arnott, R.W., Cartigny, M.J., Clare, M.A., Felletti, F., Covault, J.A., Girardclos, S., Hansen, E., Hill, P.R., Hiscott, R.N., Hogg, A.J., Hughes Clarke, J., Jobe, Z.R., Malgesini, G., Mozzato, A., 2015. Key Future Directions for Research on Turbidity Currents and Their Deposits. *Journal of Sedimentary Research*, **85**, 153–169. doi:10.2110/jsr.2015.03
- Talling, P.J., Masson, D.G., Sumner, E.J., Malgesini, G., 2012. Subaqueous sediment density flows: depositional processes and deposit types. *Sedimentology*, **59**, 1937–2003.
- Talling, P.J., Wynn, R.B., Masson, D.G., Frenz, M., Cronin, B.T., Schiebel, R., Akhmetzhanov, A.M., Dallmeier-Tiessen, S., Benetti, S., Weaver, P.P.E., Georgiopoulou, A., Zühlsdorff, C., Amy, L.A., 2007. Onset of submarine debris flow deposition far from original giant landslide. *Nature*, **450**, 541–544. doi:10.1038/nature06313
- Tilston, M., Arnott, R.W.C., Rennie, C.D., Long, B., 2015. The influence of grain size on the velocity and sediment concentration profiles and depositional record of turbidity currents. *Geology*, **43**, 839–842. doi:10.1130/G37069.1
- Van der Merwe, W.C., Hodgson, D.M., Brunt, R.L., Flint, S.S., 2014. Depositional architecture of sand-attached and sand-detached channel-lobe transition zones on an exhumed stepped slope mapped over a 2500 km² area. *Geosphere*, **10**, 1076–1093. doi:10.1130/GES01035.1
- Van Rijn, L., 1984. Sediment transport, part 2: Suspended load transport. *Journal of Hydraulic Engineering*, **110**, 1613–1641.
- Van Rijn, L.C. Van, 1993. Principles of Sediment Transport in Rivers , Estuaries and Coastal Seas. Aqua publications, Blokzijl, The Netherlands.
- Vanoni, V. a., 2006. Sedimentation Engineering. *ASCE Manual of Practice*, **54**, 1–431. doi:10.1061/9780784408230

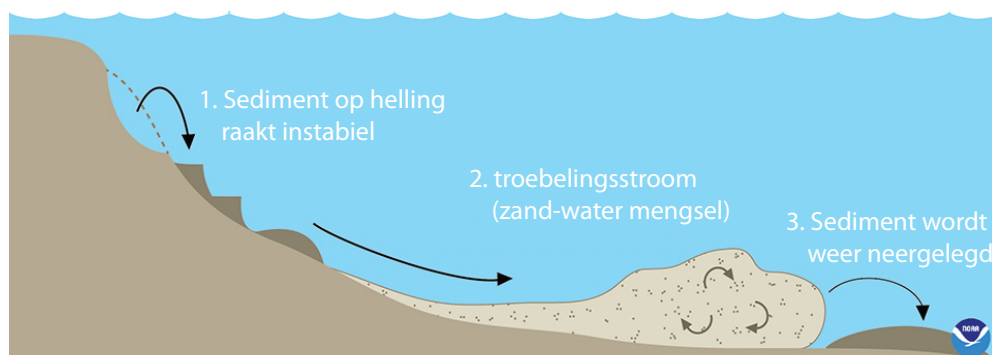
- Vanoni, V. a., 1946. Transportation of Suspended Sediment by Water. *Transactions of the American Society of Civil Engineers*, **111**, 67–102.
- Weill, P., Lajeunesse, E., Devauchelle, O., 2014. Experimental investigation on self-channelized erosive gravity currents. *Journal of Sedimentary Research*, **84**, 487–498.
- Xu, J.P., Barry, J.P., Paull, C.K., 2013. Small-scale turbidity currents in a big submarine canyon. *Geology*, **41**, 143–146. doi:10.1130/G33727.1
- Xu, J.P., Noble, M. a., Rosenfeld, L.K., 2004. In-situ measurements of velocity structure within turbidity currents. *Geophysical Research Letters*, **31**, L09311. doi:10.1029/2004GL019718
- Xu, J.P., Sequeiros, O.E., Noble, M.A., 2014. Sediment concentrations, flow conditions, and downstream evolution of two turbidity currents, Monterey Canyon, USA. *Deep-Sea Research Part I: Oceanographic Research Papers*, **89**, 11–34. doi:10.1016/j.dsr.2014.04.001
- Yu, B., Cantelli, A., Marr, J., Pirmez, C., O'Byrne, C., Parker, G., 2006. Experiments on Self-Channelized Subaqueous Fans Emplaced by Turbidity Currents and Dilute Mudflows. *Journal of Sedimentary Research*. **76**, 889–902 doi:10.2110/jsr.2006.069

Samenvatting

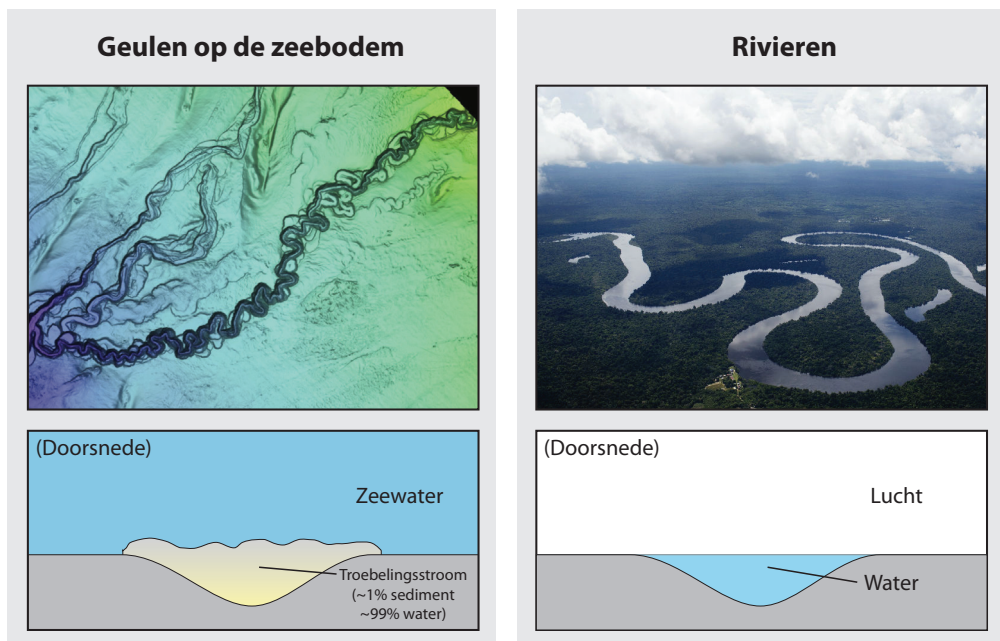
“Rivieren” op de zeebodem

Gebergten en hooggelegen gebieden zijn onderhevig aan erosie en dit vormt de bron van het sediment dat wordt getransporteerd door rivieren. Sediment kan onder andere bestaan uit kiezels, zand en klei. Wanneer rivieren uitmonden in zee wordt het meegevoerde sediment in eerste instantie vaak neergelegd in de buurt van de kust. Door verschillende oorzaken kan het sediment dat zich zo ophoopt echter weer in beweging komen. Golven tijdens een storm kunnen de zeebodem in de buurt van de kust bijvoorbeeld omwoelen of een aardbeving kan ervoor zorgen dat sediment op een helling op de zeebodem begint te schuiven. Wanneer dit gebeurt kunnen er op de zeebodem lawines van sediment vermengd met water ontstaan. Deze lawines worden troebelingsstromen genoemd (in het Engels: turbidity currents) (Figuur 1). Deze troebelingsstromen zijn soms zo krachtig dat ze pijpleidingen en communicatiekabels op de zeebodem kunnen breken. Net als bij sneeuwlawines in de bergen zijn er dus lange periodes waarin er niks gebeurt en korte episodes met krachtige stroming veroorzaakt door het plotseling instabiel worden van hellingmateriaal. Doordat troebelingsstromen een hogere dichtheid hebben dan zeewater, verplaatsen ze zich over de hellingen van de zeebodem naar het diepste deel van de oceaan. Richting de diepere oceaan nemen de hellingen van de zeebodem en de stroomsnelheid langzaam af en daardoor wordt het meegevoerde sediment weer neergelegd (Figuur 1). Op deze manier ontstaan er nieuwe lagen van sediment op de zeebodem. Vervolgens kan het losse sediment door de toenemende druk bij verdere begraving in gesteente veranderen.

Tot halverwege de twintigste eeuw was er maar weinig over troebelingsstromen bekend omdat ze door hun voorkomen op grote diepte in de oceaan moeilijk te onderzoeken waren. Sindsdien is duidelijk geworden dat troebelingsstromen in alle oceanen voorkomen en dat gesteentelagen die door dit proces zijn ontstaan wijdverbreid zijn. Uit onderzoek is onder andere gebleken dat troebelingsstromen lange geulen vormen op de zeebodem. Deze geulen zijn vaak honderden tot duizenden kilometers lang en zorgen ervoor dat troebelingsstromen grote afstanden kunnen afleggen zonder het meegevoerde sediment te verliezen. Deze geulen zijn in veel opzichten vergelijkbaar met rivieren die op land voorkomen (Figuur 2). Beide bepalen ze de route waarlangs grote hoeveelheden sediment worden verplaatst en beide zijn ze in veel gevallen kronkelend



Figuur 1: Schematische weergave van het transport van sediment van de rand van een continent naar de diepe oceaan door een troebelingsstroom. Afbeelding afkomstig van: oceanservice.noaa.gov.



Figuur 2: *Vergelijking tussen geulen op de zeebodem die zijn gevormd door een troebelingsstromen (links) en een meanderende rivier op land (rechts) met daaronder een schematische doorsnede van elk. Qua uiterlijk zijn er duidelijke overeenkomsten tussen de twee maar de aard van de stroming is verschillend: troebelingsstromen bevinden zich volledig onder water en daardoor is het verschil in dichtheid met de omgeving relatief klein.*

(meanderend). Een fundamenteel verschil met rivieren is echter dat geulen op de zeebodem zich volledig onder water bevinden. Daardoor is het verschil in dichtheid tussen de stroming in de geul en de omgeving relatief gering. Bovendien ondervinden de troebelingsstromen veel weerstand aan de bovenkant door wrijving met stilstaand zeewater. Deze verschillen hebben consequenties voor de manier waarop de geulen zich ontwikkelen en het type afzettingen dat rond de geul ontstaat. Het is echter moeilijk om de ontwikkeling van geulen op de zeebodem onder invloed van troebelingsstromen waar te nemen. Het meten van troebelingsstromen op de zeebodem is vooral lastig doordat ze met grote tussenpozen voorkomen en apparatuur op de zeebodem vaak wordt weggeslagen op het moment dat er een stroming plaatsvindt.

Geulen op de zeebodem en de troebelingsstromen die daar doorheen gaan zijn verantwoordelijk voor de zeer grootschalige verplaatsing van water, sediment en organisch materiaal over de bodem van de oceaan. Het onderzoek naar deze geulen is daarom om een aantal redenen van belang. Ten eerste blijkt dat er rond de geulen veel leven is op de zeebodem omdat troebelingsstromen voedingsstoffen en zuurstofrijk water aanvoeren. De geulen spelen daarom dus een rol in het ecosysteem van de oceanen. Ten tweede wordt er via de geulen veel zand getransporteerd. Dit zand kan op de zeebodem poreuze gesteentelagen vormen. Onder de juiste omstandigheden kunnen deze gesteentelagen vervolgens oliereservoirs worden. Bij het zoeken naar olie en gas onder de zeebodem is het daarom van belang om de locatie en eigenschappen

van de oliehoudende zandsteenlagen te kunnen voorspellen. Dit vergt een goed begrip van de processen die zand op de zeebodem verplaatsen.

Onderzoeksvragen in dit proefschrift

In deze studie ligt de nadruk op het begrijpen van de eigenschappen van troebelingsstromen in geulen op de zeebodem. De eigenschappen van de stromingen bepalen namelijk hoe de geulen zich ontwikkelen en welke gesteentelagen ontstaan op de zeebodem. Belangrijke vragen in deze context zijn: (1) hoe ontstaat een geul op een helling die oorspronkelijk egaal was? en (2) wat is de sedimentconcentratie in een troebelingsstroom in een geul en hoe is dit sediment verticaal verdeeld in de stroming? In dit proefschrift wordt gebruikgemaakt van verschillende methodes (experimenten, computermodellen en veldonderzoek) om antwoord te krijgen op deze vragen.

Vorming van geulen in experimenten

Schaalexperimenten in het laboratorium zijn een veelbelovende methode om troebelingsstromen te onderzoeken. In experimenten kunnen gedetailleerde waarnemingen worden gedaan waardoor het mogelijk is om de stromingsprocessen te relateren aan de evolutie van geulen en de eigenschappen van het neergelegde sediment. Wel moet rekening worden gehouden met schalingseffecten. Troebelingsstromingen op de zeebodem zijn namelijk tientallen tot honderden meters dik en het is niet haalbaar om op deze schaal te werken in het laboratorium. In eerdere experimenten bleek dat de relatief kleine troebelingsstromen in het laboratorium het meegevoerde sediment maar over een kleine afstand kunnen transporteren. In Hoofdstuk 2 van dit proefschrift wordt bekeken aan welke voorwaarden voldaan moet worden om ervoor te zorgen dat sediment voor een behoorlijke periode in transport blijft. Vervolgens werden experimenten gedaan waarin de juiste stromingscondities werden bereikt. De experimenten werden uitgevoerd in het Eurotank laboratorium in Utrecht. Hier staat een bak van 6 bij 11 meter die tijdens experimenten gevuld wordt met water om op schaal een oceaan na te bootsen. Vergelijken met gelijksoortige eerdere experimenten is de helling onder water steiler en is er een hogere anvoer van het zand-water mengsel dat een troebelingsstroom vormt. Tijdens de experimenten creëren troebelingsstromen spontaan een geul op de helling die zich onder water in de bak bevindt. Met behulp van de metingen tijdens de experimenten kunnen voor het eerst de interacties tussen de geulvorming en de stroming bestudeerd worden.

Doordat troebelingsstromen in veel gevallen over de rand van de geul heen stromen worden langs de geul vaak ruggen opgeworpen die oeverwallen heten. In Hoofdstuk 3 wordt gekeken naar de opbouw van deze oeverwallen en de relatie met de eigenschappen van de stroming in de geul. Naarmate de geul dieper wordt, kan een steeds kleiner deel van de stroming ontsnappen uit de geul. Daardoor nemen het volume en de korrelgrootte van de afzettingen op de oeverwal af. Met de experimenten tonen we aan dat de afname van de korrelgrootte van de oeverwallen goed valt te voorspellen als de verticale structuur van de stroming bekend is.

Stroming over de rand van de geul en bezinking van sediment naar de bodem van de geul zorgen ervoor dat er continu sediment onttrokken wordt aan troebelingsstromen. In Hoofdstuk 4 wordt aangetoond dat het volume en de korrelgrootteverdeling van het sediment dat onttrokken wordt sterk afhankelijk zijn van de breedte en diepte van de geul. Tijdens de evolutie van een geul veranderen de afmetingen continu en daardoor zal de fractie sediment die het diepste gedeelte van de oceaan bereikt dus ook veranderen.

Verdeling van sediment in troebelingsstromen

Uit de experimenten in de eerste hoofdstukken komt naar voren dat verticale verdeling van sediment in troebelingsstromen een belangrijke factor is die het gedrag van de stromingen bepaalt. Uit eerder onderzoek was al bekend dat de sedimentconcentratie en korrelgrootte afnemen met hoogte in troebelingsstromen. Twee factoren beïnvloeden de verdeling van het sediment in deze stromen: enerzijds zinken losse korrels onder invloed van de zwaartekracht naar de basis van de stroming, anderzijds zorgen wervelingen in de stroming (turbulentie) ervoor dat het sediment gemengd wordt. De balans hiertussen bepaalt hoe de verdeling van het sediment over de hoogte van de stroming eruitziet. Kleine korrels zoals kleideeltjes zinken maar langzaam naar beneden en worden daardoor homogeen gemengd terwijl grotere korrels zoals zand zich onder de meeste omstandigheden in het onderste deel van de stroming concentreren omdat ze sneller zinken. Troebelingsstromen vervoeren meestal een mengsel van fijner en grover sediment. In Hoofdstuk 5 wordt een eenvoudig computermodel gepresenteerd waarmee het profiel van concentratie en het profiel van korrelgrootte in de stroming voorspeld kunnen worden. De betrouwbaarheid van het model kunnen we bevestigen door de modelresultaten te vergelijken met metingen van troebelingsstromen uit laboratoriumexperimenten. Het model kan de metingen uit de experimenten vrij goed reproduceren. Daaruit concluderen we dat het model goed bruikbaar is om voorspellingen te doen in de natuur.

Vaak blijkt dat het neergelegde sediment rond een geul op de zeebodem geleidelijk fijnkorreliger wordt met hoogte boven de as van de geul. Dit is op verschillende plekken aangetoond door monsters te nemen van de zeebodem rond een geul. De neergelegde sedimenten rond de geul vormen daarmee een afspiegeling van de structuur van troebelingsstromen die door deze geulen hebben gestroomd. In sommige gevallen worden gesteentelagen die oorspronkelijk op de zeebodem zijn gevormd tijdens gebergtevorming omhoog gebracht en zijn ze in het landschap te bestuderen. In Hoofdstuk 6 wordt een studie gepresenteerd naar geulafzettingen in Chili die op deze manier zijn ontstaan. Ook voor deze geulafzettingen kunnen we laten zien dat het sediment in de as van de geul grofkorreliger is dan het sediment op de hooggelegen flanken van de geul. Met behulp van het computermodel uit hoofdstuk 5 hebben we vervolgens gereconstrueerd wat de eigenschappen van de stroming moeten zijn geweest om de verticale afname in korrelgrootte te verklaren. De resultaten van het model worden gebruikt om een inschatting te maken van de samenstelling en hoeveelheid sediment dat door de geul getransporteerd wordt. Door gegevens die verzameld zijn bij het veldwerk te combineren met een computermodel kan dus een inschatting worden gemaakt van de eigenschappen van troebelingsstromen die vele miljoenen jaren geleden hebben plaatsgevonden.

Acknowledgements

Many people have supported me during the past four years and helped me in one way or another to deliver this thesis.

First of all, I thank my daily supervisor Joris Eggenhuisen who gave me the opportunity to carry out my PhD project and to develop myself as a researcher. It was particularly inspiring to hear you talk in a passionate way about a sedimentary structure, a model result or the behaviour of a grain of sand. In total, we were on the road together for several months during the last four years. I really appreciated your company on the trips to Chile, South-Africa, Spain, the USA and other places.

I also thank my promotor Poppe de Boer and my co-promotor Matthieu Cartigny. Poppe, thank you for the comments on my manuscripts and for regularly stopping by at the office. Matthieu, your inputs with emphasis on the process-perspective were really valuable. Thank you for your enthusiasm and the lively discussions.

I am grateful to the dissertation committee for the constructive comments on my work and the approval of the thesis: Michelle Bolla Pittaluga, Maarten Kleinhans, Wout Krijgsman, Allard Martinius and John Reijmer.

Steve Hubbard from the University of Calgary and Brian Romans from Virginia Tech introduced us in the field area in Chile. Without their help and knowledge of the area it would not have been possible to conduct this field study as part of my project.

The Sedimentology Group has rapidly expanded since I started my PhD and this has certainly made it a more enjoyable and inspiring place to work. Florian, Joana, João, Mike and Yvonne, thanks a lot for your company and interest in my work. Florian, I enjoyed working with you in the lab and in the field and all the discussions during that time. You also showed me how to work with German rigorousness and precision, which was really useful for me. Yvonne, thank you for your contributions to Chapters 4 and 6 of this thesis. I am sure that the Sedimentology Group has a bright future and I hope to stay in touch with you guys.

The rest of the department of Earth Sciences also contributed to a good working atmosphere. It was always nice to talk to you during the FEST drinks and other activities. A special thank you goes to the staff members that joined me on the student fieldworks to Aliaga in Spain. These trips were always a highlight of the year for me. It was great to be in the field with you and to have a big late-night dinner at the hotel of Jesus afterwards.

A number of students worked with me in the Eurotank to carry out the experiments. Nienke Berends, Martijn ter Braack, Maarten Heijnen and Patrick Michielsen, I have learned a lot from you (I hope you also learned a thing or two) and working with you made my time in the lab much more enjoyable.

I also thank Thony van der Gon Netscher and Henk van der Meer for their technical assistance. You helped me to realise the experiments by supplying me with custom-made parts and useful advice. I also appreciated all the work-related and non-work-related discussions in the lab.

Mijn vrienden wil ik bij deze graag bedanken voor de nodige afleiding van mijn werk. Iedereen van “jaartje 007” en aanhang, bedankt voor de weekendjes weg, feestjes, fietstochten, levend stratego en talloze andere activiteiten. Ook mijn oud-huisgenoten van de Amsterdamsestraatweg, bedankt voor alle gezelligheid en jullie vragen over mijn zandbak.

Mijn familie en schoonfamilie bedank ik voor de interesse en steun in de afgelopen jaren. Jullie aanmoediging op de achtergrond was heel belangrijk voor me. Francien en Suzanne, veel succes met jullie promotieprojecten! Ik weet zeker dat jullie er iets moois van maken.

Marianne, bedankt voor je liefde en rust. Ook je grapjes over die gekke geologen met hun hamers en stenen zie ik natuurlijk als een blijk van liefde. Hopelijk vind je het boekje mooi geworden. Ik ben klaar voor een nieuw avontuur!

Curriculum Vitae

Jan de Leeuw was born on the 28th of June 1988 in Amsterdam, the Netherlands. He grew up in Voorburg and attended the Athenaeum of the Huygens Lyceum there. In 2007 he started studying Earth Sciences at Utrecht University. During his master's he started working as a lab assistant in the Eurotank. There, he helped with turbidity-current experiments and became interested in this topic. For his MSc thesis he studied the sedimentology of Cretaceous continental slope deposits in Southern France. In July 2013 he started a one-year position as a junior researcher at the Department of Earth Sciences at Utrecht University. This position evolved into a full PhD project about submarine channels. During the project he spent much of his time in the lab where he carried out flume experiments to study the formation of submarine channels by turbidity currents. In order not to lose touch with actual rocks, he also studied submarine-channel deposits in field (in Chilean Patagonia). Additionally, he was a teaching assistant during various courses and field classes.



Left: the author with his earlier work. Right: the author more recently.

List of publications

- de Leeuw, J., Eggenhuisen, J.T., and Cartigny, M.J.B., 2016, Morphodynamics of submarine channel inception revealed by new experimental approach. *Nature Communications*, 7, 1-7
- Eggenhuisen, J.T., Cartigny, M.J.B., and de Leeuw, J., 2017, Physical theory for near-bed turbulent particle suspension capacity. *Earth Surface Dynamics*, 5, 69–281
- de Leeuw, J., Eggenhuisen, J.T., and Cartigny, M.J.B. (in revision) Linking submarine channel-levee facies and architecture to flow structure of turbidity currents; insights from flume tank experiments. *Sedimentology*
- de Leeuw, J., Eggenhuisen, J.T., Spychala, Y.T., Heijnen, M., Pohl, F. and Cartigny, M.J.B. (in preparation) Sediment volume and grain-size partitioning between submarine channel-levee systems and lobes: An experimental study.
- de Leeuw, J., Eggenhuisen, J.T., Pohl, F. and Cartigny, M.J.B. (in preparation) Turbulent diffusion modelling of grain-size segregation in polydisperse turbidity currents; an experimental validation and possibilities for application.
- de Leeuw, J., Eggenhuisen, J.T., Spychala, Pohl, F. and Cartigny, M.J.B. (in preparation) Reconstructing turbidity current flow properties from submarine channel deposits using stratification modelling; Application to the Gabriela Channel fill, Tres Pasos Formation, Chile,

